Single-Molecule Magnets and Magnetic Refrigerants from Polynuclear Manganese Complexes and Tripodal Ligands

Maria Manoli

A Thesis Submitted for the degree of

Doctor of Philosophy

School of Chemistry

Faculty of Science and Engineering

University of Edinburgh

April 2008

Abstract

We have investigated the coordination chemistry of the tripodal alcohols H_3thme, H_3tmp, H_3tea, Br-mpH_3, H_4peol and their analogues aepH_2 and ampH_2, with a particular focus on Manganese. In combination with other bridging/chelating ligands such as carboxylates or β-diketonates a plethora of polymetallic clusters whose topologies are based on shared triangular [Mn_3] units have been synthesized. In total twenty-five new complexes are reported. These are: a family of seven "rod-like" structures (**1-7**): $[Mn_6(OAc)_6(H_2tea)_2(tmp)_2]$ (**1**), $[Mn_6(OAc)_6(H_2tea)_2(thme)_2]$ (**2**), $[Mn_6(OAc)_6(H_2tea)_2(Hpeol)_2]$ (**3**), $[Mn_6(acac)_4(OAc)_2(Htmp)_2(aep)_2]$ (**4**), $[Mn_6(OAc)_8(tmp)_2(py)_4]$ (**5**), $[Mn_6(OAc)_8(thme)_2(py)_4]$ (**6**), $[Mn_{12}(Hthme)_8(thme)_2(py)_2Br_8]$ (**7**); a family of "wheel-like" structures (**8-10**): $[Mn_{16}O_2(OMe)_{12}(tmp)_8(OAc)_{10}]$ (**8**), $[Mn_{22}O_6(OMe)_{14}(OAc)_{16}(tmp)_8(HIm)_2]$ (**9**), $[Mn_{22}O_6(OMe)_{14}(OAc)_{16}(Br\text{-}mp)_8(HIm)_2]$ (**10**); two supertedrahedra (**11-12**): $[Mn_{10}O_4Br_4(amp)_6(ampH_2)_3(HampH_2)]Br_3$ (**11**), $[Mn_{10}O_4(OH)_{1.8}I_{2.2}(amp)_6(ampH_2)(HampH_2)_3]I_5$ (**12**); a family of deca- and tetradecametallic "planar-discs" (**13-15**): $[Mn_{10}(OH)_6(amp)_4(ampH)_4I_4(EtOH)_4]I_4$ (**13**), $[Mn_{10}(OH)_6(aep)_4(aepH)_4I_4(EtOH)_4]I_4$ (**14**), $[Mn_{14}(OH)_2(Hpeol)_4(H_2peol)_6I_4(EtOH)_6]I_4$ (**15**); octahedral polymers: $Na_4[Mn_6O(OAc)_6(Br\text{-}mp)_4(MeOH)_4]$ (**16**), $Na_3[Mn_6O(OAc)_5(tmp)_4(N_3)(H_2O)_2]$ (**17**); edge-sharing bioctahedra: $[Mn_{10}O_2Br_4(thme)_6(MeOH)_4]$ (**18**), $[Mn_{12}O_2(piv)_{10}(tmp)_4(MeO)_2(MeOH)_2]$ (**19**), $[Mn_{12}O_2(piv)_{10}(thme)_4(MeO)_2(MeOH)_2]$ (**20**), $[Mn_{12}O_2(OAc)_{10}(Hpeol)_4(MeO)_2(H_2O)_4]$ (**21**), $[Mn_{12}O_2(OAc)_{10}(thme)_4(MeO)_2(H_2O)_4]$ (**22**), $[Mn_{12}O_2(OAc)_{10}(tmp)_4(MeO)_2(H_2O)_4]$ (**23**), $[Mn_{12}O_2(O_2CCPh_2)_{10}(Hpeol)_4(MeO)_2(H_2O)_2]$ (**24**), $[Mn_{12}O_2(O_2CCPh_2)_{10}(Hpeol)_4(OH)_2(H_2O)_2]$ (**25**); and a bioctahedral polymer: $Na[Mn_{12}O_2(OAc)_{11}(Hpeol)_4(MeO)(OH)(H_2O)_3]$ (**26**). Studies of the magnetic properties of **1-10** and **16-25** show that **5**, **6**, **8-10** and **19-26** are single molecule magnets, whilst complexes **11-15** display an enhanced magnetocaloric effect (MCE)

and have great potential as efficient magnetic refrigerants in low temperature applications.

Acknowledgements

I would like to thank Dr. Euan. K. Brechin for his excellent supervision during this project. I am particularly grateful for the help and the freedom to develop my ideas for the project. Moreover, I would like to thank him for the opportunity he gave me to attend two excellent conferences where I presented a poster in Victoria (British Coloumbia 2006) and gave a talk in Syros Island (Greece 2007). Ta!!! You've been a great boss and friend!!

The starting of my PhD and my everyday work would not have been the same without Dr. Costas. J. Milios. He was both teacher and friend and he helped me with my settling in Edinburgh, to improve my language skills and more importantly my skills in synthesis and the basic theories. "Ευχαριστώ ρε τον Λάκη!!!"

A big thank you goes to the Brechin group: Ian, Alessandro, Giorgos, Cedric, Richard, Ross and Dr. Leigh Jones for being nice colleagues and making my 3 years in the lab easier with funny discussions irrelevant to Chemistry, for the help with problems I faced on (especially with computers) and for working together in peace (even though we argued because the lab was always a mess☺).

I would like to particularly thank Prof. Simon Parsons and his group (past and present members): Dr. Anna Collins, Dr. Stephen Moggach, Dr. Francesca Fabbiani, Peter Wood, Frazer White, Alessandro Prescimonne, Russel Johnstone and Laura Budd) for solving my huge and terrible crystal structures!!

At this point I would like to thank all the Scientists I have worked with and/or helped analyse my samples: Dr. Marco Evangelisti for the MCE measurements; Prof. Wersdorfer Wolfgang for the single-crystal hysteresis and relaxation measurements; Prof. George Christou (Ahbudaya and Rashmi from his group) and Dr. Mark Murrie for some magnetic measurements; Sylvia Williamson for elemental analysis and Lorna Eades for ICP-OES.

Apart from the co-workers, a significant role in these past three years, has been played by my friends. I would like to thank firstly the four very special friends I met here: the first one I met Cecile (my "angel"), then Pilar Calatayud and Daniela

Natale (my "sisters") and my second flatmate Eleni Tsalapati (Μαρήήή!!). Also all the Italian/Spanish/French/Greek etc communities that I've met here: Emiliano, Michele, Alex, Giai, Gioseppe, Laurent, Beatriz, Thahn, Fred, Mourad, Christoph, Marc, Tijana, Anna, Jone, the two Havier, Lewis, Iria, Isabel, Kery, Eleine, Myriam, Pekka, Jordan, Stefani, Vicky, Giorgos, Augoustinos (my special Cypriot brother), Jordi (my Spanish brother Julio) and more recently Giorgos (the special Χίος!!!) and Antonis (the chef). Of course I cannot forget to mention my special friend Mixalis (Dr. Michael Melchart) for helping, understanding, advising and being next to me in all the problems I faced especially on the starting of my PhD and in my life in Edinburgh. Also one BIG thank you goes to my Cypriot friends because even though there was a big distance separating us, there were always next to me, either by phone or visiting me: Christiana (Nana), Christy (Χριστόφιας), the 2 Andries (οι πούλλες μου), Artemis (Arta), Elena (Eleonora), Stauriana, Michellina, Pantelis (Lakis), Stelios, Paulos, Giorgos (το πουλλί), Cotsios, Dr. Anastasios Tassiopoulos and Eleni Moushi (the crazy company in the conferences in Canada and Greece!!! I hope we will do it again!!!). Thank you all!

The last and biggest thank you goes to my family (Ευχαριστώ μάμα, παπά, Ζετα, Αγγελε και Ευάγγελε μου!!) and my relatives. Nothing would have been the same without you!! Thanks for the great support and patience during these three years and I wish to be back with you soon!!

Declaration

I hereby declare that except where specific reference is made to other sources, the work contained in this thesis is the original work of the author. It has been composed by the candidate and has not been submitted, in whole or in part, for any other degree, diploma, or other qualification.

Contents

Abstract i

Acknowledgements iii

Declaration v

Contents vi

Abbreviations ix

Chapter 1: Introduction 1

Manganese Clusters 1

Single Molecule Magnets (SMMs) 2

SMMs of Manganese 8

- The $[Mn_{12}O_{12}(O_2CR)_{16}(H_2O)_x]^{n-}$ Family: The Prototype SMMs 10
- The $[Mn_6O_2(R\text{-}sao)_6(O_2CR')_2(ROH)_{4\text{-}6}]$ Family 11
- $[Mn_{84}O_{72}(OAc)_{78}(OMe)_{24}(OH)_6(MeOH)_{12}(H_2O)_{42}]$; A Giant SMM. 13

Magnetic Refrigerants and the Magnetocaloric Effect (MCE) 14

Use of $[Mn_3]$ Triangles as Starting Materials 17

Tripodal Alcohol Ligands 18

Project Aims 23

Physical Methods 23

X-ray Crystallography 23

Supporting information 24

References 24

Chapter 2: A Family of $[Mn_6]$ Complexes and a $[Mn_{12}]$ Complex Featuring Tripodal Ligands 29

Introduction 29

Experimental Section 30

- Synthetic Procedures 30

Results and Discussion 33

- Synthesis 33
- Description of structures 35

Magnetic Studies 52

- Dc Magnetic Studies 52
- Ac Magnetic Studies 56
- Single-Crystal Hysteresis Studies 57

Theoretical Studies 60

Conclusions 65

References 65

Chapter 3: High Spin Mn Wheels 68

Introduction 68

Experimental Section 70

- Synthetic Procedures 70

Results and Discussion 71

- Synthesis 71
- Description of structures 73

Magnetic Studies 82

- Dc Magnetic Studies 82
- Ac Magnetic Studies 85
- Single-Crystal Hysteresis Studies 88

Conclusions 92

References 92

Chapter 4: Ferromagnetic Mixed-Valent Mn Supertetrahedra and Planar Discs: Towards Low-Temperature Magnetic Refrigeration with Molecular Clusters 95

Introduction 95

Experimental Section 97

- Synthetic Procedures 97

Results and Discussion 98

- Synthesis 98

- Description of structures 99

Magnetic Studies 116

- Dc Magnetic Studies 116
- ZFC/FC and Heat Capacity measurements 119

Conclusions 124

References 125

Chapter 5: Magnetic Studies of Hexa-, Deca- and Dodeca-nuclear Manganese Complexes Based on Octahedra and Edge Sharing Bioctahedra 127

Introduction 127

Experimental Section 128

- Synthetic Procedures 128

Results and Discussion 130

- Synthesis 130
- Description of structures 132

Magnetic Studies 151

- Dc Magnetic Studies 151
- Ac Magnetic Studies 155
- Single-Crystal Hysteresis Studies 157

Conclusions 161

References 161

Conclusions 163

Publications A1

Conferences Attended A3

*** A cd with all the cif files and appendices (crystallographic tables) can be found in a case at the end of this thesis** cd

Abbreviations

ac	alternating current
acac	acetylacetylonate
AcO^-	acetate
$aepH_2$	2-amino-2-ethyl-1,3-propanediol
$ampH_2$	2-amino-2-methyl-1,3-propanediol
BVS	Bond Valence Sum
Br-mpH_3	2-(Bromomethyl)-2-(hydroxymethyl)-1,3-propanediol
dc	direct current
DFT	Density Functional Theory
FC	Field Cooled
HF-EPR	High Field-Electron Paramagnetic Resonance
EPR	Electron Paramagnetic Resonance
H_3tea	triethanolamine
H_3thme	1,1,1-tris(hydroxymethyl)ethane
H_3tmp	1,1,1-tris(hydroxymethyl)propane
H_4peol	pentaerythritol
INS	Inelastic Neutron Scattering
JT	Jahn-Teller
MCE	Magnetocaloric Effect
[Mn_6Et-sao]	$[Mn^{III}_6O_2(Et\text{-}sao)_6(O_2C(Me)_2Ph)_2(EtOH)_6]$
[Mn_{12}BrAc]	$[Mn_{12}O_{12}(O_2CCH_2Br)_{16}(H_2O)_4]$
[Mn_{12}OAc]	$[Mn_{12}O_{12}(OAc)_{16}(H_2O)_4]$
OEC	Oxygen Evolving Centre
PS II	Photosystem II
py	pyridine
s.e	symmetry equivalent
SMMs	Single Molecule Magnets
ZFC	Zero Field Cooled
ZFS	Zero Field Splitting

Chapter 1
Introduction

This thesis describes the strategies for the synthesis of polynuclear manganese complexes and is particularly focused on their magnetic properties. The majority of these complexes reported herein have two potential applications: a) as Single Molecule Magnets (SMMs) and b) as low temperature magnetic refrigerants.

An introduction to the importance and relevance of manganese clusters is described including the phenomenon of single-molecule magnetism and the magnetocaloric effect. In addition, the strategies used for the synthesis of these complexes - the use of tripodal alcohol ligands - are described.

Manganese Clusters

Recent years have witnessed enormous research activity in the field of manganese cluster chemistry, partly because of their relevance to the Mn complex at the water oxidation centre of photosystem II, and partly because some of them behave as nanoscale magnets.

The specific design and synthesis of *tetranuclear* Mn clusters, although of interest from a spin frustration perspective, has mainly been pursued in order to make models for the complex which is responsible for the oxidation of water in the oxygen evolving centre (OEC) of Photosystem II (PSII) in green plants and cyanobacteria. Recent crystallographic and polarised EXAFS studies on the PSII reaction centre of Thermosynechococcus elongatus confirm the cluster to be an oxide-bridged [Mn_4Ca] complex with (mainly) peripheral carboxylate ligation [1].

The discovery that a single molecule could behave like a tiny magnet was a major scientific breakthrough with widespread potential technological implications in high-density information storage and quantum computing. Single-Molecule Magnets (SMMs) represent the smallest possible magnetic device and thus a

molecular (or bottom-up) and hence controllable approach to nanoscale magnetism, where the energy barrier to magnetization reorientation is derived from the anisotropy of the molecular spin rather than the movement of domain walls, as in bulk magnets. The main requirements for observing such behaviour in molecules are a high spin ground state, S, and a significant negative zero-field splitting (D) of that ground state. The upper limit of the energy barrier (U) for the reorientation (reversal, relaxation) of the magnetization vector is given by $S^2|D|$ and $(S^2\text{-}1/4)|D|$, for integer and half-integer S values, respectively, and its magnitude, at least in part, controls the temperature below which magnetic hysteresis and bistability are observed. The ability of Mn to exist in a variety of oxidation states makes it a popular choice for SMM synthesis since even antiferromagnetic exchange in mixed-valent clusters is likely to lead to molecules with non-zero spin ground states and the presence of Mn(III) ions guarantees a suitable source of single ion anisotropy [2].

Single Molecule Magnets (SMMs)

The ability of certain molecular transition-metal clusters to be magnetized without need for long-range cooperative interactions was discovered in the early nineties [3]. The phenomenon was first seen in a coordination complex made of twelve oxide and acetate bridged manganese ions (Figure **1.1**), with formula $[Mn_{12}O_{12}(OAc)_{16}(H_2O)_4]$ (**1**) hereafter abbreviated as $[Mn_{12}OAc]$ [4]. The bulk magnetization as induced by an external magnetic field is retained upon removal of the latter thanks to the presence of an energy barrier (U) to the thermal equilibration of all possible quantized orientations of the molecular magnetic moment (Figure **1.2**), giving rise to a hysteresis curve below a certain blocking temperature (Figure **1.3**). Such orientations correspond to the various M_S components that result from the zero-field splitting of the spin ground state, S, of the cluster (Figure **1.4**). In this manner, superparamagnetic-like behaviour was shown unambiguously in discrete molecules, and these have now been given the name Single-Molecule magnets (SMMs). This

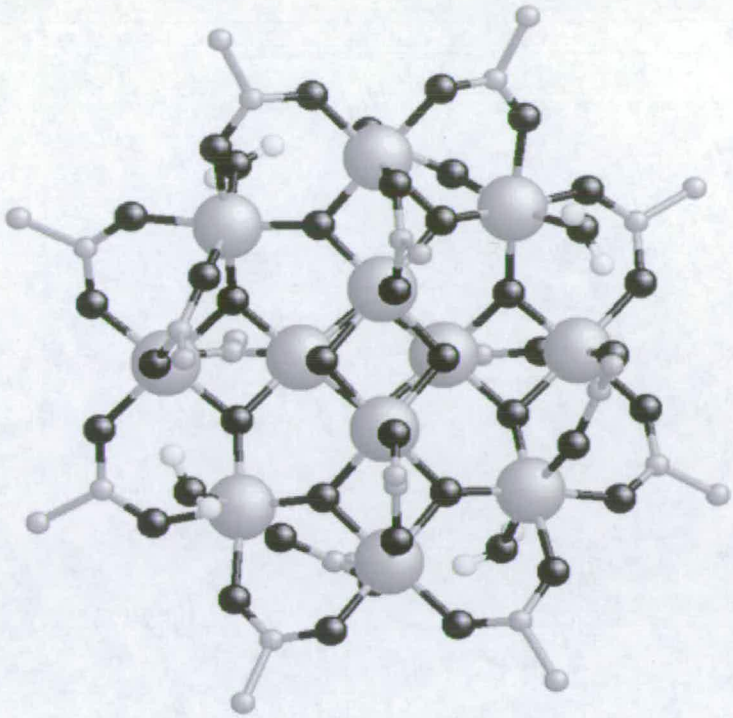

Figure 1.1. The structure of [$Mn_{12}OAc$] in the crystal.

discovery has great significance since it suggests the possibility of employing molecules as the smallest possible particle for the storage of a bit of magnetic information. The advent of single-molecule magnetism has stimulated a great deal of research in areas as diverse as physics, theoretical chemistry, spectroscopy, materials chemistry and synthetic coordination chemistry, as demonstrated by the several hundred papers published on the topic over the last twelve years. This effort has led to the experimental observation of the long-predicted phenomenon of quantum tunneling of the magnetization (QTM), and to detailed descriptions of the dynamics of relaxation of the magnetic moment in such systems [5]. The quantum tunneling takes place between the energetically matched levels on the opposite sides of the barrier (without climbing the barrier, Figure **1.5**) and leads to successive steps observed in hysteresis loops [6,7]. The magneto-crystalline anisotropy plays a significant role in these phenomena and is commonly described using an effective spin Hamiltonian of the form:

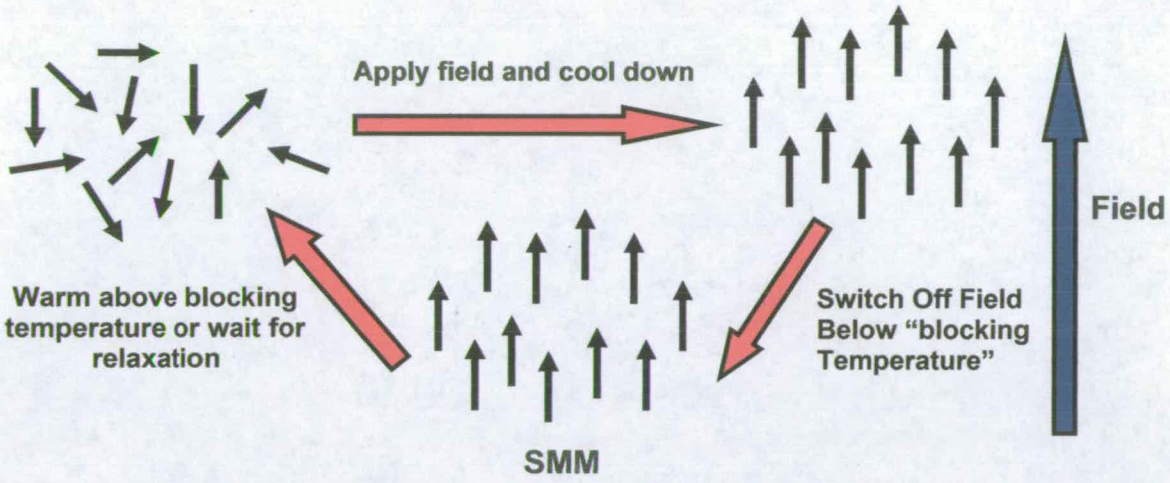

Figure 1.2. SMMs retain their spin orientation in the absence of a magnetic field

$$H=DS_z^2+E(S_x^2-S_y^2)+g\mu_B S\cdot H \qquad (1)$$

The first term is the axial anisotropy responsible for the energy barrier which separates "spin up" and "spin down" configurations as shown in Figure **1.5** [6]. At low temperature the thermally activated reversal of the magnetization follows an Arrhenius law and the characteristic time becomes macroscopically long. If it grows over the time needed to measure a hysteresis cycle, a remanent magnetization appears, with a coercive field which increases on lowering the temperature, as is shown in the example of [Mn_{12}OAc] in Figure **1.3**. A large temperature dependent remanent magnetization is observed and also almost equally spaced steps [7].

This step-like hysteresis is now considered the fingerprint of tunneling of the magnetization described in Figure **1.5a** [6]. The transverse (E) terms in the spin-Hamiltonian do not commute with the axial term at the origin of the barrier and admix the left and right well localized states, thus allowing an under-barrier mechanism. The extent of this delocalization is larger in the states close to the top of the barrier and maximum when the unperturbed levels on the opposite sides of the barrier are degenerate. In zero field (Figure **1.5a**) all the pairs coincide in energy and this corresponds to the most favourable condition to observe tunneling. Depending

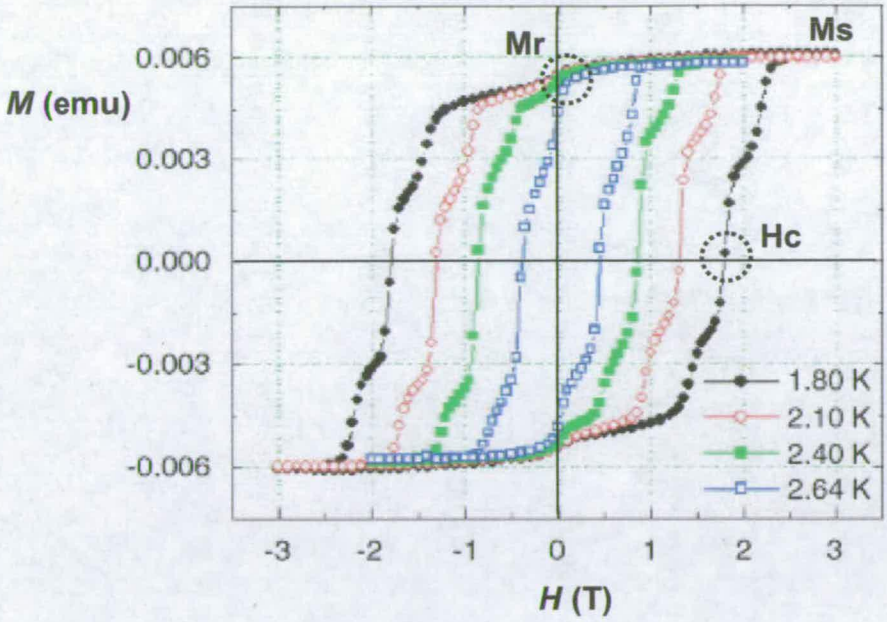

Figure 1.3. Hysteresis loops of the **[Mn_{12}OAc]** at 1.8, 2.1, 2.4, and 2.64 K, respectively. Hc, Mr and Ms stand for coercivity, remanent magnetization and saturation magnetization respectively.

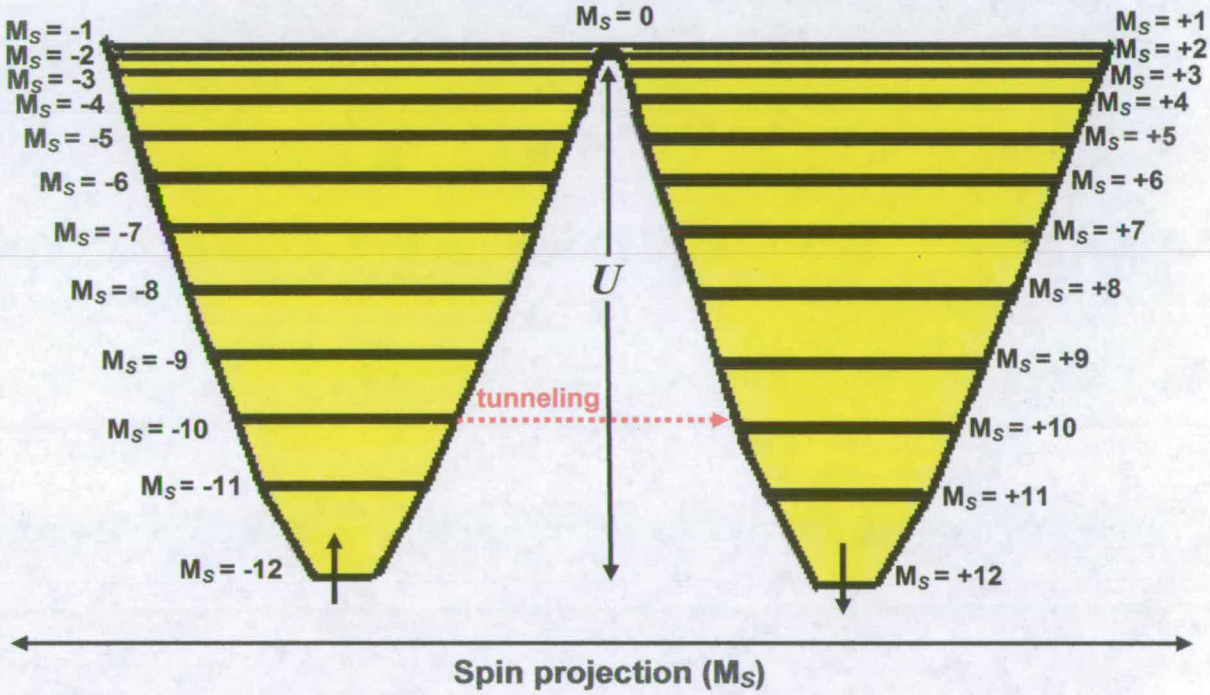

Figure 1.4. Energy diagram showing the relative positions of the zero-field split *Ms* levels of an S_T =12 system, the barrier mediating between the M_S = +12 and the M_S = -12 states and the quantum tunnelling (red line).

on the temperature and the thermal population of the levels, tunneling between the

ground states or levels higher in the barrier can compete with the thermally activated mechanism, and a "*short-cut*" of the barrier occurs with a significant acceleration of the magnetic relaxation. When a longitudinal field is applied the ±M*s* pairs are not in coincidence any more and tunneling is suppressed, as in Figure **1.5b**, except for critical values of H_z for which the levels are brought into resonance again. According to equation (1) pairs of levels are in resonance for $H_z = nD/g\mu_B$, with n integer (Figure **1.5c**). Acceleration of the relaxation due to tunneling occurs at these fields - corresponding to the steps in the hysteresis cycle [6].

Understanding and mastery of such quantum processes are of primary importance if SMMs are to be used as information storage devices or as qubits in

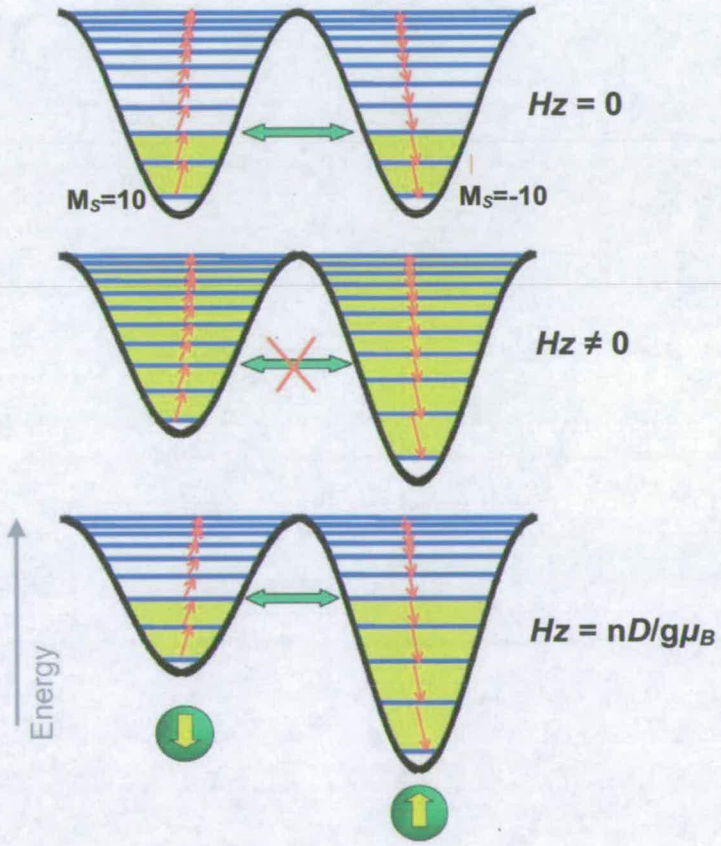

Figure 1.5. Energy levels splitting by an axial anisotropy of a system with $S = 10$ (a). Overcoming of the barrier can occur through a thermal activation or through a tunnel mechanism involving the ground doublet or thermally excited states. When an axial field is applied the levels on the opposite sides of the barrier are no more in coincidence (b) and tunneling is suppressed unless specific values of the field are reached (c).

quantum computers [8]. A remarkable achievement is the thorough description of the magnetic and electronic structure of several SMMs through the use of sophisticated techniques such as High-Field EPR [9], solid-state ^{55}Mn-NMR [10], ^{1}H-NMR [11] and ^{13}C-NMR [12], inelastic neutron scattering [13], and magnetic circular dichroism [14]. Invaluable knowledge about the properties of SMMs has also been obtained from the theoretical point perspective in form of density functional studies [15], employment of Monte Carlo methods [16] and *ab initio* calculations [17]. Much of the above progress has been made thanks to the work of synthetic chemists, who have provided the molecules of study for physicists, whose knowledge and work has, in turn, helped to highlight the next desirable synthetic targets. For example, it quickly became clear that in order to observe this behaviour from a molecular compound it is necessary to have a large spin ground state, S, and a large and negative zero-field splitting of that ground state (Figure **1.4**). The energy barrier U is proportional to $S^2|D|$ (integer spin) or $(S^2 - ¼)|D|$ (half-integer spin). Despite the large number of SMMs prepared since the property was first discovered, the value of U_{eff} in $[Mn_{12}OAc]$ (~64 K, $T_b \sim 3.5$ K) has only recently been surpassed by a family of heaxanuclear Mn(III) complexes of general formula $[Mn_6O_2(R\text{-}saoH_2)_6(O_2CR')_2(solvent)_{4\text{-}6}]$ (where $saoH_2$ = salicylaldoxime and R = H, Me, Et, Ph, etc; Scheme **1.1**) with $U_{eff} \sim 86$ K ($T_b \sim 5$ K) [18,19]. This "blocking temperature" (T_b) being very low (< 5 K) remains the main obstacle to some of the potential applications of SMMs. Important advances have also been made in other aspects; for example, the ground state spin number has risen to a record value of $S_T = 51/2 \pm 1$ in a $[Mn_{25}O_{18}(OH)_2(N_3)_{12}(pdm)_6(pdmH)_6]$ SMM [20]. Also, the family of compounds has been extended to various other metals besides manganese, including iron, vanadium, cobalt, nickel and, very recently, combinations of 3*d* with 4*d* [21], 5*d* [22] and 4*f* [23] paramagnetic ions.

Different methodologies towards the molecular assembly of such coordination compounds have been put to use. Of these, the most prolific has been serendipitous self-assembly [24]. In this method, ligands capable of coordinating to one or more ions in a variety of modes are mixed with metal salts or compounds in a

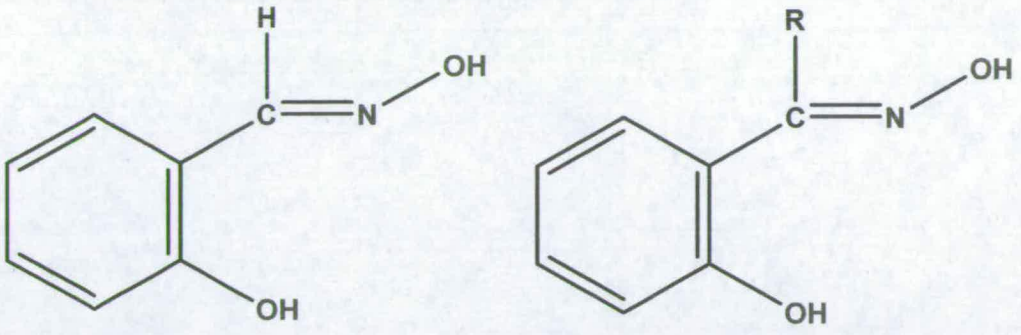

$saoH_2$ $RsaoH_2$, (R=Me, Et, Ph)

Scheme 1.1. The structural formulae of the main ligands discussed in the text.

solvent where the precise outcome is rarely predicted. Conditions can be created however for the isolation of discrete polynuclear species that, in many instances, will display interesting magnetic properties. An alternative strategy, which has proven to be more challenging, can be termed "rational molecular design". In this approach the components of the reaction system display lower flexibility, such that the geometry and properties of the products can often be forecasted. This suggests a 'customized' preparation of SMMs. Some very interesting systems have been made in this manner taking advantage of the linearity of the cyanide ligand in combination with the predictable geometry and electronic structure of specific transition metals [25].

SMMs of Manganese

Each of the complexes described in this section have been synthesized, at least initially, by the serendipitous assembly of manganese salts or pre-formed clusters of Mn with a combination of one or more flexible organic bridging ligands. These species represent the vast majority of SMMs reported to date. Mn cluster chemistry involves complicated processes in which the crystallographically

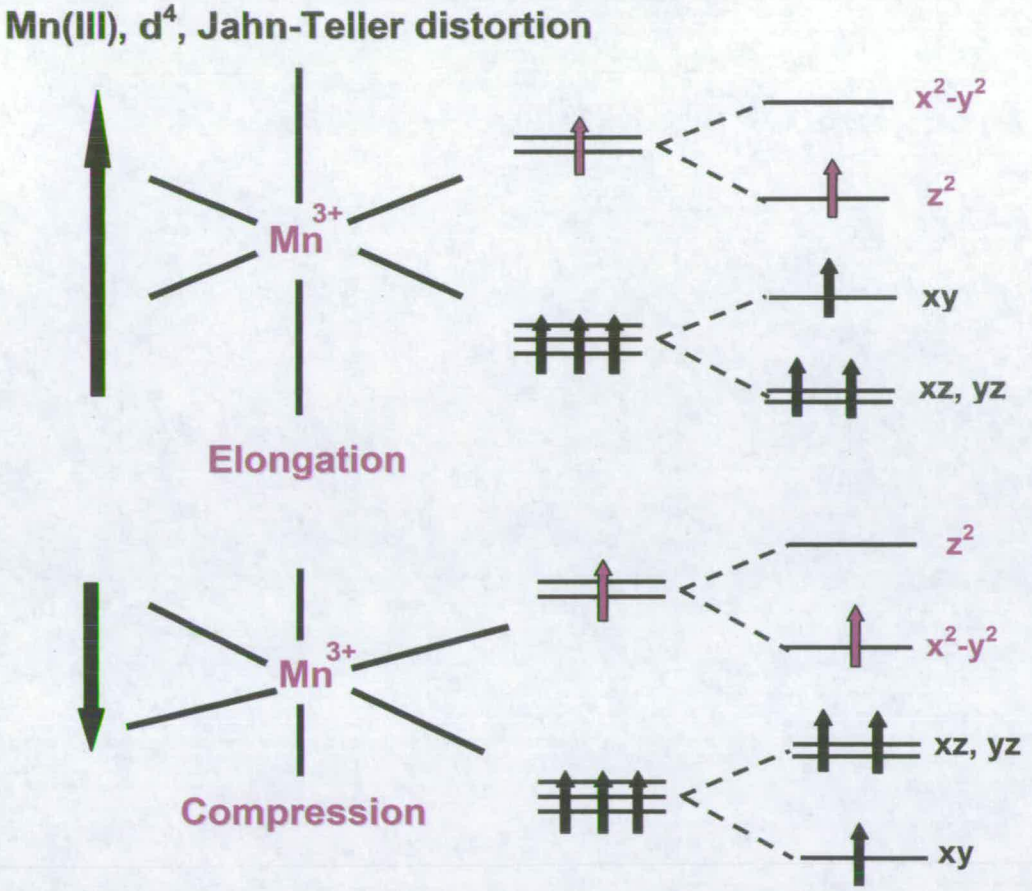

Figure 1.6. Single ion Mn^{3+} anisotropy: Jahn-Teller distortion.

characterized products are almost certainly not the only complexes present in solution at any one time and where the synthesis also involves the protonation/deprotonation, redox chemistry and structural rearrangement of many species simultaneously. Thus, mechanistic, kinetic and any other detailed studies of the reaction processes are almost impossible. Compared to other *3d* transition metals, clusters of manganese are often characterized by large spin ground states, and this, in conjunction with the presence of Jahn-Teller distorted Mn(III) ions (the source of the single-ion anisotropy; Figure **1.6**) make manganese clusters ideal candidates for SMMs. However there exists few 'simple', readily available, soluble sources of Mn(III) and thus synthetic strategies toward making polymetallic complexes containing Mn(III) ions have generally involved either, the oxidation of Mn(II)

species, the reduction of Mn(IV) or Mn(VII) species, and the use of small (or in some cases, large) pre-formed Mn(II/III/IV) containing species such as $[Mn_3O(O_2CR)_6L_3]^{0/+}$ or $[Mn_{12}O_{12}(OAc)_{16}(H_2O)_4]$ in the presence of flexible organic bridging ligands such as carboxylates and alkoxides *via* self-assembly. This has been achieved both chemically and electrochemically.

Below we give a brief overview of some well known examples of these molecules.

➢ The $[Mn_{12}O_{12}(O_2CR)_{16}(H_2O)_x]^{n-}$ Family: The Prototype SMMs

The first, and most studied family of SMMs are the dodecanuclear complexes of general formula $[Mn_{12}O_{12}(O_2CR)_{16}(H_2O)_x]^{n-}$ (n = 0, 1, 2; x = 3, 4). Of the more than one hundred different Mn clusters known to display SMM behaviour more than half the members belong to the $[Mn_{12}]$ family. $[Mn_{12}OAc]$ (Figure **1.1**) is the prototype SMM and is extremely easy to make, has led to numerous papers describing its chemistry and physics including the first examples of quantum tunneling of the magnetization [26] and quantum phase interference [27].

$[Mn_{12}OAc]$ has a spin ground state of S = 10 resulting from the antiferromagnetic interaction between the eight outer Mn(III) ions and the four inner Mn(IV) ions. This coupled with a zero-field splitting parameter of D = -0.50 cm^{-1} gave rise to the first molecule with an energy barrier to magnetization reversal, and the birth of SMM chemistry. The origin of the cluster anisotropy arises from the near-parallel alignment of the Jahn-Teller (JT) axes on the eight Mn(III) ions. Indeed the initially puzzling appearance of two separate out-of-phase ac susceptibility signals in some of the $[Mn_{12}]$ derivatives [28] has now been ascribed to the presence of separate isomers in which some of the JT axes are orientated differently [29]. The presence of JT-isomers means that there are slower and faster relaxing species within the same crystal that have different energy barriers to the reorientation of the magnetization. This is a 'problem' which has been observed throughout the $[Mn_{12}]$

family, but one that has been recently overcome with the preparation of the bromoacetate analogue $[Mn_{12}O_{12}(O_2CCH_2Br)_{16}(H_2O)_4]$ which shows only one out-of-phase ac susceptibility signal and a 'cleaner' hysteresis loop, thus simplifying the subsequent analysis [30].

Substitution of the carboxylate ligands surrounding the $[Mn_{12}]$ core can be achieved *via* ligand exchange on the original pre-formed cluster or by repetition of the original reaction in the presence of excess RCO_2H [31]. An alternative, but less efficient route to $[Mn_{12}O_{12}(O_2CR)_{16}(H_2O)_4]$ complexes is the oxidation of the appropriate oxo-centred metal triangles $[Mn_3O(O_2CR)_6(py)_3]^{0/+}$ with MnO_4^- in MeCN or CH_2Cl_2 (*vide infra*). However the yields obtained from this procedure can be 5–10 times smaller than that obtained *via* ligand substitution.

➢ The $[Mn_6O_2(R\text{-}sao)_6(O_2CR')_2(ROH)_{4\text{-}6}]$ Family

The Brechin group recently reported the synthesis and magnetic properties of a large family (~20 members) of hexanuclear Mn^{III} SMMs based on the complex $[Mn^{III}_6O_2(sao)_6(O_2CH)_2(EtOH)_4]$ ($saoH_2$ = salicylaldoxime; Scheme **1.1**) [18,19].

All display very similar molecular structures and can be described as consisting of two parallel off-set, stacked $[Mn^{III}_3(\mu_3\text{-}O)]^{7+}$ triangular subunits linked *via* two 'central' oximate O-atoms and two 'peripheral' phenoxide O-atoms (Figure **1.7**), leading to a $[Mn^{III}_6(\mu_3\text{-}O)_2(\mu_3\text{-}ONR)_2(\mu\text{-}ONR)_4]^{8+}$ core. The bridging between neighbouring Mn ions within each triangle occurs through an NO oximate group, such that each Mn_2 pair forms a –Mn-N-O-Mn- moiety, and thus the Mn_3 triangle a $(\text{-Mn-O-N-})_3$ ring. It was shown that by using derivatised versions of the oxime ligand (R-$saoH_2$, R = H, Me, Et etc; Scheme **1.1**) it was possible to significantly increase the ground spin state from $S = 4$ to $S = 12$, greatly enhancing the effective energy barrier for magnetisation reversal up to a maximum of ~86 K [20,21]. The origin of the AF→F switch arises from a structural distortion of the molecule induced by the 'twisting' of the (-Mn-N-O-) ring, as evidenced by the significant

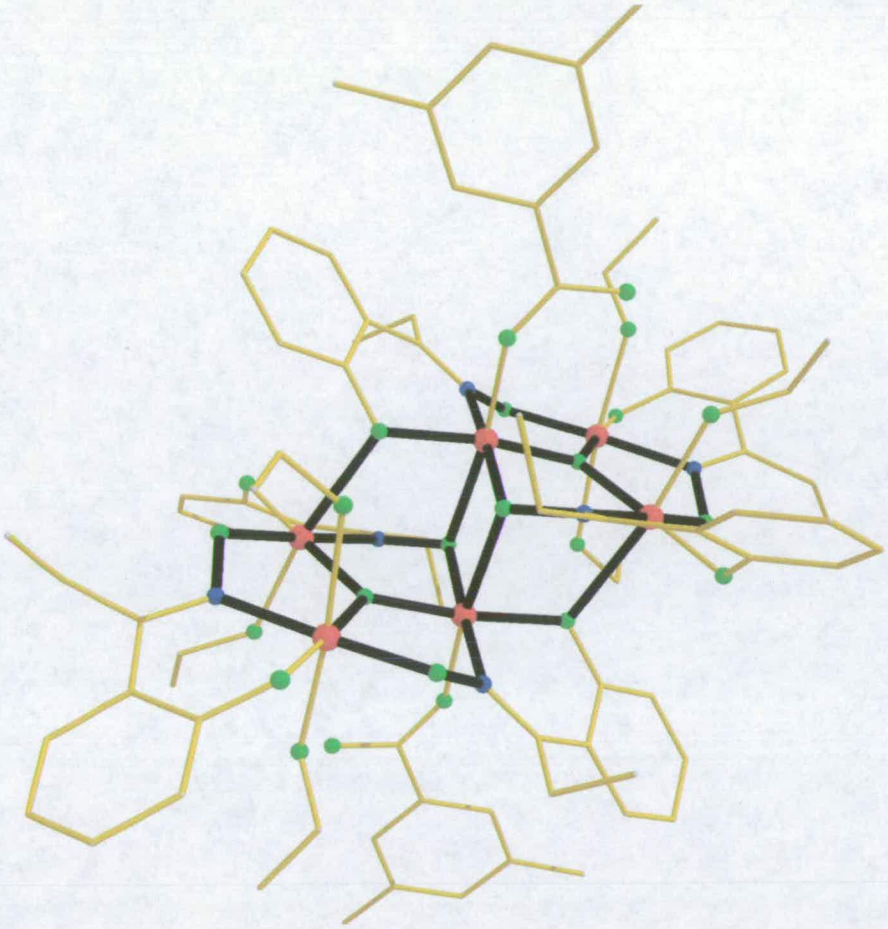

Figure 1.7. The structure of $[Mn^{III}_6O_2(Et\text{-}sao)_6(O_2C(Me)_2Ph)_2(EtOH)_6]$ in the crystal. The central $[Mn^{III}_6(\mu_3\text{-}O)_2(\mu_3\text{-}ONR)_2(\mu\text{-}ONR)_4]^{8+}$ core is show with black bonds. Colour scheme: Mn: red; O: green; N: blue; C: pale grey.

increases in the Mn-N-O-Mn torsion angles observed when bulkier salicylaldoximes are employed. The ability to deliberately switch pairwise exchange interactions in such a controllable fashion has enormous potential, but understanding in detail the underlying contributory factors in such complicated molecules is an extremely difficult task since it is the consequence of a number of different super-exchange pathways. The derivative $[Mn^{III}_6O_2(Et\text{-}sao)_6(O_2C(Me)_2Ph)_2(EtOH)_6]$ ($[Mn_6Et\text{-}sao]$, Figure **1.7**) has been established as the SMM with the largest anisotropy barrier yet known [19] and displays a spin ground state of S = 12 with D = -0.43 cm^{-1}. Relaxation studies on both powdered samples and on single crystals reveal the complex to be a single-molecule magnet with an effective energy barrier to

magnetization reversal (U_{eff}) of 86.4 K and a blocking temperature of ~5 K; the relaxation being approximately *ten times* slower than that of $[Mn_{12}O_{12}(O_2CCH_2Br)_{16}(H_2O)_4]$.

➢ $[Mn_{84}O_{72}(OAc)_{78}(OMe)_{24}(OH)_6(MeOH)_{12}(H_2O)_{42}]$; A Giant SMM

One of the most successful routes for SMM synthesis is the reaction between a pre-formed Mn cluster and (a) solvent, (b) reductant/oxidant, and/or (c) flexible organic bridging ligand. Commonly the metal complexes are the triangular species [32] $[Mn_3O(O_2CR)_6(py)_3]^{0/+}$, but all Mn_x ($x \geq 2$) clusters can, and should be, regarded as starting materials – even those already exhibiting SMM behaviour, like the series of $[Mn_{12}O_{12}(O_2CR)_{16}(H_2O)_4]$ compounds. The advantages of using pre-formed clusters are (i) they are convenient sources of Mn(III) ions; (ii) they can often be made in gram scale quantities very easily; (iii) they already contain multiple Mn ions; (iv) they may already contain multiple O^{2-}/OH^- ions; (v) they may already

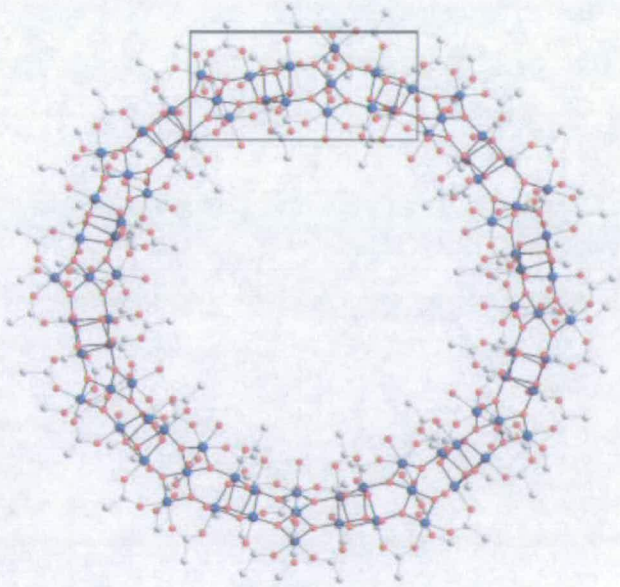

Figure 1.8. The structure of a giant SMM $[Mn_{84}]$ in the crystal.

possess large spin ground states; (vi) they may already display large anisotropies; and (vii) they may already display SMM behaviour.

One of the most spectacular examples of this is the preparation of the largest known SMM – the cluster $[Mn^{III}_{84}O_{72}(OAc)_{78}(OMe)_{24}(OH)_6(MeOH)_{12}(H_2O)_{42}]$, $[Mn_{84}]$ (Figure **1.8**) [31]. Magnetic studies on $[Mn_{84}]$ indicate a relatively small spin ground state of $S = 6$, but low temperature micro-SQUID measurements confirm the presence of temperature and sweep rate dependent hysteresis loops. $[Mn_{84}]$ is by far the largest SMM made and can be regarded as the first meeting point of the top-down and bottom-up approaches to building nanoscale magnetic materials [31].

Magnetic Refrigerants and the Magnetocaloric Effect (MCE)

Magnetic refrigeration is an energy-efficient and environmentally-friendly technology based on the magnetocaloric effect (MCE). This describes the change of magnetic entropy (ΔS_m) and (the related) adiabatic temperature (ΔT_{ad}) following a change in the applied magnetic field (ΔH). Under adiabatic conditions a magnetic field can cause cooling or heating of a material as a result of variation of its internal energy (magnetic entropy). Debye [32a] and Giauque [32b] proposed that the MCE could be exploited for refrigeration via adiabatic demagnetisation processes. This is illustrated by the magnetic entropy $S_m(T,H)$ curves for a paramagnet of spin S in Figure **1.9** [33]. A spin S has a $2S+1$ degeneracy in zero field (neglecting ZFS) and hence the full amount of the magnetic entropy is R $\ln(2S+1)$, where R is the gas constant.

When a material is magnetized by application of a magnetic field, H, the entropy associated with the magnetic degrees of freedom, S_m, is changed as the field changes the magnetic order of the material. The MCE and the associated principle of adiabatic demagnetization is readily understood looking at Figure **1.9**. The system, assumed to be a paramagnetic material, is initially in state $A(T_i, H_i)$, at temperature T_i and field H_i. Under adiabatic conditions (i.e., when the total entropy of the system

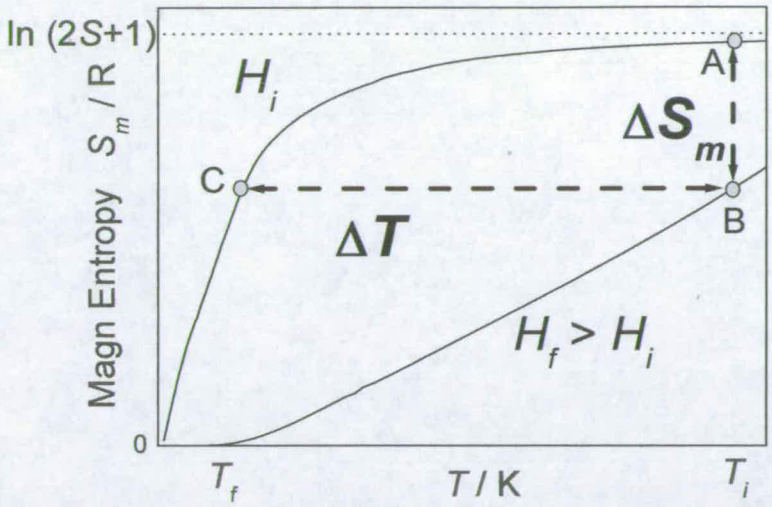

Figure 1.9. Magnetic entropy S_m as a function of temperature T, for two different applied magnetic fields H_i and H_f where $H_i < H_f$. A → B: isothermal magnetization with entropy change ΔS_m; B → C: adiabatic demagnetization with resulting temperature change $\Delta T = T_f - T_i$.

remains constant during the magnetic field change), the magnetic entropy change must be compensated for by an equal but opposite change of the entropy associated with the lattice, resulting in a change in temperature of the material. That is, the adiabatic field change $H_i \rightarrow H_f$ brings the system to state $B(T_f, H_f)$ with the temperature change $\Delta T_{ad} = T_f - T_i$ (horizontal arrow in Figure **1.9**). If the magnetic field is isothermally changed to H_f in a reversible process, the system goes to state $C(T_i, H_f)$ decreasing the magnetic entropy, thus resulting in a magnetic entropy change ΔS_m (vertical arrow in Figure **1.9**).

Both ΔS_m and ΔT_{ad} represent the characteristic parameters of the MCE. It is easy to see that if the magnetic change ΔH reduces the entropy ($\Delta S_m < 0$), then ΔT_{ad} is positive, whereas if ΔH is such that $\Delta S_m > 0$, then $\Delta T_{ad} < 0$ (Figure **1.9**). Large magnetic moments are often attainable in superparamagnetic clusters, resulting therefore in large entropies. Moreover, for certain ranges of field, temperature and cluster size, it is easier in superparamagnets than in pure materials to change the magnetic entropies by application of a field [34]. Obviously, this leads to an interest in superparamagnets in terms of MCE. The picture depicted in Figure **1.9** is still

valid for a superparamagnet with S as net cluster moment, provided that it is at temperatures above the blocking temperature. The cluster magnetic anisotropy, which indeed determines the blocking temperature, can be considered as a drawback in the MCE efficiency of superparamagnets, because by shifting the maxima of ΔS_m and ΔT_{ad} towards higher temperatures it tends to lower the value of the MCE response [34,35]. Ideal candidates for MCE applications would then be magnetic clusters with large S and small anisotropy. Isotropic high-spin ground state clusters, with potentially very large changes in S_m at low temperatures (i.e. where almost all population is in the ground state) are therefore attractive materials for low temperature cooling [36], and in principle could be more efficient than the lanthanide and intermetallic materials conventionally used for this purpose.

To date, however, the number of publications on the MCE of molecule-based materials is very small. The reason is that both cluster magnetic anisotropy and quantum phenomena limit the application of molecular magnets as magnetic refrigerants at low temperatures. One excellent recent example is the tetradecametallic cluster $[Fe^{III}_{14}(bta)_6O_6(OMe)_{18}Cl_6]$ which has a remarkably high electronic spin ground state of S = 25 [33]. This is only surpassed by $[Mn_{25}O_{18}(OH)_2(N_3)_{12}(pdm)_6(pdmH)_6]$ cluster (S = 51/2±1) [20]. Despite its very large value of S, $[Fe_{14}]$ does not behave as an SMM because the ZFS of the ground state is negligible ($D \approx 0$ cm^{-1}). However, the magnetically *isotropic* nature of its giant spin leads to an enormous magnetocaloric effect (MCE) below 10 K [33]. Tejada and co-workers performed similar measurements [37] for the archetypal SMMs $[Mn_{12}O_{12}(O_2CPh)_{16}(H_2O)_4]$ and $[Fe_8O_2(OH)_{12}(tacn)_6]Br_8$ both of which have S = 10 ground states. However, the significant ZFS of the ground states breaks the $2S$+1 degeneracy in zero field, leading to blocking of the magnetisation at low temperature. This results in a lower MCE [38] therefore limiting the potential of SMMs in this area. In contrast, the very large and isotropic spin ground state of $[Fe_{14}]$ results in a huge MCE at low temperatures, with characteristic parameters of -ΔS_m = 17.6±2.8 Jkg^{-1}K^{-1} and ΔT = 5.8±0.8 K for T_i = 6 K and a magnetic field change of 0 - 7 T, determined from variable temperature, variable field specific heat

and magnetisation measurements [33]. In other words, it should be possible to cool $[Fe_{14}]$ to 6 K by conventional methods, and then to achieve temperatures well below 1 K by an isothermal magnetisation-adiabatic demagnetisation cycle.

Micro-refrigeration can be employed in astrophysics for ultra-sensitive X-ray detectors [39]. The task of the molecular nanorefrigerants would then be the cooling of the "absorber", that is the film-component capable of intercepting the energy to be measured. In addition, magnetic refrigeration is particularly suited for X-ray microanalysis in outer space, since this technique is a valid alternative to ^3He-^4He dilution refrigeration whose use is complicated by the absence of gravity. In present devices and equipment, the trend is to reduce the size of all components.

Use of $[Mn_3]$ Triangles as Starting Materials

Probably the most successful use of pre-formed Mn clusters as starting materials in SMM synthesis involves the triangular complexes of general formula: $[Mn_3O(O_2CR)_6(L)_3]^{0/+}$ (where L is a terminal ligand such as H_2O, MeCN or pyridine). These complexes are easily made in a short timescale and their reactivity is highly versatile. They are stable in solution, accessible to ligand variation – i.e. the nature of the carboxylate can be changed at will as can the terminal ligand L, and they can be prepared with either three Mn(III) ions to give the charged complexes $[Mn_3O(O_2CR)_6(L)_3]X$ ($X^- = ClO_4^-$, NO_3^-, etc.) or with two Mn(III) ions and one Mn(II) ion to give the neutral complexes $[Mn_3O(O_2CR)_6(L)_3]$. For the charged complexes the nature of the anion is an additional reaction variable. These variables allow for a systematic synthetic strategy which, if successful, can help to produce large families of related compounds. Indeed, the prototype SMMs $[Mn_{12}O_{12}(O_2CR)_{16}(H_2O)_x]$ can be made *via* the oxidation of the appropriate $[Mn_3O(O_2CR)_6(L)_3]^{0/+}$ complex with MnO_4^- in MeCN or CH_2Cl_2, albeit in rather poor yields.

Tripodal Alcohol Ligands

Tripodal alcohol ligands such as 1,1,1-tris(hydroxymethyl)ethane (H_3thme); 1,1,1-tris(hydroxymethyl)propane (H_3tmp) and pentaerythritol (H_4peol) (Scheme **1.2**) have previously been used by Zubieta et al. in the synthesis of (diamagnetic) oxo-vanadium and oxo-molybdenum clusters [40], but until recently, they have been used sparingly in the synthesis of paramagnetic 3d transition metal clusters [41]. Zubieta et al. introduced this ligand type to expand the coordination chemistry of polyoxoanions both by providing charge compensation by the substitution of peripheral O^{2-} groups with mono-negative ligands in "classical" compact polyanion structures and by allowing structure expansion and/or modification through bridging

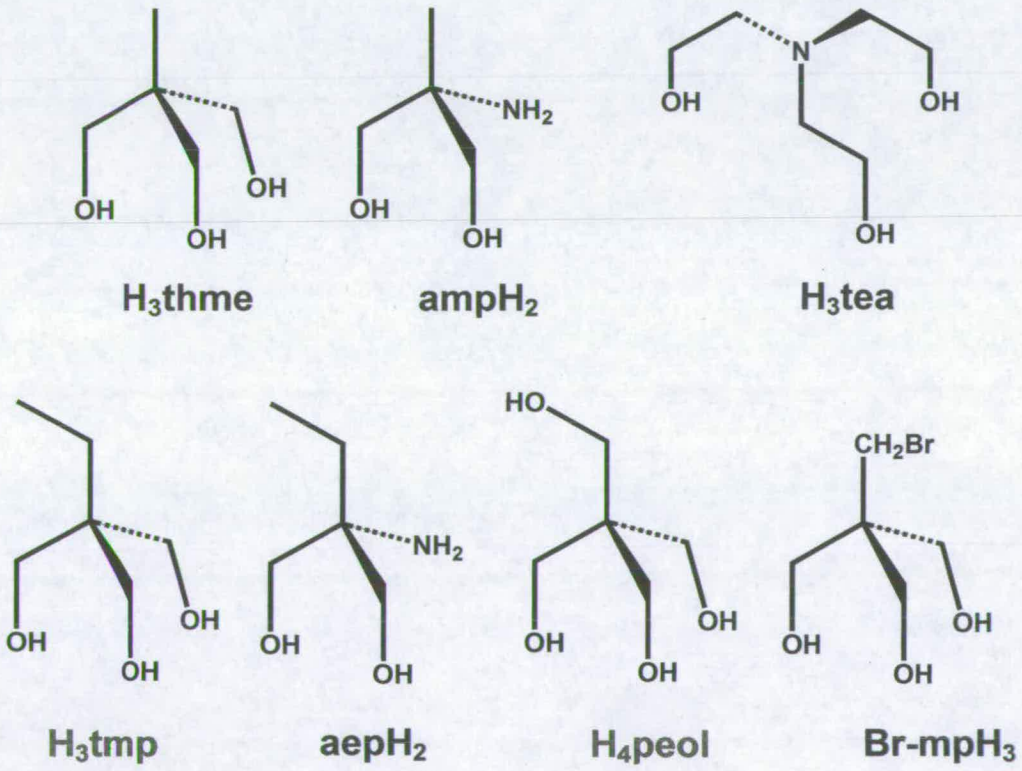

Scheme 1.2. The structures of 1,1,1-tris(hydroxymethyl)ethane (H_3thme); 2-Amino-2-methyl-1,3-propanediol ($ampH_2$); triethanolamine (H_3tea); 1,1,1-tris(hydroxymethyl)propane (H_3tmp); 2-amino-2-ethyl-1,3-propanediol ($aepH_2$); pentaerythritol (H_4peol); 2-(Bromomethyl)-2-(hydroxymethyl)-1,3-propanediol (Br-mpH_3).

interactions. While "naked" polyanion structures exhibit frameworks constructed exclusively from $\{MO_5\}$ square pyramids and/or $\{MO_6\}$ octahedra, the structural diversity of the tripodal alkoxide coordination clusters reflected the introduction of ligand-directed tetrahedra into the cluster frameworks. The polyoxoalkoxymetalates $[M_aO_b(OR)_c]$ represent a particularly prominent subclass of polyanion coordination compounds that are of considerable interest by virtue of their relationship to the oligomeric metal alkoxides (Scheme **1.3**), a major class of inorganic materials. Consequently, a variety of tri-, tetra-, hexa-, deca-, and decahexa- nuclear oxo-vanadium and oxo-molybdenum clusters were synthesized using tri-alcohol ligands which displayed coordination modes from μ_2 to μ_5 (TA2-TA3; Scheme **1.3**). Some prominent examples are: $[\{RC(CH_2O)_3V_3\}P_2W_{15})_{59}]^{6-}$ (a), $[V_2Mo_2O_8(OMe)_2\{RC(CH_2O)_3\}_2]^{2-}$ (b), $[V_6O_{13}\{RC(CH_2O)_3\}_2]^{2-}$ (c) (when R= Me, Et), $[V_{10}O_{13}(thme)_5]^{1-}$ (d), and $[V_{16}O_{20}\{RC(CH_2O)_8\}(H_2O)_4]^{2-}$ (e) whose structures are based on octahedral sub-cores.

The use of such tripodal ligands for the synthesis of paramagnetic 3d transition metal clusters is much rarer. The first example of a mixed-valent Mn cluster was the decanuclear $(Et_4N)_2[Mn_{10}O_2Cl_8(thme)_6]$ [41d] whose structure is based on an edge-sharing bi-octahedron. This reflects the role of the trisalkoxy ligand types in stabilizing trinuclear $[M_3(tripod)]$ structural fragments that condense into larger aggregates that often display classical polyoxoanion structural cores. Hegetschweiler et al. reported the hexanuclear cluster $[Fe_6O(thme)_6]^{2-}$ [41], whose structure is again based on an octahedral core. The basis of the steric requirement of the tripod^{3-} ligand, that there are two possibilities for bridging such a ligand to an $\{M_6O\}$ moiety (Scheme **1.4**): a coordination mode where all three alkoxo groups bind as μ_2-bridges (type **A**) and a mode with one terminally coordinating and two bridging alkoxo groups (type **B**). If more than one tripod^{3-} ligand interacts with the OM_6 unit, a variety of different arrangements have to be taken into consideration, thus expanding the coordination chemistry.

The basic, though perhaps over-simplistic, principle of using tripodal alcohols in this thesis is to link paramagnetic metal ions together into triangular arrays (Figure

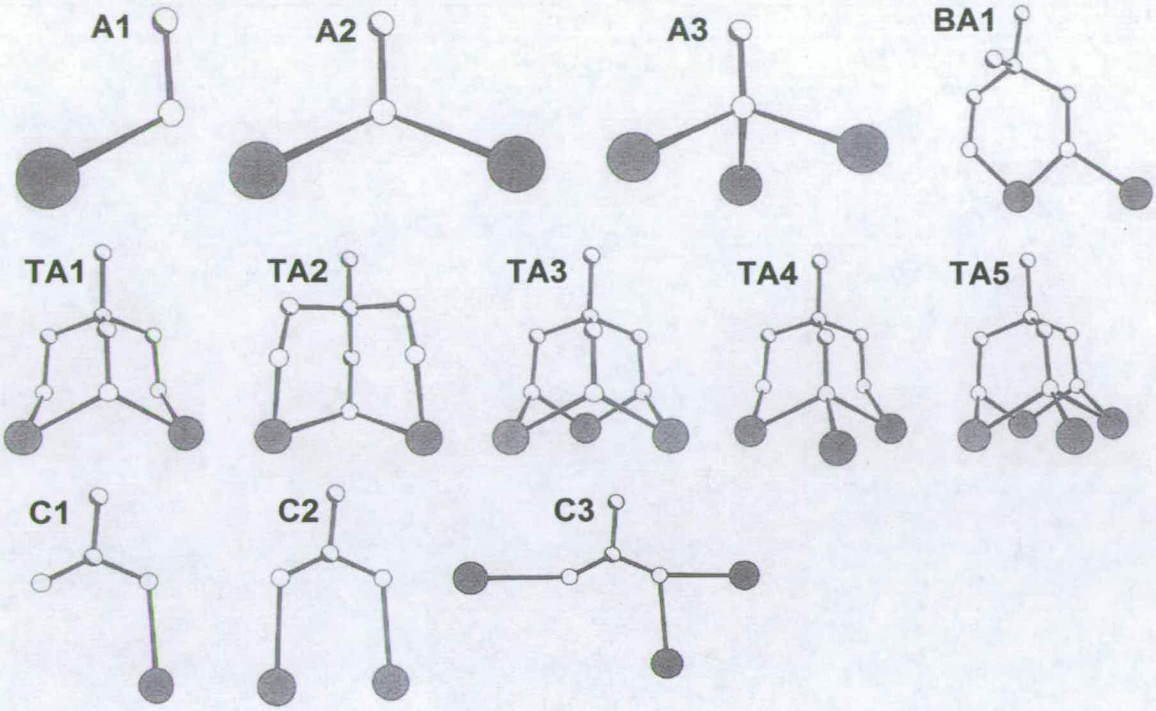

Scheme 1.3. Schematic views of representative coordination modes adopted by oxygen-donor ligands. The labelling scheme is: A1:terminal alkoxide; A2: μ_2-bridging alkoxide; A3: μ_3-bridging alkoxide; BA1: mixed bridging and terminal mode adopted by bisalkoxides; TA1-TA5: coordination modes adopted by trisalkoxide ligands types and C1-C3: coordination modes adopted by carboxylate ligands.

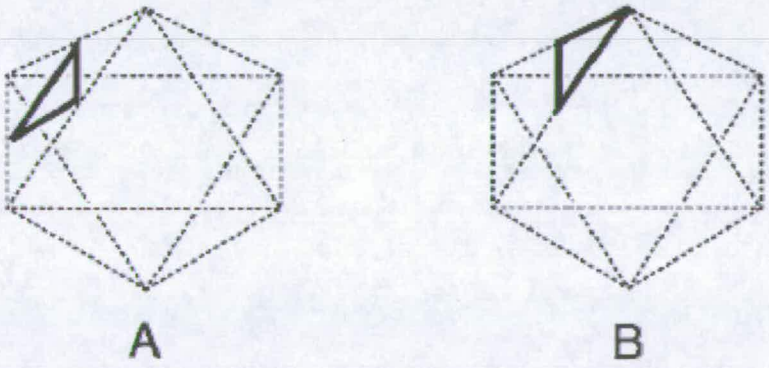

Scheme 1.4. Possible interactions of thme^{3-} with the OFe_6 unit and connectivity diagrams of the two different coordination modes. The [Fe_6] octahedron is shown by dashed lines; the three coordinated oxygens of a thme^{3-} ligand are indicated by a solid triangle.

1.10) which may lead to molecules with large spin ground states [42]. If these arrays

consist of simple [M_3] equilateral triangles then the resultant competing exchange interactions or "spin frustration" stabilizes the non-zero spin ground state. If the arrays consist of [M_4] centred triangles (or "metal stars") in which the three peripheral ions are connected only to the central ion and not to each other, then antiferromagnetic interactions between these ions stabilizes the large spin ground state. If these "high spin" triangular units can be linked together into elaborate polymetallic arrays then the resultant complexes could well be characterizes by large spin ground states. The disposition of the three alkoxide arms of the *tri-anion* directs the formation of triangular [M_3] units where each arm of the ligand bridges one edge of the triangle - in polyoxometallate chemistry this results in clusters based on octahedra. For clusters of 3d metals however, these [M_3] units can be combine in more diverse ways and produce more elaborate products whose structures are depended on both (a) the level of deprotonation of the ligand *i.e.* tripod^{3-}, Htripod^{2-} on H_2tripod^{1-} and (b) the presence of other bridging/chelating ligands such as

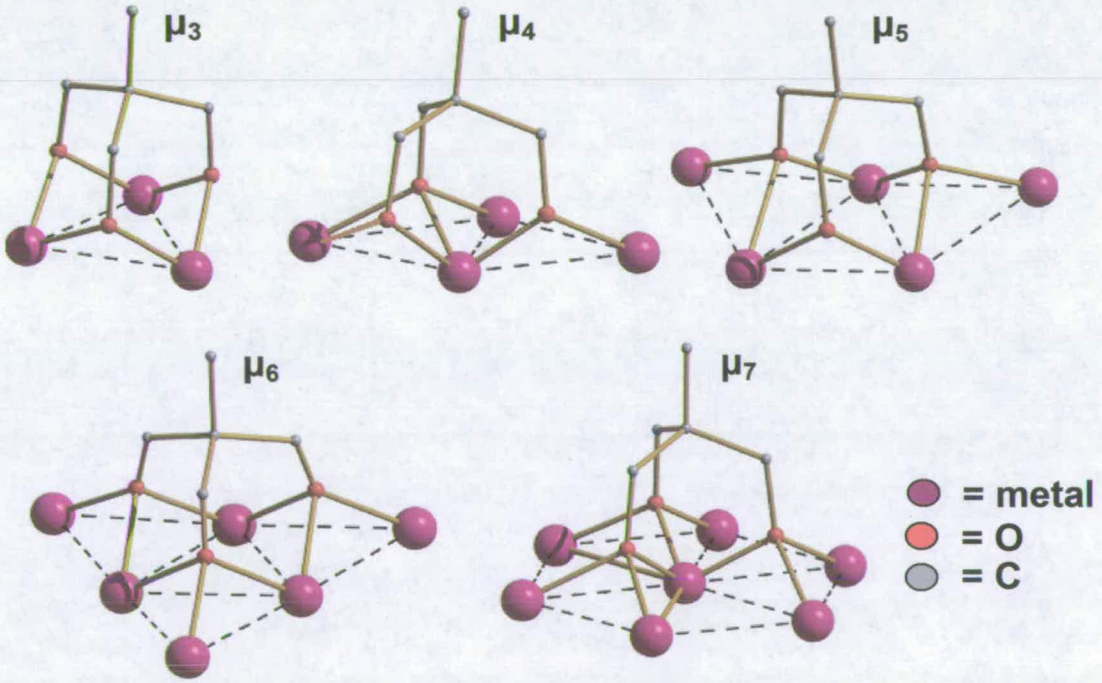

Figure 1.10. The triangular arrays formed by the alcohol ligands linking the metal ions together.

carboxylates or and/or terminal co-ligands such as carboxylates or β-diketonates etc. Indeed these triangles have been shown self-assemble to give a plethora of polymetallic clusters whose metallic skeletons are based on rods, discs, tetrahedra, octahedra and icosahedra [42].

For example, reaction of $[Mn_3O(OAc)_6(py)_3]$ with H_3thme in MeCN produces the enneanuclear complex $[Mn_9O_7(thme)(OAc)_{11}(py)_3(H_2O)_2]$ [Mn_9thme] [44]. This complex has a core of four Mn(III) and two Mn(II) ions surrounding a central triangle of Mn(IV) ions - a structure with obvious parallels to $[Mn_{12}OAc]$. Indeed the observed S = 17/2 ground state also arises from the antiferromagnetic interaction between the ferromagnetically coupled inner Mn(IV) ions and the peripheral Mn(III/II) ions. Low temperature micro-SQUID measurements of [Mn_9thme] provide a beautiful example of temperature and sweep rate dependent hysteresis loops in which the QTM steps are clearly seen. Repetition of the reaction that produced [Mn_9thme] but using the benzoate triangle $[Mn_3O(O_2CPh)_6(py)_3]$ does not produce an analogous compound but the species $[Mn_{12}O_4(OH)_2(O_2CPh)_{12}(thme)_4(py)_2]$ [Mn_{12}thme] [45]. This complex consists of a series of ten edge-sharing triangular units, as directed by the tripodal organic ligands, which combine to form a long, thin, rod-like complex. The presence of so many triangular units and thus the presence of many competing exchange interactions, results in an intermediate spin ground state of S = 7. Repetition of the same reaction but utilising a number of different carboxylates leads to the formation of a large family of rod-like Mn species of differing nuclearities and spins [46].

A natural extension to these studies is the investigation of the coordination chemistry of analogous organic molecules in which one (or more) of the alcohol 'arms' is replaced by an alternative functional group(s), for example an amine group (see $ampH_2$ and $aepH_2$ ligands in Scheme **1.2**). While each alkoxide arm has the potential to bridge up to three metals (and thus a maximum of seven metals per tripodal ligand) [43], the $-NH_2$ 'arm' is likely to act solely as a monodentate/terminal capping unit and thus a number of related, yet different, structural topologies.

Project Aims

The project is focused on the syntheses of polynuclear manganese clusters using tripodal ligands (all the ligands used are shown in Scheme **1.2**) for use as single-molecule magnets and magnetic refrigerants.

➢ Physical Methods

Elemental analysis (C, H, N) were performed by the EaStCHEM microanalysis service. Variable-temperature, solid-state direct current (dc) magnetic susceptibility data down to 5 K were collected on a Quantum Design MPMS-XL SQUID magnetometer equipped with a 7 T dc magnet. Diamagnetic corrections were applied to the observed paramagnetic susceptibilities using Pascal's constants. Magnetization versus field hysteresis and dc decay measurements at temperatures below 1.8 K were performed on single-crystals using a micro-SQUID instrument [47]. Specific heat experiments down to 0.3 K and up to 7 T were carried out with the PPMS. Magnetization and susceptibility measurements below 2 K were performed using homemade Hall microprobes. In this case, the grain-like samples consisted of collections of small crystallites of ca. 10^{-3} mm^3. For measurements performed on powder samples, the calculated fits were obtained taking into account random spin orientations.

➢ X-ray Crystallography

Diffraction data were collected on a Bruker Smart Apex CCD diffractometer equipped with an Oxford Cryosystems LT device. The structures were solved by direct methods (SHELXS) and refined by full-matrix least squares against F^2 (CRYSTALS) [48].

➢ **Supporting Information**

Crystallographic data and structure refinement details are listed in Tables A.2.1 – A.2.3, for complexes **1** – **7**; Table A.3.1, for complexes **8** – **10**; Tables A.4.1 – A.4.2, for complexes **11** – **15** and Tables A.5.1 – A.5.3 for complexes **16** – **23** in the appendices. Full details can be found in the accompanying CIF files (attached CD).

References

[1] (a) V.K. Yachandra, K. Sauer and M.P. Klein., Chem. Rev., 1996, 96, 2927. (b) V.K. Yachandra, K. Sauer., Biochim. Biophys. Acta., **2004**, *140*, 1655. (c) B. Kok, B. Forbrush and M. McGloin, Photochem. Photobiol., **1970**, *11*, 457. (d) M. Haumann, P. Liebisch, C. Muller, M. Barra, M. Grabolle and H. Dau., Science, **2005**, *310*, 1019. (d) S. Mukhopadhyay, S.K. Mandal, S. Bhaduri, and W. H. Armstrong,Chem. Rev., **2004**, *104*, 3981.3. (e) J. Yano, J. Kern, K. Sauer, M.J. Latimer, Y. Pushkar, J. Biesiadka, B. Loll, W. Saenger, J. Messinger, A. Zouni and V.K. Yachandra., *Science*, **2006**, *314*, 821. (f) . (c) B. Loll, W. Saenger, J. Messinger, A. Zouni and J. Biesiadka., Nature, **2005**, *438*, 1040. 4.

[2] (a) D. Gatteschi, R. Sessoli, *Angew. Chem. Int. Ed.*, **2003**, *42*, 268. (b) G. Christou, D. Gatteschi, D.N. Hendrickson, R. Sessoli, *MRS Bull.*, **2000**, *25*, 66.

[3] (a) A. Caneschi, D. Gatteschi, R. Sessoli, A.L. Barra, L.C. Brunel, M. Guillot, *J. Am. Chem. Soc.* **1991**, *113*, 5873. (b) R. Sessoli, D. Gatteschi, A. Caneschi, M.A. Novak, *Nature* **1993**, *365*, 141.

[4] (a) R. Sessoli, H.L. Tsai, A.R. Schake, S.Y. Wang, J.B. Vincent, K. Folting, D. Gatteschi, G. Christou, D.N. Hendrickson, *J. Am. Chem. Soc.* **1993**, *115*, 1804. (b) D.N. Hendrickson, G. Christou, H. Ishimoto, J. Yoo, E.K. Brechin, A. Yamaguchi, E.M. Rumberger, S.M.J. Aubin, Z.M. Sun, G. Aromi, *Polyhedron* **2001**, *20*, 1479. (c) T. Lis, *Acta Cryst.*, **1980**, *B36*, 2042.

[5] (a) J.F. Fernandez, F. Luis, J. Bartolome, *Phys. Rev. Lett.*, **1998**, *80*, 5659. (b) W. Wernsdorfer, S. Bhaduri, R. Tiron, D.N. Hendrickson, G. Christou, *Phys. Rev. Lett.*, **2002**, 89. (c) L. Bokacheva, A.D. Kent, M.A. Walters, *Polyhedron*, **2001**, *20*, 1717.

[6] (a) D. Gatteschi and R. Sessoli, *Angew. Chem. Int. Ed.*, **2003**, *42*, 268. (b) R. Sessoli, *Europhysics News*, **2003**, *34*.

[7] L.Thomas, F. Lionti, R. Ballou, D. Gatteschi, R. Sessoli and B. Barbara, Nature (London), **1996**, *383*, 145.

[8] M.N. Leuenberger, D. Loss, *Nature*, **2001**, *410*, 789.

[9] (a) A.L. Barra, D. Gatteschi, R. Sessoli, *Chem.-Eur. J.*, **2000**, *6*, 1608. (b) A. L. Barra, *Appl. Magn. Reson.*, **2001**, *21*, 619. (c) A. Bouwen, A. Caneschi, D. Gatteschi, E. Goovaerts, D. Schoemaker, L. Sorace, M. Stefan, *J. Phys. Chem. B,* **2001**, *105*, 2658. (d) D. Zipse, J.M. North, N.S. Dalal, S. Hill, R.S. Edwards, *Phys. Rev. B*, **2003**, *68*.

[10] (a) A. Morello, O.N. Bakharev, H.B. Brom, L.J de Jongh, *J. Magn. Magn. Mater.*, **2004**, *272-76*, 1015. (b) A. Morello, O.N. Bakharev, H.B. Brom, L.J. de Jongh, *Polyhedron*, **2003**, *22*, 1745.

[11] D. Procissi, B.J. Suh, A. Lascialfari, F. Borsa, A. Caneschi, A. Cornia, *J. Appl. Phys.*, **2002**, *91*, 7173.

[12] R.M. Achey, P. L. Kuhns, W.G. Moulton, A. P. Reyes, N.S. Dalal, *Polyhedron*, **2001**, *20*, 1745.

[13] (a) S. Carretta, E. Liviotti, G. Amoretti, R. Caciuffo, A. Caneschi, D. Gatteschi, *Phys. Rev. B*, **2002**, *65*. (b) H. Andres, R. Basler, H.U. Gudel, G. Aromi, G. Christou, H. Buttner, B. Ruffle, *J. Am. Chem. Soc.*, **2000**, *122*, 12469.

[14] E.J.L. McInnes, E. Pidcock, V.S. Oganesyan, M.R. Cheesman, A.K. Powell, A.J. Thomson, *J. Am. Chem. Soc.*, **2002**, *124*, 9219.

[15] (a) T. Baruah, M.R. Pederson, *Int. J. Quantum Chem.*, **2003**, *93*, 324. (b) J. Kortus, M.R. Pederson, T. Baruah, N. Bernstein, C.S. Hellberg, *Polyhedron,* **2003**, *22*, 1871. (c) K. Park, M.R. Pederson, S.L. Richardson, N. Aliaga-Alcalde, G. Christou, *Phys. Rev. B,* **2003**, *68*.

[16] C. Benelli, J. Cano, Y. Journaux, R. Sessoli, G.A. Solan, R.E.P. Winpenny, *Inorg. Chem.*, **2001**, *40*, 188.

[17] A.E. Clark, E. R. Davidson, *J. Chem. Phys.*, **2001**, *115*, 7382.

[18] (a) C.J. Milios, R. Inglis, A. Vinslava, R. Bagai, W. Wernsdorfer, S. Moggach, S. Parsons, S.P. Perlepes, G. Christou, E.K. Brechin, *J. Am. Chem. Soc.*, **2007**, *129*, 12505. (b) C.J. Milios, A. Vinslava, W. Wernsdorfer, A. Prescimone, P.A. Wood, S. Parsons, S.P. Perlepes, G. Christou, E.K. Brechin, *J. Am. Chem. Soc.*, **2007**, *129*, 6547. (c) C.J. Milios, A. Vinslava, P.A. Wood, S. Parsons, W. Wernsdorfer, G. Christou, S.P. Perlepes, E.K. Brechin, *J. Am. Chem. Soc.*, **2007**, *129*, 8.

[19] C.J. Milios, A. Vinslava, W. Wernsdorfer, S. Moggach, S. Parsons, S.P. Perlepes, G. Christou, E.K. Brechin, *J. Am. Chem. Soc.*, **2007**, *129*, 2754.

[20] M. Murugesu, M. Habrych, W. Wernsdorfer, K.A. Abboud, G. Christou, *J. Am. Chem. Soc.*, **2004**, *126*, 4766.

[21] J.J. Sokol, A.G. Hee, J.R. Long, *J. Am. Chem. Soc.*, **2002**, *124*, 7656.

[22] E.J. Schelter, A.V.Prosvirin, K.R. Dunbar, *J. Am. Chem. Soc.*, **2004**, *126*, 15004.

[23] (a) S. Osa, T. Kido, N. Matsumoto, N. Re, A. Pochaba, J. Mrozinski, *J. Am. Chem. Soc.*, **2004**, *126*, 420. (b) C.M. Zaleski, E.C. Depperman, J.W. Kampf, M.L. Kirk, V.L. Pecoraro, *Angew. Chem. Int. Ed.*, **2004**, *43*, 3912. (c) A. Mishra, W. Wernsdorfer, K.A. Abboud, G. Christou, *J. Am. Chem. Soc.*, **2004**, *126*, 15648.

[24] R.E.P. Winpenny, *J. Chem. Soc.-Dalton Trans.*, **2002**, 1.

[25] (a) V. Marvaud, C. Decroix, A. Scuiller, C. Guyardduhayon, J. Vaissermann, F. Gonnet, M. Verdaguer, *Chem., Eur. J.*, **2003**, *9*, 1692.

[26] J.R. Friedman, M.P. Sarachik, J. Tejada, J. Maciejewski, R. Ziolo, *J. Appl. Phys.*, **1996**, *79*, 6031.

[27] W. Wernsdorfer, R. Sessoli, *Science*, **1999**, *284*, 133.

[28] H.J. Eppley, H.L. Tsai, N. Devries, K. Folting, G. Christou, D.N. Hendrickson, *J. Am. Chem. Soc.*, **1995**, *117*, 301.

[29] S.M.J. Aubin, Z.M. Sun, H.J. Eppley, E.M. Rumberger, I.A. Guzei, K. Folting, P.K. Gantzel, A.L. Rheingold, G. Christou, D.N. Hendrickson, *Inorg. Chem.*, **2001**, *40*, 2127.

[30] G. Christou, *Accounts Chem. Res.*, **1989**, *22*, 328.

[31] A.T. Tasiopoulos, A. Vinslava, W. Wernsdorfer, K.A. Abboud, G. Christou, *Angew. Chem. Int. Ed.*, **2004**, *43*, 2117

[32] (a) P. Debye, *Ann. Phys.*, **1926**, *81*, 1154. (b) W.F. Giauque, *J. Am. Chem. Soc.*, **1927,** *49*, 1864.

[33] (a) M. Evangelisti, A. Candini, A. Ghirri, M. Affronte, E.K. Brechin, E.J.L. McInnes, *Appl. Phys. Lett.*, **2005**, *87*, 072504. (b) M. Evangelisti, A. Candini, A. Ghirri, M. Affronte, S. Piligkos, E.K. Brechin, E.J.L. McInnes, *Polyhedron*, **2005**, *24*, 2573.

[34] (a) R.D. McMichael, R.D. Shull, L.J. Swartzendruber, L.H. Bennett, R.E. Watson, *J. Magn. Magn. Mater.*, **1992**, *111*, 29. (b) L.H. Bennett, R.D. McMichael, H.C. Tang, R.E. Watson, *J. Appl. Phys.*, **1994**, *75*, 5493.

[35] X.X. Zhang, H.L. Wei, Z.Q. Zhang, L. Zhang, *Phys. Rev. Lett.*, **2001**, *87* 157203.

[36] For a recent review see: M. Evangelisti, F. Luis, L.J de Jongh, M. Affronte, *J. Mater. Chem.*, **2006**, *16*, 2534.

[37] (a) F. Torres, J.M. Hernández, X. Bohigas, J. Tejada, *Appl. Phys. Lett.*, **2000**, *77*, 3248. (b) F. Torres, X. Bohigas, J.M. Hernández. J. Tejada, *J. Phys. Cond. Matter.*, **2003**, *15*, L119.

[38] For a recent review see: M. Evangelisti, F. Luis, L.J de Jongh, M. Affronte, *J. Mater. Chem.*, **2006**, *16*, 2534.

[39] (a) High-resolution, energy dispersive microcalorimeter spectrometer for X-ray microanalysis, D. A. Wollman, K. D. Irwin, G. C. Hilton, L. L. Dulcie, D. E. Newbury, and J. M. Martinis, *J. Microscopy*, **1997**, *188*, 196. (b) A high spectral resolution observation of the soft X-ray diffuse background with thermal detectors, D. McCammon et al., *ApJ*, **2002**, *576*, 188. (c) See, e.g., Opportunities for mesoscopics in thermometry and refrigeration: Physics and applications, F. Giazotto, T. T. Heikkila, A. Luukanen, A. M. Savin, and J. P. Pekola, *Rev. Mod. Phys.*, **2006**, *78*, 217, and references therein.

[40] M. I. Khan and J. Zubieta, *Prog. Inorg. Chem.*, **1995**, *43*, 1.

[41] (a) R. C. Finn and J. Zubieta, *J. Cluster Sci.*, **2000**, *11*, 4. (b) K. Hegetschweiler, H. Schmalle, H.M. Streit and W. Schneider, *Inorg. Chem.*, **1990**, *29*, 3625. (c) K. Hegetschweiler, H. Schmalle, H. M. Streit, V. Gramllicj, H.U. Hund and I. Erni, *Inorg. Chem.*, **1992**, *31*, 1299. (d)M. Cavaluzzo, Q. Chen and J. Zubieta, *J. Chem.* Soc., *Chem. Commun.*, **1993**, *131*. (e) K. Hegetschweiler, D. Gatteschi, A. Cornia, L. Hausherr-Primo and V. Gramlich, *Inorg. Chem.*, **1996**, *33*, 4414. (f) C. Boskovic, H.U. Gudel, G. Labat, A. Neels, W. Wernsdorfer, B. Moubaraki and K. S. Murray, *Inorg. Chem.*, **2005**, *44*, 3181. (g) A. Cornia, A C. Fabretti, P. Garrisi, C. Mortalo, D. Bonacchi, D. Gatteschi, R. Sessoli, L. Sorace, W. Wernsdorfer and A.L. Barra, *Angew. Chem., Int. Ed.*, **2004**, *43*, 1136. The first reported examples of SMMs containing the related ligand triethanolamine (H_3tea, [$N(CH_2CH_2OH)_3$]) are: (h) B. Pilawa, M.T. Kelemen, S. Wanka, A. Geisselmann and A.L. Barra, *Europhys. Lett.*, **1998**, *43*, 7. (i) L.M. Wittick, K.S. Murray, B. Moubaraki, S.R. Batten, L. Spiccia and K.J. Berry, *Dalton Trans.*, **2004**, 1003. (j) M. Murugesu, W. Wernsdorfer, K.A. Abboud and G. Christou, *Angew. Chem., Int. Ed.*, **2005**, *44*, 892.

[42] E.K. Brechin, *Chem. Commun.*, **2005**, 5141.

[43] (a) M. Moragues-CanovPs, C.E. Talbot-Eeckalaers, L. Catala, W. Wernsdorfer, E.K. Brechin, T. Mallah, *Inorg. Chem.*, **2006**, *45*, 7038

[44] E.K. Brechin, M. Soler, J. Davidson, D.N. Hendrickson, S. Parsons, G. Christou, *Chem. Commun.*, **2002**, 2252.

[45] E.K. Brechin, M. Soler, G. Christou, M. Helliwell, S.J. Teat, W. Wernsdorfer, *Chem. Commun.*, **2003**, 1276.

[46] G. Rajaraman, M. Murugesu, E.C. Sanudo, M. Soler, W. Wernsdorfer, M. Helliwell, C. Muryn, J. Raftery, S.J. Teat, G. Christou, E.K. Brechin, *J. Am. Chem. Soc.*, **2004**, *126*, 15445.

[47] W. Wernsdorfer, *Adv. Chem. Phys.*, **2001**, *118*, 99.

[48] P.W. Betteridge, J.R. Carruthers, R.I. Cooper, K. Prout, D.J. Watkin, *J. Appl. Crystallogr.*, **2003**, *36*, 1487.

Chapter 2
A Family of [Mn_6] Complexes and a [Mn_{12}] Complex Featuring Tripodal Ligands

Introduction

From the Brechin group previous experience of employing tripodal alcohol ligands in manganese carboxylate chemistry we have been able to isolate high spin molecules and SMMs with nuclearities ranging from two to thirty two, suggesting that such ligands are indeed excellent candidates for the preparation of polynuclear manganese complexes with interesting magnetic properties [1,2]. The majority of these complexes have been isolated using the basic manganese carboxylate *'triangles'* of general formula $[Mn_3O(O_2CR)_6L_3]^{0/+}$ (R = Me, Ph, etc.; L = py, MeCN, H_2O, etc.), and we therefore decided to extend these studies to include the use of manganese β-diketonate salts and various other *'simple'* manganese sources. Herein we report the syntheses, structures and magnetic properties of a new family of hexanuclear manganese complexes and one dodecanuclear complex built by tripodal ligands (H_3thme, H_3tmp, H_4peol, H_3tea, aepH_2; Scheme **1.2**). All six hexanuclear complexes display very similar structures, yet their observed magnetic behaviour ranges from $S = 0$ ground state to single-molecule magnetism, and this allows us to examine the effect that subtle changes in geometry have on the nature of the individual pairwise exchange interactions and the resultant ground states.

Experimental Section

All manipulations were performed under aerobic conditions, using materials as received. $[Mn_3O(OAc)_6(py)_3]\cdot py$, $NBu^n_4MnO_4$ and $[Mn_{12}O_{12}(OAc)_{16}(H_2O)_4]\cdot 2AcOH\cdot 4H_2O$ were prepared as previously described [3,4].

➢ Synthetic Procedures

$[Mn_6(OAc)_6(H_2tea)_2(tmp)_2]\cdot 2MeCN$ (**1**·2MeCN). To a stirred suspension of $Mn(acac)_2$ (0.500 g, 1.97 mmol) in MeCN (30 ml) were added H_3tmp (0.265 g, 1.97 mmol), H_3tea (0.331 g, 1.97 mmol) and pyridine (5 ml). The resulting yellow-brown solution was left stirring overnight, during which time its colour changed to dark-brown, filtered and layered with two volumes of n-hex/Et_2O (1/1). After one week, the dark-brown crystals that had formed were isolated by filtration, washed with Et_2O, and dried *in vacuo*; yield 35 %. A sample for X-ray crystallography was kept in the mother liquor to prevent solvent loss. Anal. Calcd (Found) for **1**·2MeCN, $C_{40}H_{70}Mn_6N_4O_{24}$: C, 36.38 (36.62); H, 5.34 (5.35); N 4.24 (4.09) %.

$[Mn_6(OAc)_6(H_2tea)_2(thme)_2]\cdot 2py$ (**2**·2py). To a stirred suspension of $Mn(acac)_2$ (0.500 g, 1.97 mmol) in MeCN (30 ml) were added H_3thme (0.237 g, 1.97 mmol), H_3tea (0.331 g, 1.97 mmol) and pyridine (5 ml). The resulting yellow-brown solution was left stirring overnight, during which time it changed colour to dark-brown, filtered and layered with two volumes of n-hex/Et_2O (1/1). After one week, the dark-brown crystals that had formed were isolated by filtration, washed with Et_2O, and dried *in vacuo*; yield 45 %. Anal. Calcd (Found) for **2**·2py, $C_{44}H_{74}Mn_6N_4O_{24}$: C, 38.50 (38.33); H, 5.43 (5.27); N 4.08 (4.01) %.

$[Mn_6(OAc)_6(H_2tea)_2(Hpeol)_2]\cdot py$ (**3**·py). To a stirred solution of $Mn(acac)_2$ (0.500 g, 1.97 mmol) in MeCN (30 ml) were added H_4peol (0.269 g, 1.97 mmol), H_3tea (0.331 g, 1.97 mmol) and pyridine (5 ml). The resulting yellow-brown suspension was left stirring overnight, during which time it changed colour to dark-brown, filtered and layered with two volumes of n-hex/Et_2O (1/1). After one week,

the dark-brown crystals that had formed were isolated by filtration, washed with Et_2O, and dried *in vacuo*; yield 55 %. A sample for X-ray crystallography was kept in the mother liquor to prevent solvent loss. Anal. Calcd (Found) for **3**·py, $C_{39}H_{71}Mn_6N_3O_{26}$: C, 35.28 (34.93); H, 5.39 (5.28); N 3.17 (3.15) %.

$[Mn_6(acac)_4(OAc)_2(Htmp)_2(aep)_2]$ (4). To a stirred suspension of $Mn(acac)_2$ (0.500 g, 1.97 mmol) in MeCN (30 ml) were added H_3tmp (0.265 g, 1.97 mmol) and $aepH_2$ (0.236 g, 1.97 mmol). The resulting yellow-brown solution was left stirring overnight, during which time it changed to dark-brown, filtered and left undisturbed to evaporate slowly. After five days dark-brown crystals were formed and were separated by filtration, washed with Et_2O, and dried *in vacuo*; yield 30 %. A sample for X-ray crystallography was kept in the mother liquor to prevent solvent loss. The dried sample analyzed as solvate-free. Anal. Calcd (Found) for **4**, $C_{46}H_{80}Mn_6N_2O_{22}$: C, 41.25 (41.36); H, 2.09 (2.20); N, 6.01 (6.12) %.

$[Mn_6(OAc)_8(tmp)_2(py)_4]$·2py (5·2py).

Method 1. Treatment of a pale pink solution of $Mn(OAc)_2·4H_2O$ (0.245 g, 1.00 mmol) in py (25 ml) with $NBu^n_4MnO_4$ (0.120 g, 0.33 mmol) resulted in a dark red-brown solution. To this solution was slowly added H_3tmp (0.135 g, 1.00 mmol) to give a dark-brown solution, which was left stirring for 45 min. The solution was then filtered and layered with two volumes of Et_2O to give dark-brown crystals after 3 days. The crystals were collected by filtration, washed with Et_2O, and dried *in vacuo*; yield 30 %. A sample for X-ray crystallography was kept in the mother liquor to prevent solvent loss. The dried sample analyzed as solvate-free. Anal. Calcd (Found) for **5,** $C_{48}H_{64}Mn_6N_4O_{22}$: C, 41.82 (41.67); H, 4.68 (4.74); N, 4.06 (3.99) %.

Method 2. To a stirred dark brown solution of $[Mn_3O(OAc)_6(py)_3]$·py (0.425 g, 0.50 mmol) in py (25 ml) was added solid H_3tmp (0.405 g, 1.50 mmol), which dissolved to give a solution of the same color. The new solution was stirred for 45 min, layered with two volumes of Et_2O to give dark-brown crystals of **5**·2py after three days. The crystals were collected by filtration, washed with Et_2O and dried under vacuum; yield 35 %. The dried sample analyzed satisfactorily as solvent-free **5**.

Method 3. Treatment of a dark-brown solution of $[Mn_{12}O_{12}(OAc)_{16}(H_2O)_4]\cdot 2AcOH\cdot 4H_2O$ (0.500 g, 0.25 mmol) in py (25 ml) with H_3tmp (0.203 g, 1.5 mmol) gave a solution of essentially the same colour. The new solution was left stirring for 45 min, filtered and layered with two volumes of Et_2O to form dark-brown crystals of **5**·2py after two days. The crystals were collected by filtration, washed with Et_2O and dried under vacuum; yield 25 %. The dried sample analyzed satisfactorily as solvent-free **5**.

$[Mn_6(OAc)_8(thme)_2(py)_4]\cdot 2py$ (**6**·2py).

Method 1. Treatment of a pale pink solution of $Mn(OAc)_2\cdot 4H_2O$ (0.245 g, 1.00 mmol) in py (25 ml) with $NBu^n_4MnO_4$ (0.120 g, 0.33 mmol) resulted in a dark red-brown solution. To this solution was slowly added H_3thme (0.125 g, 1.00 mmol) to give a dark-brown solution, which was left stirring for 45 min. The solution was filtered and layered with two volumes of Et_2O to give dark-brown crystals after 3 days. The crystals were collected by filtration, washed with Et_2O, and dried *in vacuo*; yield 35 %. A sample for X-ray crystallography was kept in the mother liquor to prevent solvent loss. The dried sample analyzed as solvate-free. Anal. Calcd (Found) for **6,** $C_{46}H_{60}Mn_6N_4O_{22}$: C, 40.91 (40.96); H, 4.48 (4.71); N, 4.15 (4.20) %.

Method 2. Method 2 for complex **5**·2py was repeated using H_3thme (0.188 g, 1.5 mmol) in place of H_3tmp. The method resulted in the formation of X-ray quality dark-brown crystals of **6**·2py, as was confirmed by crystallography; yield 35 %.

Method 3. Method 3 for complex **5**·2py was repeated using H_3thme (0.188 g, 1.5 mmol) in place of H_3tmp. The method yielded dark-brown crystals of **6**·2py; yield 25 %. The dried sample analyzed satisfactorily as solvent-free, **6**.

$[Mn_{12}(Hthme)_8(thme)_2(py)_2Br_8]\cdot 2py$ (**7**·2py). To a stirred suspension of $MnBr_2\cdot 4H_2O$ (0.500 g, 1.74 mmol) in MeCN (30 ml) were added H_3thme (0.209 g, 1.74 mmol), H_3tea (0.292 g, 1.74 mmol) and 5 ml of pyridine. The resulting brown solution was left upon stirring overnight, during which time it changed its colour to dark-brown, filtered and layered with Et_2O (1/1). After one week, the black crystals that had formed were isolated by filtration, washed with Et_2O, and dried *in vacuo*;

yield 10 %. Anal. Calcd (Found) for **7**·2py, $C_{70}H_{110}Mn_{12}N_4O_{30}Br_8$: C, 30.18 (30.03); H, 3.98 (3.03); N, 2.01 (2.17) %.

Results and Discussion

➢ Synthesis

The reaction between $Mn(acac)_2$ and tripodal alcohols (H_3tmp, H_3thme or H_4peol) in the presence of H_3tea in MeCN gives the complexes $[Mn_6(OAc)_6(H_2tea)_2(tmp)_2]$ (**1**), $[Mn_6(OAc)_6(H_2tea)_2(thme)_2]$ (**2**) and $[Mn_6(OAc)_6(H_2tea)_2(Hpeol)_2]$ (**3**), respectively. Complexes **1-3** are mixed-valent containing four Mn^{II} and two Mn^{III} ions each. Given that the starting manganese source contains exclusively Mn^{II} ions, it is apparent that the Mn^{III} ions are generated upon oxidation by atmospheric O_2, a process common in manganese cluster chemistry. To our initial surprise there were no β-diketonate ligands and six acetates in the product despite the starting material being $Mn(acac)_2$. The transformation of β-diketonates to carboxylates is in itself not surprising and has been seen in a number of other polynuclear cluster compounds [5], but it is rare to find the conversion in "100 % yield" with no β-diketonates in the crystallized product (from a total yield of 35%; see the Experimental Section). The retro-Claisen condensation responsible is base-assisted and here the excess H_3tea has clearly acted to mediate the reaction in high yield (*vide infra*) [6].

With the identity of complex **1** (**2** and **3**) established, and in an attempt to incorporate some $acac^-$ ligands into the final product, we repeated the reaction using exactly the same reaction conditions (*e.g.* reaction time, concentrations, *etc.*) but replacing H_3tea (pKa ~ 13) with $aepH_2$ (pKa ~ 11). The result was the isolation of complex **4** in which both $acac^-$ and OAc^- ligands are present and where the $acac^-$ to OAc^- transformation is 77% less than that observed for complex **1**. In addition,

complex **4** contains only doubly deprotonated $Htmp^{2-}$ ligands, while in complex **1** both are fully deprotonated tmp^{3-}, as might be expected by the use of a weaker base.

The syntheses of complexes **5** and **6** can both be regarded as either *'reductive aggregations'* and/or as comproportionations depending on the method used. Comproportionation is the simple reaction between a Mn^{II} salt [e.g. $Mn(OAc)_2{\cdot}4H_2O$] and a source of Mn^{VII} (e.g. $NBu_4^nMnO_4$), while reductive aggregation is a process whereby high oxidation state Mn sources are reacted in reducing conditions that force a reduction of the metal centres (e.g. Mn^{III} to Mn^{II}) and structural rearrangement (in the presence or absence of additional bridging ligands) that results in the formation of a new product. For example, complex **5** is made from the reaction of $Mn(OAc)_2{\cdot}4H_2O$ and $NBu_4^nMnO_4$ in pyridine in the presence of the tripodal bridging ligand H_3tmp. When mixed together the $Mn(OAc)_2{\cdot}4H_2O$ and $NBu_4^nMnO_4$ initially form a bright purple solution which then turns dark brown upon stirring as the Mn^{VII} ions are reduced and the Mn^{II} ions oxidized. At this stage the H_3tmp is added (to avoid ligand oxidation) with the deprotonation and complexation of the ligand accompanied by a further reduction in the metal oxidation states as the solution colour turns (over several hours) light brown. Complex **6** can be made from the reaction of $[Mn_{12}O_{12}(OAc)_{16}(H_2O)_4]$ with H_3thme. The $[Mn_{12}]$ cluster contains Mn^{IV} and Mn^{III} ions and the tripodal ligand is added in its fully protonated form (H_3thme) yet the product contains a $[Mn^{III}_2Mn^{II}_4]$ core held together by triply deprotonated $thme^{3-}$ ligands. Clearly as is the case with almost all Mn cluster chemistry, complexes **1-6** are unlikely to be the only species present, and their formation and crystallization is an extremely complicated process that also involves the protonation/deprotonation, structural rearrangement and redox chemistry of many other species present in solution.

The success of these comproportionation reactions also led us to attempt the synthesis of similar $[Mn_6]$ complexes but in different oxidation levels – particularly those complexes with a higher Mn^{III}: Mn^{II} ratio. Reactions involving using greater ratios of MnO_4^- and in the presence of additional anions were examined in detail but resulted only in the formation of identical complexes – albeit in differing yields.

Similarly when the reductive aggregation route was employed replacing the $[Mn^{III}_3]$ triangles with higher oxidation state sources such as $[Mn_{12}O_{12}(OAc)_{16}(H_2O)_4]$ (which comprises four Mn^{IV} and eight Mn^{III} ions), only the same products could be crystallized. The relatively high yields these hexanuclear clusters can be obtained in, and their ease of crystallization, suggests their formation to be more thermodynamically favourable than that of any higher oxidation state analogue(s) that may also be present in solution.

Complex **7** was prepared by reacting $MnBr_2 \cdot 4H_2O$ with H_3thme and H_3tea in MeCN and pyridine. The complex is mixed–valence containing six Mn(II) and six Mn(III) ions. Two of the ten H_3thme ligands are fully deprotonated, $thme^{3-}$, and the remaining eight are doubly deprotonated, $Hthme^{2-}$. There are no H_3tea ligands in the product, suggesting its role is only as base. The bromides solely act as terminal ligands and fill the coordination spheres of manganese ions, an approach which here we have found particularly useful (vide infra).

➢ Description of structures

$[Mn_6(OAc)_6(H_2tea)_2(tmp)_2]$ (**1**) crystallizes in the monoclinic space group *C2/c* (Figure **2.1**; selected bond lengths and angles are given in Table A.2.4). The complex consists of a rod-like $[Mn^{II}_4Mn^{III}_2(\mu\text{-OR})_6(\mu_3\text{-OR})_4]^{4+}$ unit of four edge-sharing Mn triangles. The core is trapped-valence with Mn1 and its symmetry equivalent being the sole Mn^{III} ions, and can be described as consisting of four edge-sharing $[Mn_3(OR)]$ triangles (Figure **2.2**). All six Mn ions effectively lie on the same plane and are in distorted octahedral geometries, except Mn3 and Mn3' which can be considered as *pseudo* seven-coordinate with a long contact to the N atom of the triethanolamine ligand (Mn3-N1B, 2.523 Å). The two Mn^{III} ions display Jahn-Teller elongations (Mn1-O1D, 2.177 Å; Mn1-O2A', 2.238 Å and s.e), which are co-parallel and at an angle of ~ 37° with respect to the plane of the six Mn ions. The two tripodal alcohol ligands are fully deprotonated, tmp^{3-}, and located directly above and below

the [Mn_6] plane, each binding in a $\eta^3:\eta^3:\eta^2:\mu_5$ fashion to five metal centres that form three edge sharing triangles (Figure **2.3**).

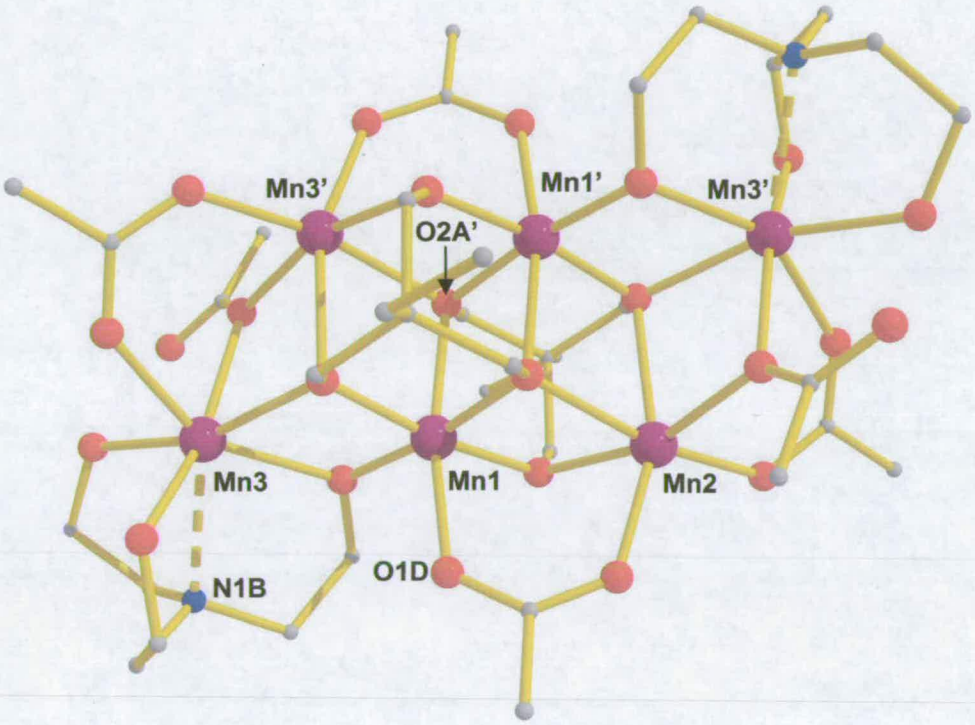

Figure 2.1. The structure of **1** in the crystal. Hydrogen atoms and solvent molecules have been omitted for clarity. Colour scheme: Mn: purple; O: red; N: blue; C: grey.

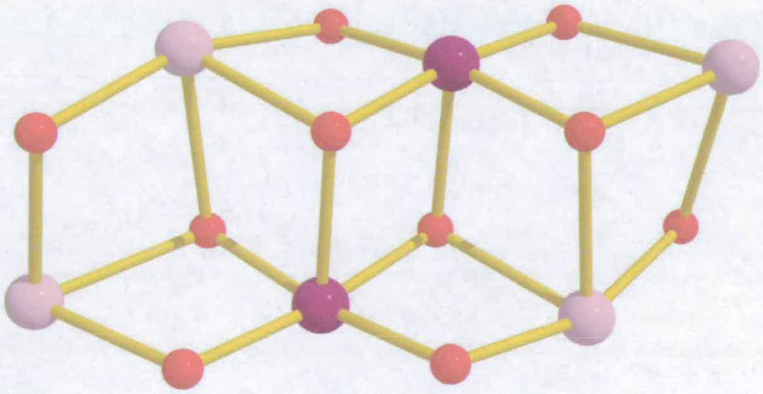

Figure 2.2. The core of **1** in the crystal. Colour scheme: Mn(III): purple; Mn(II): pink; O: red.

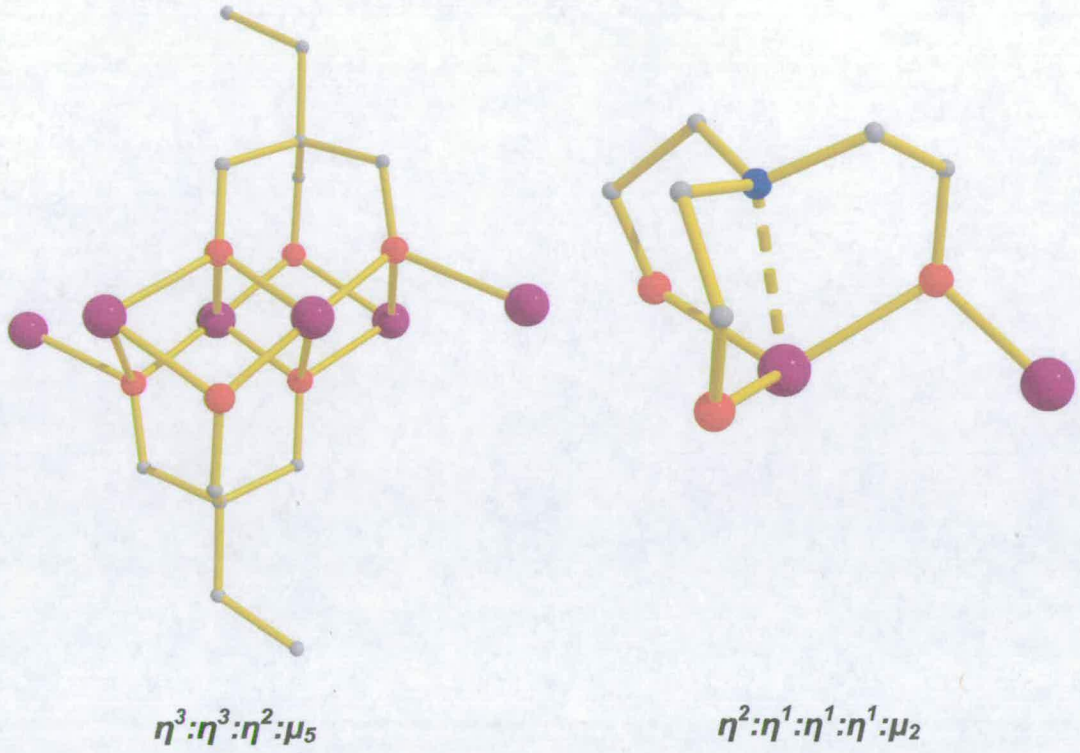

Figure 2.3. The μ_5-coordination mode of the alcohol tripodal ligands present in **1-7** and the triethanolamine ligand present in **1-3**. Colour scheme: Mn: purple; O: red; N: blue; C: grey.

The six carboxylates coordinate in two different ways: four are in the usual $\eta^1:\eta^1:\mu$-mode, and two in the monoatomic μ mode. The triethanolamine ligands are doubly protonated, H_2tea^{1-}, capping each end of the molecule in a $\eta^2:\eta^1:\eta^1:\eta^1:\mu$-mode (Figure **2.3**). Both protonated arms of each H_2tea^{1-} ligand are involved in hydrogen bonding; one arm forms an intermolecular H-bond to an O-atom of the monoatomic acetate belonging to a neighboring [Mn_6] unit, while the second protonated arm forms an intramolecular H-bond to the O-atom of the monoatomic acetate belonging to the same [Mn_6] unit. The molecules in the crystal lattice stack directly upon each other, forming sheets with the solvent molecules, occupying the space within these sheets. The closest intermolecular Mn···Mn distance is 8.06 Å between adjacent sheets, and 7.86 Å within the same sheet (Figure **2.4**). Each unit

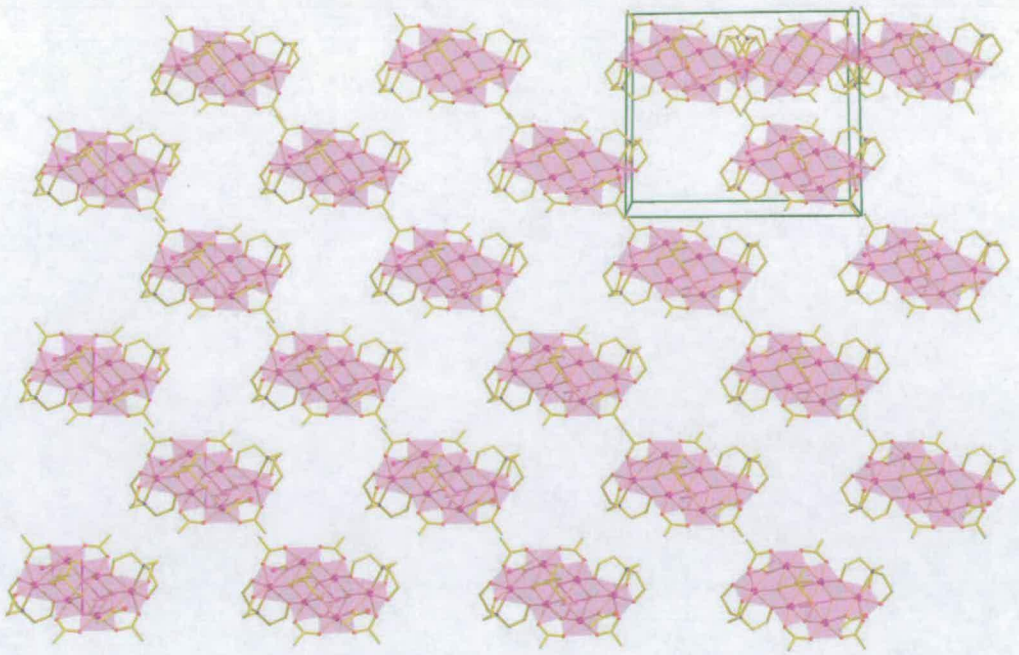

Figure 2.4. The packing of the molecules of **1** in the crystal, viewed parallel to the [Mn_6] inner. Colour scheme same as complex **1**.

cell of **1** contains eight 'half' [Mn_6] molecules such that the clusters are in a common observed brickwall pattern.

[$Mn_6(OAc)_6(H_2tea)_2(thme)_2$] (**2**) crystallizes in the triclinic space group $P\bar{1}$ (Figure **2.5**; selected bond lengths and angles are given in Table A.2.5). Complex **2** consists of a rod-like $[Mn^{II}_4Mn^{III}_2(\mu\text{-OR})_6(\mu_3\text{-OR})_4]^{4+}$ unit and a Mn-O core similar to **1** with Mn3 and Mn3' being the sole Mn^{III} ions (Figure **2.2**). The *pseudo* seven-coordinate Mn1 has a long bonding distance of Mn1-N11 2.506 Å (and s.e) contact to the N-atom and the triethanolamine ligand. The two Mn^{III} display Jahn-Teller elongations (Mn3-O34, 2.181 Å; Mn3-O45', 2.243 Å; and s.e), which are co-parallel and form an angle of ~38° with respect to the plane of the six Mn ions. The $thme^{3-}$ and H_2tea^{1-} ligands and the carboxylates coordinate as in complex **1** (Figure **2.3**). The molecules of **2** pack in the common observed brickwork pattern. The closest intermolecular Mn···Mn distance is 8.07 Å between adjacent sheets, and 7.41 Å within the same sheet (Figure **2.6**).

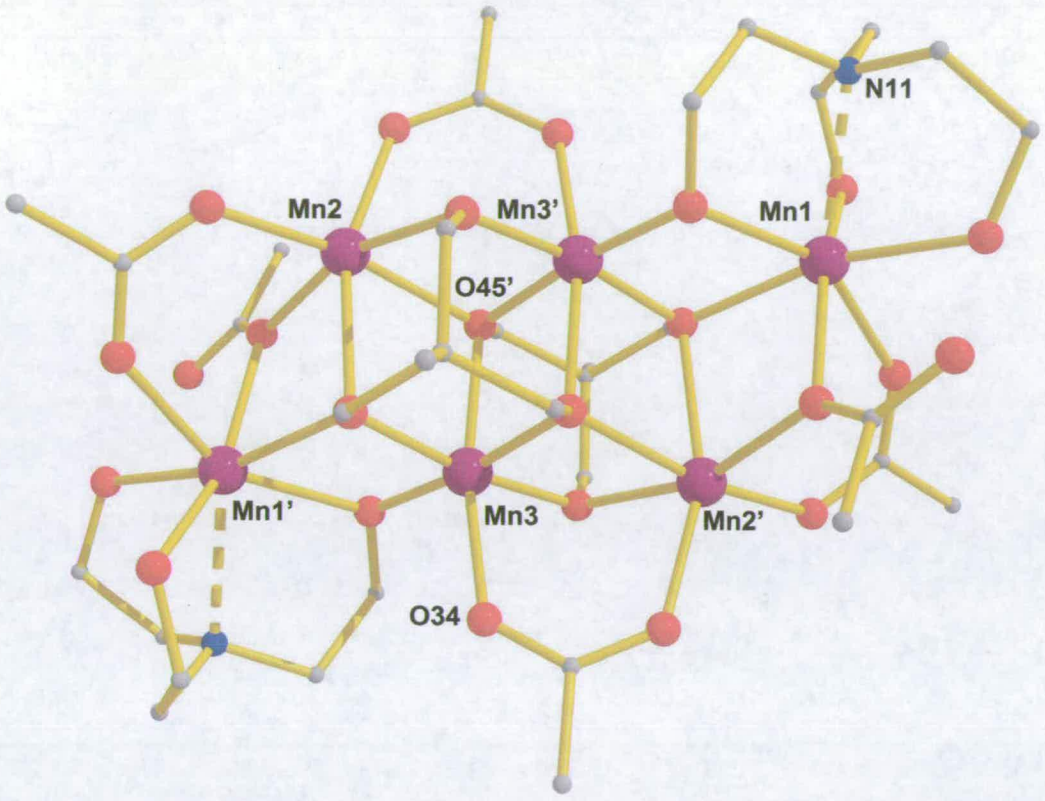

Figure 2.5. The structure of **2**. Hydrogen atoms and solvent molecules have been omitted for clarity. Colour scheme same as complex **1**.

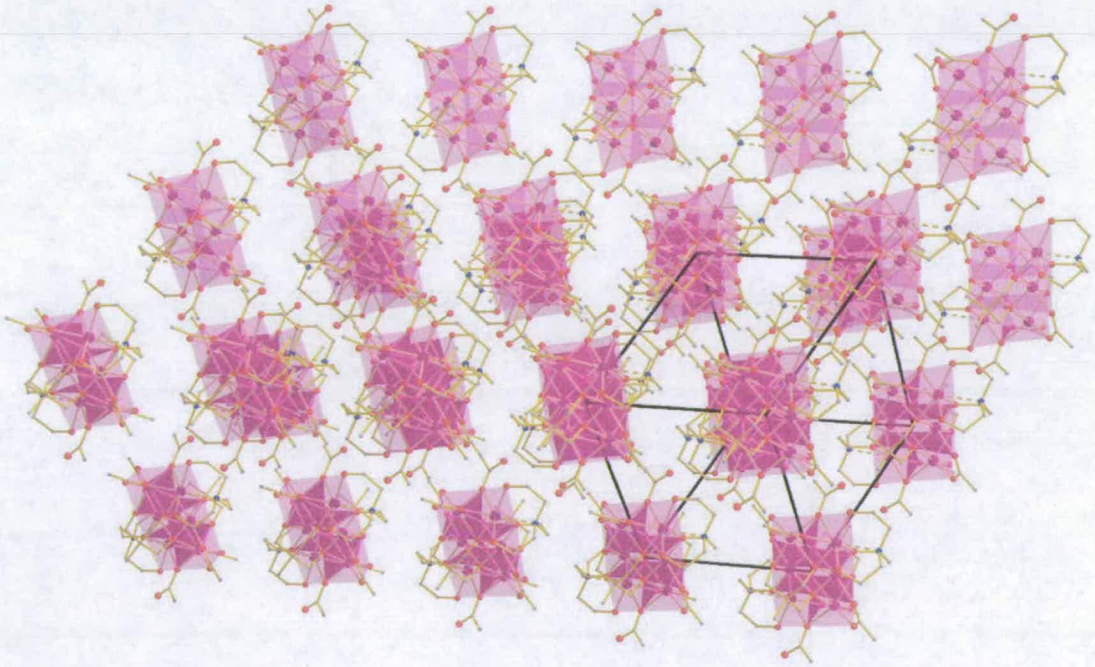

Figure 2.6. The packing of the molecules of **2** in the crystal, viewed perpendicular to the $[Mn_6]$ inner. Colour scheme same as complex **1**.

$[Mn_6(OAc)_6(H_2tea)_2(Hpeol)_2]$ (3) crystallizes in the monoclinic space group $P2_1/n$ (Figure **2.7**; selected bond lengths and angles are given in Tables A.2.6). Complex **3** consists of a rod-like unit and Mn-O core similar to **1** with Mn2 (and s.e) being the Mn^{III} ions (Figure **2.2**). The *pseudo* seven-coordinate Mn1 (and Mn1'), having long bonding distances of 2.470 Å to N11-atom. The two Mn^{III} display Jahn-Teller elongations (Mn2-O323, 2.199 Å; Mn2-O7, 2.240 Å and s.e). Both JT axes are co-parallel and at an angle of ~35° with respect to the $[Mn_6]$ plane. The two tripodal alcohol ligands are triply deprotonated, $Hpeol^{3-}$, using the three of their four alkoxide arms and are located directly above and below the $[Mn_6]$ plane in μ_5-mode such as in **1** and **2** (Figure **2.3**). The carboxylates and the triethylamine ligands again coordinate in a similar fashion to **1** and **2.** For complex **3,** the closest intermolecular Mn···Mn distance is 6.82 Å (Figure **2.8**).

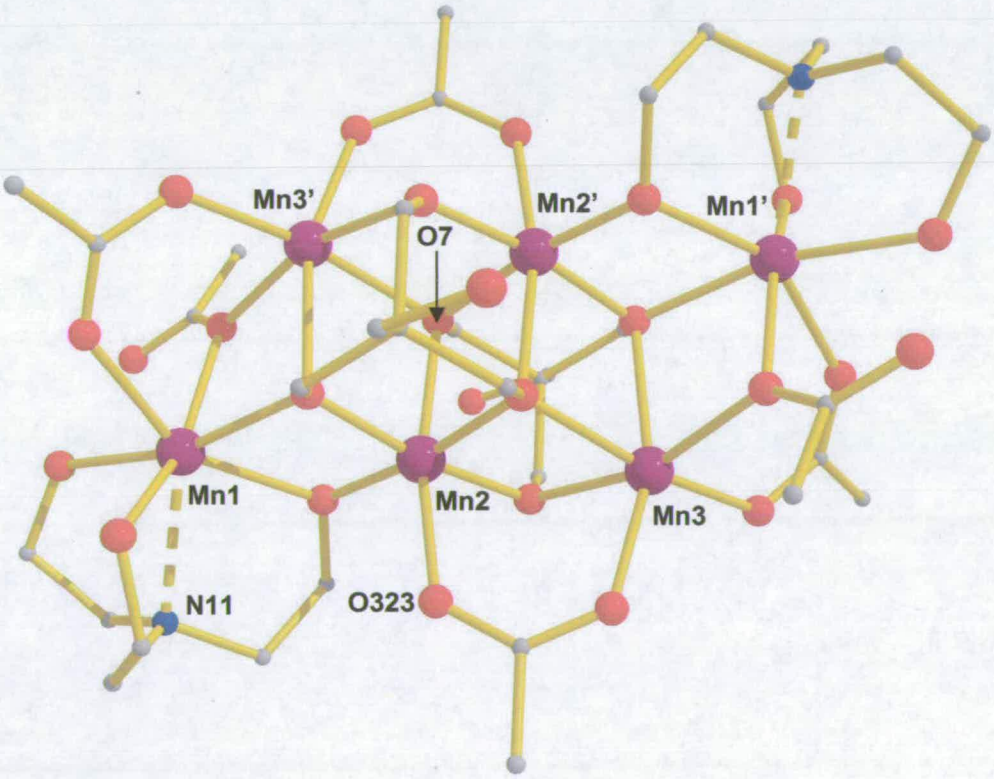

Figure 2.7. Structure of **3** in the crystal. Hydrogen atoms and solvent molecules have been omitted for clarity. Colour scheme same as complex **1**.

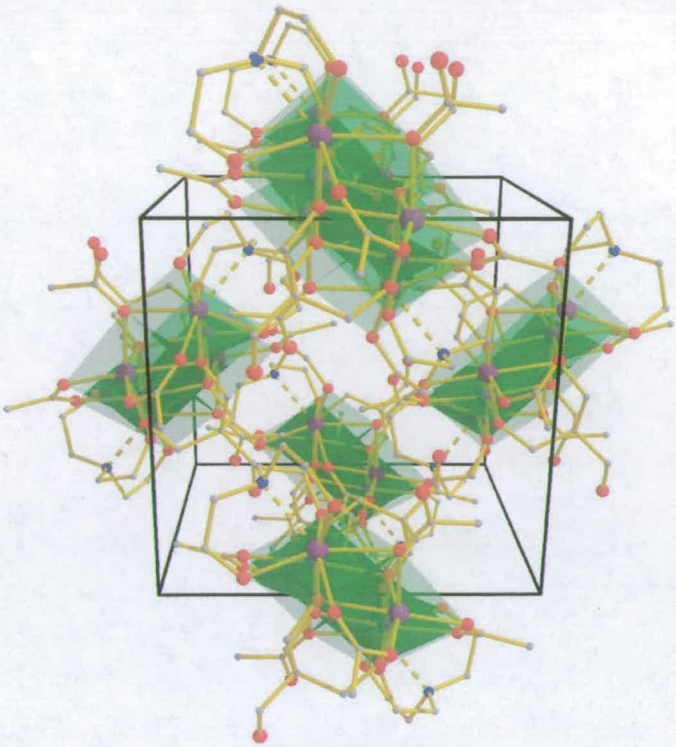

Figure 2.8. The packing of the molecules of **3** in the unit cell in the crystal. Colour scheme same as complex **1**.

$[Mn_6(acac)_4(OAc)_2(Htmp)_2(aep)_2]$ (4), crystallizes in the monoclinic space group $P2_1/n$ (Figure **2.9**; selected bond lengths and angles are given in Table A.2.7). Its core consists of a rod-like planar $[Mn^{III}_2Mn^{II}_4(\mu\text{-OR})_6(\mu_3\text{-OR})_4]^{4+}$ unit comprising four edge-sharing triangles, as in **1-3** (Figure **2.2**). The sole Mn^{III} ions (Mn1 and Mn1') are located in the centre of the core, with all six manganese ions lying in the same plane. All are hexa-coordinate adopting distorted octahedral geometries with the Mn^{III} ions displaying the expected Jahn-Teller elongations (Mn1-N21, 2.308 Å; Mn1-O31', 2.260 Å) and are again co-parallel and at an angle of ~29° with respect to the central plane of the Mn ions. The two tripodal alcohol ligands are doubly deprotonated, $Htmp^{2-}$, sitting above and below the $[Mn_6]$ plane coordinating *via* only two of their three arms in a $\eta^2:\eta^2:\mu_3$-fashion linking three Mn ions together in a linear array. The two 2-amino-2-ethyl-1,3-propanediol ligands are doubly deprotonated, aep^{2-}, lying above and below the $[Mn_6]$ plane, coordinating in a $\eta^3:\eta^3:\eta^1:\mu_5$-mode to

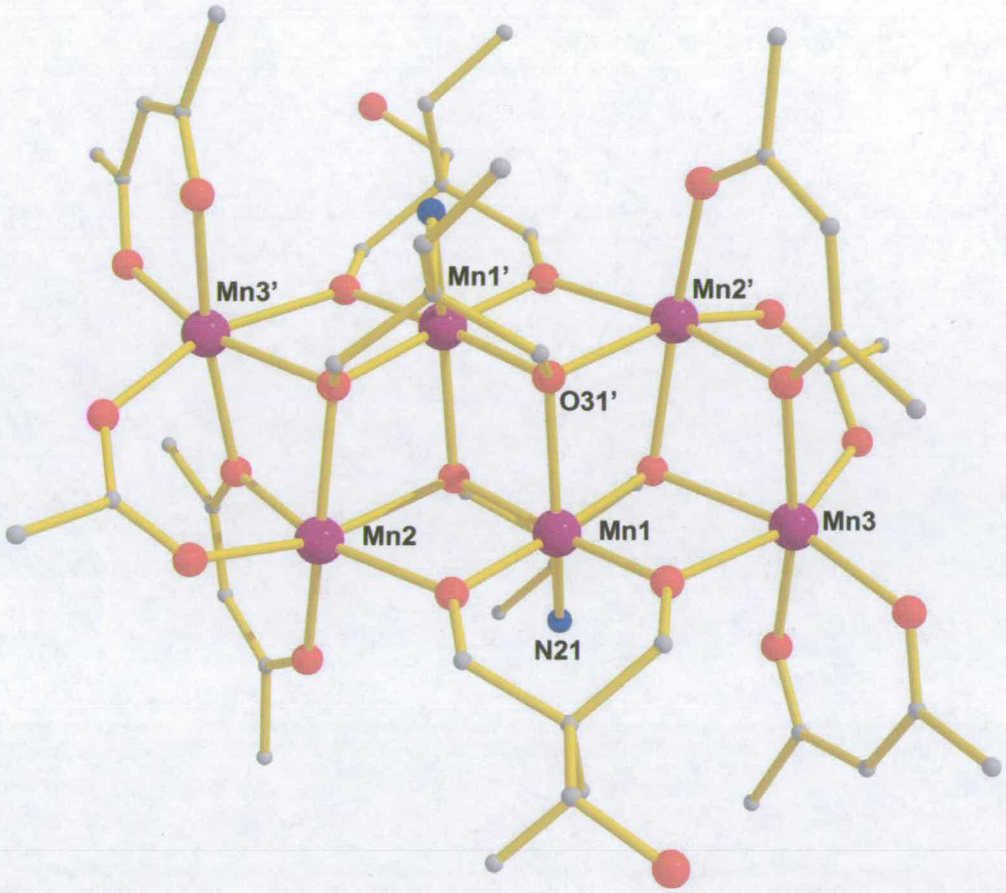

Figure 2.9. Structure of **4** in the crystal. Hydrogen atoms have been omitted for clarity. Colour scheme same as complex **1**.

five metal centres that form three edge-sharing triangles. Two of the acac$^-$ ligands adopt their common chelating mode, while the remaining two bond in the more unusual $\eta^2:\eta^1:\mu$-fashion. The coordination spheres of the peripheral Mn ions are completed by the presence of $\eta^1:\eta^1:\mu$-acetates that bridge between Mn2 and Mn3' (and s.e).

The protonated OH group of the non-deprotonated arm of each Htmp^{2-} forms an intermolecular H-bond to an O-atom belonging to a bridging acetate of a neighbouring [Mn_6] unit. As a result of these interactions, each [Mn_6] unit forms four H-bonds (two from the Htmp^{2-} ligands and two from the bridging acetates) to four different neighbouring [Mn_6] species belonging to the same sheet and, thus, the

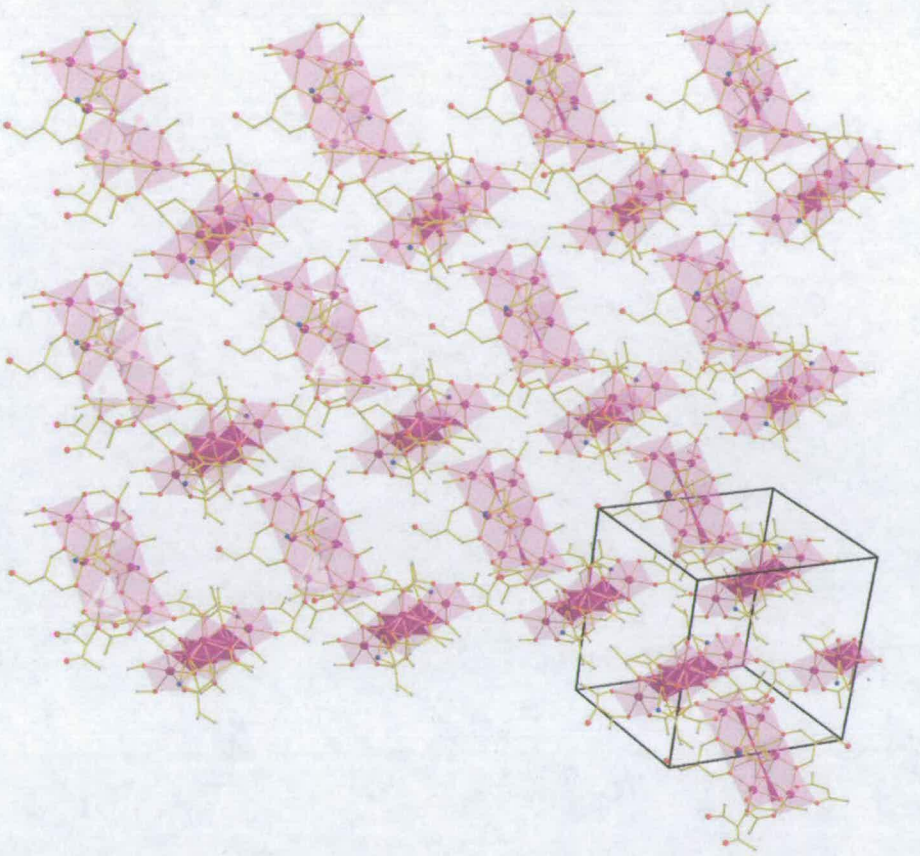

Figure 2.10. The packing of the molecules of **4** in the crystal. Colour scheme same as complex **1**.

molecules form 2D sheets held together by a complicated network of H bonds. These 2D networks stack upon each other leaving no solvent accessible void, with the closest Mn···Mn distance in the same sheet of 8.48 Å and 7.62 Å between adjacent sheets (Figure **2.10**).

$[Mn_6(OAc)_8(tmp)_2(py)_4]$ (**5**), crystallizes in the triclinic space group $P\bar{1}$ (Figure **2.11**; selected bond lengths and angles are given in Table A.2.8). Its core can be described as a non-planar $[Mn^{III}_2Mn^{II}_4(\mu\text{-}OR)_2(\mu_3\text{-}OR)_4]^{8+}$ unit, or again more conveniently as a central planar $[Mn^{III}_2Mn^{II}_2]$ rhomb (comprising Mn2, Mn3 and s.e) with two peripheral Mn ions (Mn1 and Mn1') above and below the plane at distances of 1.107 and -1.107 Å, respectively (Figure **2.12**). The two Mn^{III} ions are Mn3 and Mn3' with their JT elongations described by the Mn3-O23 (2.124 Å) and Mn3-O21' (2.289 Å) directions at an angle of ~57° with respect to the $[Mn_4]$ plane. The tripodal

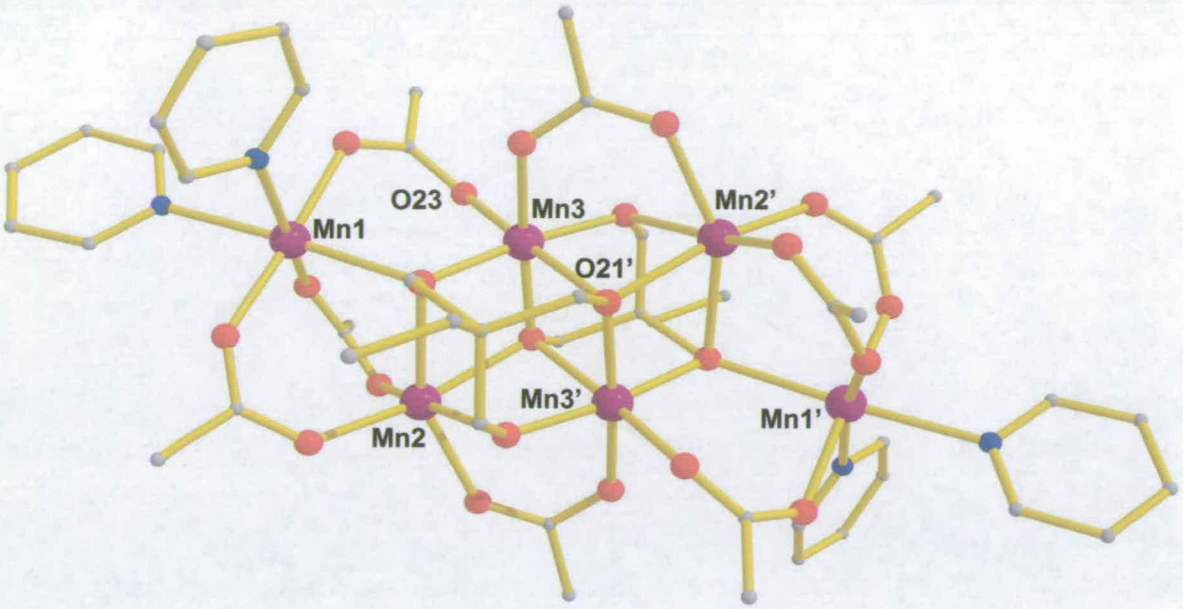

Figure 2.11. The crystal structure of complex **5**. Colour scheme same as complex **1**.

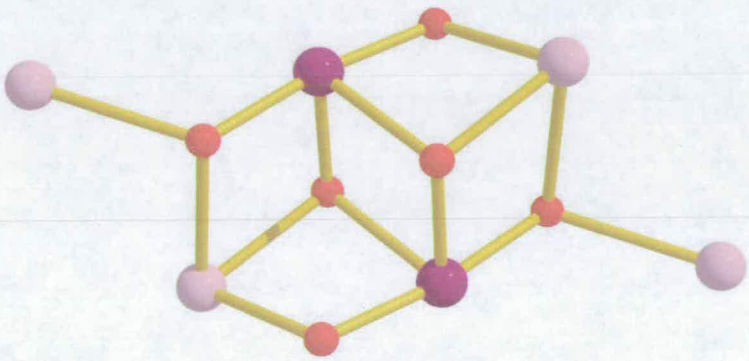

Figure 2.12. The core of complex **5**. Colour scheme: Mn(III): purple; Mn(II): pink; O: red.

alcohols are fully deprotonated, tmp^{3-}, sitting one above and one below the $[Mn_4]$ plane coordinating in a $\eta^3:\eta^3:\eta^2:\mu_5$-fashion bridging five metals to form three edge-sharing triangles. All eight acetates adopt a $\eta^1:\eta^1:\mu$-bridging mode, while the coordination environment of the peripheral Mn ions are completed by four terminal pyridine ligands.

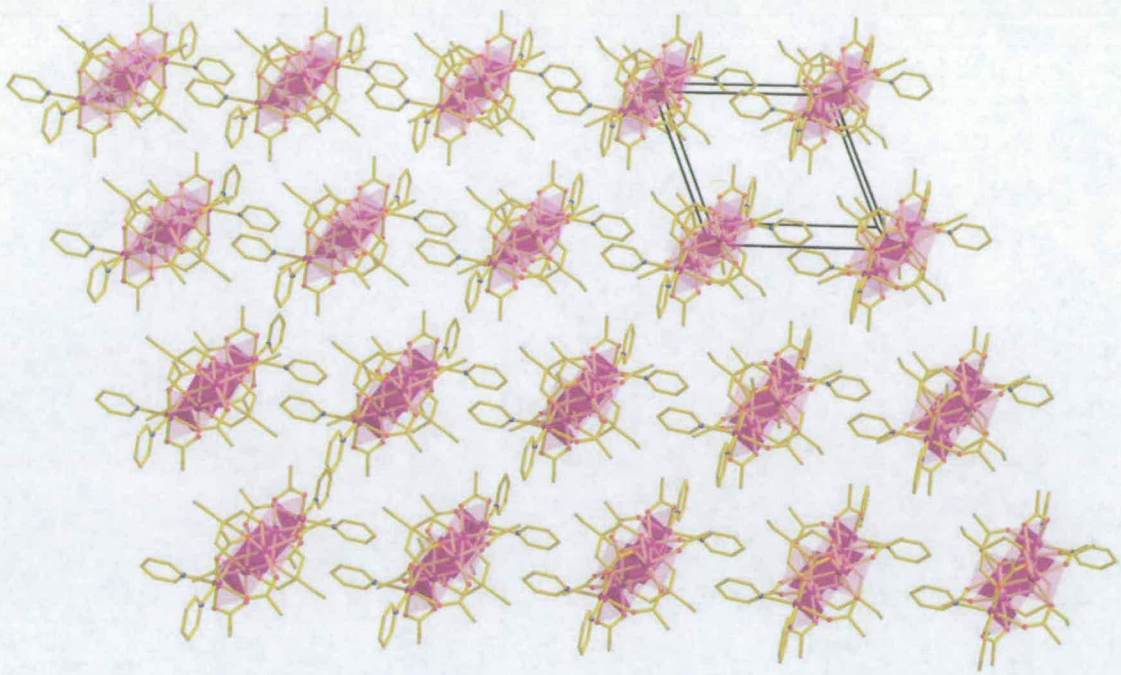

Figure 2.13. The packing of the molecules of **5** in the crystal. Colour scheme same as complex **1**.

In the crystal lattice the molecules pack upon each other forming sheets with the pyridine solvate molecules lying in the space between adjacent sheets. There are no intermolecular or intramolecular H-bonds present between [Mn_6] units, while the closest Mn···Mn distance is ~7.7 Å. The molecules of **5** pack in the common observed brickwall pattern (Figure **2.13**).

[$Mn_6(OAc)_8(thme)_2(py)_4$] (**6**), crystallizes in the triclinic space group $P\bar{1}$ (Figure **2.14**; selected bond lengths and angles are given in Table A.2.9). The structure consists of a non-planar $[Mn^{II}_4Mn^{III}_2(\mu\text{-OR})_4(\mu_3\text{-OR})_4]^{6+}$ unit, and as in the case of **5**, the core can be described as consisting of a central [Mn_4] plane (comprising Mn2, Mn3 and s.e) with two Mn1 and Mn1' ions, located above and below the plane (Figure **2.15**) at a distance of ±1.167 Å. The Mn^{III} ions are Mn3 and Mn3', with the JT elongations being Mn3-O14 (2.148 Å) and Mn3-O21' (2.303 Å) and s.e at an angle of ~57° with respect to the [Mn_4] plane, as in **5**.

All Mn ions are six-coordinate adopting distorted octahedral geometries, except Mn2, Mn2' which are *pseudo* seven-coordinate, displaying a long bonding

distance to O22 (and s.e) of 2.818 Å. Both tripodal alcohol ligands are fully deprotonated, thme^{3-}, coordinating in a $\eta^3:\eta^3:\eta^2:\mu_5$-fashion, bridging five metals, while the acetates adopt two different coordination modes; six of them are in the usual $\eta^1:\eta^1:\mu$-bridging mode, while the remaining two bond in a $\eta^2:\eta^1:\mu$-fashion. The coordination spheres of the peripheral Mn ions are completed by terminal pyridine ligands.

$[Mn_{12}(Hthme)_8(thme)_2(py)_2Br_8]$ (7), crystallizes in the triclinic space group $P\bar{1}$ (Figure **2.16**; selected bond lengths and angles are given in Table A.2.10). The core consists of a non-planar $[Mn^{II}_6Mn^{III}_6(\mu\text{-OR})_{14}(\mu_3\text{-OR})_8]^{8+}$ unit with Mn2, Mn4, Mn5 (and s.e) being the Mn^{III} ions, and can be described as consisting of eight edge-sharing $[Mn_3(OR)]$ triangles which are linked together forming a central $[Mn_{10}]$ plane (Figure **2.17**). Alternatively, it can be described as four edge-sharing $[Mn_4O_2]$ butterfly ('planar diamond') units. The six Mn^{III} display Jahn-Teller elongations (Mn2-O24, 2.260 Å; Mn2-O33, 2.178 Å; Mn4-O36, 2.222 Å; Mn4-O44, 2.225 Å; Mn5-O35, 2.225 Å; Mn5-O34, 2.290 Å; and s.e), which are co-parallel at an angle of ~70° with respect to the $[Mn_{10}]$ plane. The two peripheral Mn^{II} ions Mn1 (and s.e) lie above and below the $[Mn_{10}]$ plane at distance of 2.507 Å. The ten central Mn ions are in distorted octahedral geometries, whereas the two outermost ions (Mn1 and Mn1'), can be considered five-coordinate.

There is a range of structural types intermediate between the idealized square-pyramidal and trigonal-bipyramidal. In a five-co-ordinate system such as that represented in Scheme **2.1**, ideally square-pyramidal geometry is associated with $\alpha = \beta = 180°$, for **A** as the axial ligand (β is the greater of the basal angles, **BMC**). For perfectly trigonal-bipyramidal geometry, α becomes 120° and **BMC** the principal axis. In the great majority of real square-pyramidal systems **M** is displaced out of the **BCDE** plane [7] toward **A**, so that these C_{4v} geometries usually have $\alpha = \beta < 180°$, and can be characterized by the value of $(\beta - \alpha)$, which is 0° for a C_{4v}, and 60° for a D_{3h} co-ordination polyhedron.

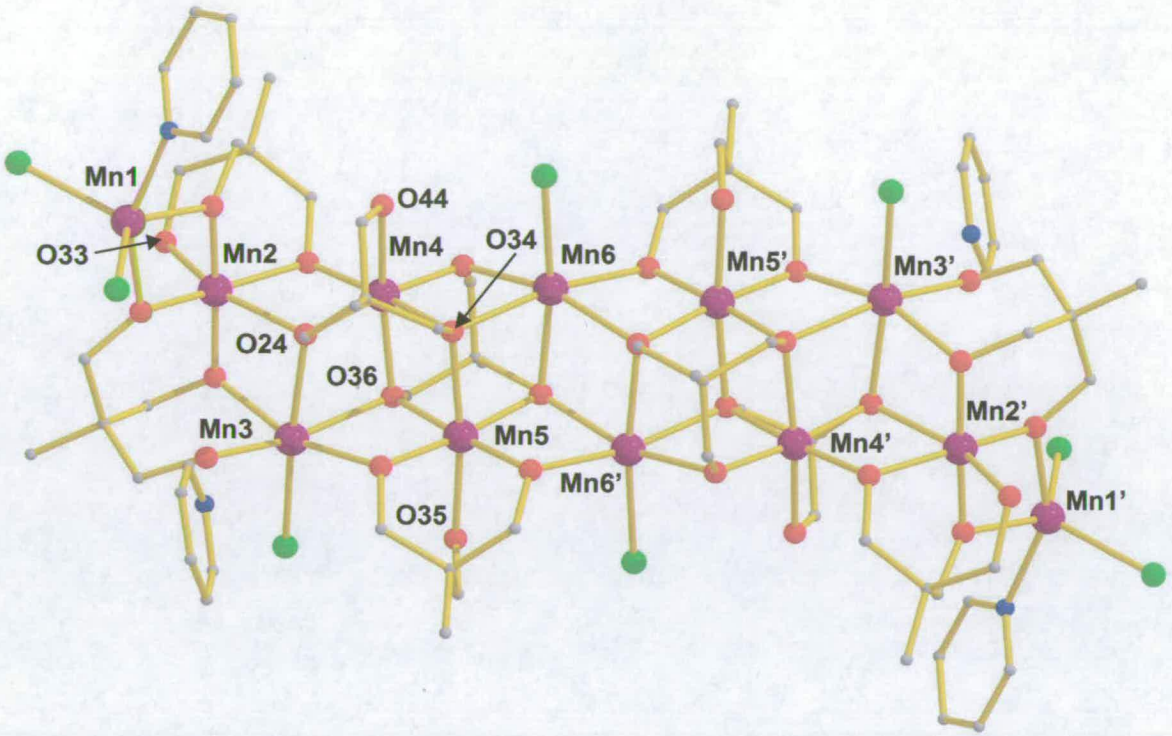

Figure 2.16. The crystal structure of complex **7**. Colour scheme: Mn: purple; O: red; N: blue; C: grey; Br: green.

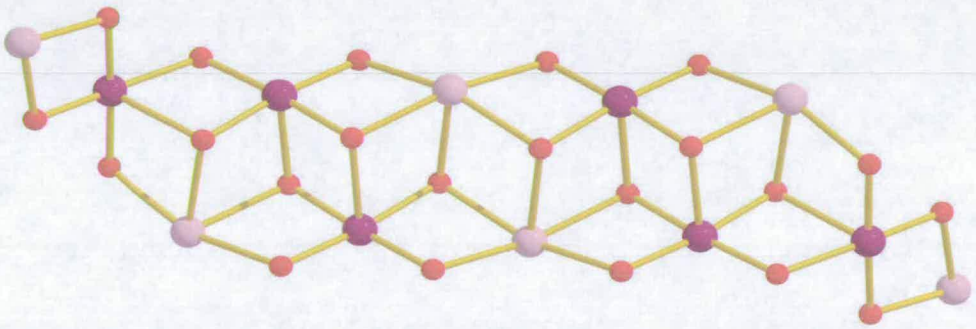

Figure 2.17. The core of complex **7**. Colour scheme: Mn(III): purple; Mn(II): pink; O: red.

The two fully deprotonated ligands, $thme^{3-}$, are located directly above and below the $[Mn_{10}]$ plane bridging in a $\eta^3:\eta^3:\eta^2:\mu_5$-fashion to five metal centres that describe three edge-sharing triangles. The other eight tripodal ligands are doubly deprotonated ($Hthme^{2-}$) and coordinate in two different ways: two in a $\eta^3:\eta^3:\eta^1:\mu_5$-fashion linking five metals into three edge-sharing triangles; and six in a $\eta^1:\eta^2:\eta^2:\mu_3$-

fashion linking five metals into three edge-sharing triangles; and six in a $\eta^1:\eta^2:\eta^2:\mu_3$-fashion linking three metals in a near-linear array. Four of the eight bromides are coordinated terminally to the Mn^{II} ions in the central $[Mn_{10}]$ plane, with the remaining four bonded to the peripheral five-coordinate Mn^{II} ions. The coordination sphere of these ions is completed by two terminal pyridines. For complex **7**, the closest intermolecular Mn···Mn distance is 11.29 Å between adjacent sheets, and 7.89 Å within the same sheet (Figure **2.18**).

In all cases, the oxidation states of the metal ions were assigned using a combination of bond length, charge balance considerations and BVS calculations (Table **2.1**) [8].

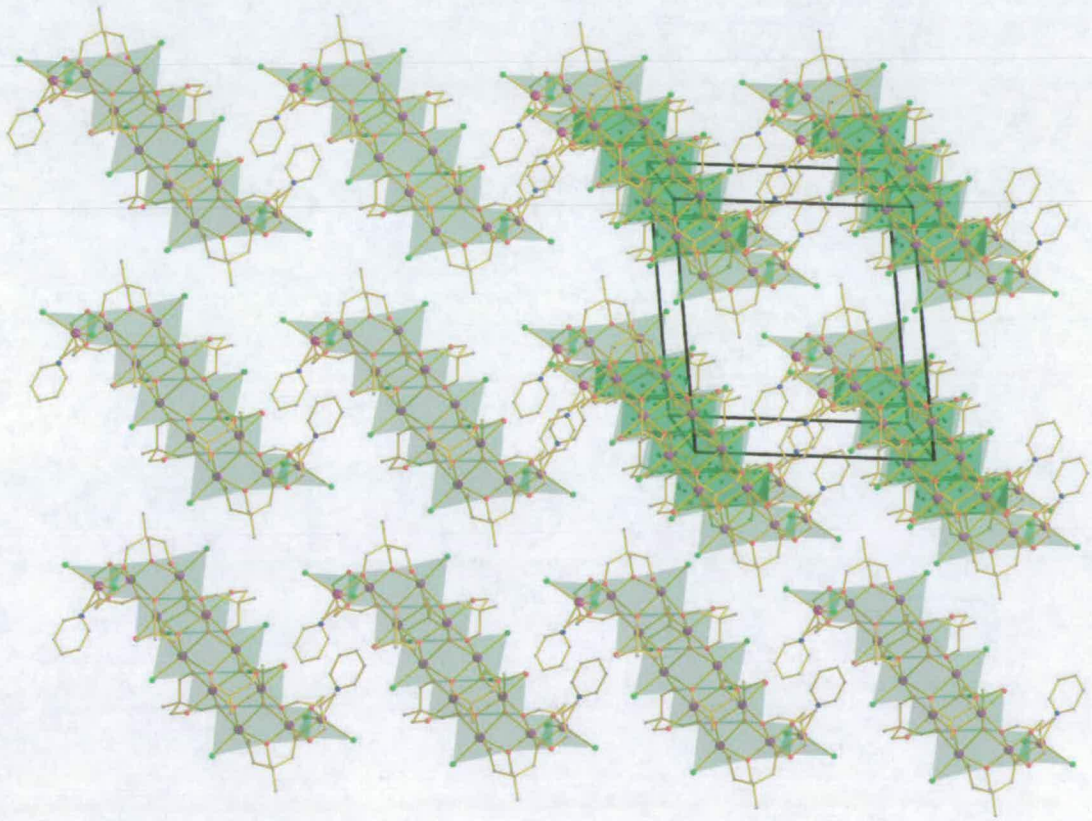

Figure 2.18. The packing of the molecules of **7** in the crystal, viewed parallel to the $[Mn_{12}]$ inner. Colour scheme same as complex **1**.

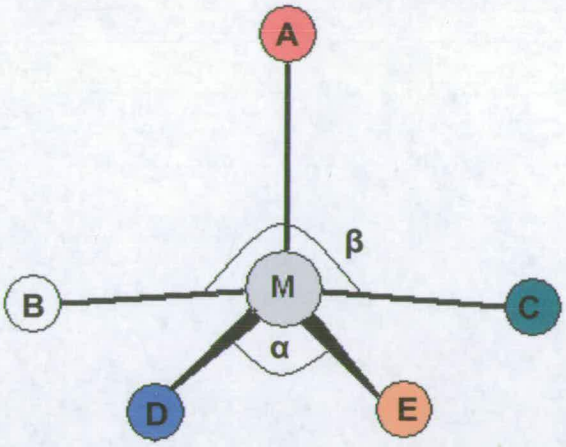

Scheme 2.1. Ranges of structural types intermediate between the idealized square-pyramidal and trigonal-bipyramidal in five-coordinate systems.

Table 2.1. Bond valence sum calculations for complexes **1-7**.

	Complex **1**				Complex **2**				Complex **3**			
Atom	**Mn^{2+}**	**Mn^{3+}**	**Mn^{4+}**	**Ox.**	**Mn^{2+}**	**Mn^{3+}**	**Mn^{4+}**	**Ox.**	**Mn^{2+}**	**Mn^{3+}**	**Mn^{4+}**	**Ox.**
Mn1	3.47	3.20	3.14	3+	1.78	1.63	1.60	2+	1.78	1.64	1.61	2+
Mn2	2.13	1.97	1.93	2+	2.07	1.91	1.87	2+	3.45	3.18	3.32	3+
Mn3	1.75	1.62	1.59	2+	3.46	3.19	3.13	3+	2.13	1.96	1.92	2+
	Complex **4**				Complex **5**				Complex **6**			
Atom	**Mn^{2+}**	**Mn^{3+}**	**Mn^{4+}**	**Ox.**	**Mn^{2+}**	**Mn^{3+}**	**Mn^{4+}**	**Ox.**	**Mn^{2+}**	**Mn^{3+}**	**Mn^{4+}**	**Ox.**
Mn1	3.48	3.22	3.15	3+	1.97	1.85	1.81	2+	2.05	1.96	1.88	2+
Mn2	2.12	1.95	1.92	2+	2.12	1.96	1.92	2+	2.00	1.84	1.81	2+
Mn3	2.19	2.02	1.98	2+	3.39	3.12	3.06	3+	3.35	3.09	3.03	3+
	Complex **7**											
Atom	**Mn^{2+}**	**Mn^{3+}**	**Mn^{4+}**	**Ox.**	**Atom**	**Mn^{2+}**	**Mn^{3+}**	**Mn^{4+}**	**Ox.**			
Mn1	-	-	-	2+	Mn4	3.44	3.18	3.12	3+			
Mn2	3.47	3.20	3.14	3+	Mn5	3.43	3.17	3.11	3+			
Mn3	1.85	1.64	1.61	2+	Mn6	1.82	1.65	1.63	2+			

The structures of complexes **1-6** are clearly related (Figure **2.19**). Complexes **1-6** consist of four edge-sharing [Mn_3] triangles forming 'rods' of 8.45, 8.42, 8.40,

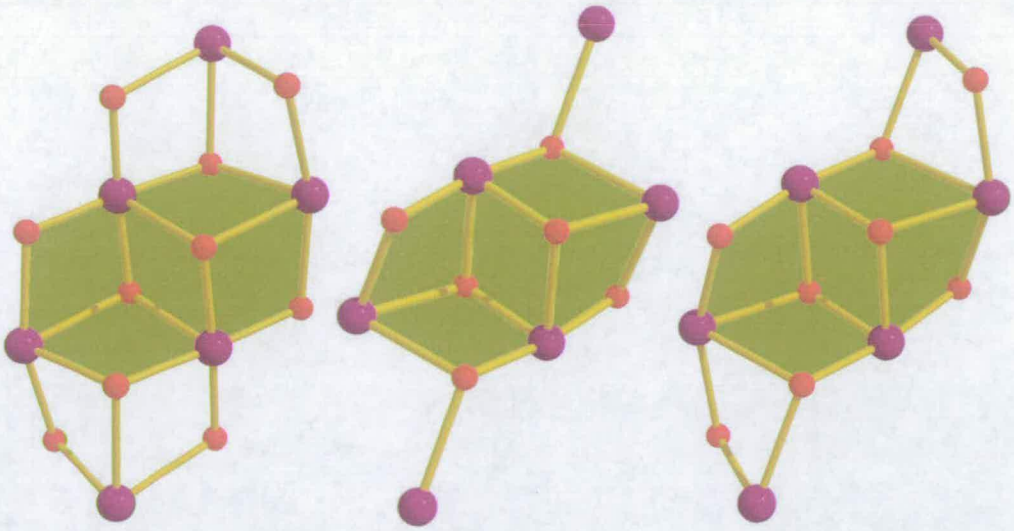

Figure 2.19. Comparison of the metallic cores of complexes **1- 6**.

8.38, 9.23, 8.96 Å in length, respectively. In complexes **1-4** all six Mn ions effectively lie on the same plane. In contrast, in complexes **5** and **6** there are two peripheral Mn ions which lie above and below the central [Mn_4] plane. The metal topology in each case may be considered to be directed by the presence of the two μ_5-tripodal ligands sitting directly above and below the 'metal plane' (Figure **2.2**). Although the central {$Mn^{III}_2Mn^{II}_2(\mu\text{-OR})_4(\mu_3\text{-OR})_2$} rhomb present in all complexes **1-7** is planar, there are some subtle differences in Mn-O-Mn angles (Scheme **2.1** and Table **2.2**) in this unit that are crucial for the magnetic behaviour of the complexes (*vide infra*). Although there is no obvious trend, complexes **5** and **6** (*in general*) display smaller a, b and d angles and larger c and e angles. The [$Mn^{III}_2Mn^{II}_2$] rhomb is connected to the two peripheral Mn^{II} ions in different ways in **1-6**: *via* only one μ_3-O atom in complex **5**; *via* one μ_3- and one μ-O atoms in complex **6**; and *via* one μ_3- and two μ-O atoms in complexes **1-4** (Figure **2.19**).

This planar unit is connected to the two peripheral Mn^{II} ions in different ways in **1-6**; In complex **5**, two of the four μ-OR alkoxides further bridge to the remaining terminal Mn^{II} ions, thus becoming μ_3-OR, while in **6** this is combined with the

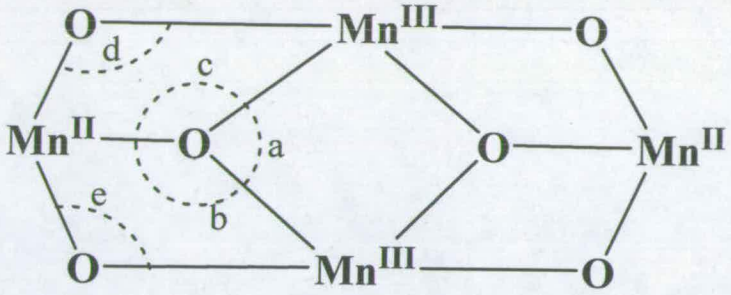

Scheme 2.2. The schematic structure of the central $\{Mn^{III}_2Mn^{II}_2(\mu\text{-OR})_4(\mu_3\text{-OR})_2\}$ rhomb found in complexes **1- 7**.

presence of two μ-OR (from the monoatomic acetate bridge), forming the $[Mn^{II}_4Mn^{III}_2(\mu_2\text{-OR})_4(\mu_3\text{-OR})_4]^{4+}$ core. In complexes **1-4**, the $[Mn^{II}_4Mn^{III}_2(\mu\text{-OR})_6(\mu_3\text{-OR})_4]^{4+}$ unit is formed by the precursor $\{Mn_4(\mu\text{-OR})_4(\mu_3\text{-OR})_2\}$ in the same way as in **6** upon further addition of two μ-OR alkoxides (one from the monoatomic bridge of the acetate and one from the monoatomic bridge of the μ-OR arm of the H_2tea^- ligand). In complex **7**, the $[Mn^{II}_6Mn^{III}_6(\mu\text{-OR})_{14}(\mu_3\text{-OR})_8]^{8+}$ is formed by four edge-sharing $\{Mn_4(\mu\text{-OR})_4(\mu_3\text{-OR})_2\}$ butterflies giving a $[Mn_{10}]$ plane. This plane is connected to the two peripheral Mn^{II} ions by four μ-OR alkoxides (from the monoatomic bridge of the μ-OR arm of four different $Hthme^-$ ligands).

Table 2.2. Bond angles for the planar $\{Mn^{III}_2Mn^{II}_2(\mu_2\text{-OR})_4(\mu_3\text{-OR})_2\}$ unit in **1-7**.

	Angles (°)				
Complex	**a**	**b**	**c**	**d**	**e**
1	99.1(2)	95.5(1)	98.7(3)	100.9(1)	98.1(1)
2	99.2(3)	95.9(0)	99.3(2)	101.9(6)	98.6(0)
3	99.6(8)	95.9(1)	99.5(5)	101.4(4)	97.6(1)
4	97.0(1)	95.5(1)	96.1(2)	107.6(3)	104.6(1)
5	98.8(1)	89.5(1)	104.8(1)	99.4(3)	102.7(3)
6	97.6(1)	90.3(1)	108.2(6)	97.1(7)	103.2(4)
7	95.7(3)	95.6(5)	112.8(0)	83.5(3)	77.2(6)

This planar diamond $\{Mn^{III}_2Mn^{II}_2(\mu_2\text{-}OR)_4(\mu_3\text{-}OR)_2\}$ core is rather common in manganese carboxylate chemistry and has been previously reported in the tetranuclear complexes $[Mn^{III}_2Mn^{II}_2(hmp)_6(NO_3)_2(MeCN)_2]^{2+}$ (**a**), $[Mn^{III}_2Mn^{II}_2(hmp)_6(NO_3)_4]$ (**b**), $[Mn^{III}_2Mn^{II}_2(hmp)_4(acac)_2(MeO)_2]^{2+}$ (**c**) [9], $[Mn^{III}_2Mn^{II}_2(OAc)_2(pdmH)_6]^{2+}$ (**d**) [10], $[Mn^{III}_2Mn^{II}_2Br_2(hmp)_6(H_2O)_2]^{2+}$ (**e**) [11], $[Mn^{III}_2Mn^{II}_2(OAc)_2(LH)_2(LH_2)_2(H_2O)_2]^{2+}$ (**f**) [12], $[Mn^{III}_2Mn^{II}_2(O_2CPh)_2(LH)_2(LH_2)_2(H_2O)_2]^{2+}$ (**g**) [12], and $[Mn^{III}_2Mn^{II}_2(O_2CEt)_2(LH)_2(LH_2)_2(H_2O)_2]^{2+}$ (**h**) [12], (where hmpH = 2-hydroxymethylpyridine; $pdmH_2$ = pyridine-2,6-dimethanol; LH_3 = triethanolamine); in the heptanuclear complex $[Mn^{III}_5Mn^{II}_2(O_2CPh)_9(thme)_2(py)_3]$ (**i**) [2b]; in the octanuclear complex $[Mn^{III}_4Mn^{II}_4(piv)_2(tmp)_2(Htmp)_4Br_4(H_2O)_2]$ (**j**) [2c]; and in the dodecanuclear complex $[Mn^{III}_{10}Mn^{II}_2O_4(OH)_2(O_2CPh)_{12}(thme)_4(py)_2]$ (**k**) [2b]. The $[Mn^{III}_2Mn^{II}_4(\mu\text{-}OR)_6(\mu_3\text{-}OR)_4]^{4+}$ core of complexes **1-4** has been seen previously in the hexanuclear complex $[Mn^{III}_2Mn^{II}_4(OAc)_6(thme)_2(H_2tea)_2]$ (**l**) [2b], while the $[Mn^{III}_2Mn^{II}_4(\mu\text{-}OR)_4(\mu_3\text{-}OR)_4]^{6+}$ core of **6** has been previously reported in the complex $[Mn^{III}_2Mn^{II}_4(piv)_8(tmp)_2(py)_2]$ (**m**) [2b]. However, to the best of our knowledge, the $[Mn^{III}_2Mn^{II}_2(\mu\text{-}OR)_2(\mu_3\text{-}OR)_4]^{8+}$ topology of complex **5** is observed for the first time. "Reverse" rhomboidal clusters with $\{Mn^{II}_2Mn^{III}_3O_x\}$(x= 2 and 3) cores in which the Mn^{III} ions are the wing tips and the Mn^{II} ions are the body ions have also been reported [12b].

Magnetic Studies

➢ Dc Magnetic Studies

Direct current magnetic susceptibility studies were performed on polycrystalline samples of complexes **1**, **3-6** in the 5 – 300 K range in an applied field of 0.1 T. The results are plotted as the $\chi_M T$ product vs T (Figure **2.20**). The $\chi_M T$

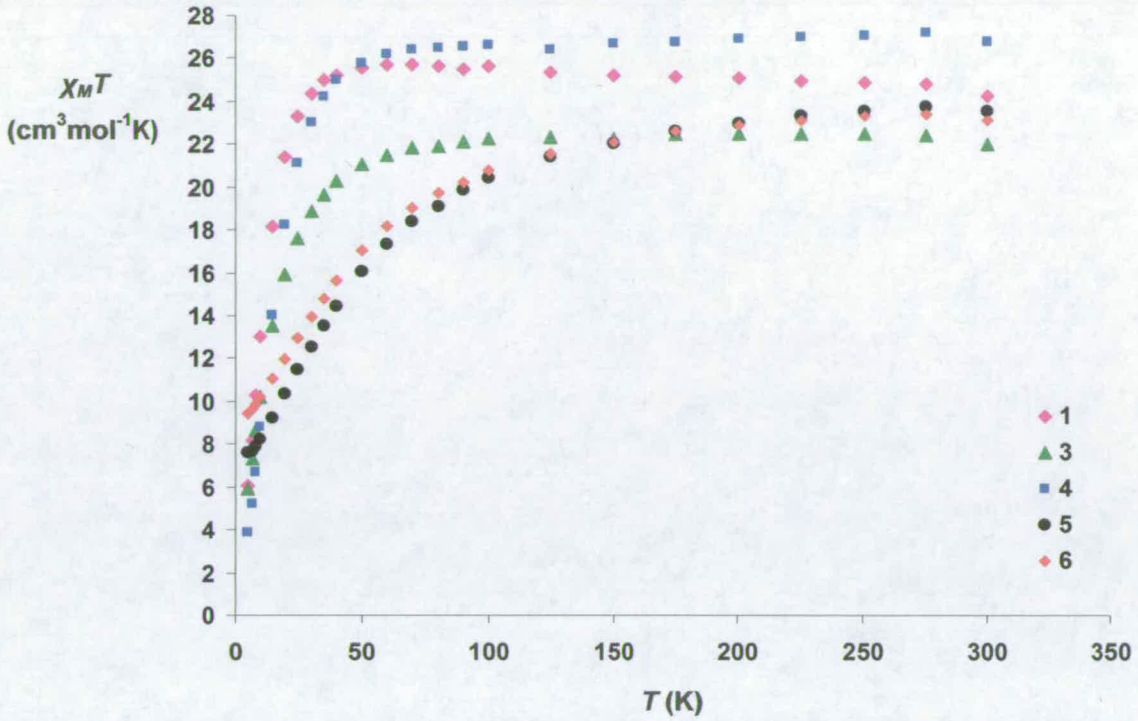

Figure 2.20. Plot of $\chi_M T$ vs. T for complexes **1, 3-6** in the 5-300 K temperature range in a field of 0.1 T.

values at 300 K are 24.20, 21.92, 26.72, 23.49 and 23.10 cm^3 K mol^{-1} for **1, 3-6,** respectively, close to the spin-only (g = 2) value of 23.5 cm^3 K mol^{-1} expected for a $[Mn_6]$ unit comprising two high-spin Mn^{III} and four high-spin Mn^{II} ions. For complexes **1, 3** and **4,** the $\chi_M T$ value remains essentially constant as the temperature decreases until ca. 50 K where it then decreases rapidly to a value of 6.02, 5.93 and 3.84 cm^3 K mol^{-1} at 5 K respectively. For complexes **5** and **6**, the room temperature $\chi_M T$ values of 23.49 and 23.10 cm^3 K mol^{-1}, decreases gradually as the temperature decreases until ca. 125 K when they both begin to decrease more rapidly and steadily to the 7.56 and 9.42 cm^3 K mol^{-1}, at 5 K, respectively. For complex **7**, the behaviour is rather similar: the room temperature $\chi_M T$ value of approximately 43.15 cm^3 K mol^{-1} (0.1 T) is slightly lower than that expected for a complex comprising four Mn^{III} and four Mn^{II} ions- 44.24 cm^3 K mol^{-1} with g = 2.00- (Figure **2.21**). The value of $\chi_M T$ remains almost constant as the temperature is decreased until *ca.* 50 K where it then decreases rapidly to a value of approximately 14.63 cm^3 K mol^{-1} at 5.0 K. In

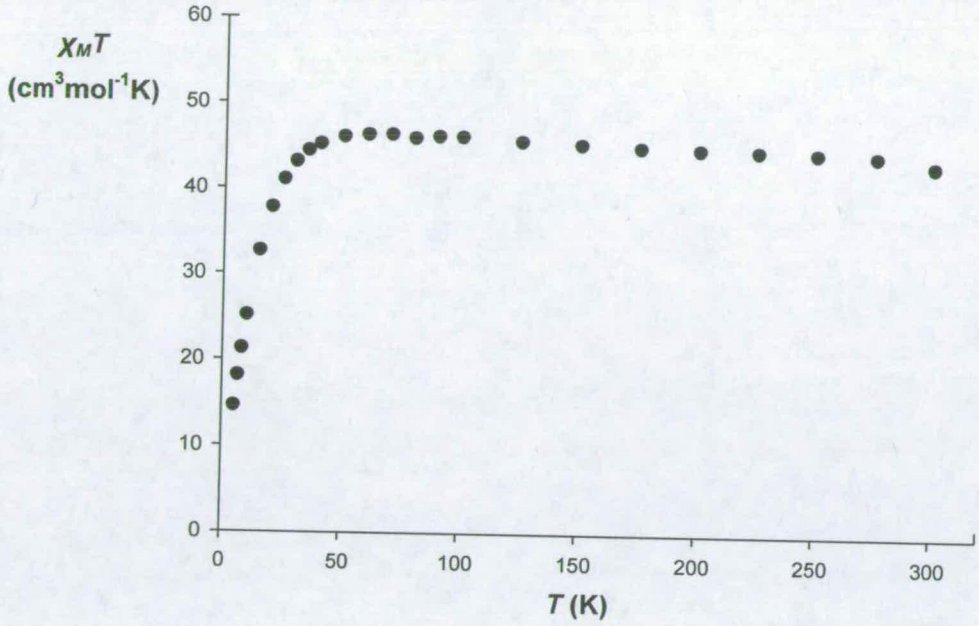

Figure 2.21. Plot of $\chi_M T$ vs. T for complex **7** in the 5-300 K temperature range in a field of 0.1 T.

all cases, this behaviour is consistent with the presence of dominant antiferromagnetic interactions between the metal centres, with the low-temperature values indicating relatively small, $S \leq 4$, spin ground-states for **1**, **3-6** and $S = 0$ or 1 for **7**.

In order to determine the ground states of complexes **1-7,** variable temperature, variable-field dc magnetization data were collected in the ranges 1.8 – 10 K and 0.1 – 7 T. The data were fitted by a matrix-diagonalization method to a model that assumes only the ground-state is populated, includes axial zero-field splitting ($D\hat{S}_z^2$), and carries out a full powder average [13]. The corresponding Hamiltonian is given by:

$$\hat{H} = D\hat{S}_z^2 + g\mu_B\mu_0 \hat{S}H \qquad (1)$$

where D is the axial anisotropy, μ_B is the Bohr magneton, μ_0 is the vacuum permeability, $\hat{S}_z$ is the easy-axis spin operator, and H is the applied field.

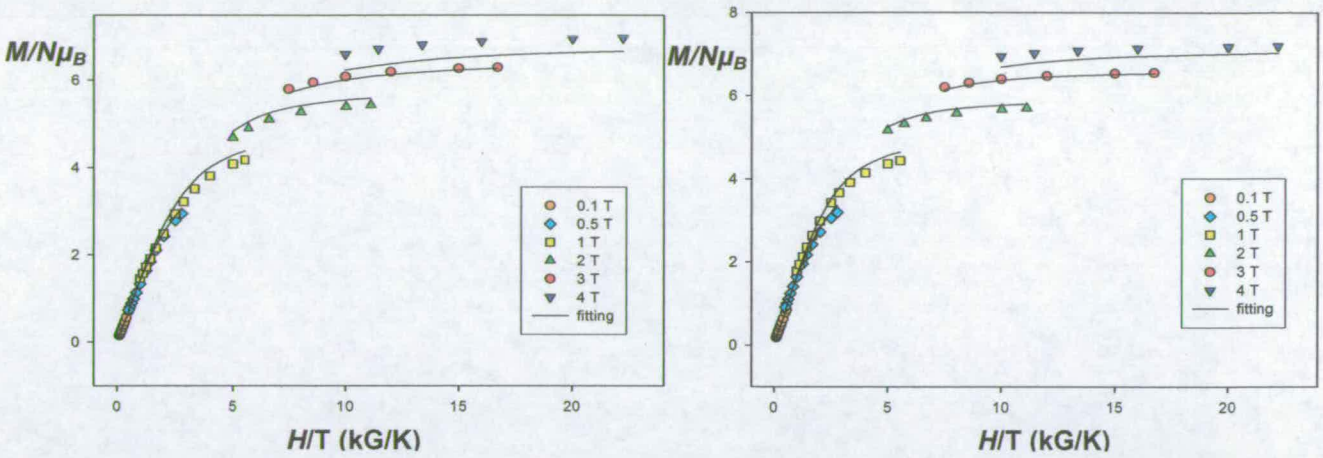

Figure 2.22. Plot of reduced magnetization ($M/N\mu_B$) vs. H/T for complexes **5** (left) and **6** (right) in the ranges 0.1 – 4 T and 1.8 – 6 K. The solid lines are the fit of the data to an $S = 4$, $D = -0.44$ cm^{-1} and g = 1.82 (for **5**) and $S = 4$, $D = -0.58$ cm^{-1} and g = 1.97 (for **6**).

For complexes **1-4** and **7**, no satisfactory fit of the data was possible since the magnetization rises almost linearly with applied magnetic field indicating the existence of small ($S \approx 0$) spin ground states with the presence of many low-lying excited states of larger multiplicity that become populated with increasing field. Low-lying excited states are a common problem in large clusters, particularly when there are multiple Mn^{II} ions present, as is the case here, since these give weak exchange interactions. The data for complexes **5** and **6** are plotted as reduced magnetization ($M/N\mu_B$) versus H/T in (Figure **2.22**). The best fits (obtained using only the low field data (≤ 4 T)) gave $S = 4$, g = 1.82 and $D = -0.44$ cm^{-1} for complex **5** and $S = 4$, g = 1.97 and $D = -0.58$ cm^{-1} for complex **6**. When fields up to 7 Tesla were employed a poorer quality fit was obtained. This is characteristic of low-lying excited states with S values greater than the ground state of $S = 4$. Clearly the g-value for **5** is well below the expected value e.g. 1.95 – 2.00 for such a complex and is a direct consequence of assuming only the ground state is populated. This is unlikely to be true. A more accurate determination of g (and all the parameters in equation (1)) will require HF-EPR spectroscopy and INS.

➢ Ac Magnetic Studies

Ac magnetization measurements were performed on complexes **1-7** in the 1.8 to 10 K range in zero applied dc field and a 3.5 G ac field oscillating at 50-1300 Hz (Figure **2.23**). For complexes **1-4** and **7**, extrapolation of the in-phase $\chi_M'T$ signal to 0 K suggest the existence of $S = 0$ spin ground states. In addition, the slope of the plots all decrease rapidly with decreasing temperature revealing the presence of several spin states of larger S values lying very close to the ground-state, consistent with the dc data.

For complexes **5** and **6** frequency-dependent out-of-phase (χ_M'') ac susceptibility signals are seen below approximately 2.5 K, but no peaks are observed and the magnitude of the signals are small (Figure **2.24**; for well-established SMMs χ_M'' and $\chi_M'T$ are roughly of the same order of the magnitude). For **5**, the in-phase $\chi_M'T$ signal increases slightly with a decrease in the temperature, while for **6**, the signal decreases. This is consistent with the presence of excited states with smaller and larger S values, respectively. The magnitudes of the in-phase $\chi_M'T$ vs T signals support the assignment of $S = 4$ ground states for both complexes.

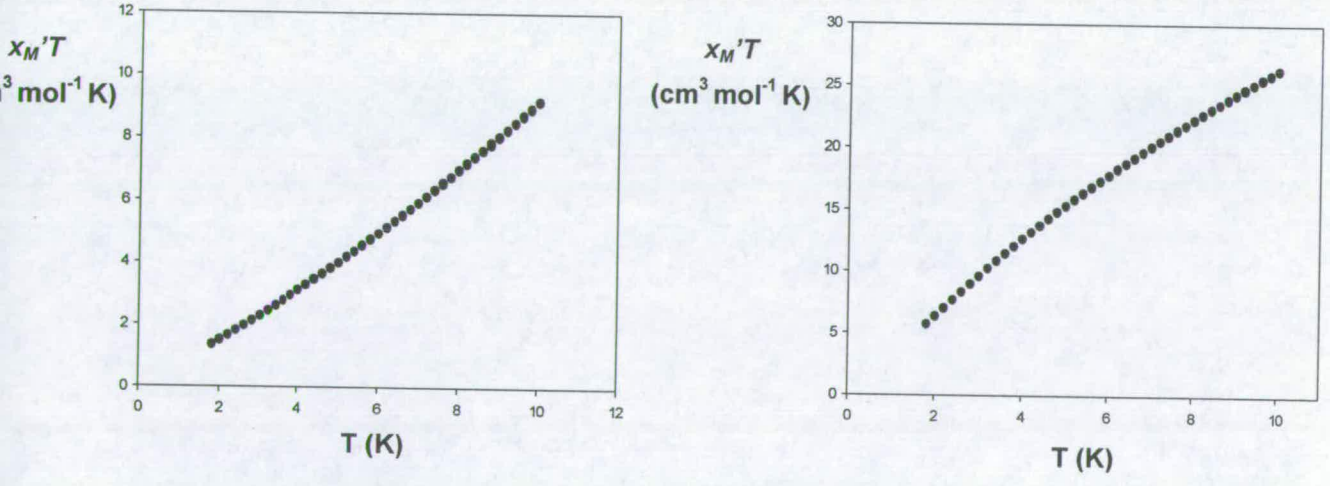

Figure 2.23. Plots of the in-phase (χ_M') signal in ac susceptibility studies *vs.* temperature in a 3.5 G field oscillating at the indicated frequencies, for complexes **4** (left) and **7** (right).

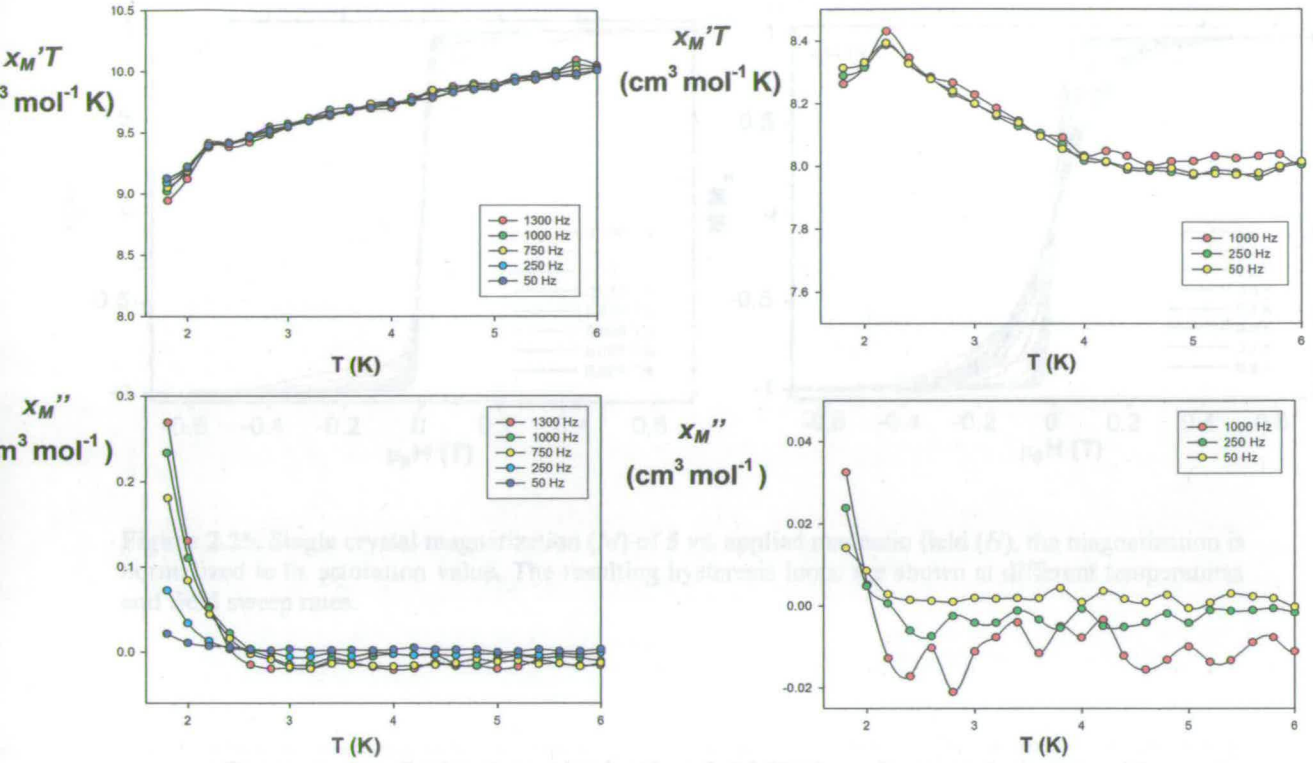

Figure 2.24. Plots of the in-phase (χ_M') signal as $\chi_M'T$ and out-of-phase (χ_M'') signal in ac susceptibility studies *vs.* temperature in a 3.5 G field oscillating at the indicated frequencies, for complexes **5** (left) and **6** (right).

➢ Single-Crystal Hysteresis Studies

The S and D values obtained above for **5** and **6** suggest that these complexes may exhibit single-molecule magnetism behaviour, with upper limits to the potential energy barrier (U) to magnetization reversal of $U = S^2|D| \approx 7.0$ cm^{-1} (~10 K) and 9.3 cm^{-1} (~13 K), respectively. To probe the possible SMM behaviour further, single crystal hysteresis loop and relaxation measurements were performed using a micro-SQUID setup [14]. Figures **2.25** and **2.26** present typical magnetization (M) vs. applied dc field (H) measurements at different temperatures and scan rates with the field applied in the direction of the easy axis; the applied magnetic field was swept between –1 and 1 Tesla.

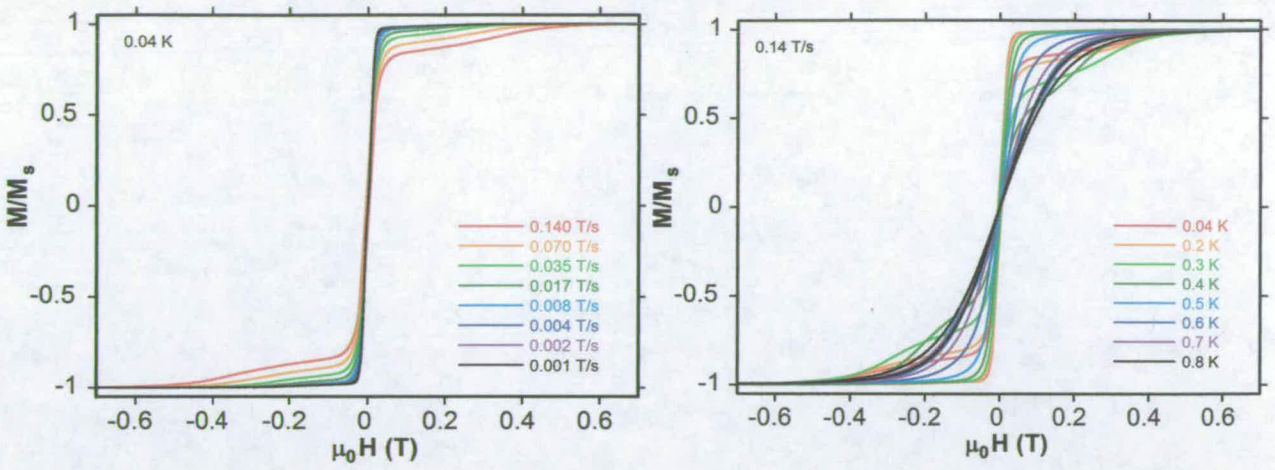

Figure 2.25. Single crystal magnetization (M) of **5** vs. applied magnetic field (H), the magnetization is normalized to its saturation value. The resulting hysteresis loops are shown at different temperatures and field sweep rates.

For complex **5**, the data obtained at 0.04 K show hysteresis loops with a very large step at zero field (Figure **2.25**). A step indicates the occurrence of rapid relaxation of the magnetization at a given magnetic field where a level crossing is avoided. At H = - 1 T all the molecules are in the M_S = +4 state. When the field is swept in a positive direction there is resonance between the +4 and -4 M_S levels at H = 0, and part of the molecules tunnel. The height of the step, in this case, indicates that the tunneling process is relatively fast. Upon increasing the field above zero, another step corresponding to the molecules tunneling from the M_S = +4 to the M_S = -3 sub-level should occur at $H \approx D/g\mu_B$. However, for systems with relative large tunnel splittings like complex **5**, a direct relaxation process between the M_S = +4 ground state levels becomes possible. This leads to a smeared step which is further broadened by very weak intermolecular interactions (exchange and dipolar). When the same experiment is carried out at higher field sweep rates (Figure **2.25**) the number of molecules tunnelling at zero field decreases and the hysteresis loop is larger. In the variable temperature experiment hysteresis loops appear below *ca.* T = 0.4 K indicating that below this temperature the magnetization is blocked. As the temperature is decreased the number of molecules that undergo relaxation by thermal

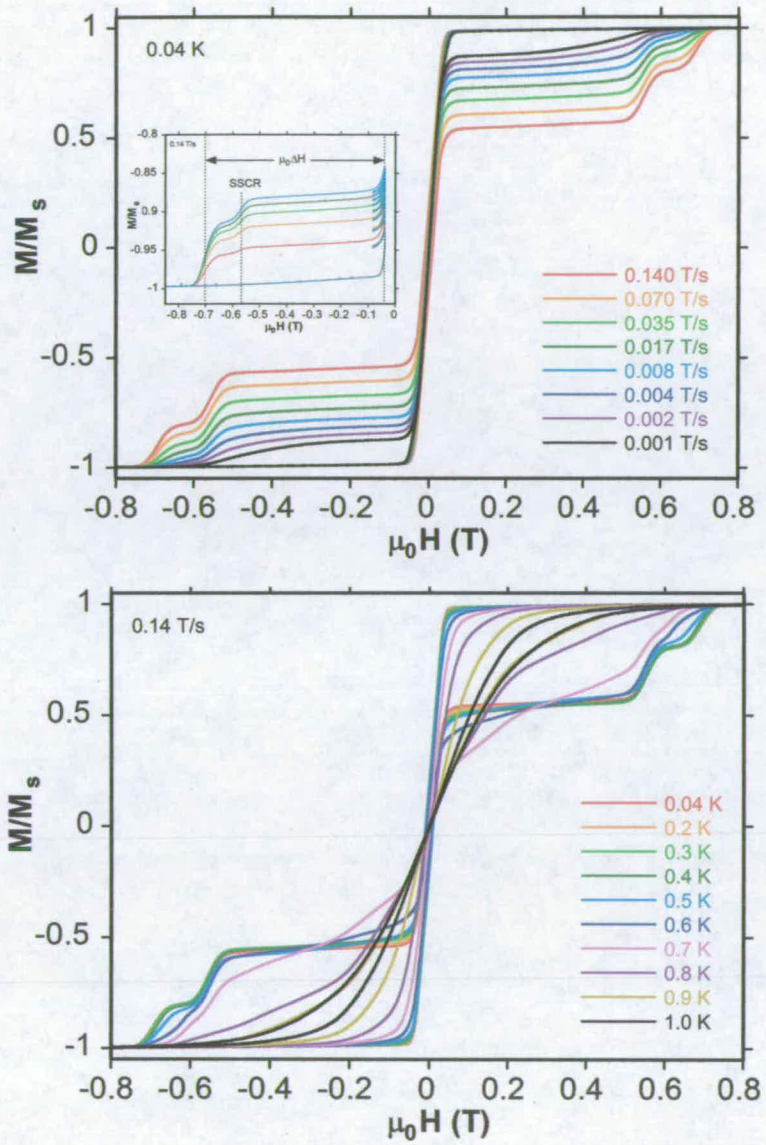

Figure 2.26. Single crystal magnetization (*M*) of **6** vs. applied magnetic field (*H*), the magnetization is normalized to its saturation value. The resulting hysteresis loops are shown at different temperatures and field sweep rates.

activation also decreases and those relaxing by tunnelling increase, resulting in a narrowing of the hysteresis loop with a sharper step at $H = 0$.

Complex **6** shows similar behaviour, but with the blocking of the magnetization appearing below approximately 0.7 K and a pronounced sweep rate dependence (Figure **2.26**). In the 0.04 K plot there are clear steps at *ca.* +-0.56 T and

+-0.7 T. We used minor hysteresis loops (inset of Figure **2.26**) to assign these steps [15]. The step at +-0.7 T is due to tunneling from the M_S = +4 to the M_S = -3 sub-level and the step at +-0.56T is due to spin-spin cross-relaxation (SSCR) [16]. This phenomenon is the result of weak dipolar and intermolecular exchange interactions between two (or more) SMMs in the crystal. A transition (i.e. one molecule transferring to a lower energy state and one to a higher energy state) can occur if SMMs are coupled because the transverse terms of the interaction allow a tunnel splitting between two quantum states. It is important to note that SSCR occur in almost all SMMs, but are often covered by other effects, for example, the direct relaxation processes for compound **5**.

Theoretical Studies

The calculation of magnetic exchange interactions between two (or more) metal centres using density functional theory (DFT) is a new and appealing approach. In order to gain further insight into the electronic structure of these hexanuclear species, DFT calculations have been performed on **1-6** by Dr. Joan Cano of the theoretical magnetic group in Barcelona. In earlier decades, several qualitative models were proposed to calculate the exchange interactions in dinuclear complexes and two important models were widely employed: the Hey-Thibeault-Hoffman model (HTH) [17] and the Kahn model [18]. However, both used several approximations such as the active electron approximation, whereby only the unpaired electrons of the metal are taken into account while the contributions from core electrons are ignored, and subsequently both models did not provide good estimates of the J values compared to experiment. Later, Noodleman developed the broken symmetry model based on non-orthogonal magnetic orbitals, that has proven to yield good numerical estimates of the J constant, even for very large systems [19-21]. The exchange interaction can be evaluated from the energy difference between the high spin state and the broken symmetry state using the following expression [20]:

$$J = \frac{2(E_{BS} - E_{HS})}{S_{HS}(S_{HS} + 1)} \quad \textbf{(2)}$$

where E_{HS} stands for the energy of high spin state, E_{BS} stands for energy of broken symmetry state and S_{HS} is the spin on the metal centres. This method has recently been successfully extended to encompass polynuclear complexes by Alvarez and co-workers who proposed a pairwise interaction model to calculate the magnetic exchange interactions [20-23].

Here we have employed the same approach to calculate the five different exchange interactions present in complexes **1-6**. Although all are structurally very similar, being hexanuclear and presenting the same central $\{Mn^{III}_2Mn^{II}_2(OR)_6\}$ core and with only small differences in bond lengths and angles, they display remarkably different magnetic properties: complexes **1-4** have diamagnetic spin ground states whilst **5** and **6** are SMMs. DFT calculations were performed using the B3LYP functional with Ahlrich's triple-ζ-quality basis set on the metal atoms and a double-ζ-quality basis set on the others. All the calculations have been performed using the *Jaguar* (version 5.0) program [24].

The five different exchange interactions in **1-6** are illustrated in Figure **2.27**. The structural cores are similar to a family of manganese compounds reported previously by the Brechin group and therefore the same calculation procedure has been adopted here to compute the magnetic exchange interactions [2b]. The structures can be broken down into three different types: complexes **1-4,** complex **5,** and complex **6** (Figure **2.19**), and the calculations have been performed on the crystal structures of **4-6**. The bridging units that mediate the exchange between the metal centres, their important structural parameters together with the DFT-calculated J constants are given in Table **2.3**. For complex **4**, the strong interactions are J_1, J_2 and J_5 and all are antiferromagnetic in nature. J_3 is calculated to be ferromagnetic, while J_4 is antiferromagnetic, but very small. Assigning the spins on the metal centres based on the calculated sign of the J values immediately reveals that for **4** the spin

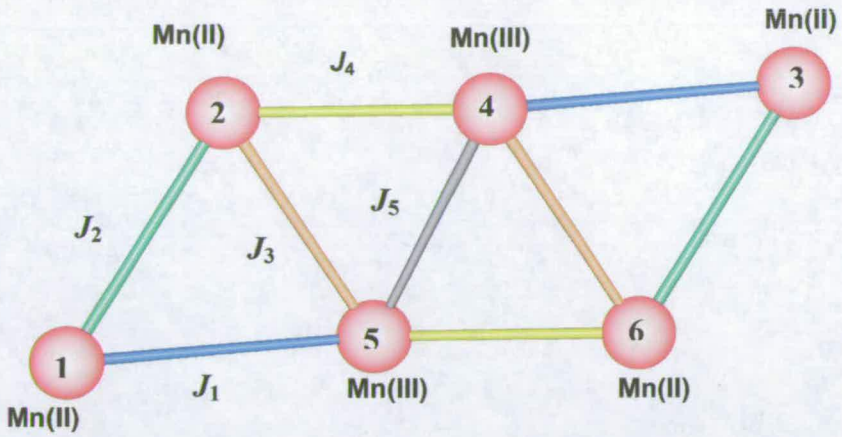

Figure 2.27. The different exchange interactions present in complexes **1-6**.

ground state is $S = 0$, which arises directly from the non-competing antiferro/ferromagnetic interactions: Mn1, Mn4, and Mn6 will be '*spin-up*' while Mn2, Mn3 and Mn5 will be '*spin-down*'. Although complexes **5** and **6** are different, the structural parameters which control the magnitude and sign of the J values are very similar and only the strength of the calculated J values differs between **5** and **6**: J_1 and J_2 are antiferromagnetic while the remaining interactions are ferromagnetic. Assigning '*spin-up*' and '*spin-down*' based on the calculated sign of the J values, results in an $S = 4$ ground state: Mn2, Mn4, Mn5 and Mn6 being '*spin-up*', Mn1 and Mn3 being '*spin-down*'.

The magnitude and sign of the DFT calculated exchange interactions can be rationalized with the structural parameters summarized in Table **2.3**. The interaction between high spin Mn^{II} ions and high spin Mn^{III} ions becomes less antiferromagnetic at larger Mn-O-Mn angles [2b]. If there are different bridging units (μ-OR *vs.* μ-O_2CR) that mediate the exchange between metal centres then orbital counter-complementarity effects must also be considered. This changes the energies of the magnetic orbitals and thus greatly influences the magnetic exchange, and is particularly important when the exchange interactions are small. For example, in the case of J_1, although the angles in **5** and **6** are larger than in **4**, the strength of the Js are similar, and this is attributed to the counter-complimentary effect of the

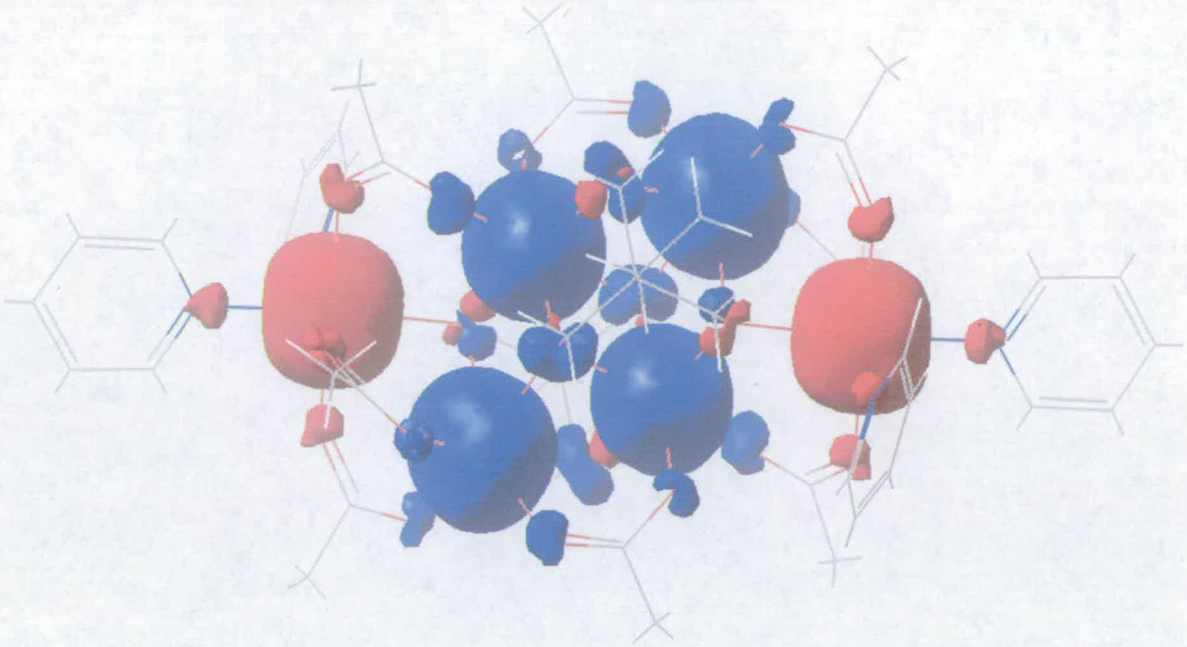

Figure 2.28. Ground state spin density distribution in complex **5**.

dissimilar bridging units found in **5** and **6**. The interactions which are responsible for the '*switch*' in ground state between these two sets of compounds are J_4 and J_5: both interactions are antiferromagnetic in **4,** but ferromagnetic in **5** and **6**. Although the Mn-O-Mn angles of all three complexes are close, the additional carboxlyate bridge present in **5** and **6** changes the nature of interaction. J_5 describes the interaction between the two central high spin Mn^{III} ions. Here, larger Mn-O-Mn angles favour an antiferromagnetic interaction (**4**), and smaller Mn-O-Mn angles a ferromagnetic interaction (**5**, **6**). Thus, a subtle change in the angle alters the sign of J_5 seen in complex **4** to that seen in **5** and **6,** leading to a diamagnetic ground state for **4** and S = 4 ground states for **5** and **6**.

The calculated spin density plot of the ground state spin structure for complex **5** is shown in Figure **2.28**. The modulus of the spin density on the Mn^{II} and Mn^{III} ions is very close to the free ion values (4.80 and 3.89) and thus very little spin density is distributed to the bridging ligands. The mechanism of the spin density distribution for the Mn^{II} ions is an interplay between spin delocalization and spin polarization

with the predominant effect being spin delocalization, and thus the ligand atoms coordinated to the metal atoms have same spin as the metal. For the Mn^{III} ions both spin delocalization and spin polarization operate, with spin delocalization predominating along the Jahn-Teller elongated axes. Such a spin distribution has been previously observed in a trinuclar Mn^{III} complex [25].

Table 2.3. Structural parameters and DFT calculated *J*-values for **4-6**.

	complex **4**			complex **5**		
	bridging ligand	**d(Mn-Mn) (Å)**	J_{DFT}	**bridging ligand**	**d(Mn-Mn) (Å)**	J_{DFT}
J_1	μ-OR (2.115; 97.1) μ-OR (2.005; 104.6)	3.177	-7.1	μ-OR (2.162; 116.6) μ-O_2CR (2.131; 126.0)	3.685	-7.6
J_2	μ-OR (2.201; 95.8) μ-OR (2.237; 93.8) μ-O_2CR (2.117; 130.3)	3.267	-7.8	μ-OR (2.366; 96.7) μ-O_2CR (2.111; 134.5) μ-O_2CR (2.108; 135.1)	3.534	-5.0
J_3	μ-OR (2.270; 96.1) μ-OR (2.090; 107.7)	3.337	+2.6	μ-OR (2.073; 104.8) μ-OR (2.149; 99.9)	3.289	+6.8
J_4	μ-OR (2.098; 99.4) μ-OR (2.034; 103.6)	3.205	-0.9	μ-OR (2.246; 89.5) μ-OR (2.021; 102.7) μ-O_2CR (2.090; 257.8)	3.163	+0.2
J_5	μ-OR (2.106; 100.7) μ-OR (2.106; 100.7)	3.250	-6.8	μ-OR (2.117; 98.8) μ-OR (2.117; 98.8)	3.222	+0.7

	complex **6**		
	bridging ligand	**d(Mn-Mn) (Å)**	J_{DFT}
J_1	μ-OR (2.100; 118.9) μ-O_2CR (2.136; 129.3)	3.621	-5.2
J_2	μ-OR (2.155; 102.9) μ-OR (2.388; 89.6) μ-O_2CR (2.129; 131.3)	3.369	-2.2
J_3	μ-OR (2.222; 97.2) μ-OR (2.068; 108.3)	3.354	+0.5
J_4	μ-OR (2.245; 90.3) μ-OR (2.029; 103.2) μ-O_2CR (2.069; 129.4)	3.185	+2.1
J_5	μ-OR (2.125; 97.7) μ-OR (2.125; 97.7)	3.208	+4.9

Conclusions

The use of tripodal alcohols has led to the synthesis of a family of hexanuclear (and one dodecanuclear) mixed-valent, rod-like Mn complexes whose structures are all based on edge-sharing triangles. Despite the structural similarities, their magnetic behaviour ranges from diamagnetic spin ground states to single-molecule magnetism, and this has allowed us to examine the effect that subtle changes in geometry have on the nature of the individual pairwise exchange interactions that govern the resultant ground states. The interactions which are responsible for the '*switch*' in ground state from $S = 0$ to $S = 4$ (for the hexanuclear complexes) between the two sets of compounds differ only in terms of small changes in bridging angles, and in the presence of an additional carboxylate bridge that introduces a counter-complementarity effect. Both affect the relative magnitude of the various exchange interactions, ultimately leading to a diamagnetic ground state for **4** and $S = 4$ ground states for **5** and **6**.

References

[1] (a) A. Mishra, W. Wernsdorfer, S. Parsons, G. Christou, E.K. Brechin, *Chem. Commun.*, **2005**, 2086.

[2] (a) M. Murugesu, J. Raftery, W. Wernsdorfer, G. Christou, E.K. Brechin, *Inorg. Chem.*, **2004**, *43*, 4203. (b) G. Rajaraman, M. Murugesu, M. Soler, W. Wernsdorfer, M. Helliwell, S.J. Teat, G. Christou, E.K. Brechin, *J. Am. Chem. Soc.*, **2004**, *126*, 15445. (c) C.J. Milios, F.P.A. Fabbiani, S. Parsons, M. Murugesu, G. Christou, E.K. Brechin, *Dalton Trans.*, **2005**, 351.

[3] R. Sessoli, H.L. Tsai, A.R. Schake, S.Y. Wang, J.B. Vincent, K. Folting, D. Gatteschi, G. Christou, D.N. Hendrickson, *J. Am. Chem. Soc.*, **1993**, *115*, 1804.

[4] (a) J.B. Vincent, H.R. Chang, K. Folting, J.C. Huffman, G. Christou, D.N. Hendrickson, *J. Am. Chem. Soc.*, **1987**, *109*, 5703. (b) J.B. Vincent, K. Folting, J.C. Huffman, G. Christou, *Inorg. Chem.*, **1986**, *25*, 996.

[5] (a) S. Wang, Z. Pang, K.D.L. Smith, Y.-S. Hua, C. Deslippe, M.J. Wagner, *Inorg. Chem.*, **1995**, *34*, 908. (b) S.R. Drake, A. Lyons, D.J. Otway, Williams, *Inorg. Chem.*, **1994**, *33*, 1230. (c) C.J. Milios, E. Kefalloniti, C.P. Raptopoulou, A. Terzis, R. Vicente, S.P. Perlepes, *Polyhedron*, **2004**, *23*, 83. (d) C.J. Milios, P. Kyritsis, C.P. Raptopoulou, A. Terzis, R. Vicente, A. Escuer, S.P. Perlepes, *Dalton Trans.*, **2005**, 501.

[6] (a) E. Bouwman, J.C. Huffman, E.B. Lobkovsky, G. Christou, *Inorg. Chem.*, **1992**, *31*, 4436. (b) E. Bouwman, K. Caulton, G. Christou, K. Folting, C. Gasser, D.N. Hendrickson, J.C. Huffman, E.B. Lobkovsky, J.D. Martin, P. Michel, H.-L. Tsai, Z. Xue, *Inorg. Chem.*, **1993**, *32*, 3463.

[7] B.F. Hoskins and F.D. Whillans, *Coord. Chem. Rev.*, **1972**, *9*, 365.

[8] (a) H.H. Thorp, *Inorg. Chem.*, **1992**, *31*, 1585. (b) W. Liu, H.H. Thorp, *Inorg. Chem.*, **1993**, *32*, 4102.

[9] E.C. Yang, N. Harden, W. Wernsdorfer, L. Zakharov, E.K. Brechin, A.L. Rheingold, G. Christou, *Polyhedron*, **2003**, *22*, 1857.

[10] J. Yoo, E.K. Brechin, A. Yamaguchi, M. Nakano, J.C. Huffmann, A.L. Maniero, L.-C. Brunel, K. Awaga, H. Ishimoto, G. Christou, D.N. Hendrickson, *Inorg. Chem.*, **2000**, *39*, 3615.

[11] J. Yoo, A. Yamaguchi, M. Nakano, J. Krzystek, W. Streib, L.C. Brunel, H. Ishimoto, G. Christou, D.N. Hendrickson, *Inorg. Chem.*, **2001**, *40*, 4604.

[12] (a) L.M. Wittick, K.S. Murray, B. Moubaraki, S.R. Batten, L. Spiccia, J.K. Berry, *Dalton Trans.*, **2004**, 1003; (b) L.M. Wittick, L.F. Jones, P. Jensen, B. Moubaraki, L. Spiccia, K.J. Berry, S.M. Keith, *Dalton Trans.*, **2006**, 1534.

[13] MAGNET, E.R. Davidson, Indiana University.

[14] W. Wernsdorfer, *Adv. Chem. Phys.*, **2001**, *118*, 99.

[15] W. Wernsdorfer, S. Bhaduri, A. Vinslava, G. Christou, *Phys. Rev. B*, **2005**, *72*, 214429.

[16] W. Wernsdorfer, S. Bhaduri, R. Tiron, D.N. Hendrickson, G. Christou, *Phys. Rev. Lett.*, **2002**, *89*, 197201.

[17] P.J. Hey, J.C. Thibeault, R.J. Hoffmann, *Am. Chem. Soc.*, **1975**, *17*, 4884.

[18] O. Kahn, *Molecular Magnetism*, VCH publishers, New York., **1993**.

[19] L.J. Noodleman, *Chem. Phys.*, **1981**, *74*, 5737.

[20] E. Ruiz, S. Alvarez, A. Rodriguez-Fortea, P. Alemany, Y. Pouillon, C. Massobiro, in *Magnetism: Molecules to Materials II*, edited by J.S. Miller, M. Drillon, Wiley-VCH; Weinheim, **2001**, 227.

[21] (a) A.H. Abu-Nawwas, J. Cano, P. Christian, T. Mallah, G. Rajaraman, S.J. Teat, R.E.P. Winpenny, Y. Yukawa, *Chem. Commun.*, **2004**, 314. (b) G. Rajaraman, E.C. Sañudo, M. Helliwell, S. Piligkos, W. Wernsdorfer, G. Christou, E.K. Brechin, *Polyhedron,* **2005**, *24*, 2450.

[22] E. Ruiz, J. Cano, S. Alvarez, A. Caneschi, D. Gatteschi, *J. Am. Chem. Soc.*, **2003**, *152*, 6791.

[23] (a) E. Ruiz, G. Rajaraman, S. Alvarez, B. Gillon, J. Stride, R. Clerac, L. Larionova, S. Decurtins, *Angew. Chem. Int. Ed.*, **2005**, *117*, 2771. (b) G. Rajaraman, K.E. Christensen, F.K. Larsen, G.A. Timco, R.E.P. Winpenny, *Chem. Comm.*, **2005**, 3053. (c) G. Rajaraman, J. Cano, E.K. Brechin, E.J.L. McInness, *Chem. Comm.*, **2004**, 1476.

[24] Jaguar 5.0: Schrodinger Inc, Portland, OR, **2003**.

[25] L.F. Jones, G. Rajaraman, J. Brockman, M. Murugesu, J. Raftery, S.J. Teat, W. Wernsdorfer, G. Christou, E.K. Brechin, D. Collison, *Chem. Eur. J.*, **2004**, *10*, 5180.

Chapter 3
"High Spin Mn Wheels"

Introduction

SMMs vary in nuclearity from two to eighty-four and form a plethora of aesthetically pleasing topologies ranging from simple dimers, triangles and cubes, to discs, icosahedra and wheels [1-4]. This latter class of complexes are extremely rare in Mn^{III} chemistry despite being rather common for Fe^{III}, Cr^{III} and V^{III} [5-8], though there are reports of isostructural Fe and Mn clusters: for example $[Mn^{III}(C_{14}H_9N_2O_3)(MeOH)]_{10}$ and $[Fe^{III}(C_{14}H_9N_2O_3)(MeOH)]_{10}$ [7a].

The nuclearity of Mn wheels varies from six to eighty-four and can be divided into three main categories. The first describes metal-centered complexes or 'metallocycles' [7a-g] with the most common being the heptanuclear $\{Mn^{II}[Mn^{II}_2Mn_4{}^{III}]\}$ clusters (neutral, anionic or cationic), examples of which include $\{Mn^{II}[Mn^{II}_2Mn^{III}_4Cl_6(L^3)_6]\}$ (L= N-n-butyldiethanolamine) (a), $\{Mn^{II}[Mn^{II}_2Mn^{III}_4(OMe)_{12}(dbm)_6]\}$ (Hdbm= dibenzoyldimethane) (b), $\{Mn^{II}[Mn^{II}_2Mn^{III}_4Cl_6(L^4)_6]\}$ (H_3L^4= *N*-(2-hydroxy-5-nitrobenzyl)iminodiethanol) (c), $\{Mn^{II}[Mn^{II}_2Mn^{III}_4Cl_6(L^{1,5,6})_6]\}^-$ ($H_2L^{1,5,6}$= *N*-methyl-, *N*ethyl-,and *N*-benzyl-diethanolamine) (d), $\{Mn^{II}[Mn^{II}_2Mn^{III}_4Cl_3(OH)_3(hmp)_9]\}^{2+}$ (Hhmp= 2-hydroxymethylpyridine) (e), and $\{Mn^{II}[Mn^{II}_2Mn^{III}_4(HL^2)_3(L^2)_3]\}^{2+}$ (H_3L^2= triethanolamine) (f). The second contains wheels built from simple linked 'mononuclear units' sometimes referred to as "single-stranded loops" [7a-f], examples of which include: $[Mn^{III}(C_{14}H_9N_2O_3)(MeOH)]_{10}$ ($C_{14}H_9N_2O_3$= N-phenylsalicylhydrazidate) (g), $[Mn_6{}^{II}(hfac)_{12}(NITPh)_6]$ (hfac= hexafluoroacetylacetonate; NITPh= 2-phenyl-4,4,5,5-tetramethyl-4,5-dihydro-1H-imidazolyl-1-oxyl 3-oxide) (h), $[Mn^{III}{}_6Mn^{II}{}_6(OAc)_{14}(mdea)_8]$ (mdea= N-methyldiethanol amine) (i), $[Mn^{III}{}_4Mn^{II}{}_4(O_2CCH_2{}^tBu)_{12}(teaH)_4]$ ($teaH_3$= triethanolamine) (j), and $[Mn^{III}{}_8Mn^{II}{}_8(OAc)_{16}(teaH)_{12}]$ (k). The third category consists of wheels based on repeating polymetallic units [8] such as cubes or

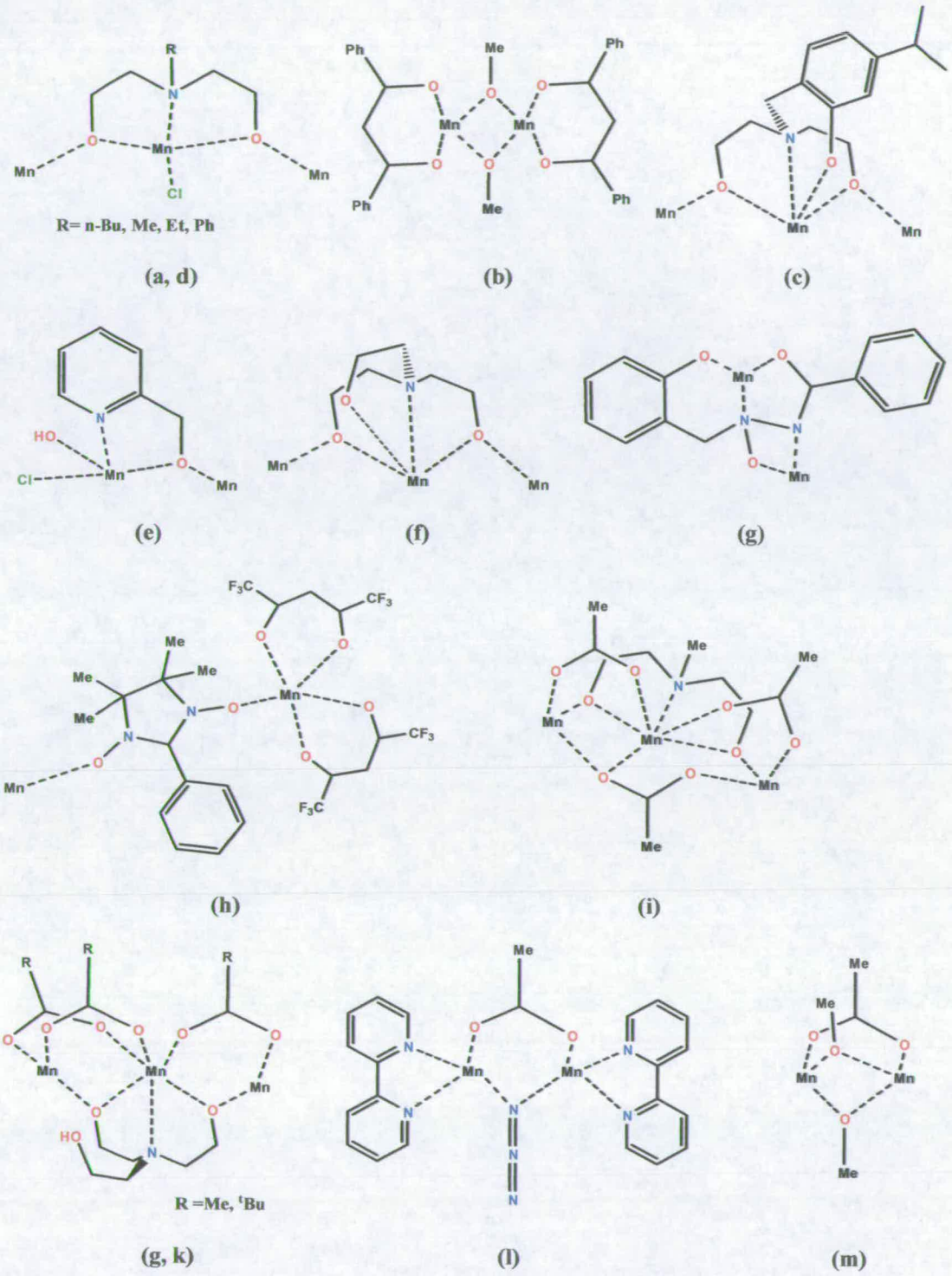

Scheme 3.1. The bonding modes employed by a variety of ligands for the assembly of Mn-wheels.

triangles examples of which include $[Mn^{IV}_6Mn^{II}_{18}(bpy)_{24}(OAc)_6(N_3)_6(tmp)_{12}]^{12+}$ (bpy

= bipyridine; H_3tmp = 1,1,1-tris(hydroxymethyl)propane) (l) and $[Mn^{III}_{84}O_{72}(OH)_6(OMe)_{24}(OAc)_{78}(MeOH)_{12}(H_2O)_{42}]$ (m). An interesting point is the similarity of the ligands/co-ligands used to generate the above complexes - the most commonly employed being carboxylates in combination with alkoxides each bridging in a μ-coordination mode (though in some cases end-on (μ) azides or analogous N-based ligands fulfil the role of the alkoxides). Scheme **3.1** shows examples (**a-m**) of how such ligands bridge Mn centers forming the curvature necessary for wheel formation.

Herein we describe the syntheses, structures and magnetic properties of three Mn wheels which belong to the third category of compounds – unusual $[Mn_{16}]$ and $[Mn_{22}]$ clusters formed from self-assembled 'rod-like' and 'sheet-like' moieties [9]. The three complexes $[Mn^{IV}_4Mn^{III}_{10}Mn^{II}_2O_2(OMe)_{12}(tmp)_8(OAc)_{10}]$ (**8**), $[Mn^{IV}_2Mn^{III}_{18}Mn^{II}_2O_6(OMe)_{14}(OAc)_{16}(tmp)_8(HIm)_2]$ (**9**), $[Mn^{IV}_2Mn^{III}_{18}Mn^{II}_2O_6(OMe)_{14}(OAc)_{16}(Br\text{-}mp)_8(HIm)_2]$ (**10**) are high-spin molecules that behave as SMMs.

Experimental Section

All manipulations were performed under aerobic conditions using $[Mn_3O(OAc)_6(HIm)_3]\cdot(OAc)$, prepared as previously described [10].

➢ Synthetic Procedures

$[Mn^{IV}_4Mn^{III}_{10}Mn^{II}_2O_2(OMe)_{12}(tmp)_8(OAc)_{10}]\cdot 3Et_2O$ (**8**·3Et2O). To a stirred red-brown solution of $[Mn_3O(OAc)_6(HIm)_3]\cdot(OAc)$ (0.500 g, 0.60 mmol) in MeOH (20 ml) was added solid H_3tmp (0.067 g, 0.60 mmol). The mixture was stirred for 30 minutes, filtered and the resulting solution layered with diethyl-ether (Et_2O). After 7 days black crystals of **8**·3Et_2O formed and were collected by filtration, washed with Et_2O and dried *in vacuo*. The yield was ~20 %. A sample for

X-ray crystallography was kept in the mother liquor to prevent solvent loss. The dried complex analyzed as solvent free: Anal. Calcd (Found) for $C_{80}H_{154}Mn_{16}O_{58}$: C, 32.87(32.44); H, 5.31(5.00) %.

$[Mn^{IV}_2Mn^{III}_{18}Mn^{II}_2O_6(OMe)_{14}(OAc)_{16}(tmp)_8(HIm)_2]\cdot 2MeOH$ (**9**·2MeOH). To a stirred red-brown solution of $[Mn_3O(OAc)_6(HIm)_3](OAc)$ (0.500 g, 0.60 mmol) in MeOH (20 ml) was added solid H_3tmp (0.067 g, 0.60 mmol) and NaOMe (0.032 g, 0.60 mmol). The mixture was stirred for 12 hours, filtered, and the resulting solution layered with diethyl-ether (Et_2O). After 7 days the resulting black crystals of **9**·2MeOH were collected by filtration, washed with Et_2O and dried *in vacuo*. The yield was ~15 %. The dried complex analyzed as solvent free: Anal. Calcd. (found) for $C_{100}H_{186}Mn_{22}O_{76}N_4$: C, 31.04 (31.21); H, 4.85 (5.13); N, 1.45 (1.78)%.

$[Mn^{IV}_2Mn^{III}_{18}Mn^{II}_2O_6(OMe)_{14}(OAc)_{16}(Br\text{-}mp)_8(HIm)_2]\cdot 2hex\cdot 5MeOH$ (**10**·2hex·5MeOH). The synthetic procedure was similar to that followed for **9** but with the addition of solid Br-mpH_3 (0.119 g, 0.60 mmol) instead of H_3tmp. The mixture was stirred for 40 minutes and then filtered, and the solution layered with diethyl-ether (Et_2O). After 2 weeks the resulting black crystals of **10**·2hex·5MeOH were collected by filtration, washed with Et_2O and dried *in vacuo*. The yield was ~10 %. The dried complex analyzed as solvent free: Anal. Calcd. (found) for $C_{92}H_{160}Br_8Mn_{22}O_{76}N_4$: C, 25.19 (25.09); H, 3.68 (3.46); N, 1.28 (1.47)%.

Results and Discussion

➢ Synthesis

Reaction of the metal triangle $[Mn^{III}_3O(OAc)_6(HIm)_3](OAc)$ (HIm = imidazole) with one equivalent of 1,1,1-tris(hydroxymethyl)propane (H_3tmp) in MeOH for 30 minutes affords the mixed-valent species $[Mn^{IV}_4Mn^{III}_{10}Mn^{II}_2O_2(OMe)_{12}(tmp)_8(OAc)_{10}]$ (**8**). If the reaction is repeated in the presence of NaOMe and for a period of at least 12 hours, the complex

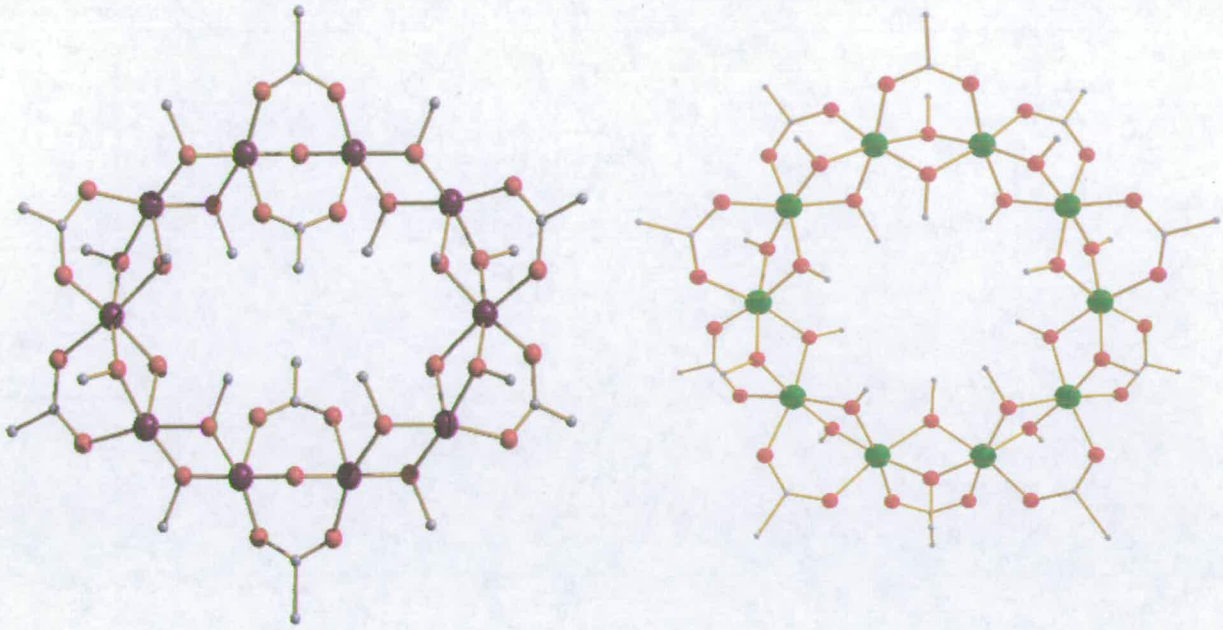

Scheme 3.2. The central Mn^{III}_{10} wheel present in **8-10** (left) and its comparison to the decametallic wheels of general formula $[M^{III}_{10}(OR)_{20}(O_2CR)_{10}]$ (right).

$[Mn^{IV}_2Mn^{III}_{18}Mn^{II}_2O_6(OMe)_{14}(tmp)_8(OAc)_{16}(HIm)_2]$ (**9**) forms. If the latter reaction is repeated with 2-(Bromomethyl)-2-(hydroxymethyl)-1,3-propanediol (Br-mpH_3) with stirring for 40 minutes, the complex $[Mn^{IV}_2Mn^{III}_3Mn^{II}_{18}O_6(OMe)_{14}(OAc)_{16}$(Br-mp$)_8$(HIm$)_2$] (**10**) forms. It is difficult to speculate on the reaction pathways that lead to the formation of the three complexes - as is the case with all Mn cluster chemistry - but it has been shown previously that μ_5-bridging (the most commonly observed coordination mode for these ligands) fully deprotonated tripodal alcohols favour the formation of one dimensional 'rod-like' complexes in Mn carboxylate chemistry [3d]. Additionally the use of alcohol as solvent and the consequent presence of μ-bridging MeO^- ions may also favor the formation of the inner Mn^{III}_{10} wheel (*vide infra*). Decametallic wheels of general formula $[M^{III}_{10}(OR)_{20}(O_2CR)_{10}]$ (R = Me, Et *etc.*) are well known for Fe^{III}, Cr^{III}, Ga^{III} and V^{III} and can be made easily from the reaction of the appropriate M^{III} triangle $([M^{III}_3O(O_2CR)_6L_3]^+$ (L = H_2O, MeOH *etc.*) with alcohol [5]. These complexes describe a near-planar circular array of M^{III} ions in which each pair of metal ions is bridged by two μ-alkoxides and one μ-

carboxylate. The central $[Mn^{III}_{10}O_2(OR)_{16}(O_2CR)_8]$ core displayed by **8-10** is remarkably similar (Scheme **3.2**), perhaps suggesting that the initial step in the syntheses is the formation of a decametallic Mn^{III} wheel, to which further metal ions are added as a result of the presence of additional bridging (tripodal) alkoxides. This in turn suggests that the Mn^{III} analogue of $[M^{III}_{10}(OR)_{20}(O_2CR)_{10}]$ can be made by simply reacting $[Mn^{III}_3O(O_2CR)_6L_3]^+$ species with alcohol. This is currently under investigation.

➢ Description of structures

Complex **8** crystallizes in a triclinic space group $P\bar{1}$ (Figure **3.1**; selected bond lengths and angles are given in Table **A.3.3**). The core of **8** consists of a central near-planar $[Mn^{III}_{10}]$ single-stranded loop (containing Mn2, Mn4, Mn6, Mn7, Mn8, and symmetry equivalents) to which six further Mn ions are attached (Mn1, Mn3, Mn5, and s.e.) – three above and three below opposite 'sides' of the Mn_{10} wheel (Figure **3.2**). The metallic skeleton of complex **8** (Figure **3.5**) thus describes two off-set stacked parallel $[Mn_7]$ 'rods' (containing Mn1-Mn7 and comprising five edge-sharing triangles) linked by two apical Mn ions (Mn8 and s.e.) into a loop. Each 'half' of the $[Mn_{16}O_{30}]^{10-}$ metal-oxygen core describes two $[Mn_3O_4]$ partial cubes (Mn1, Mn2, Mn4; Mn5-Mn7) linked to a central $[Mn_3O]$ triangle (Mn3, Mn4, Mn6, O1) *via* the oxygen atoms of one $\eta^1:\eta^1:\eta^2:\mu$-tmp^{3-}, one $\eta^2:\eta^2:\eta^2:\mu_3$-$tmp^{3-}$, one μ_3-OMe^- and one μ-OAc^- ligands, with the two halves then linked at the apical Mn sites *via* a combination of two μ-OMe^- and two μ-OAc^- ligands (Figure **3.2**). The oxygen atoms of the $[Mn_3O_4]$ partial cubes are derived from two $\eta^2:\eta^2:\eta^2:\mu_3$-$tmp^{3-}$ (O21-O31-O41 and O24-O34-O44), two μ_3-OMe^- (O110, O111) ligands, and those of the $[Mn_3O]$ triangles of the sole O^{2-} ions (O1 and s.e).

Complexes **9** and **10** (Figure **3.3**; selected bond lengths and angles are given in Tables **A.3.4-7**) crystallize in the orthorhombic space group *Pbca*. Remarkably the same $[Mn_{16}O_{30}]^{10-}$ metal-oxygen core is maintained, with two additional $[Mn_3O_4]$

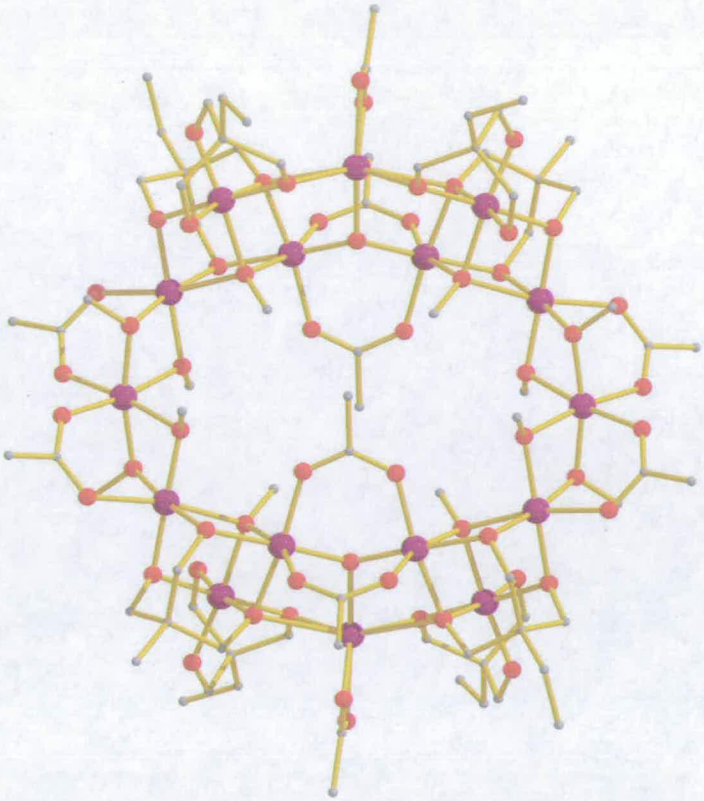

Figure 3.1. The molecular structure of complex **8**. Colour scheme: Mn: purple; O: red; C: grey.

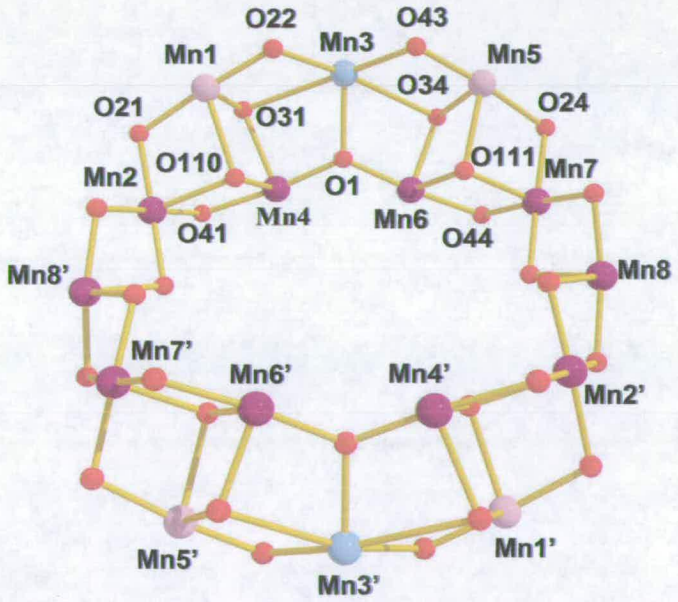

Figure 3.2. The core of complex **8**. Colour scheme: Mn(II): pink; Mn(III): purple; Mn(IV): blue; O: red.

partial cubes (Mn9-Mn11 and s.e.) attached *via* the oxygen atoms of one $\eta^2:\eta^2:\eta^2:\mu_3$-

Br-mp^{3-} (O23, O33, O43), one μ-OAc$^-$ (O60), and four μ-OAc$^-$ ligands on each side (one above and one below) the two 'Mn_7 rods' (Figure **3.4**). Thus the metallic skeletons of **9** and **10** describe two off-set Mn_{10} 'triangular sheets' (containing Mn1-Mn11 and s.e.) comprising nine edge-sharing triangles linked by two apical Mn^{III} ions (Mn8 and s.e) into a loop (Figure **3.5**).

The tripodal alcohol ligands in complexes **8-10** are all triply deprotonated, tripod^{3-}, and bridge in two different modes for complex **8**, and three for **9** and **10**; these are shown in Figure **3.6**. In **8**, four adopt the $\eta^2:\eta^2:\eta^2:\mu_3$-mode (Figure **3.6a**) and four adopt the $\eta^2:\eta^1:\eta^1:\mu$-mode (**3.6d**). In **9** and **10**, two coordinate in a $\eta^2:\eta^2:\eta^2:\mu_3$-fashion (**3.6a,e**), four coordinate in a $\eta^3:\eta^2:\eta^2:\mu_4$-fashion (**3.6b,f**), and two chelate (**3.6c,g**) - bonding only to Mn11 (and s.e.). The MeO$^-$ ligands adopt two coordination modes: a μ_3-mode, each forming a corner of the $[Mn_3O_4]$ partial cubes

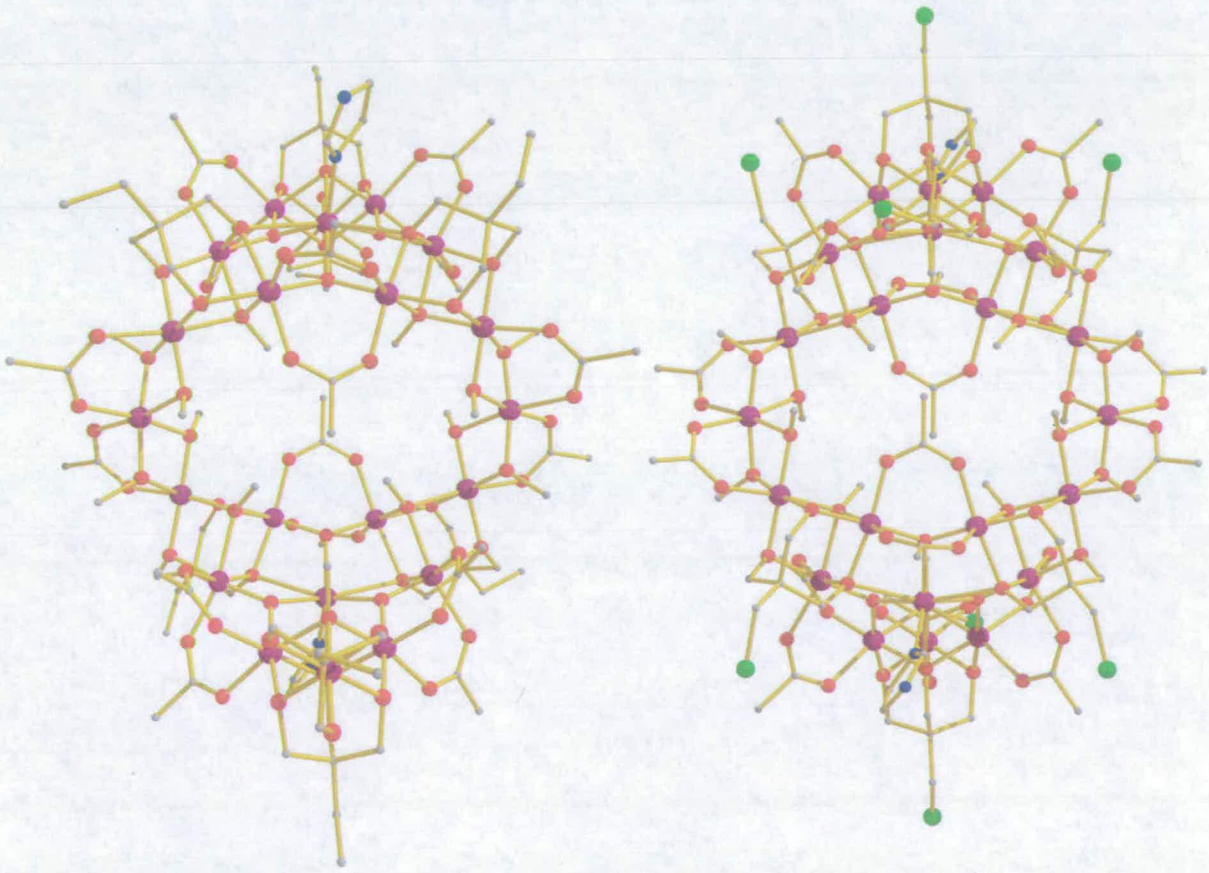

Figure 3.3. The molecular structures of complexes **9** (left) and **10** (right). Colour scheme: Mn: purple; O: red; N: blue; C: grey; Br: green.

(thus appearing four times in **8** and six times in **9**, **10**); and the simple μ-mode, bridging Mn_2 pairs. For **8** all the MeO^- ligands are found bridging within the central Mn_{10} wheel. For **9** and **10**, the one 'additional' μ_3-methoxide resides in the peripheral $[Mn_3O_4]$ partial cube. The OAc^- ligands in **9**, **10** all bond in the expected μ-mode (with the two HIm ligands bonding terminally to the tetrahedral Mn^{II} ions) but in complex **8** one acetate (and s.e) adopts the more unusual chelating mode, bonding only to the five-coordinate Mn^{II} ion. The cavities within the central Mn_{10} wheels are oval-shaped with metal-metal distances of: Mn8-Mn8' 11.15 Å (**8**), 10.99 Å (**9**) and 10.93 Å (**10**); Mn4-Mn6' 8.07 Å (**8**), 8.37 Å (**9**) and 8.47 Å (**10**).

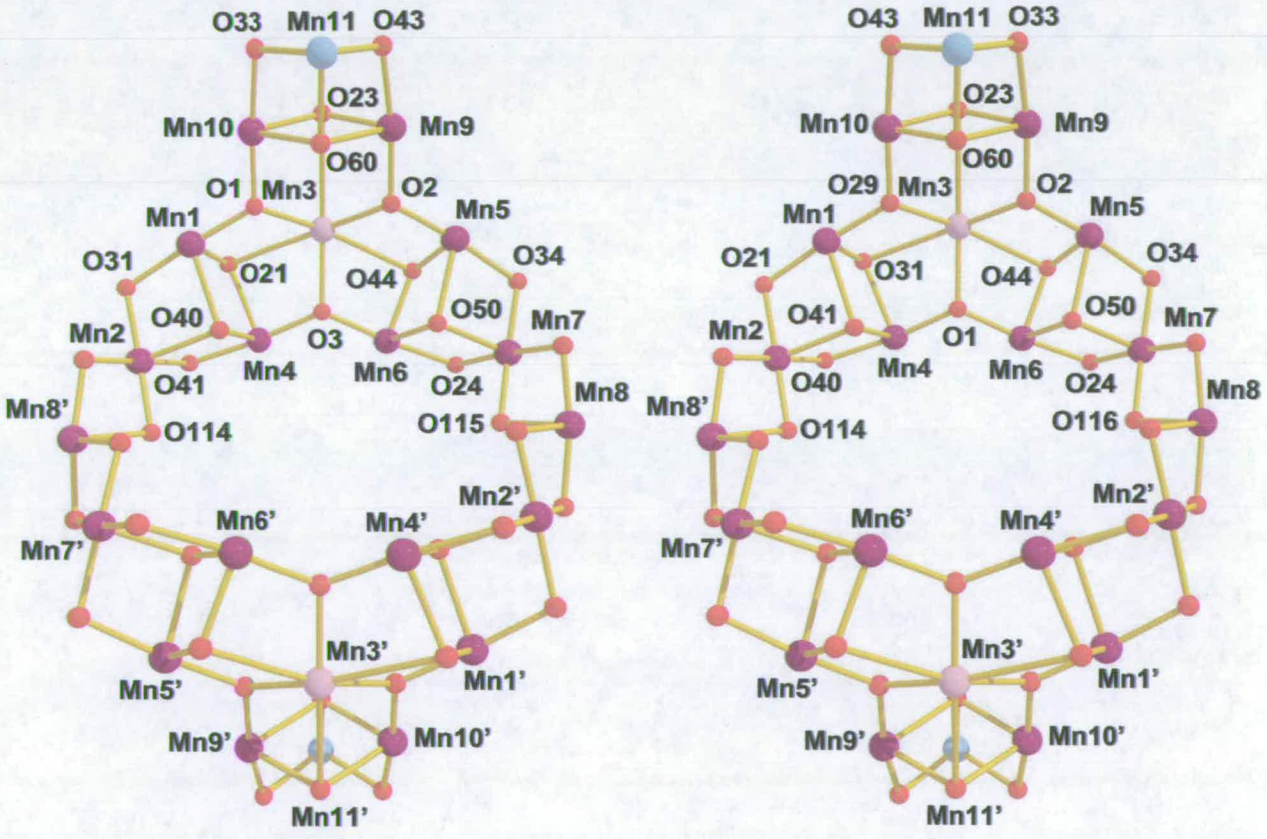

Figure 3.4. The Mn-O cores for **9** (left) and **10** (right). Colour scheme: Mn(II): pink; Mn(III): purple; Mn(IV): blue; O: red.

All oxidation states were assigned using a combination of bond lengths, charge balance considerations and bond valence sum (BVS) calculations (Table **3.1**) [11].

Table 3.1. Bond Valence Sum calculations for **8-10**.

Complex **8**

Atom	Mn^{2+}	Mn^{3+}	Mn^{4+}	Ox.	Atom	Mn^{2+}	Mn^{3+}	Mn^{4+}	Ox.
Mn1	4.50	4.15	4.07	4+	Mn5	4.46	4.11	4.04	4+
Mn2	3.42	3.15	3.09	3+	Mn6	3.44	3.17	3.11	3+
Mn3	2.01	1.63	1.60	2+	Mn7	3.42	3.16	3.09	3+
Mn4	3.44	3.17	3.11	3+	Mn8	3.42	3.16	3.09	3+

Complex **9**

Atom	Mn^{2+}	Mn^{3+}	Mn^{4+}	Ox.	Atom	Mn^{2+}	Mn^{3+}	Mn^{4+}	Ox.
Mn1	3.23	2.96	3.11	3+	Mn7	3.26	2.95	3.10	3+
Mn2	3.25	2.97	3.12	3+	Mn8	3.30	3.02	3.17	3+
Mn3	1.61	1.47	1.54	2+	Mn9	3.29	3.01	3.16	3+
Mn4	3.22	2.94	3.09	3+	Mn10	3.24	2.96	3.11	3+
Mn5	3.24	2.96	3.11	3+	Mn11	3.89	3.56	3.74	4+
Mn6	3.11	2.84	2.98	3+					

Complex **10**

Atom	Mn^{2+}	Mn^{3+}	Mn^{4+}	Ox.	Atom	Mn^{2+}	Mn^{3+}	Mn^{4+}	Ox.
Mn1	3.37	3.11	3.05	3+	Mn7	3.37	3.10	3.04	3+
Mn2	3.35	3.09	3.03	3+	Mn8	3.41	3.15	3.09	3+
Mn3	1.78	1.66	1.63	2+	Mn9	3.43	3.16	3.11	3+
Mn4	3.34	3.08	3.02	3+	Mn10	3.39	3.13	3.07	3+
Mn5	3.47	3.19	3.14	3+	Mn11	4.41	4.07	3.99	4+
Mn6	3.40	3.14	3.08	3+					

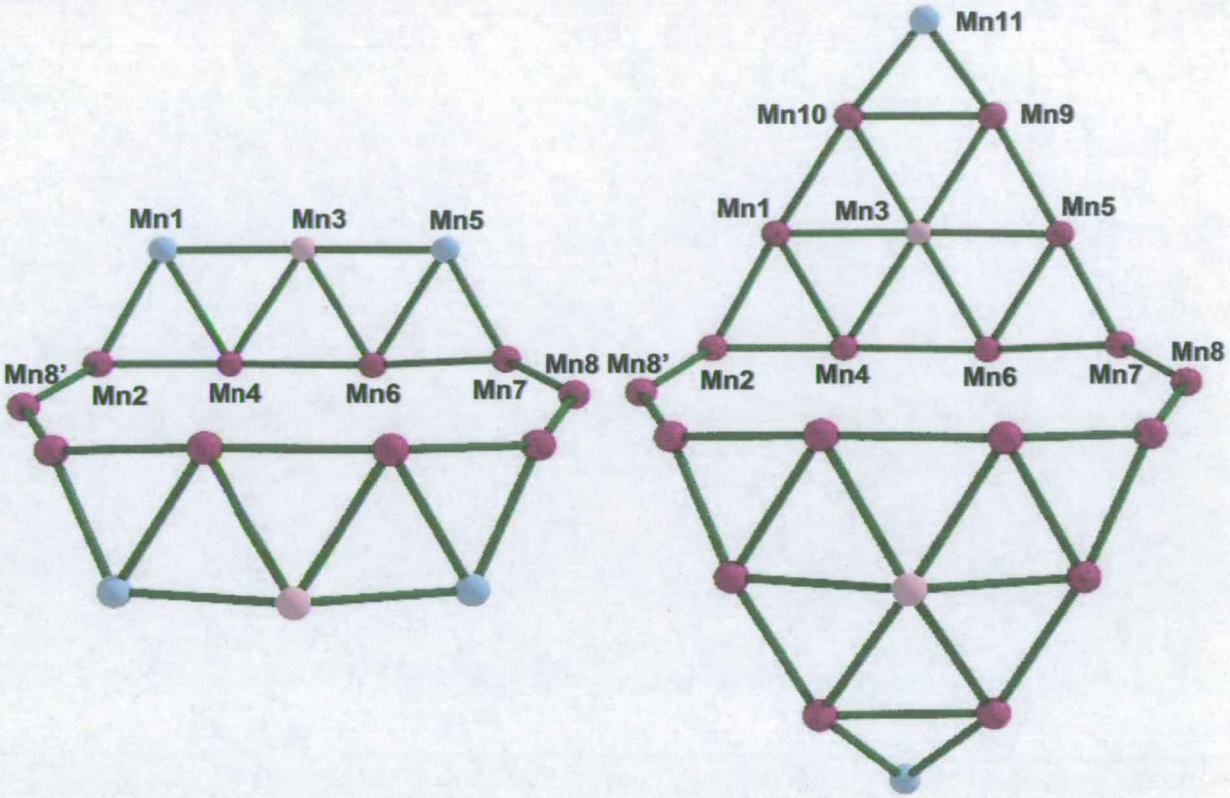

Figure 3.5. Metallic skeletons of complexes **8** (left) and **9, 10** (right). Colour scheme: Mn(II): pink; Mn(III): purple; Mn(IV): blue.

Figures **3.7-8** show the packing diagrams of complexes **8** and **9/10**, respectively. Complex **8** crystallizes in the triclinic space group $P\bar{1}$ and contains two 'half' $[Mn_{16}]$ molecules in the unit cell such that the clusters are orientated in the same direction throughout the crystal. There are 'no' inter-molecular H-bonds (see cif for details of disordered Et_2O), with the shortest intermolecular interactions of ~3.3 Å between the methyl group of an acetate on one molecule and an O-atom of an acetate ligand on its neighbour (Figure **3.7**). Complexes **9** and **10** crystallize in orthorhombic space group *Pbca* and contain four $[Mn_{22}]$ molecules per unit cell, oriented in two different directions. Here the intermolecular H-bonds are extensive: the O-arms of the terminally bound tripod^{3-} ligands H-bond to either a MeOH solvate molecule (e.g. O5-O39, 2.860 Å) or to an imidazole on a neighboring molecule; the protonated N-atom of the HIm ligands H-bond to OAc^- ligands on neighbouring molecules (e.g. N2-O4, 2.882 Å; N2-O7, 2.925 Å), as do the MeOH solvent

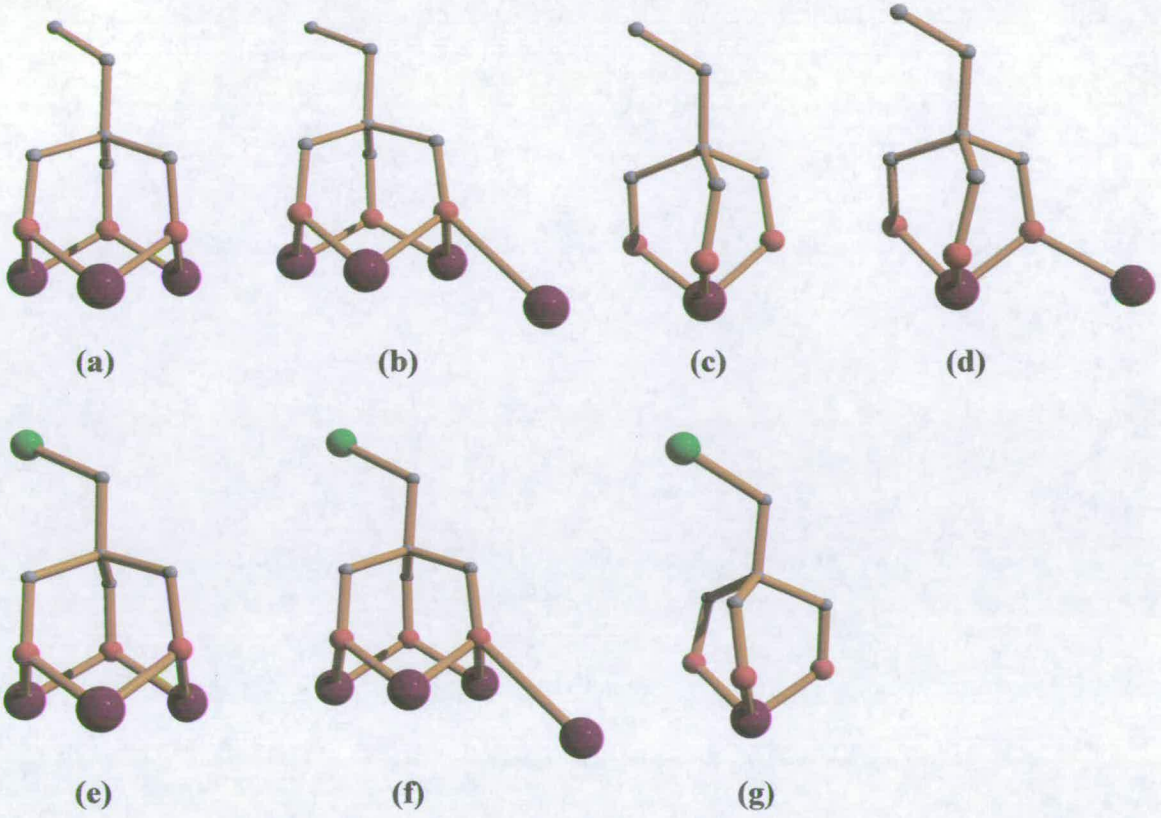

Figure 3.6. Coordination modes of the tripod^{3-} ligands, H_3tmp and Br-mpH_3, in complexes **8-10**. Colour scheme: Mn: purple; O: red; C: grey; Br: green.

molecules. The closest distance between individual [Mn_{22}] molecules occurs between the protonated N-atom of the HIm ligand and the O-atoms of the tripod^{3-} ligand (e.g. N2-O22, 2.935 Å). For all three compounds the clusters pack in a 'head-to-tail' fashion forming an overall serpentine-like or zig-zag packing of the molecules in the crystal. For **9** and **10** the peripherally attached [Mn_3O_4] partial cubes enhance the "*S*-shape" of the individual [Mn_{22}] clusters with respect to the [Mn_{16}] molecule making this packing motif even more pronounced (Figure **3.8**).

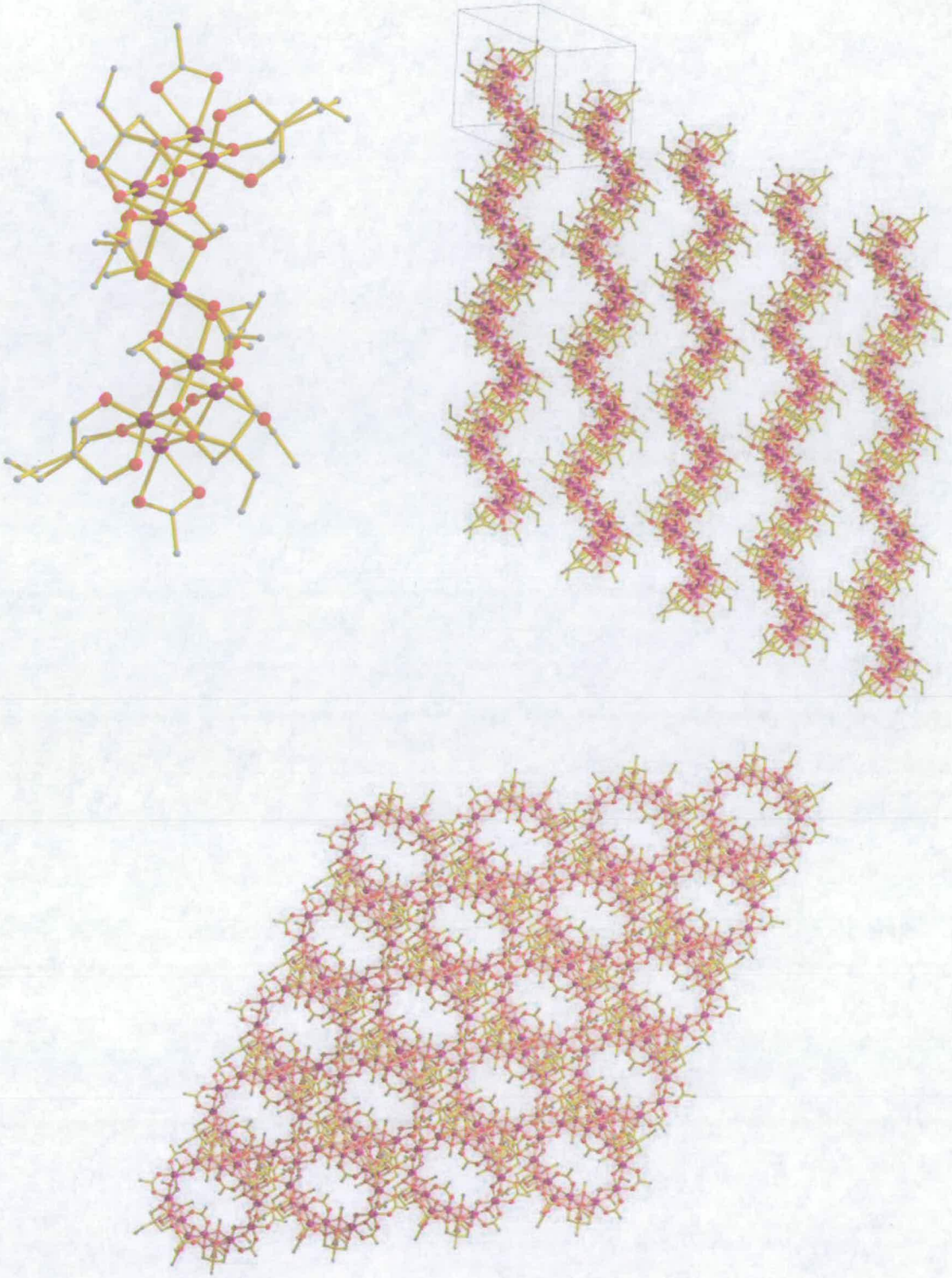

Figure 3.7. A "side-view" (i.e. parallel to the Mn_{10} inner wheel) of complex **8** highlighting its "*S*-shape" (top left). The packing of molecules of **8** in the crystal, highlighting the "serpentine-like" chains (top right), and the "figures-of-eight" chains (bottom), viewed parallel and perpendicular to the Mn_{10} inner wheels, respectively.

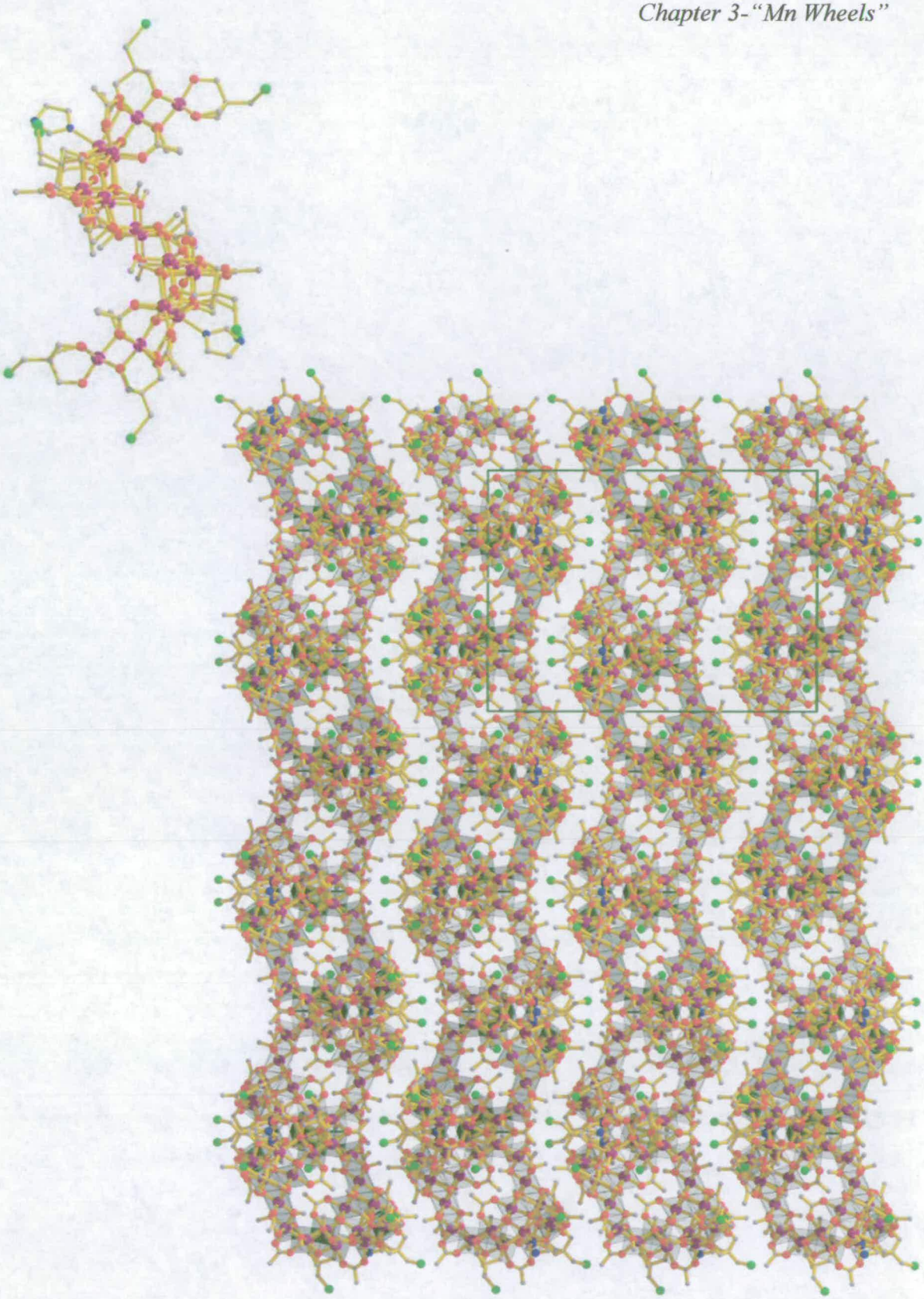

Figure 3.8. A "side-view" (i.e. parallel to the Mn_{10} inner wheel) of complex **10** highlighting its "*S*-shape" (left), and the packing of molecules of **10** in the crystal highlighting the "serpentine-like" chains (right).

Magnetic Studies

➢ Dc Magnetic Studies

Dc magnetic susceptibility measurements (χ_M) were performed on powdered crystalline samples of **8-10** in the temperature range 5-300 K under an applied field 0.1 T. These are plotted as $\chi_M T$ vs T in Figure **3.9**. For complex **8** the $\chi_M T$ value at 300 K of 47.4 cm^3 K mol^{-1} is higher than the spin-only (g = 2) value of 46.3 cm^3 K mol^{-1} expected for two Mn^{II}, ten Mn^{III} and four Mn^{IV} ions. Upon cooling the $\chi_M T$ value increases slightly to a value of 51.4 cm^3 K mol^{-1} at 50 K, then increases rapidly and reaches a maximum value of 88.4 cm^3 mol^{-1} K at 6.5 K before falling to 87.9 cm^3 K mol^{-1} at 5 K. The low temperature (maximum) $\chi_M T$ value suggests a spin ground state of $S = 14\pm1$ (88.4 cm^3 K mol^{-1}).

The room temperature $\chi_M T$ value for complex **9** is ~56 cm^3 K mol^{-1}, lower than the expected spin-only value of 66.5 cm^3 K mol^{-1} expected for two Mn^{IV},

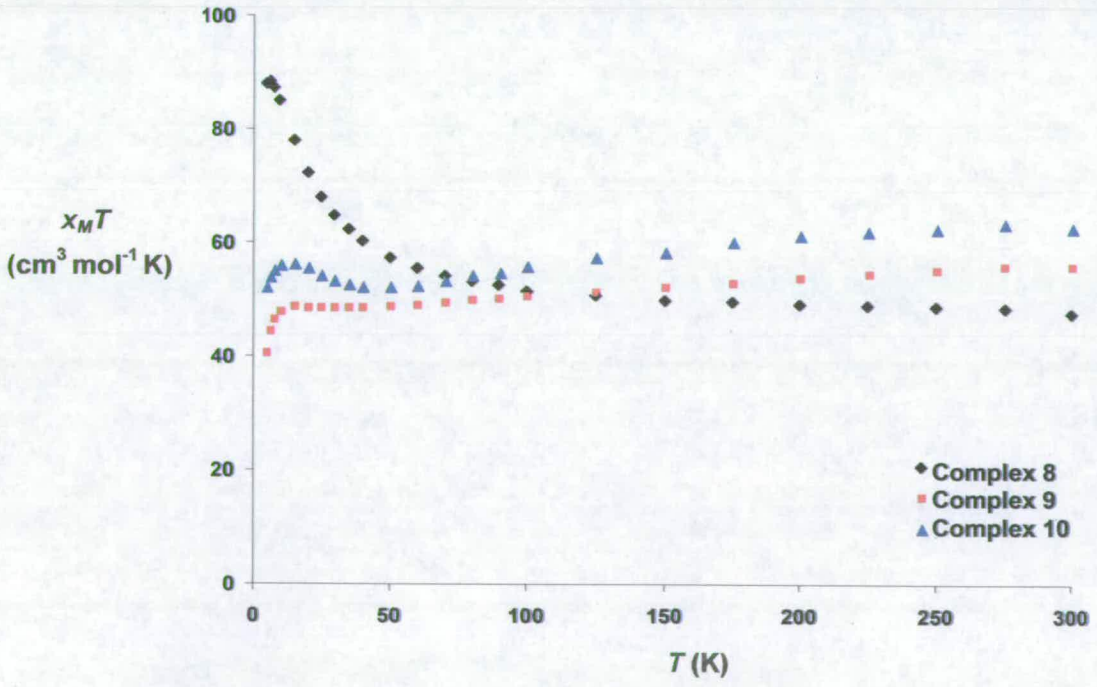

Figure 3.9. Plot of $\chi_M T$ vs T for complexes **8-10** in the 5- 300 K temperature range in a field of 0.1 T.

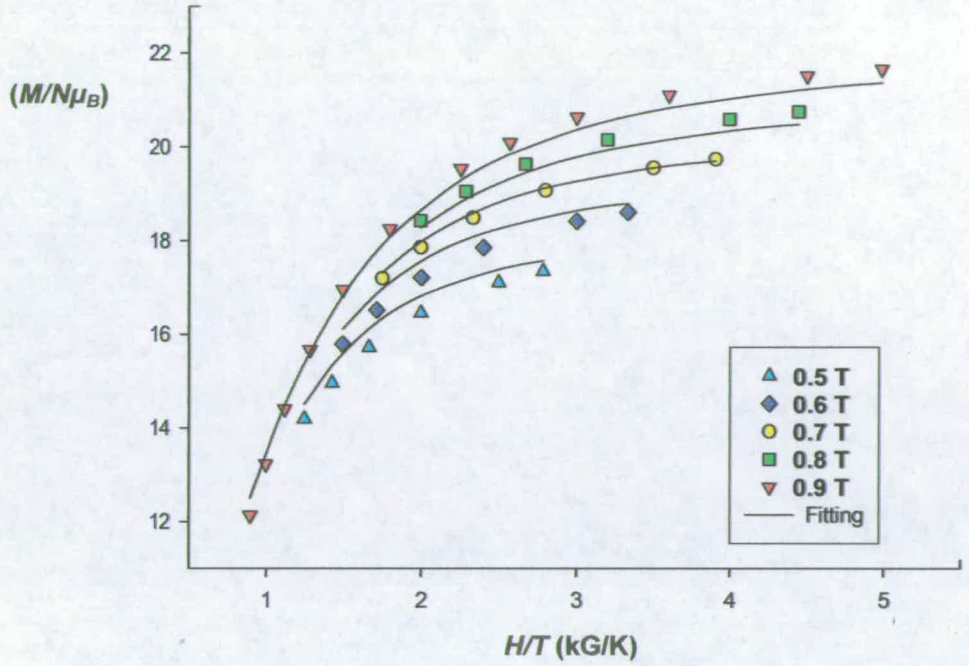

Figure 3.10. Plot of reduced magnetization ($M/N\mu_B$) vs H/T for **8**. The solid lines are the fit of the data to an $S = 14$ state with $D = -0.040$ cm^{-1} and g = 1.85.

eighteen Mn^{III}, and two Mn^{II} ions. The $\chi_M T$ value decreases steadily upon cooling to 48.3 cm^3 K mol^{-1} at 30 K, and then slightly increases to reach a maximum value of 48.6 cm^3 K mol^{-1} at 15 K before dropping rapidly to 40.3 cm^3 K mol^{-1} at 5 K. The 15 K value indicates an approximately $S = 10\pm1$ (48. cm^3 K mol^{-1}) spin ground state. For complex **10**, the $\chi_M T$ value at 300 K is ~62.5 cm^3 K mol^{-1}. Upon cooling it decreases steadily to ~52.5 cm^3 mol^{-1} K at 50 K, before increasing to reach a maximum value of ~57 cm^3 K mol^{-1} at 15 K, and then dropping rapidly to 52 cm^3 K mol^{-1} at 5 K. The low temperature maximum is suggestive of $S = 10\pm1$. The decreases in $\chi_M T$ values at low temperature are likely a consequence of Zeeman effects from the dc field, zfs and/or the presence of intermolecular antiferromagnetic interactions.

Magnetization measurements in the 1.8 to 10 K and 0.1 to 7 T temperature and field ranges were carried out in order to determine the spin ground state values for **8-10**. The data were fit by a matrix-diagonalization method to a model that

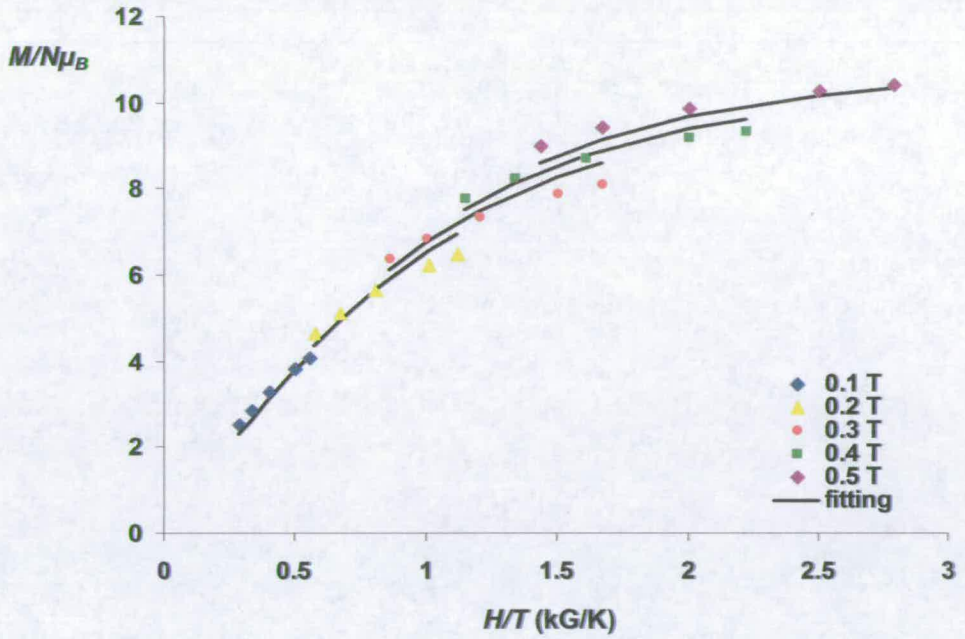

Figure 3.11. Plot of reduced magnetization ($M/N\mu_B$) vs H/T for **10**. The solid lines are the fit of the data to an $S = 9$ state with $D = -0.165$ cm^{-1} and $g = 2.02$.

assumes only the ground state is populated, includes axial zero-field splitting ($D\hat{S}_z^2$), and carries out a full powder average. The corresponding Hamiltonian is:

$$\hat{H} = D\hat{S}_z^2 + g\mu_B\mu_0\,\hat{S}\cdot H$$

where D is the axial anisotropy, μ_B is the Bohr magneton, μ_0 is the vacuum permeability, $\hat{S}_z$ is the easy-axis spin operator, and H is the applied field. The data is plotted as reduced magnetization ($M/N\mu_B$) versus H/T in Figures **3.10-11**. The best fit for complex **8** gave $S = 14$, $g = 1.85$ and $D = -0.04$ cm^{-1} using only low field (≤1 T) data. When fields up to 7 T were employed poorer quality fits were obtained. This behaviour is characteristic of the presence of low-lying excited states. In such cases the population of excited states is difficult to avoid-even at very low temperatures. Because the fitting procedure assumes only the ground state is populated at low temperatures, the use of data collected at higher fields tends to over-estimate the value of S, and consequently the use of only low field data in the fits helps to avoid

this problem, providing more reliable results. For example, for complex **8**, the value of $M/N\mu_B$ rises to approximately 36 in a field of 7 T, suggestive of $S = 18$. However this is not the true ground state, and attempts to fit the magnetization data with $S = 18$ resulted in much poorer quality fits with unreasonable parameters (D and g). The magnitude of $|D|$ is consistent with the non-parallel allignment of the Jahn–Teller axes of the Mn^{III} ions. The best fit for complex **9** was $S = 9$, g = 2.00 and $D = -0.129$ cm^{-1}; and for complex **10**, $S = 9$, g = 2.02 and $D = -0.165$ cm^{-1}, both using data collected in the field range 0.1-2 T. The S and D values obtained for complexes **8-10** suggest all three may exhibit single-molecule magnetism behaviour.

➢ Ac Magnetic Studies

In-phase (χ_M') and out-of-phase (χ_M'') ac susceptibility measurements were performed on complexes **8-10** in the 1.8-10 K range in a 3.5 G ac field oscillating at 5-1000 Hz. For complex **8** (Figure **3.12**), there is first an increase in the value of $\chi_M'T$ with decreasing temperature to approximately 6 K, followed by a 'plateau' until ~3 K, suggesting the presence of low lying excited states with smaller S values. Such low lying excited states are a common feature in many Mn clusters that are either of high nuclearity and thus possess a large density of spin states, or contain multiple Mn^{II} ions that typically promote weak exchange. Extrapolation to 0 K (from >3 K to avoid decreases due to effects such as intermolecular interactions, *etc.*) gives a value of ~94 cm^3 mol^{-1} K, consistent with a spin ground state of $S = 14$, in agreement with the dc data. Frequency dependent out-of-phase χ_M'' ac susceptibility signals are seen for below approximately 2.5 K, but no peaks are observed (Figure **3.12**).

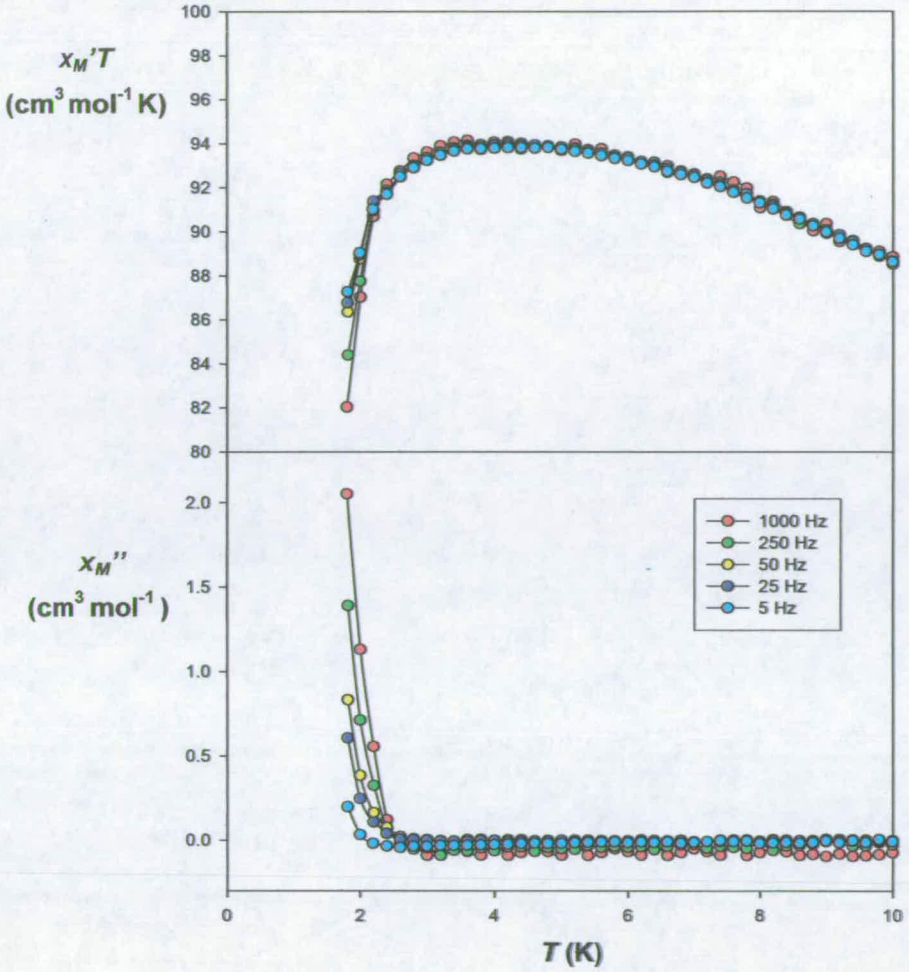

Figure 3.12. Plot of the in-phase (as $\chi_M'T$) (top) and out-of-phase (χ_M'') ac susceptibility signal (bottom) vs. temperature for complex **8**.

The behaviour of **9** and **10** is similar: below 10 K, both show sloping lines with a slight decrease in $\chi_M'T$ with decreasing temperature, suggesting the presence of excited states with larger S values (Figure **3.13**). Extrapolation of the slopes to 0 K gives values of ~53 cm^3 mol^{-1} K for both, suggesting spin ground states of $S = 10\pm1$, in agreement with the dc data. Frequency-dependent out-of-phase (χ_M'') ac susceptibility signals are seen for both complexes below approximately 3 K, but no peaks are observed, along with a concomitant decrease in the in-phase-signal. The presence out-of-phase signals is suggestive of single-molecule magnetism behaviour and is caused by the inability of **8-10** to relax quickly enough, at these temperatures, to keep up with the oscillating field.

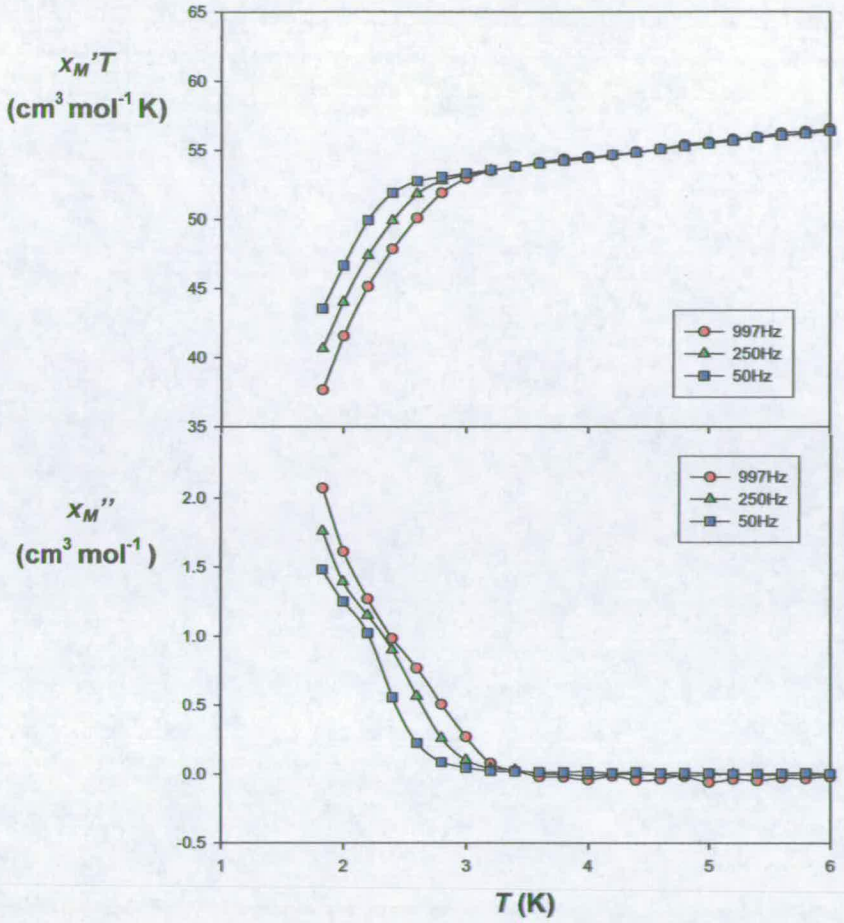

Figure 3.13. Plots of the in-phase (as $\chi_M'T$) (top) and out-of-phase (χ_M'') (bottom) ac susceptibility signal *vs*. temperature for complex **10**.

➢ Single-Crystal Hysteresis Studies

In order to probe the possible single-molecule magnetism behaviour, single crystal hysteresis loop and relaxation measurements were performed using a micro-SQUID setup [12]. Studies of the magnetization performed at very low temperature and high fields show that all three complexes behave as SMMs with long relaxation times. Figures **3.14-16** present typical magnetization (*M*) vs. applied dc field measurements at different field sweep rates and temperatures. In each case hysteresis loops were observed, whose coercivities increase with decreasing temperature or increasing field sweep rate, as expected for the superparamagnetic-like behavior of a

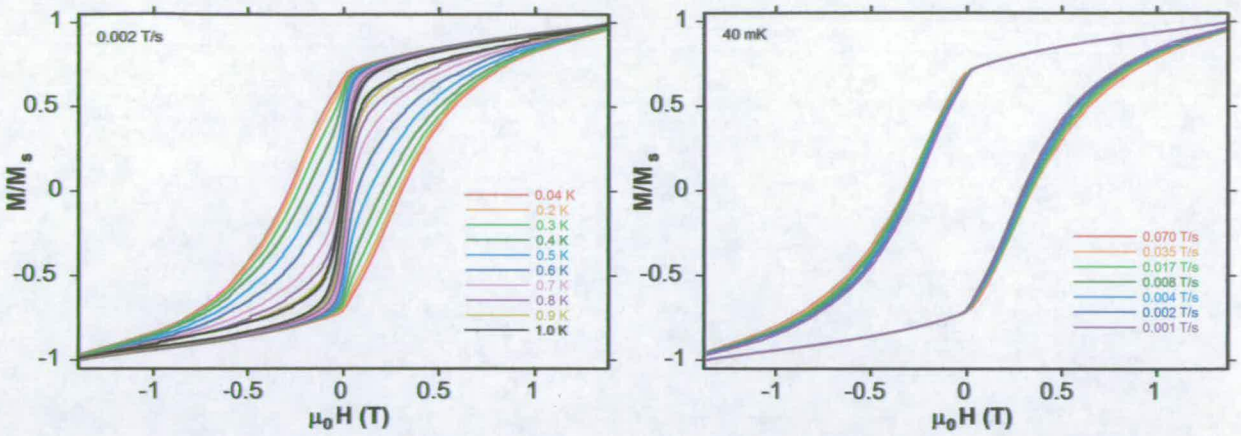

Figure 3.14. Magnetization (*M*) *vs.* dc field hysteresis loops for **8**, at a field scan rate of 0.002 T/s in the temperature range 1.0-0.04 K (left) and at a temperature of 0.04 K and in the field sweep rates 0.07-0.001 T/s (right). *M* is normalized tp its saturation value.

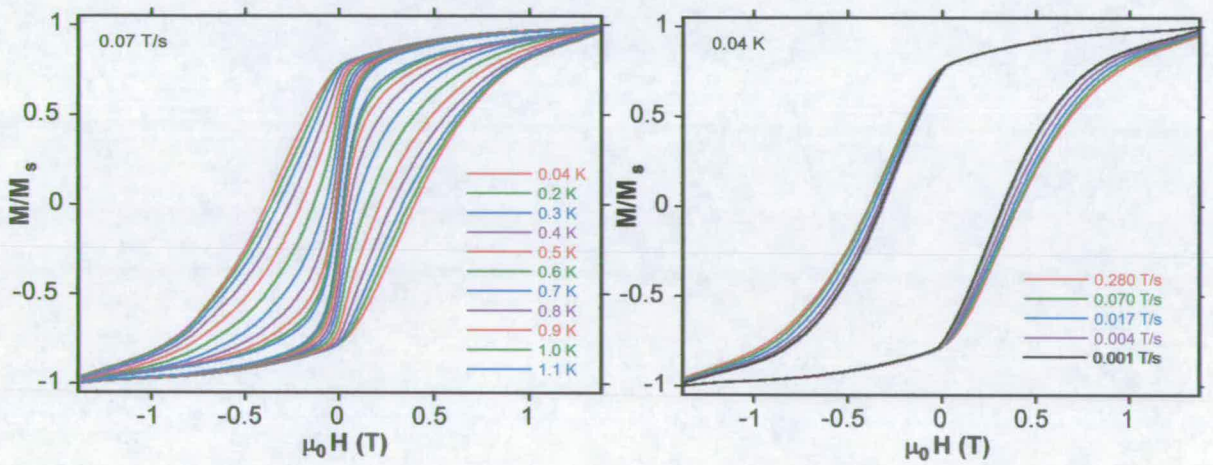

Figure 3.15. Magnetization (*M*) *vs.* dc field hysteresis loops for **9**, at a field scan rate of 0.07 T/s in the temperature range 1.1-0.04 K (left); and at a temperature of 0.04 K in the field scan rates 0.280-0.01 T/s (right). *M* is normalized tp its saturation value.

SMM. Above ~1.3 K there is no hysteresis, *i.e.* the spin relaxes faster to equilibrium than the timescale of the hysteresis loop measurement. The hysteresis loops do not show the step-like features indicative of resonant quantum tunneling of magnetization between the energy states of the molecule. This absence is commonplace for large SMMs and can be rationalized as primarily due to a distribution of molecular environments and thus a distribution of magnetization

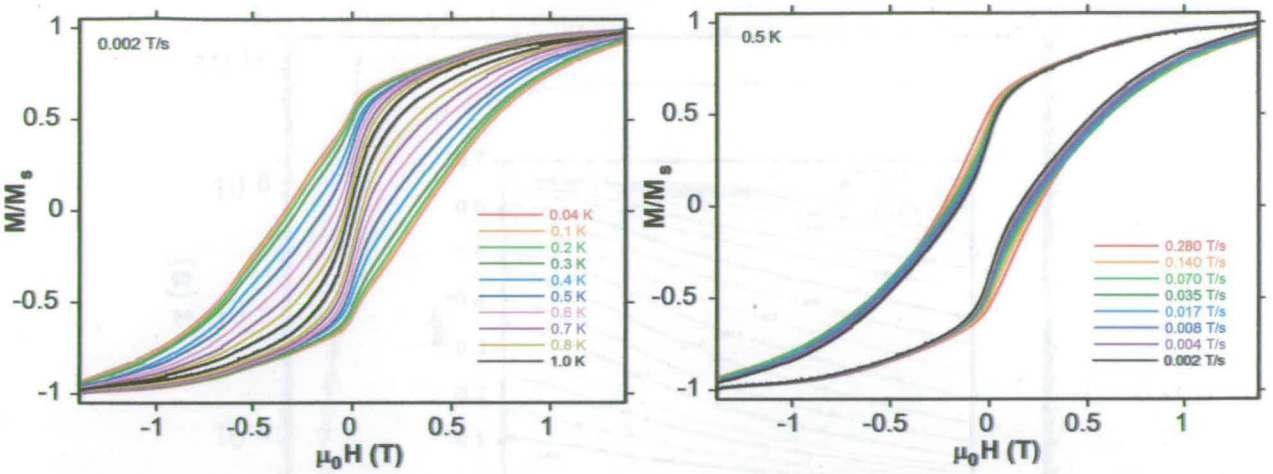

Figure 3.16. Magnetization (*M*) *vs.* dc field hysteresis loops for **10,** at a field scan rate of 0.002 T/s in the temperature range 1.0-0.04 K (left); and at a temperature of 0.5 K in the field scan rates 0.280-0.02 T/s (right). *M* is normalized tp its saturation value.

relaxation barriers. Weak intermolecular interactions (exchange and/or dipolar), and low-lying excited states will also contribute to step-broadening [13].

Single crystal relaxation data collected for **8-10** with the field applied along the easy axis of magnetization are shown in Figures **3.17-3.18**. The observed non-exponential relaxations and Arrhenius plots are typical for such large molecules with rather weak anisotropy and low-lying excited spin states. It is clear that the giant spin approximation works badly for such molecules (*i.e.* the ground state spin is not well defined) and that the slow relaxation is due to relaxation between different spin states, as well as between "up" and "down" states of a given multiplet. The relaxations are also influenced by intermolecular interactions and the distribution of molecular environments, leading to a broad distribution of relaxation times. Despite these difficulties (and by employing a single scaling function $f(t/\tau(T))$ [16] we could extract the mean relaxation times $\tau(T)$ for all three complexes, which are shown in Figures **16-18** in the form of Arrhenius plots. The straight lines are fits to the Arrhenius law, yielding the values $\tau_0 = 9 \times 10^{-11}$ s and $U_{eff} = 19$ K for **8**, $\tau_0 = 3 \times 10^{-11}$ s and $U_{eff} = 19$ K for **9**, and $\tau_0 = 2 \times 10^{-11}$ s and $U_{eff} = 19.8$ K for **10**.

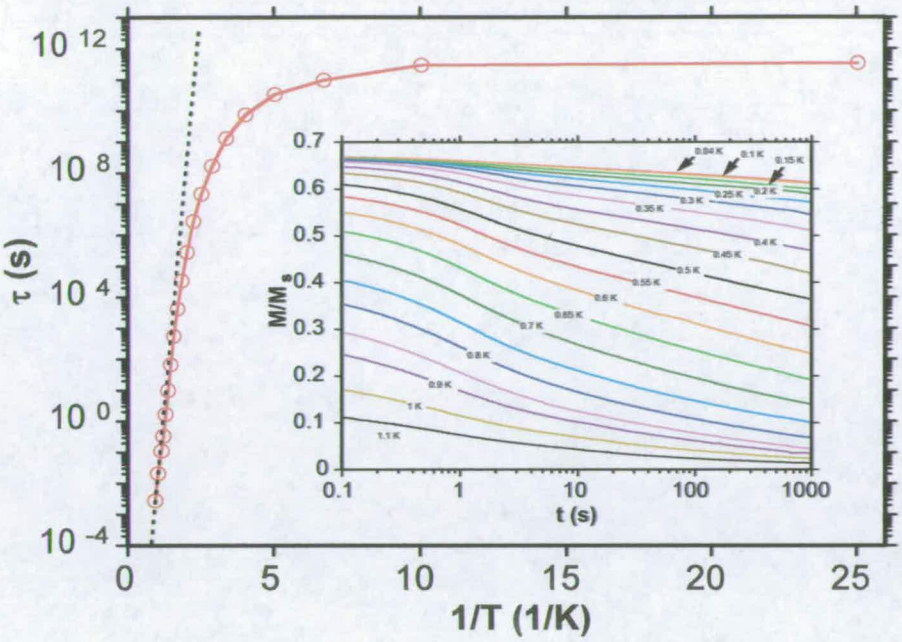

Figure 3.17. Arrhenius plot for **8** using dc relaxation data (inset). The dashed line is the fit of the thermally activated region to the Arrhenius equation.

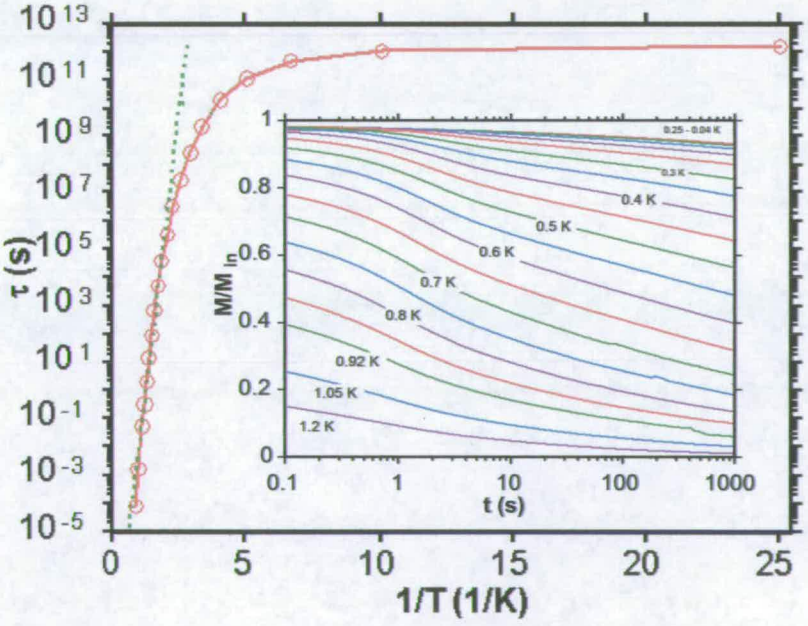

Figure 3.18. Arrhenius plot for **9** using dc relaxation data (inset). The dashed line is the fit of the thermally activated region to the Arrhenius equation.

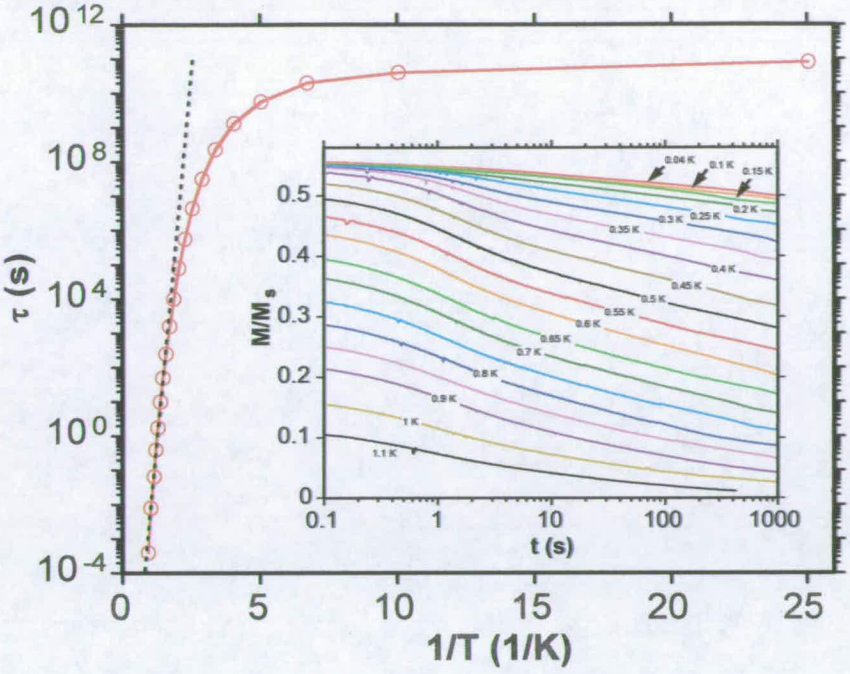

Figure 3.19. Arrhenius plot for **10** using dc relaxation data (inset). The dashed line is the fit of the thermally activated region to the Arrhenius equation.

Conclusions

In conclusion, we have synthesized rare examples of high-nuclearity, high-spin Mn wheels. The complexes were isolated from the same reaction, but in different time-scales and/or with different tripodal alcohols - demonstrating the versatility of a simple reaction system. All three structures are near-identical with the differences being limited to the oxidation levels of the Mn ions and the presence of two additionally attached $[Mn_3O_4]$ partial cubes in the Mn_{22} complexes. In each case their synthesis *may* be governed by the initial formation of a decametallic inner wheel with the tripodal alcohols directing 'Mn_7 rod-like' moieties consisting of three edge-sharing triangles that are attached either side of the Mn_{10} wheel. The alcohol-induced formation of M^{III}_{10} wheels is well known for Fe, Cr, Ga and V suggesting that the Mn analogue may be isolable from the simple reaction of $[M^{III}_3O(O_2CR)_6L_3]^+$ with alcohol. Complexes **8-10** are amongst the largest nuclearity

and highest spin Mn SMMs known - indeed the $S = 14$ ground state displayed by **8** is the largest seen for any Mn wheel.

References

[1] (a) R. Sessoli, H-L. Tsai, A.R. Schake, S.Y. Wang, J.B. Vincent, K. Folting, D. Gatteschi, G. Christou, D.N. Hendrickson, *J. Am. Chem. Soc.*, **1993**, *115*, 1804. (b) R. Sessoli, D. Gatteschi, A. Caneschi, M.A. Novak, *Nature*, **1993**, *365*, 141. (c) D. Gatteschi, R. Sessoli, *Angew. Chem. Int. Ed.*, **2003**, *42*, 268. (e) A. Caneschi, D. Gatteschi, R. Sessoli, A.L. Barra, L.C. Brunel, M. Guillot, *J. Am. Chem. Soc.*, **1991**, *113*, 5873.

[2] G. Aromí, E.K. Brechin, *Struct. Bonding*, **2006**, *122*, 1.

[3] (a) D. Gatteschi, R. Sessoli, *Angew. Chem. Int. Ed.*, **2003**, *42*, 268. (b) R. Bircher, G. Chaboussant, C. Dobe, H.U. Güdel, S.T. Ochsenbein, A. Sieber, O. Waldman, *Adv. Funct. Mater.*, **2006**, *16*, 209. (c) G. Christou, *Polyhedron*, **2005**, *24*, 2065. (d) E.K. Brechin, *Chem. Commun.*, **2005**, 5141. (e) D.N. Hendrickson, G. Christou, H. Ishimoto, J. Yoo, E.K. Brechin, A.E. Yamaguchi, M. Rumberger, S.M.J. Aubin, Z. Sun, G. Aromí, *Mol. Cryst. Liq. Cryst.*, **2002**, *376*, 301.

[4] See for example: (a) S.M.J. Aubin, N.R.Dilley, M.W. Wemple, M.B. Maple, G. Christou, D.N. Hendrickson, *J. Am. Chem. Soc.*, **1998**, *120*, 839. (b) J. Yoo, E.K. Brechin, A. Yamaguchi, M. Nakano, J.C. Huffman, A.L. Maniero, L.C. Brunel, K. Awaga, H. Ishimoto, G. Christou, D.N. Hendrickson, *Inorg. Chem.*, **2000**, *39*, 3615. (c) S. Koizumi, M. Nihei, M. Nakano, H. Oshio, *Inorg. Chem.*, **2005**, *44*, 1208. (d) G. Rajaraman, M. Murugesu, E.C. Sanudo, M. Soler, W. Wernsdorfer, M. Helliwell, C. Muryn, J. Raftery, S.J. Teat, G. Christou, E.K. Brechin, *J. Am. Chem. Soc.*, **2004**, *126*, 15445.

[5] See for example: (a) E.J.L. McInnes, S. Piligkos, G.A. Timco, R.E.P. Winpenny, *Coord. Chem. Rev.*, **2005**, *249*, 2577. (b) R.H. Laye, E.J.L. McInnes, *Eur. J. Inorg.*

Chem., 2004, 2811. (c) K.L. Taft, C.D. Delfs, G.C. Papaefthymiou, S. Foner, D. Gatteschi, S.J. Lippard, *J. Am. Chem. Soc.*, **1994**, *116*, 823.

[6] (a) R.W. Saalfrank, A. Scheurer, R. Prakash, F.W. Heinemann, T. Nakajima, F. Hampel, R. Leppin, B. Pilawa, H. Rupp, P. Muller, *Inorg. Chem.*, **2007**, *46*, 1586. (b) G.L. Abbati, A. Cornia, A.C. Fabretti, A. Ganeschi, D. Gatteschi, *Inorg. Chem.*, **1998**, *383*, 145. (c) S. Koizumi, M. Nihei, M. Nakano, H. Oshio, *Inorg. Chem.*, **2005**, *44*, 1208. (d) R.W. Saalfrank, T. Nakajima, N. Mooren, A. Scheurer, H. Maid, F. Hampel, C. Trieflinger, J. Daub, *Eur. J. Inorg. Chem.*, **2005**, 1149. (e) M.A. Bolcar, S.M.J. Aubin, K. Folting, D.N. Hendrickson, G. Christou, *J. Chem. Soc. Chem. Commun.*, **1997**, 1485. (f) N.C. Harden, M.A. Bolcar, W. Wernsdorfer, K.A. Abboud, W.E. Streib, G. Christou, *Inorg. Chem.*, **2003**, *42*, 7067. (g) B. Pilawa, M.T. Kelemen, S. Wanka, A. Geisselmann, A.L. Barra, *Europhys. Lett.*, **1998**, *43*, 7.

[7] (a) S. Liu, B. Lin, C. Lin, J. Huang, *Angew. Chem. Int. Ed.*, **2001**, *40*, 1084. (b) A. Ganeschi, D. Gatteschi, J. Laugier, P. Rey, R. Sessoli, C. Zanchini, *J. Am. Chem. Soc.*, **1988**, *110*, 2795. (c) E.M. Rumberger, S.J. Shah, C.C. Beedle, L.N. Zakharov, A.L. Rheingold, D.N. Hendrickson, *Inorg. Chem.*, **2005**, *44*, 2742. (d) E.M. Rumberger, L.N. Zakharov, A.L. Rheingold, D.N. Hendrickson, *Inorg. Chem.*, **2004**, *43*, 6531. (e) D. Foguet-Albiol, T.A. O'Brien, W. Wernsdorfer, B. Moulton, M.J. Zaworotko, K.A. Abboud, G. Christou, *Angew. Chem. Int. Ed.*, **2005**, *44*, 897. (f) M. Murugesu, W. Wernsdorfer, K.A. Abboud, G. Christou, *Angew. Chem. Int. Ed.*, **2005**, *44*, 892.

[8] (a) R.T.W. Scott, C.J. Milios, A. Vinslava, D. Lifford, S. Parsons, W. Wernsdorfer, G. Christou, E.K. Brechin, *Dalton Trans.*, **2006**, 3161. (b) A.J. Tasiopoulos, A. Vinslava, W. Wernsdorfer, K.A. Abboud, G. Christou, *Angew. Chem. Int. Ed.*, **2004**, *43*, 2117.

[9] (a) M. Murugesu, W. Wernsdorfer, J. Raftery, G. Christou, E.K. Brechin, *Inorg. Chem.*, **2004**, *43*, 4203. (b) M. Manoli, A. Prescimone, K.A. Mishra, S. Parsons, G. Christou, E.K. Brechin, *Dalton Trans.*, **2007**, *5*, 532.

[10] J.B. Vincent, H.R. Chang, K. Folting, J.C. Huffman, G. Christou, D.N. Hedrickson, *J. Am. Chem. Soc.*, **1987**, *109*, 5703.

[11] H. H. Thorp, *Inorg. Chem.*, **1992**, *31*, 1585.

[12] W. Wernsdorfer, *Adv. Chem. Phys.*, **2001**, *118*, 99.

[13] See for example: (a) E.C. Sañudo, E.K. Brechin, C. Boskovic, W. Wernsdorfer, J. Yoo, A. Yamaguchi, T.R. Concolino, K.A. Abboud, A.L. Rheingold, H. Ishimoto, D.N. Hendrickson, G. Christou, *Polyhedron*, **2003**, *23*, 2267. (b) L.F. Jones, E.K. Brechin, D. Collison, A. Harrison, S.J. Teat, W. Wernsdorfer, *Chem. Commun.*, **2002**, 2974. (c) M. Soler, E. Rumberger, K. Folting, D.N. Hendrickson, G. Christou, *Polyhedron*, **2001**, *20*, 1365. (d) M. Soler, W. Wernsdorfer, K. Folting, M. Pink, G. Christou, *J. Am. Chem. Soc.*, **2004**, *126*, 2156.

[14] (a) L. Thomas, A. Caneschi, B. Barbara, *Phys. Rev. Lett.*, **1999**, *83*, 2398. (b) M. Affronte J.C. Lasjaunias, W. Wernsdorfer, R. Sessoli, D. Gatteschi, S.L. Heath, A. Fort, A. Rettori, *Phys. Rev. B.*, **2002**, *66*, 064408.

Chapter 4
Ferromagnetic Mixed-Valent Mn Supertetrahedra and High Spin Planar Discs: Towards Low-Temperature Magnetic Refrigeration with Molecular Clusters

Introduction

Polymetallic complexes of paramagnetic transition metals possessing large spin ground states are of interest since they can display either single-molecule magnetism behaviour, or an enhanced magnetocaloric effect (MCE) [1,2]. The latter, describing the change of magnetic entropy, S_m, upon applied-field change, has potential technological use in cooling applications [2]. Isotropic high-spin molecules are good candidates for magnetic refrigeration for two reasons: a) the higher the spin, the larger the magnetic entropy; b) important MCE are obtained whenever relatively small applied-field changes are sufficient to fully change the polarization of the magnetic molecules [2], and this requires the anisotropy of the molecule to be negligible. The molecules $[Fe_{14}]$, $[Fe_{17}]$ and $[Mn_{10}]$ have shown much promise so far [3]. Notably, we observed MCEs that are comparable and *even larger* than that reported for the best intermetallic and lanthanide alloys conventionally studied and employed for low-temperature cooling applications. The challenge is to find ways of enhancing the MCE even further. Adding low-lying (hence accessible) spin states other than the ground state is, for instance, an efficient method for increasing the degrees of freedom of the system, leading to an excess of magnetic entropy. In terms of MCE, the efficiency of a magnetic system with degenerate spin states can theoretically exceed that of an equivalent (super)paramagnet by more than an order of magnitude. The molecular energy scheme, in particular the presence of low-lying excited spin states is determined by the nature of the intramolecular magnetic

interactions and can be induced by either promoting frustration, or (more simply) generating relatively weak exchange interactions [3]. In what follows we report the very large MCE of an isotropic ferromagnetic manganese-based molecule with a well-defined spin ground state. We then make a similar molecule in which the bridging oxides holding the metallic core together have been replaced with bridging hydroxides, promoting weaker pairwise exchange - this leads to an enhanced MCE. We then make a third molecule that contains a higher ratio of Mn^{2+} ions creating new, weak and antiferromagnetic, Mn^{2+}-Mn^{2+} interactions. This, results in a truly *enormous* enhancement of the MCE making them the very best cooling refrigerants for low-temperature applications ever reported.

Additionally, we investigate the coordination chemistry of analogous organic molecules of the tripodal alcohols H_3thme, H_3tmp, H_4peol (Scheme**1.2**) in which one (or more) of the alcohol 'arms' is replaced by an alternative functional group(s), for example an amine group ($ampH_2$ and $aepH_2$ ligands; Scheme **1.2**). While each alkoxide arm has the potential to bridge up to three metals (and thus a maximum of seven metals per tripodal ligand) [4], the $-NH_2$ 'arm' is likely, if bonded, to act solely as a monodentate/terminal capping unit and should give rise to a number of related, yet different, structural topologies.

Here we report the syntheses and structures of two decametallic mixed-valent Mn supertetrahedra using 2-amino-2-methyl-1,3-propanediol ($ampH_2$); two decametallic mixed-valent Mn planar discs using 2-amino-2-methyl-1,3-propanediol ($ampH_2$) and 2-amino-2-ethyl-1,3-propanediol ($aepH_2$) and a tetradecametallic mixed-valent Mn planar disc, using pentaerythritol (H_4peol). The decametallic complexes display dominant ferromagnetic exchange and spin ground states of S = 22 and the tetradecametallic complex dominant antiferromagnetic exchange and a spin ground state of $S = 7\pm1$. All display large (the former) and enormous (the latter) MCE; the former as a result of negligible zero-field splitting of the ground state, the latter as a result of possessing a high spin-degeneracy at finite low temperatures.

Experimental Section

All manipulations were performed under aerobic conditions, using materials as received.

➢ Synthetic Procedures

$[Mn_{10}O_4Br_4(amp)_6(ampH_2)_3(HampH_2)]Br_3 \cdot 8hex$ (11·8hex). $MnBr_2 \cdot 4H_2O$ (0.500 g, 1.74 mmol) and $ampH_2$ (0.184 g, 1.74 mmol) were stirred in MeOH for 1 hour. The solution was then filtered and layered with hexanes. Crystals of **1**·$8C_6H_{14}$ formed in 3 days in a yield of approximately 20%. Anal. Calcd (found) for **1**·2.5hex $C_{55}H_{135}Mn_{10}N_{10}Br_7O_{24}$: C 26.84 (26.98), H 5.53 (5.49), N 5.69 (5.49).

$[Mn_{10}O_4(OH)_{1.8}I_{2.2}(amp)_6(ampH_2)(HampH_2)_3]I_5 \cdot 5hex$ (12·5hex). To a stirred suspension of MnI_2 (0.500 g, 1.62 mmol) and tertabutylammonium iodide (TBAI: 0.598 g, 1.62 mmol) were added $ampdH_2$ (0.170 g, 1.62 mmol). The resulting solution left upon 3 hours stirring in MeOH for 3 hour. The solution was then filtered and layered with hexanes. Crystals of **2**·$4C_6H_{14}$ formed in 10 days in a yield of approximately 25%. Anal. Calcd (found) for **2**·4hex, $C_{64}H_{155.8}$ $Mn_{10}I_{7.2}N_{10}O_{25.8}$: C 27.19 (27.08), H 5.60 (5.54), N 5.77 (5.71).

$[Mn^{III}_6Mn^{II}_4(OH)_6(amp)_4(ampH)_4I_4(EtOH)_4]I_4$ (13). MnI_2 (0.500 g, 1.62 mmol) and $ampH_2$ (0.170 g, 1.62 mmol) was stirred in EtOH for 5 hours. The solution was then filtered and layered with hexane. Slow evaporation of the solution produced crystals of **4** during 5 days in a yield of approximately 30%. Anal.Calcd (found) for **4** $C_{40}H_{90}Mn_{10}N_8I_8O_{26}$: C 18.04 (15.99), H 3.41 (3.90), N 4.21 (3.93).

$[Mn^{III}_6Mn^{II}_4(OH)_6(aep)_4(aepH)_4I_4(EtOH)_4]I_4$ (14). MnI_2 (0.500 g, 1.62 mmol) and $aepH_2$ (0.193 g, 1.62 mmol) was stirred in EtOH for 5 hours. The solution was then filtered and layered with hexane. Slow evaporation of the solution produced crystals of **5** during 10 days in a yield of approximately 30%. Anal.Calcd (found) for **5** $C_{44}H_{98}Mn_{10}N_8I_8O_{26}$: C 19.43 (19.52), H 3.63 (4.27), N 4.12 (3.64).

$[Mn^{III}_6Mn^{II}_8(OH)_2(Hpeol)_4(H_2peol)_6I_4(EtOH)_6]I_4$ (15). MnI_2 (0.500 g, 1.62 mmol) and H_4peol (0.220 g, 1.62 mmol) were stirred in EtOH for 5 hours. The solution was then filtered and layered with hexane. Crystals of **3** formed in 8 days in a yield of approximately 15%. Anal. Calcd (found) for **3** $C_{58}H_{126}Mn_{14}I_8O_{48}$: C 20.64 (18.73), H 3.76 (3.71).

Results and Discussion

➢ Synthesis

Reaction of the $MnBr_2{\cdot}4H_2O$ with one equivalent of 2-amino-2-methyl-1,3-propanediol ($ampH_2$) affords the mixed-valent supertetrahedron $[Mn_{10}O_4Br_4(amp)_6(ampH_2)_3(HampH_2)]Br_3$ (**11**). When the reaction is repeated replacing $MnBr_2{\cdot}4H_2O$ with MnI_2 in a presence of tetrabutylammonium iodide, the analogous complex $[Mn_{10}O_4(OH)_{1.8}I_{2.2}(amp)_6(ampH_2)(HampH_2)_3]I_5$ (**12**) forms. If the latter reaction is repeated in EtOH instead of MeOH the planar complex $[Mn^{III}_6Mn^{II}_4(OH)_6(amp)_4(ampH)_4I_4(EtOH)_4]I_4$ (**13**) forms. If 2-amino-2-methyl-1,3-propanediol ($ampH_2$) is replaced with 2-amino-2-ethyl-1,3-propanediol ($aepH_2$) in the equivalent reaction the analogous complex $[Mn^{III}_6Mn^{II}_4(OH)_6(aep)_4(aepH)_4I_4(EtOH)_4]I_4$ (**14**) results, but when replaced with pentaerythritol (H_4peol), the tetradecametallic $[Mn^{III}_6Mn^{II}_8(OH)_2(Hpeol)_4(H_2peol)_6I_4(EtOH)_6]I_4$ (**15**) forms.

It is difficult to speculate on the reaction pathways that lead to the formation of the five complexes, but an examination of their structures shows that they are clearly all related. In particular the differences between the decametallic supertetrahedra and the decametallic discs are minimal - both contain $[Mn^{III}_6Mn^{II}_4]$ cores in which each metal ion has a nearest neighbor of different oxidation state, surrounded by (8-10) ligands bridging in a similar fashion. The major change appears to be the presence of oxides in the central cores of the supertetrahedra and

hydroxides in the planar discs. The former being tetrahedral and forming four bonds, the latter being pyramidal /pseudo-planar and forming three bonds; *i.e.* the oxides template the formation of "3D" tetrahedra and the hydroxides template the formation of "2D" planar discs. The formation of the larger tetradecametallic disc (**15**) in comparison to the decametallic discs can be attributed to the change in bridging ligand. While the anions of $ampH_2$ and $aepH_2$ tend to bridge around the periphery of the clusters, the anions of tripodal alcohols such as H_4peol tend to sit directly above and below the centers of planar cores [5]. The presence of three alkoxide arms allows for greater coordination than two alkoxides and one amine. For example, the tetradecametallic complex **15** contains four centrally located $Hpeol^{3-}$ anions each bridging in a μ_6-fashion encompassing a total of ten central metal ions, while the largest coordination mode seen for the anions of $ampH_2$ and $aepH_2$ is μ_5-, occurring only twice in **13** and **14** and encompassing a total of eight metal ions.

➢ Description of structures

$[Mn_{10}O_4Br_4(amp)_6(ampH_2)_3(HampH_2)]Br_3$ (**11**) crystallizes in the rhombohedral space group *R*-3 (Figure **4.1**; selected bond lengths and angles are given in Tables A.4.3-4). The $[Mn_{10}]^{3+}$ cation contains a metallic skeleton that describes a mixed-valent $[Mn^{III}_6Mn^{II}_4]$ supertetrahedron, (Mn1, Mn2 = 2+, Mn3, Mn4 = 3+) in which each nearest neighbour is of a different oxidation state (Figures **4.2-3**). The Mn^{2+} ions define the four apices of the tetrahedron with the Mn^{III} ions lying along each edge. The Mn^{III} ions themselves therefore describe a trigonal antiprism (Figure **4.3**). The metal ions are connected by four central tetrahedral oxide ions to give a $[Mn^{III}_6Mn^{II}_4O_4]^{18+}$ core such that the supertetrahedron can be thought of as being built from four vertex-sharing $[Mn^{III}_3Mn^{II}O]^{9+}$ tetrahedral (Figure **4.2**). The tripodal ligands are of two types: six are doubly deprotonated (amp^{2-}) bridging in a $\eta^2:\eta^2:\mu_3$-fashion along each edge of the tetrahedron, and four remain fully protonated ($ampH_2$) chelating each Mn^{2+} vertex ion (Figure **4.4**). The pendant $-NH_2$

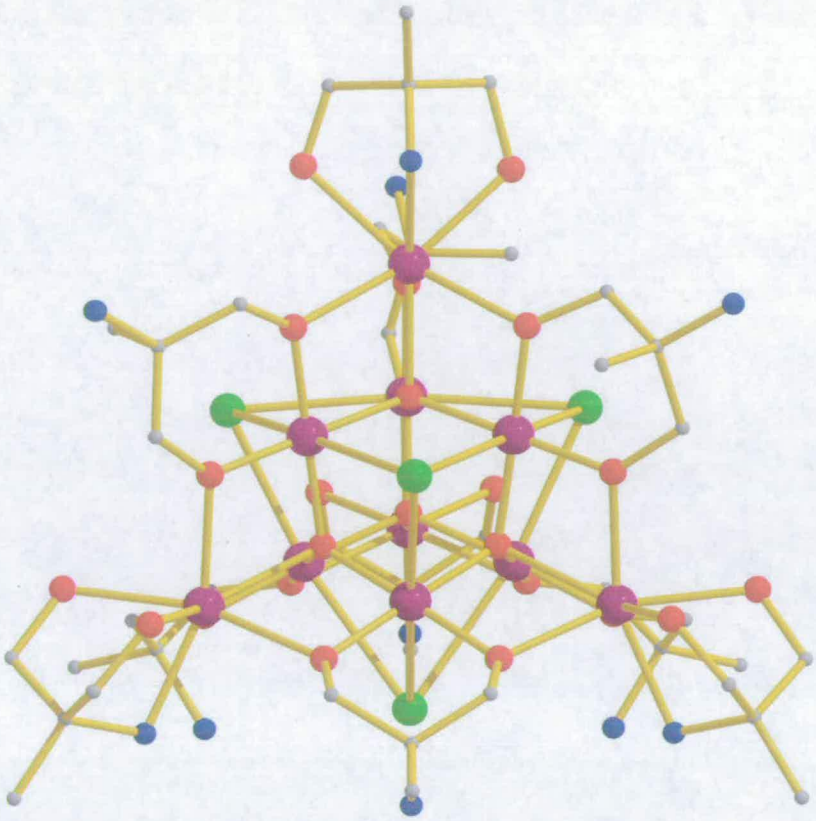

Figure 4.1. The structure of **11** in the crystal. Colour scheme: Mn: purple; O: red; N: blue; C: grey; Br: green.

'arms' of the amp^{2-} ligands at the triangular "base" of the cluster are H-bonded to Br^- counter ions that lie between neighbouring Mn_{10} molecules. Each N-atom is H-bonded to two Br^- ions at distances of approximately 3.2Å forming head-to-head $[Mn_{10}]_2$ dimers throughout the crystal (Figure **4.5**).

The four bromide ions each cap one face of the tetrahedron. The Jahn-Teller axes of the octahedral Mn^{3+} ions are directed by the presence of the long Mn-Br bonds: thus for Mn4 their direction is defined by Br1 and Br2, and for Mn3 their direction is defined by Br2 and symmetry equivalent. All the Mn^{2+} ions are 7-coordinate bound to a $\{O_6N\}$ set of atoms. Triply bridging Br^- (halide) ions have been seen before in Mn chemistry, in the complexes $[Mn_4O_3X(O_2CR)_3(dbm)_3]$ (X = halide, Hdbm = dibenzoylmethane) in which the halide sits in the corner of a distorted cubane; $[Mn_6O_4Br_4(R_2dbm)_6]$ in which the halide caps the face of an

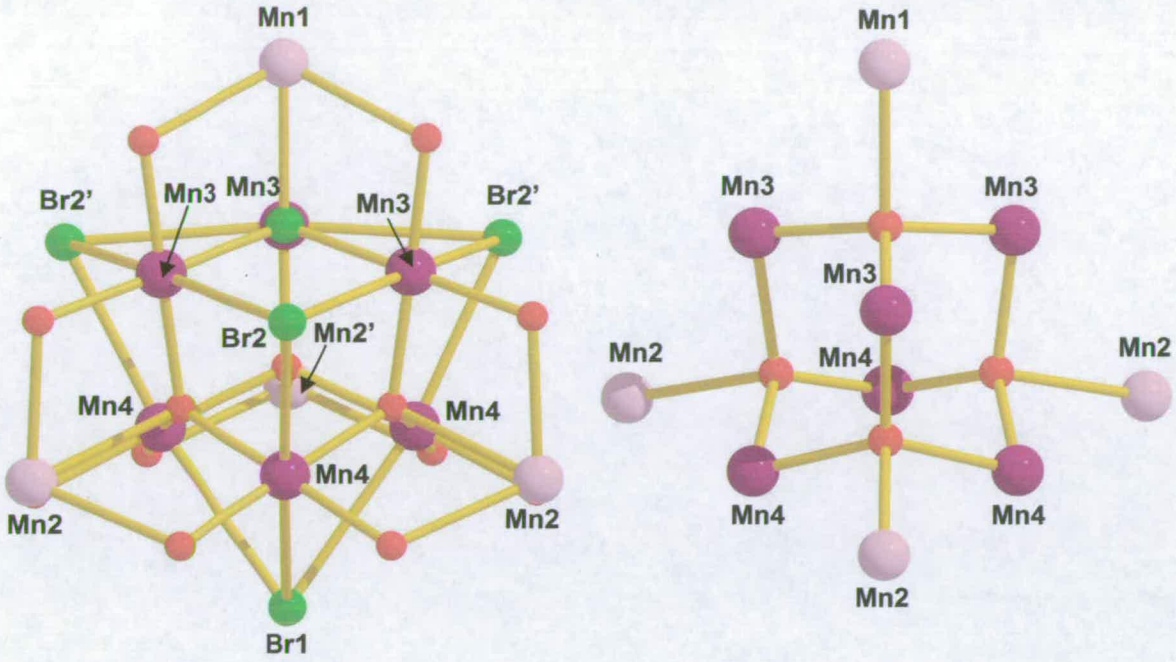

Figure 4.2. The Mn-O-Br core of **11** (left) and the central metal-oxide core (right). Colour scheme: Mn(III): purple; Mn(II): pink; O: red; Br: green.

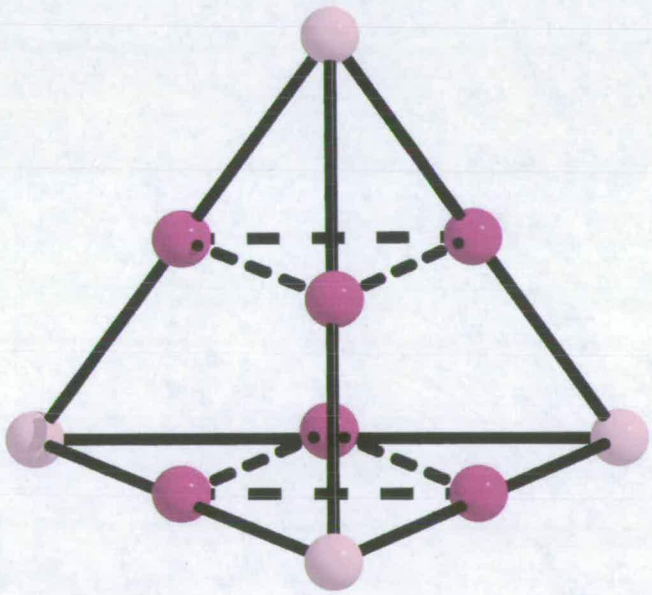

Figure 4.3. The metallic skeleton of **11** and **12** in the crystal. The trigonal antiprism is defined by the Mn^{3+} ions and is shown with the dashed lines. Colour scheme: Mn(III): purple; Mn(II): pink.

octahedron; and $[NMe_4]_4[Mn_{10}O_4(biphen)_4Br_{12}]$ (biphen = 2,2'-biphenoxide) in

which the μ_3-halides form an $\{Mn_4Br_6\}$ adamantane-like core [6]. In each of these

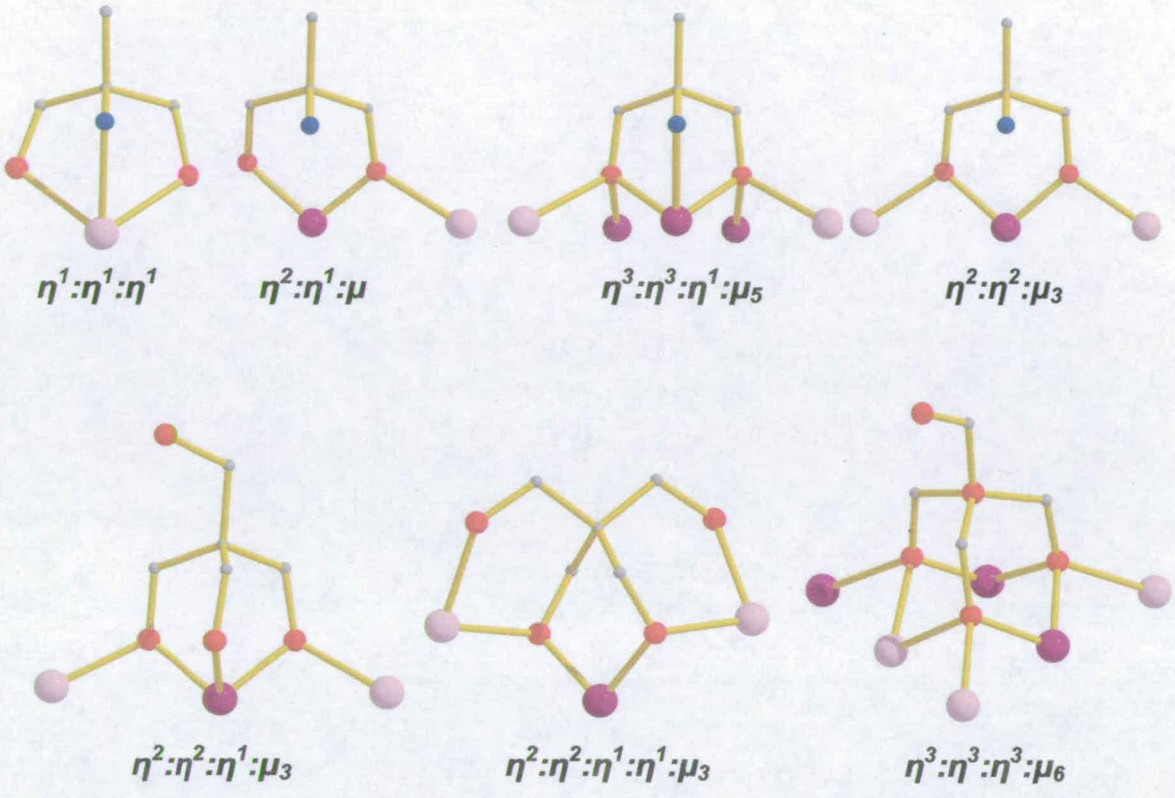

Figure 4.4. The coordination modes of $ampH_n^{(2-n)-}$ and $aepH_n^{(2-n)-}$ (top) and $H_npeol^{(4-n)-}$ (bottom) in **11-15**.

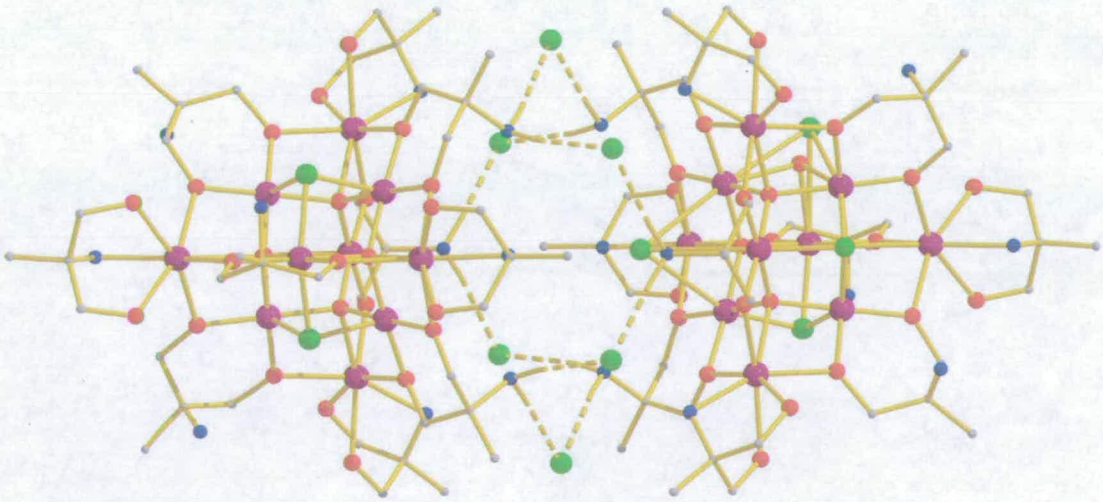

Figure 4.5. The head-to-head $[Mn_{10}]_2$ dimmers of **12** throughout the crystal. Colour scheme: Mn: purple; O: red; N: blue; C: grey; I: green.

complexes the μ_3-Br^- ions sit on an axially elongated site with average Mn^{3+}-Br distances in the range ~2.79-2.84Å, consistent with the values seen here (Mn-Br(av) = 2.82Å). The charge balance of the complex is completed by the presence of the Br^- counter ions and an additional proton. Significant disorder within the $[Mn_{10}]$ unit and in the interstitial solvent molecules (see CIF for full details) makes knowing its exact location difficult, though we have assumed it is disordered over the pendant $-NH_2$ moieties, thus giving the complex the overall formula $[Mn_{10}O_4Br_4(amp)_6(ampH_2)_3(HampH_2)]Br_3$ (**1**).

The analogous complex $\mathbf{[Mn_{10}O_4(OH)_{1.8}I_{2.2}(amp)_6(ampH_2)(HampH_2)_3]I_5}$ (**12**) crystallizes in the trigonal space group *R*-3 (Figure **4.6**; selected bond lengths and angles are given in Tables A.4.5-6). The core (Figures **4.7**) and metallic skeleton

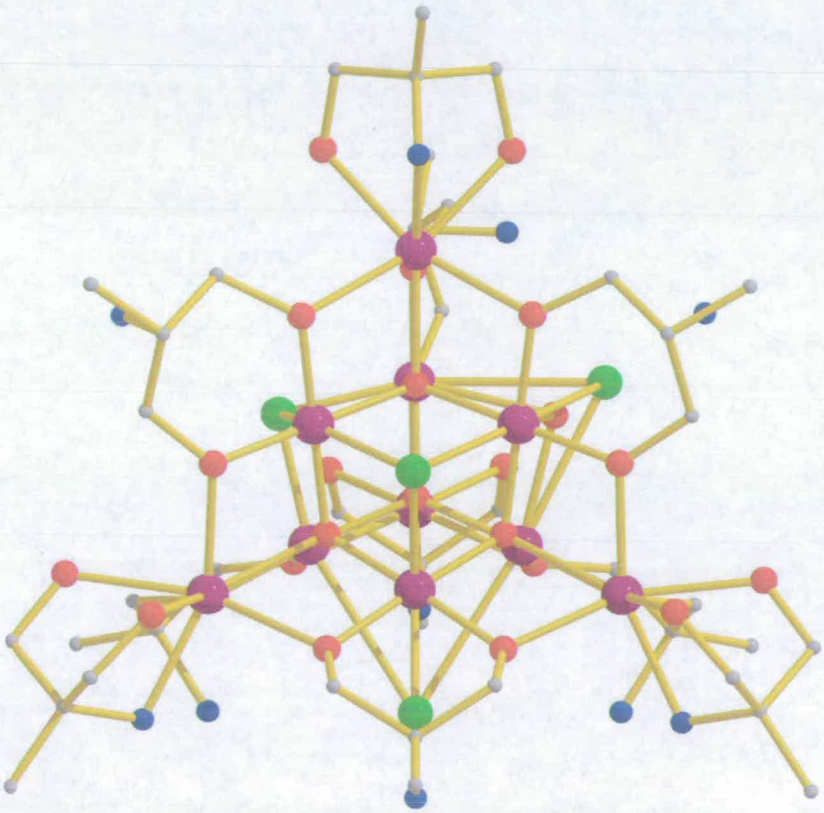

Figure 4.6. The structure of **12** in the crystal. Colour scheme: Mn: purple; O: red; N: blue; C: grey; I: green.

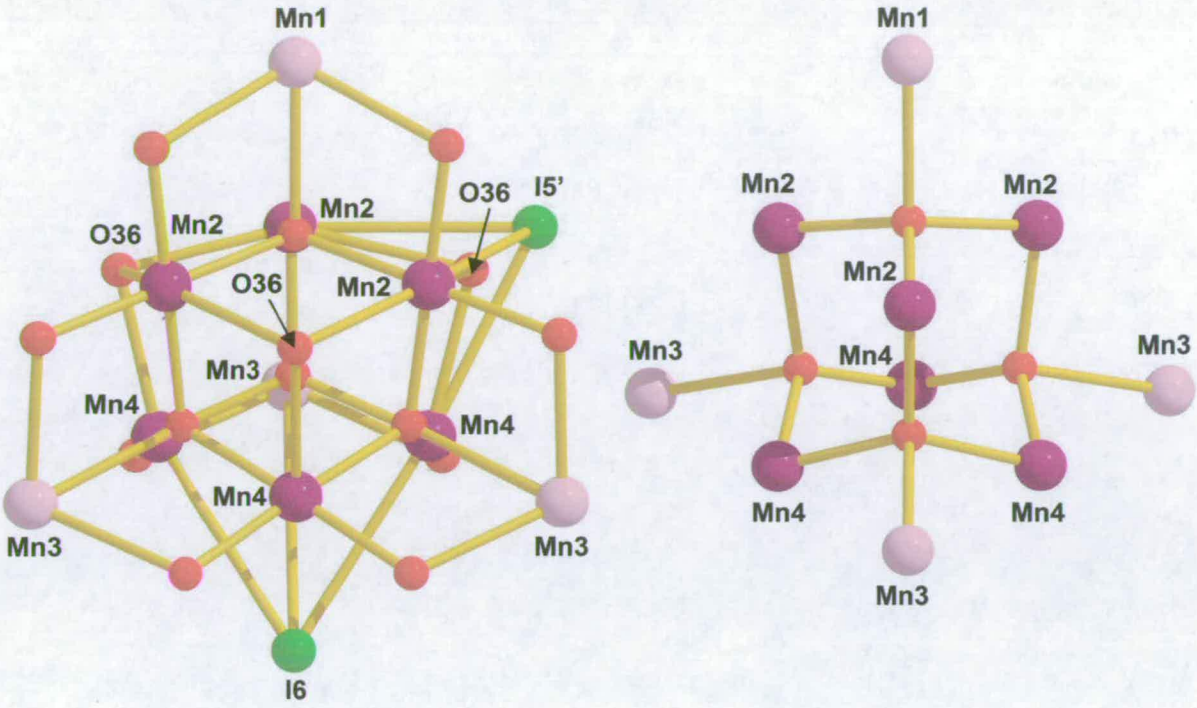

Figure 4.7. The Mn-O-I core of **12** (left) and the central metal-oxide core (right). Colour scheme: Mn(III): purple; Mn(II): pink; O: red; I: green.

(Figures **4.3**) of **12** are analogous to complex **11**, but here the capping halides are disordered with hydroxide ions in a 2.2:1.8 ratio. The presence of a fifth halide counter ion leads to an overall formulation of $[Mn_{10}O_4(OH)_{1.8}I_{2.2}(amp)_6(ampH_2)_4]I_5$. Again the halide counter ions lie in between neighboring clusters in the crystal, H-bonding to the pendant -NH_2 moieties creating $[Mn_{10}]_2$ dimers (Figure **4.8**). For both complexes (**11**, **12**) when viewed down the *c*-axis these dimers form aesthetically pleasing "hexagonal" columns (Figure **4.8**). The closest inter-molecular Mn···Mn distances are 9.37 Å and 9.77 Å for **11** and **12**, respectively.

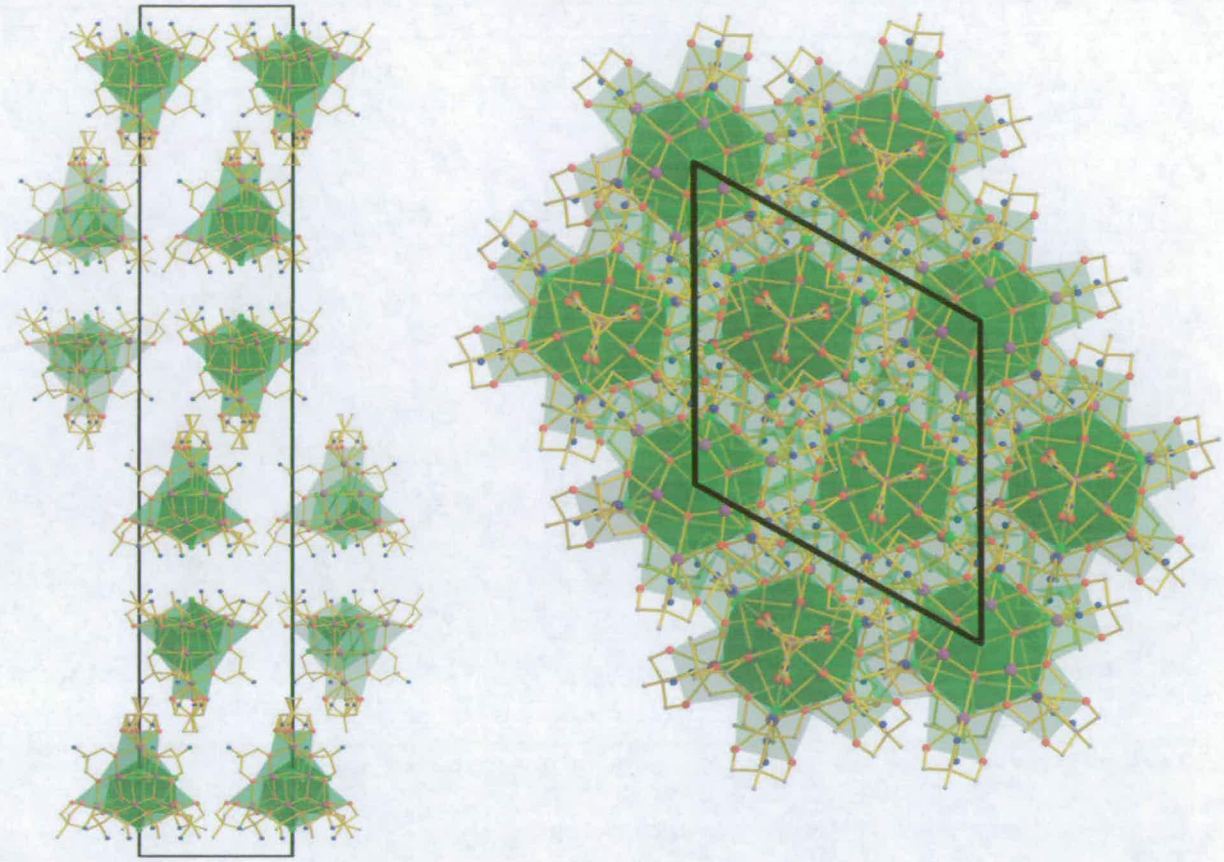

Figure 4.8. The packing of the molecules of **12** in the crystal viewed down the *c* (right) and *b* (left) axes.

$[Mn^{III}_6Mn^{II}_4(OH)_6(amp)_4(ampH)_4I_4(EtOH)_4]I_4$ (13) crystallizes in the monoclinic space group $P2_1/n$ (Figure **4.9**; selected bond lengths and angles are given in Tables A.4.7-8). The Mn-O core of **13** describes a planar disc of ten Mn ions linked by six central μ_3-OH^- ions and forms a central $[Mn^{III}_6Mn_4{}^{II}(OH)_6]^{20+}$ core (Figure **4.10**). The metallic skeleton thus comprises ten edge-sharing triangles which form '2-D planar-disc' (Figure **4.11**). The tripodal ligands bridge in three distinct ways. The four central ligands are doubly deprotonated (amp^{2-}) and bridge in two ways: two in a $\eta^3{:}\eta^3{:}\eta^1{:}\mu_5$-fashion, and two in a $\eta^2{:}\eta^2{:}\mu_3$-fashion. The four peripheral ligands are singly deprotonated ($ampH^-$) each bridging in a $\eta^2{:}\eta^1{:}\mu$-fashion (Figure **4.4**).

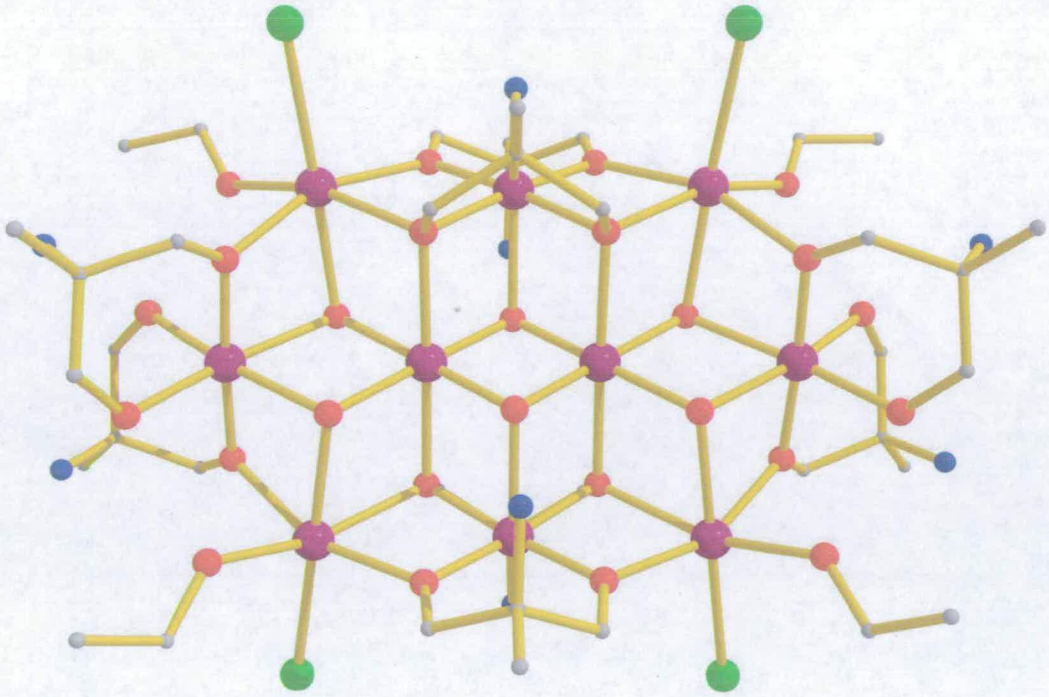

Figure 4.9. The structure of **13** in the crystal. Colour scheme: Mn: purple; O: red; N: blue; C: grey; I: green.

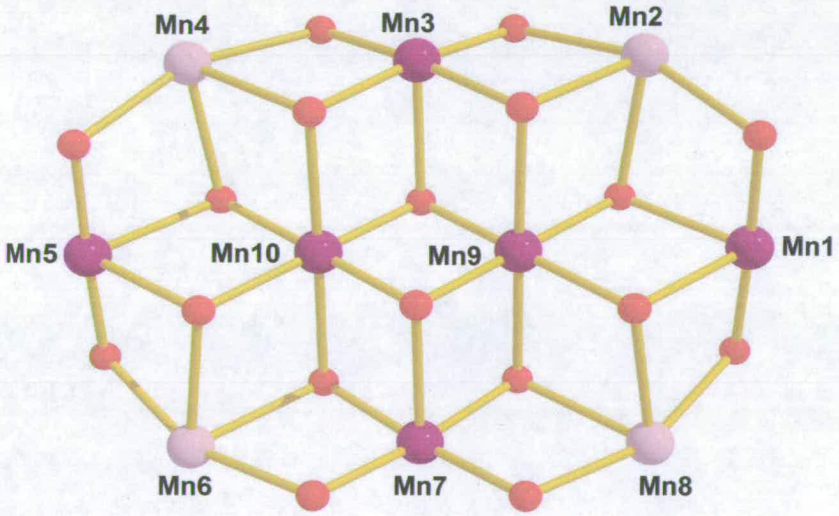

Figure 4.10. The Mn-O core of **13** in the crystal. Colour scheme: Mn(III): purple; Mn(II): pink; O: red.

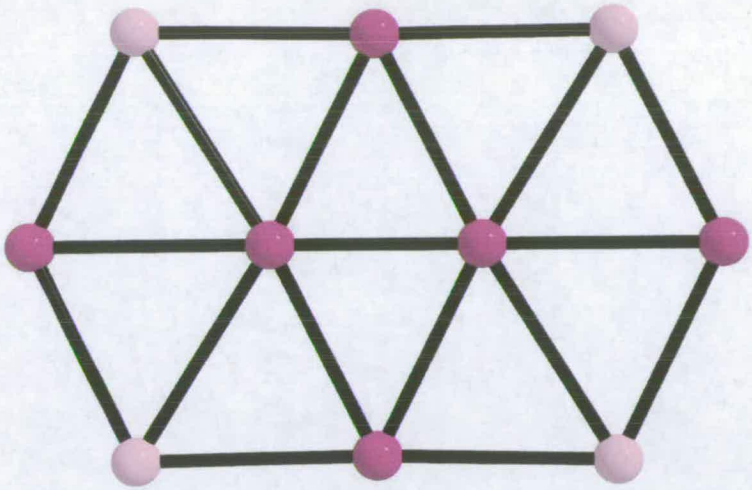

Figure 4.11. The metallic skeleton of **13** and **14** in the crystal. Colour scheme: Mn(III): purple; Mn(II): pink.

Four terminally bound I^- ions and four EtOH molecules fill the vacant coordination sites on the Mn^{II} ions. The Mn^{3+} ions are six-coordinate and in distorted octahedral geometries, but unusually, show two distinct geometries: Mn3, Mn7, Mn9 and Mn10 display the usual axial elongation, but Mn1 and Mn5 are axially compressed. There are a significant number of intra- and inter-molecular H-bonds and short contacts. On the periphery of the cation the $ampH^-$ molecules are H-bonded to the terminal EtOH molecules (O…O, ~2.6 Å) and the NH_2-arm of another $ampH^-$ ligand bonded to the same Mn ion (N…O, ~2.8 Å); while the non-bonded NH_2-arms of the centrally located amp^{2-} ions are H-bonded to the μ_3-bridging OH^- ions (O…O, ~2.7 Å) and the I^- counter ions (O…I, ~3.5-3.8 Å). The latter interaction is propagated in all three directions in the crystal directing the packing of the cations into sheets and chains (Figure **4.12**). The closest intermolecular Mn···Mn distance in the same sheet is 7.25 Å and between adjacent sheets is 9.65 Å. In Figure **4.13**, the outer molecules of the unit cell take of opposite directions from the inner molecules.

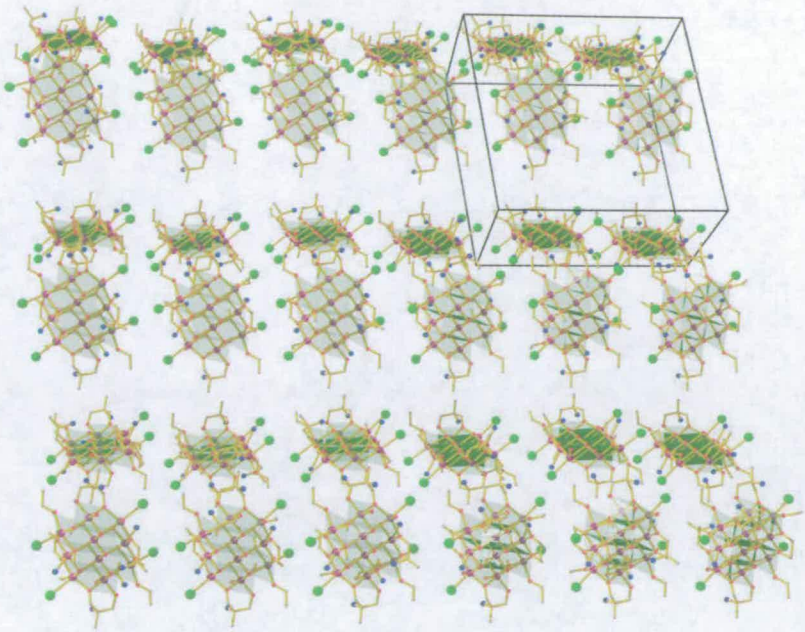

Figure 4.12. The packing of the molecules of **13** in the crystal viewed down the *b* axis.

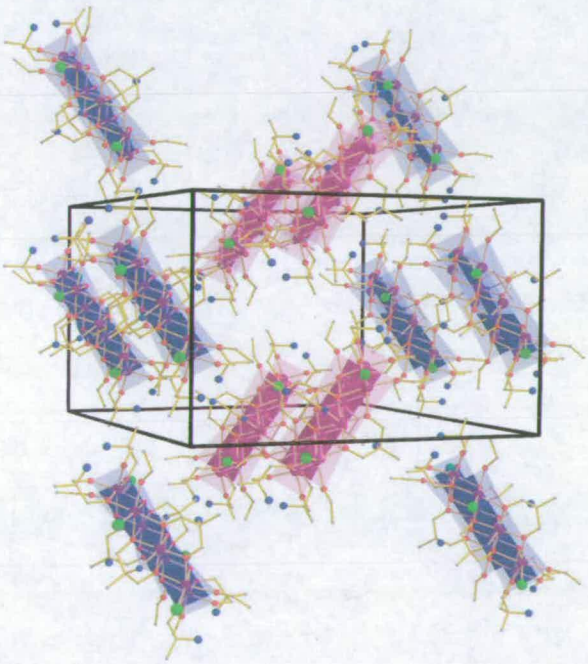

Figure 4.13. The packing of the molecules of **13** in the crystal.

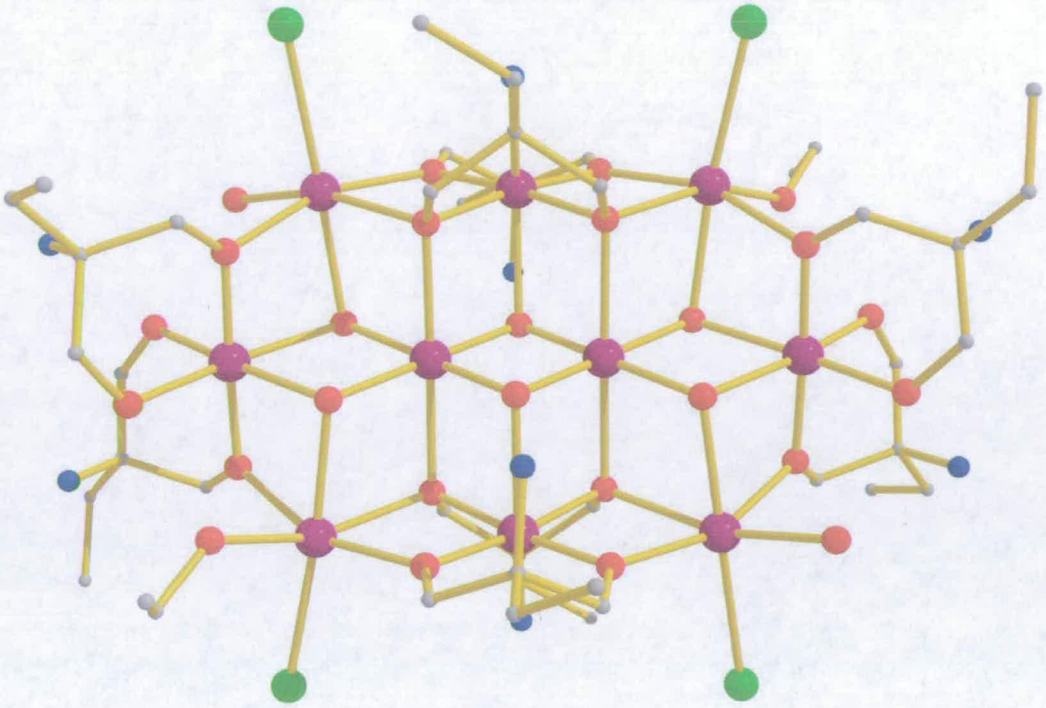

Figure 4.14. The structure of **14** in the crystal. Colour scheme: Mn: purple; O: red; N: blue; C: grey; I: green.

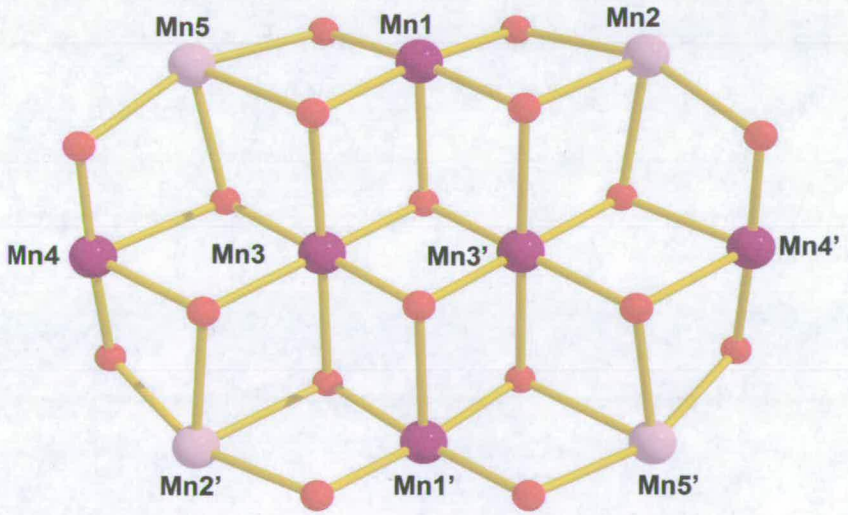

Figure 4.15. The Mn-O core of **14** in the crystal. Colour scheme: Mn(III): purple; Mn(II): pink; O: red.

$[Mn^{III}_6Mn^{II}_4(OH)_6(aep)_4(aepH)_4I_4(EtOH)_4]I_4$ (**14**) has a structure analogous to **13** but crystallizes in the orthorhombic space group *Pbcn* (Figure **4.14**; selected bond lengths and angles are given in Tables A.4.9-10). The Mn-O core, thus the metallic skeleton of **14** are analogous to **13** (Figures **4.15** and **4.11**, respectively). There are numerous intra- and inter-molecular H-bonds and short contacts propagated in all three directions in the crystal directing the packing of the cations (Figure **4.16**). When viewed down the *c* axis, the molecules, each perpendicular to its nearest neighbor, form cross- or X-shaped columns (Figure **4.17**). The closest intermolecular Mn···Mn distance within the same sheet is 10.29 Å and between adjacent sheets is 10.35 Å.

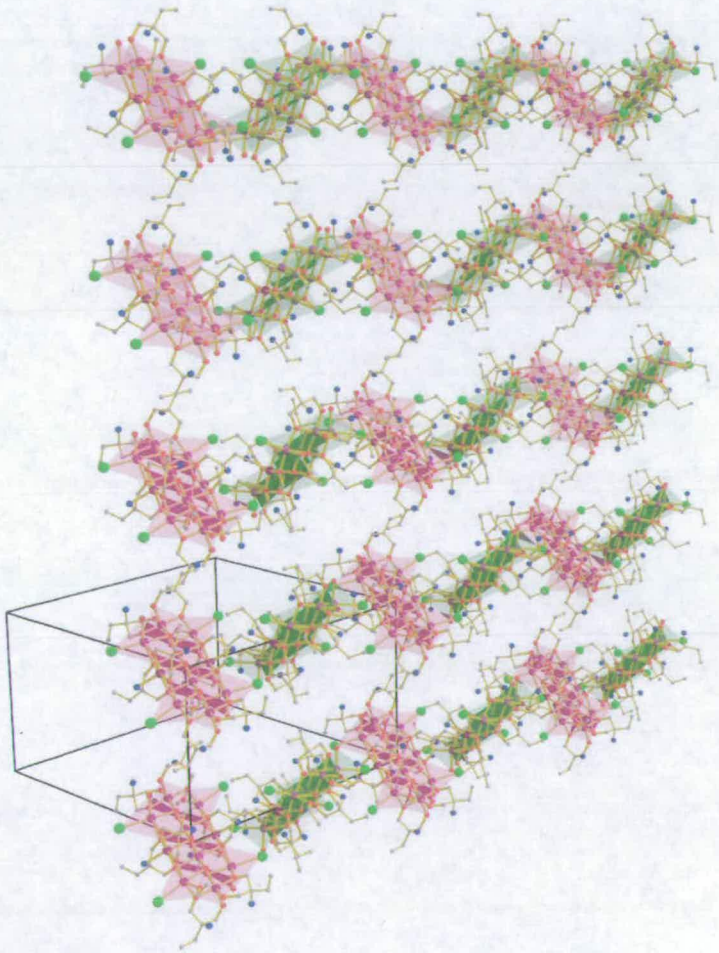

Figure 4.16. The packing of molecules of **14** in the crystal highlighting the rows of the molecules. The change of the colour in each molecule shows the change of their direction.

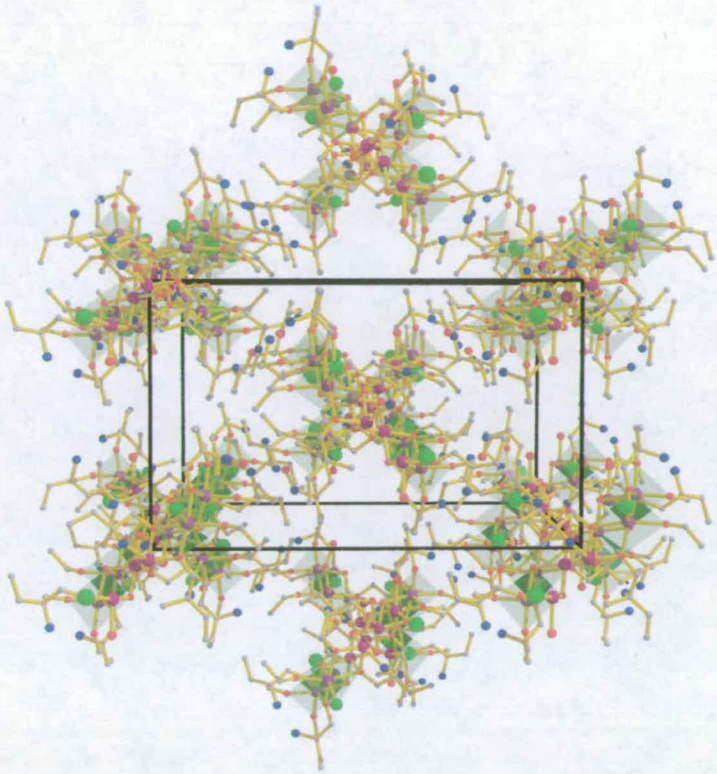

Figure 4.17. The packing of the molecules of **14** in the crystal viewed down the *c* axis.

$[Mn^{III}_6Mn^{II}_8(OH)_2(Hpeol)_4(H_2peol)_6I_4(EtOH)_6]I_4$ (15) crystallizes in the monoclinic space group $P2_1/n$ (Figure **4.18**; selected bond lengths and angles are given in Tables A.4.11-12). The Mn-O core describes a planar 'rectangular' disc of fourteen Mn ions linked together by a combination of hydroxide and alkoxide ions to form a metallic skeleton of fourteen edge-sharing triangles (Figure **4.19-20**). The two central OH^- ions (O58) each bridge in a μ_3-fashion, while the tripodal ligands adopt three distinct coordination modes (Figure **4.4**). Four are triply deprotonated ($Hpeol^{3-}$) and sit above and below the Mn_{14} plane bridging in a $\eta^3:\eta^3:\eta^3:\mu_6$-fashion. Six are doubly deprotonated (H_2peol^{2-}) and can be divided into two categories: four bridge across the long edges of the rectangle in a $\eta^2:\eta^2:\eta^1:\mu_3$-fashion, and two bridge across the short edges of the rectangle in a $\eta^2:\eta^2:\eta^1:\eta^1:\mu_3$-fashion. This is the first time the later coordination mode has been seen. The central metal-oxygen core is thus

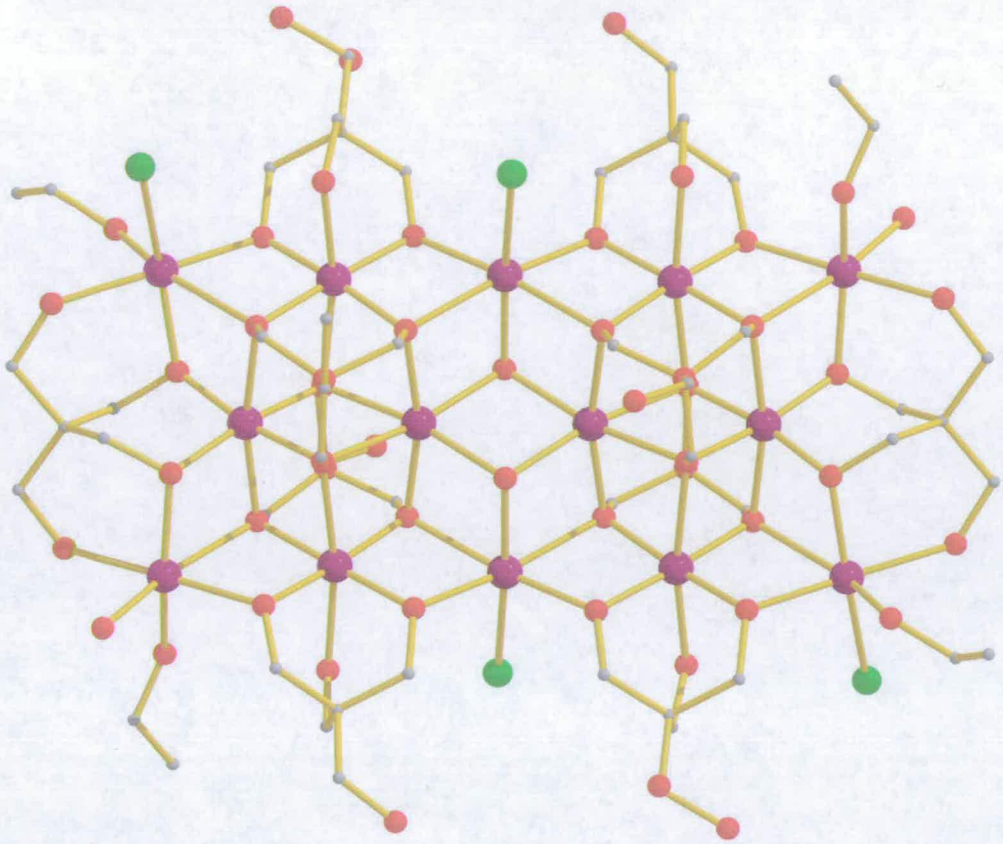

Figure 4.18. The structure of **15** in the crystal. Colour scheme: Mn: purple; O: red; N: blue; C: grey; I: green.

$[Mn^{III}_6Mn^{II}_8(OH)_2(OR)_{24}]^{8+}$. The Mn ions are six-coordinate and in distorted octahedral geometries with the Mn^{3+} ions displaying the usual Jahn-Teller elongations; each of which lie "parallel" to the short edges of the rectangle. Four terminally bound I^- ions and six EtOH molecules fill the vacant coordination sites on the Mn^{2+} ions. There are a significant number of intra- and intermolecular H-bonds: the terminal I^- ions are H-bonded to the terminally bonded O-arms of H_2peol^{2-} ligands (I…O, ~3.4 Å); the unbonded arms of the same ligands and the $Hpeol^{3-}$ ligands are H-bonded to the I^- counter ions (O…I, ~3.3 Å), and the O-H arms of H_2peol^{2-} ligands and terminal EtOH molecules on neighbouring molecules (O…O, ~2.6-2.8 Å). The result is an extensive, complicated H-bonded network of $[Mn_{14}]^{4+}$

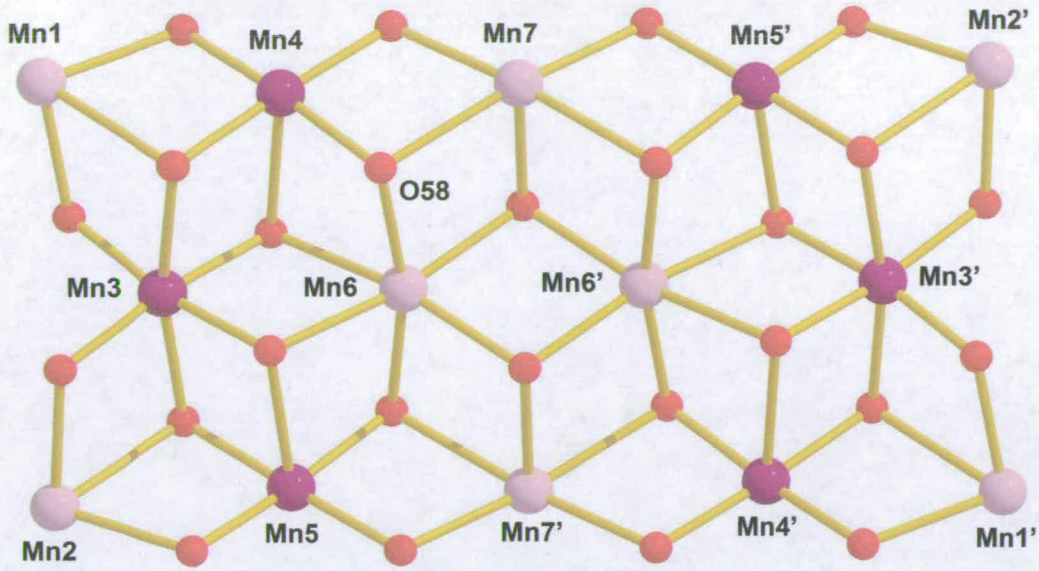

Figure 4.19. The Mn-O core of **15** in the crystal. Colour scheme: Mn(III): purple; Mn(II): pink; O: red.

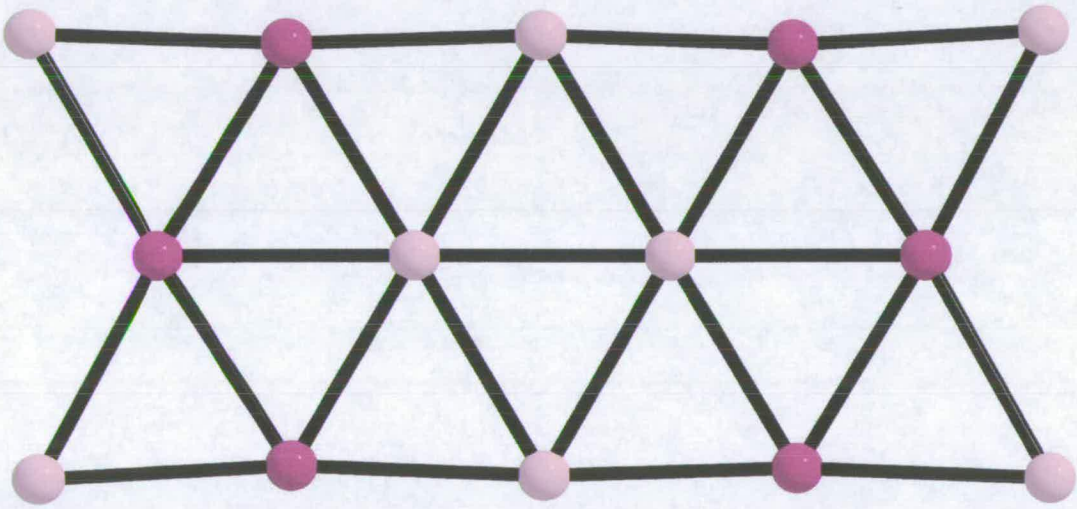

Figure 4.20. The metallic skeleton of **15** in the crystal. Colour scheme: Mn(III): purple; Mn(II): pink.

cations throughout the crystal. The molecules of **15** pack in the common observed brickwall pattern (Figure **4.21**).

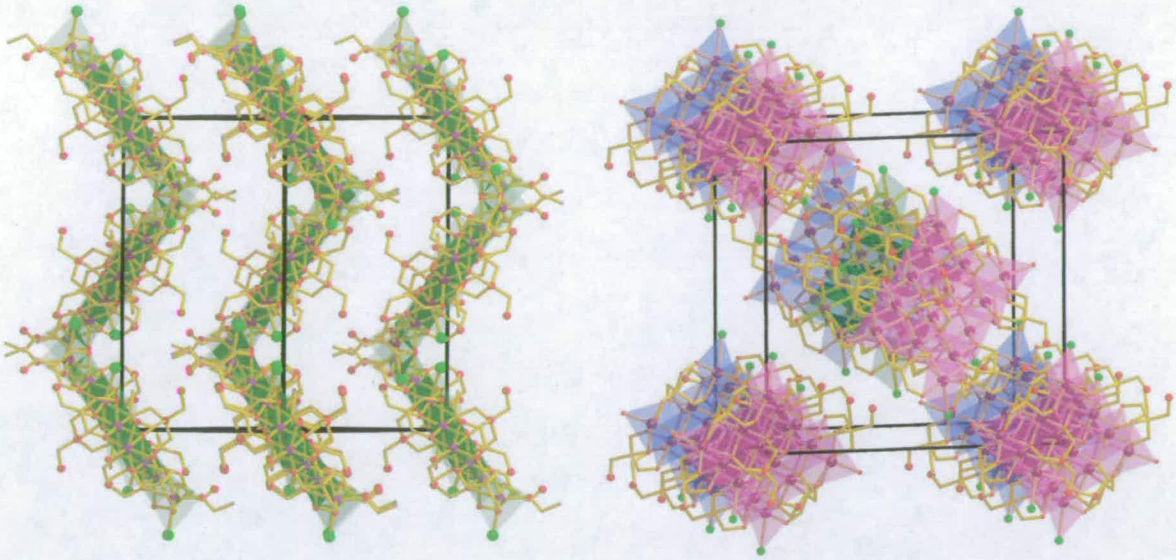

Figure 4.21. The packing of the molecules of **15** in the crystal along the *b* axis (left) and in viewed down the *a* axis (right).

Table 4.1. Ranges of selected interatomic distances (Å) and angles (deg) for **11-15**:

Ranges of selected interatomic distances (Å):

Complexes	Mn^{3+} - O^{2-}	Mn^{2+} - O^{2-}	Mn^{3+} - OH^-	Mn^{2+} - OH^-	Mn^{3+} - halide$^-$	Mn^{2+} - halide$^-$
Complex **11**	1.896-1.933	2.225-2.304	-	-	2.771-2.963	-
Complex **12**	1.901-1.922	2.260-2.277	-	-	2.962-3.228	-
Complex **13**	-	-	1.870-2.293	2.284-2.293	-	2.804-2.821
Complex **14**	-	-	1.862-2.325	2.280-2.290	-	2.775-2.832
Complex **15**	-	-	-	2.118-2.180	-	2.815-2.858

Ranges of selected interatomic angles (deg):

Complexes	Mn^{3+} - O^{2-} - Mn^{3+}	Mn^{3+} - O^{2-} - Mn^{2+}	Mn^{3+} - OH^- -Mn^{3+}	Mn^{3+} - OH^- -Mn^{2+}	Mn^{2+} - OH^- -Mn^{2+}	Mn^{3+} - halide$^-$-Mn^{3+}
Complex **11**	112.86-121.78	100.54-103.07	-	-	-	68.26-69.44
Complex **12**	111.13-123.33	101.21-103.04	-	-	-	62.93-64.17
Complex **13**	-	-	95.75-102.51	93.34-105.72	-	-
Complex **14**	-	-	95.76-102.31	92.36-105.59	-	-
Complex **15**	-	-	-	-	98.66-100.65	-

Table 4.2. Bond Valence Sum calculations for **11-15**.

Complex **11**

Atom	Mn^{2+}	Mn^{3+}	Mn^{4+}	Ox.	Atom	Mn^{2+}	Mn^{3+}	Mn^{4+}	Ox.
Mn1	1.88	1.75	1.71	2+	Mn3	3.09	2.85	2.80	3+
Mn2	2.02	1.88	1.84	2+	Mn4	3.14	2.90	2.84	3+

Complex **12**

Atom	Mn^{2+}	Mn^{3+}	Mn^{4+}	Ox.	Atom	Mn^{2+}	Mn^{3+}	Mn^{4+}	Ox.
Mn1	2.05	1.91	1.87	2+	Mn3	2.00	1.86	1.83	2+
Mn2	3.09	2.85	2.80	3+	Mn4	2.98	2.75	2.70	3+

Complex **13**

Atom	Mn^{2+}	Mn^{3+}	Mn^{4+}	Ox.	Atom	Mn^{2+}	Mn^{3+}	Mn^{4+}	Ox.
Mn1	3.46	3.19	3.13	3+	Mn6	1.76	1.62	1.59	2+
Mn2	1.78	1.64	1.61	2+	Mn7	3.46	3.20	3.14	3+
Mn3	3.45	3.19	3.13	3+	Mn8	1.80	1.66	1.62	2+
Mn4	1.79	1.65	1.62	2+	Mn9	3.33	3.07	3.01	3+
Mn5	3.45	3.18	3.12	3+	Mn10	3.33	3.07	3.01	3+

Complex **14**

Atom	Mn^{2+}	Mn^{3+}	Mn^{4+}	Ox.	Atom	Mn^{2+}	Mn^{3+}	Mn^{4+}	Ox.
Mn1	3.41	3.16	3.10	3+	Mn4	3.49	3.22	3.16	3+
Mn2	1.81	1.67	1.63	2+	Mn5	1.77	1.63	1.60	2+
Mn3	3.38	3.12	3.06	3+					

Complex **15**

Atom	Mn^{2+}	Mn^{3+}	Mn^{4+}	Ox.	Atom	Mn^{2+}	Mn^{3+}	Mn^{4+}	Ox.
Mn1	1.72	1.58	1.55	2+	Mn5	3.41	3.15	3.09	3+
Mn2	2.14	1.97	1.94	2+	Mn6	2.18	2.02	1.98	2+
Mn3	3.48	3.20	3.14	3+	Mn7	1.71	1.58	1.55	2+
Mn4	3.34	3.08	3.02	3+					

Magnetic Studies

➢ Dc Magnetic Studies

Magnetic susceptibility studies were carried out on powdered microcrystalline samples of **11-15** in the 0.3 – 300 K temperature range and for several applied fields. The field-dependencies of **11** and **13** are essentially identical to that of **12** and **14**, respectively. Here we show the data for **11** and **13** only, in addition to **15** (Figure **4.22**). For **11**, the room temperature $\chi_M T$ value of approximately 48 cm^3 K mol^{-1} increases upon cooling to a maximum value of ~ 224 cm^3 K mol^{-1} at 10 K before dropping to approximately 160 cm^3 K mol^{-1} at 1.8 K. The $\chi_M T$ value expected for an uncoupled $[Mn^{III}_6Mn^{II}_4]$ unit (g = 2.00) is approximately 36 cm^3 K mol^{-1}, less than the measured value at 300 K. For **13**, the room temperature $\chi_M T$ value of ~37 cm^3 K mol^{-1} gradually increases with decreasing temperature reaching a maximum value of ~ 79 cm^3 K mol^{-1} at ~ 14 K, before falling rapidly to a value of ~ 40 cm^3 K mol^{-1} at 2.0 K (Figure **4.22**). For both complexes, the behavior is suggestive of dominant ferromagnetic exchange between the metal centers, resulting in a spin ground state S = 22 for both **11** and **13** (and similarly for **12** and **14**). The dramatic difference in the low temperature maxima is assigned to a combination of intermolecular interactions and the weaker intramolecular exchange in the latter (vide infra). Ferromagnetic mixed-valent Mn clusters with nuclearity greater than four are exceptionally rare. For **15**, the room temperature $\chi_M T$ value of ~55.6 cm^3 K mol^{-1} collected for H = 1 kG is nearly constant down to ~ 150 K, below which it starts falling reaching a value of ~ 24.3 cm^3 K mol^{-1} at 2.0 K (Figure **4.22**). The expected (spin-only) value at 300 K is ~ 53 cm^3 K mol^{-1}. The linear extrapolation of the susceptibility collected for 2 K < T < 20 K down to zero-temperature yields S ≅ 7 ± 1.

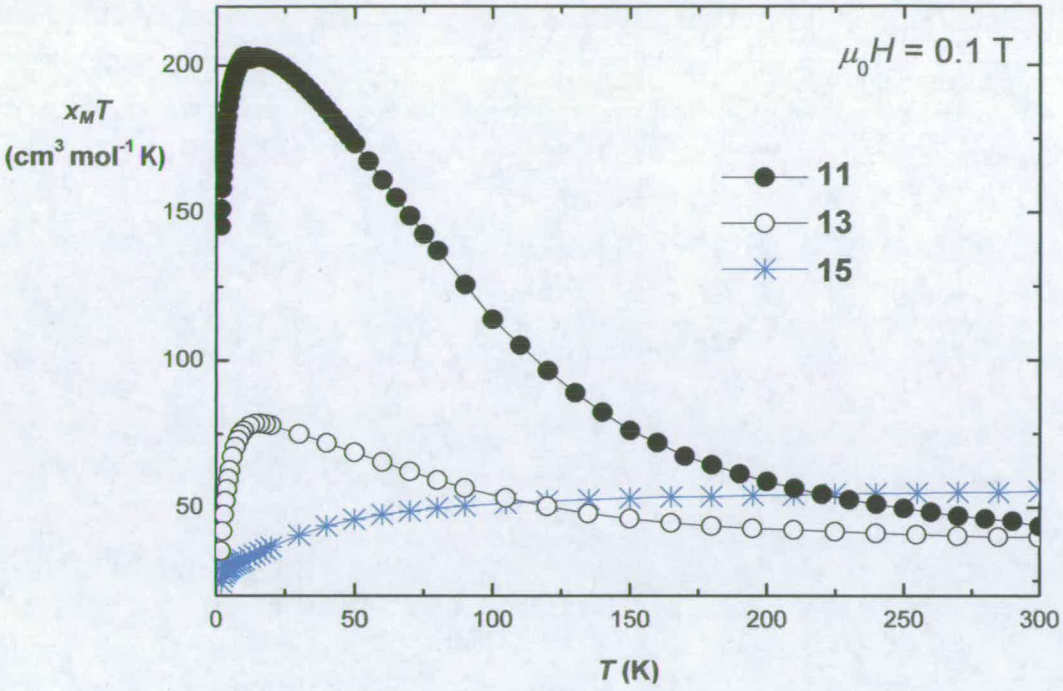

Figure 4.22. Plot of $\chi_M T$ vs T for complexes **11, 13** and **15** in a field of 0.1 T and in the 1.8 - 300 K temperature range. Solid lines are guides to the eyes.

In order to ascertain the spin ground states, magnetization data (M) were collected in the ranges (0 – 70) kG and (0.3 – 20) K - the results of which are plotted in Figure **4.23**. For **11-14** the tendency toward parallel alignment of the Mn spins is corroborated by the large magnetization exceeding 40 μ_B/f.u. at 7 T and below ~ 2 K. In particular for **11** and **12**, the fit of M by a matrix-diagonalization method affords the parameters $S = 22$, $g = 2.0$ and $D = 0$ cm^{-1} (Figure **4.24**). Given the molecular symmetry (approximately T_d) of the complex, a value for the zero-field splitting of, or close to, zero is expected. Thus despite the large S value, complex **11** (and **12**) does not behave as a single-molecule magnet, as confirmed by the lack of an out-of-phase (χ''_M) signal in ac-susceptibility studies. The low-temperature in-phase $\chi'_M T$ vs. T data are superimposable on the dc-data. The negligible anisotropy suggests that the decrease in $\chi_M T$ below 10 K (Figure **4.22**) is likely assigned to weak intermolecular antiferromagnetic interactions, consistent with the 'dimeric' $[Mn_{10}]_2$ structure in the crystal. For **13** and **14**, the magnetization measurements cannot be described solely by Brillouin curves corrected for finite magnetic anisotropies (Figure **4.23**). The

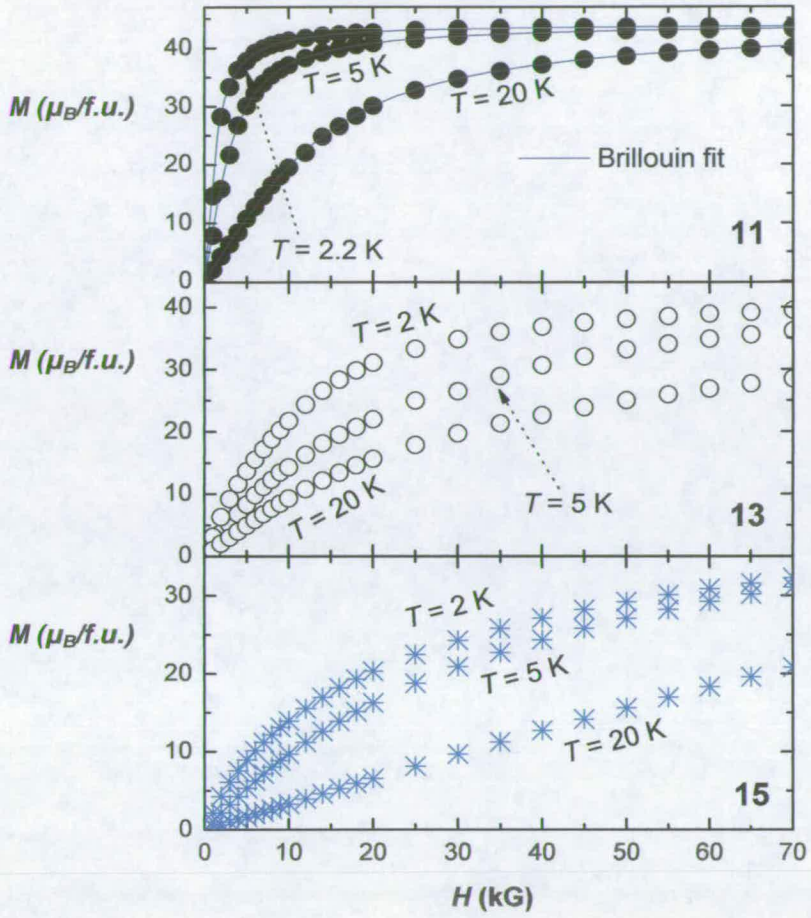

Figure 4.23. Magnetisation (M) vs. field (H) for **11**, **13** and **15** from top to bottom, respectively, in the indicated temperature and field ranges. For **11**, solid lines are the Brillouin fits.

same holds for **15**, whose magnetization achieves saturation values (i.e. 32 μ_B/f.u. for 2 K and 7 T) consistent with large field-stabilized spin states (Figure **4.23**). As we shall infer below from the specific heat experiments, the field-dependencies of **13** to **15** are complicated by the influence of (many) low-lying excited S states, whose occupancy strongly depends on the applied magnetic field.

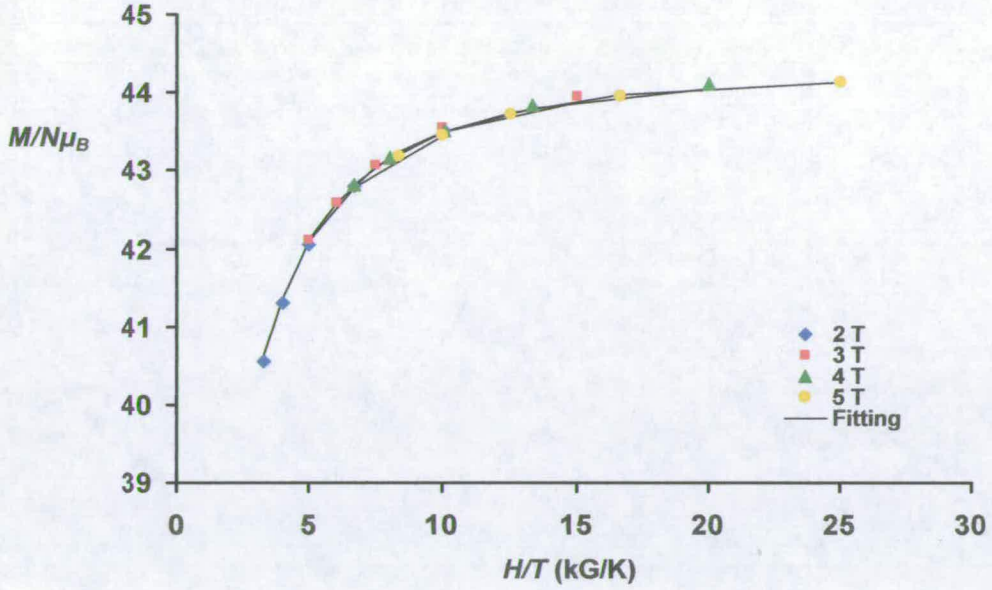

Figure 4.24. Reduce magnetization ($M/N\mu_B$) vs. field (H) for **11** in the ranges T= 1.8-6 K and H= 20-50 kG; the solid lines are a fit of the data with the parameters S= 22 and D= 0 cm^{-1}.

➢ ZFC/FC and Heat Capacity measurements

Experiments at temperatures below 2 K reveal different behaviors for the investigated complexes. The specific heat C of **11** shows a broad anomaly that shifts towards higher temperatures on increasing applied field (Figure **4.25**). At much higher temperatures, the lattice contribution dominates over the magnetic one and the experimental specific heat increases constantly with temperature. The magnetic contribution to $C(T,H)$ for $H \geq 10$ kG is due to Schottky-type Zeeman splitting of the otherwise degenerate (D = 0 cm^{-1}) energy spin states. The fit (solid lines in Figure **4.25**) of the experimental data to the calculated Schottky curves is excellent, and provides S = 22, g = 2 and D = 0 cm^{-1}, in agreement with the $M(H)$ data. Given that $[Mn_{10}]_2$ dimers are formed one would expect the appearance of an exchange field acting on each molecule that, similar to the external applied field, causes a Zeeman splitting of the molecular spin ground-state. This shows up in the experimental C

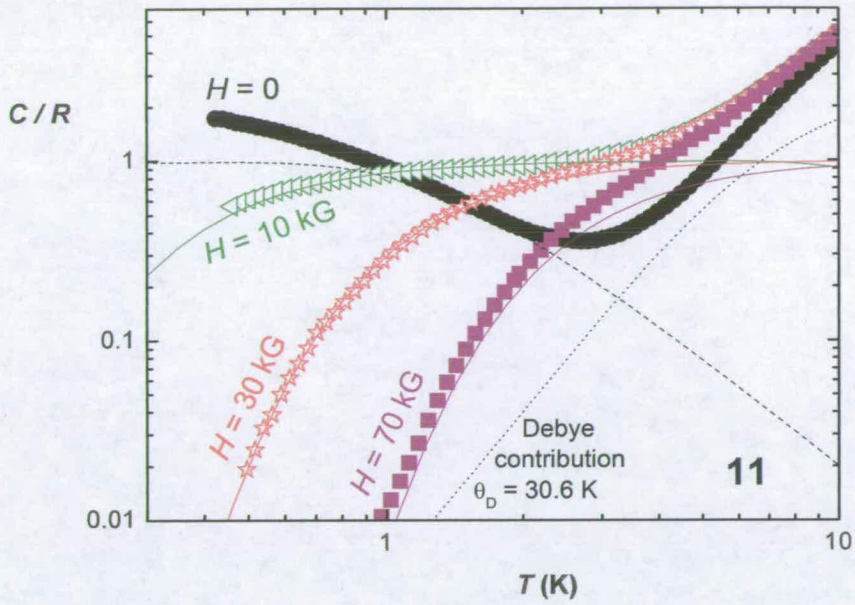

Figure 4.25. Specific heat (C) normalized to the gas constant (R) vs. temperature (T) for **11** at several applied fields. The solid and dashed lines are the fits to the Schottky contributions (see text); the dashed line is the Debye fit of the lattice contribution.

collected at zero applied-field that follows the Schottky behavior (dashed line, Figure **4.25**) calculated for $S = 22$, $g = 2$ and $D = 0$ cm^{-1}, and an exchange field $H_{ex} = 820$ G down to 1 K. For decreasing temperatures below 1 K, the intermolecular correlations become dominant overwhelming the single-molecule behavior, and the experimental C keeps increasing down to the minimum temperature accessible by our instrument. From the estimate of H_{ex} and given that $g\mu_B H_{ex} S = nJS^2$, we obtain the absolute value of $nJ \approx 5$ mK for the intermolecular exchange coupling.

For **13**, zero-field-cooled (ZFC) and field-cooled (FC) magnetic susceptibility measurements for $H = 1$ kG reveal a sharp feature at about 1.4 K as well as an additional peak at the much lower temperature of ~ 0.5 K, accompanied by magnetic irreversibility (Figure **4.26**). A peak in the susceptibility can be accounted for by: (*i*) a magnetic phase transition, or (*ii*) superparamagnetic blocking of the molecular spins. For a phase transition to occur however, one would expect the specific heat to detect a *sharp* anomaly at the ordering temperature [2]. No such critical feature is experimentally seen, rather *broad smooth* anomalies are seen at the corresponding temperatures in the specific heat (Figure **4.26**). Their presence is likely associated

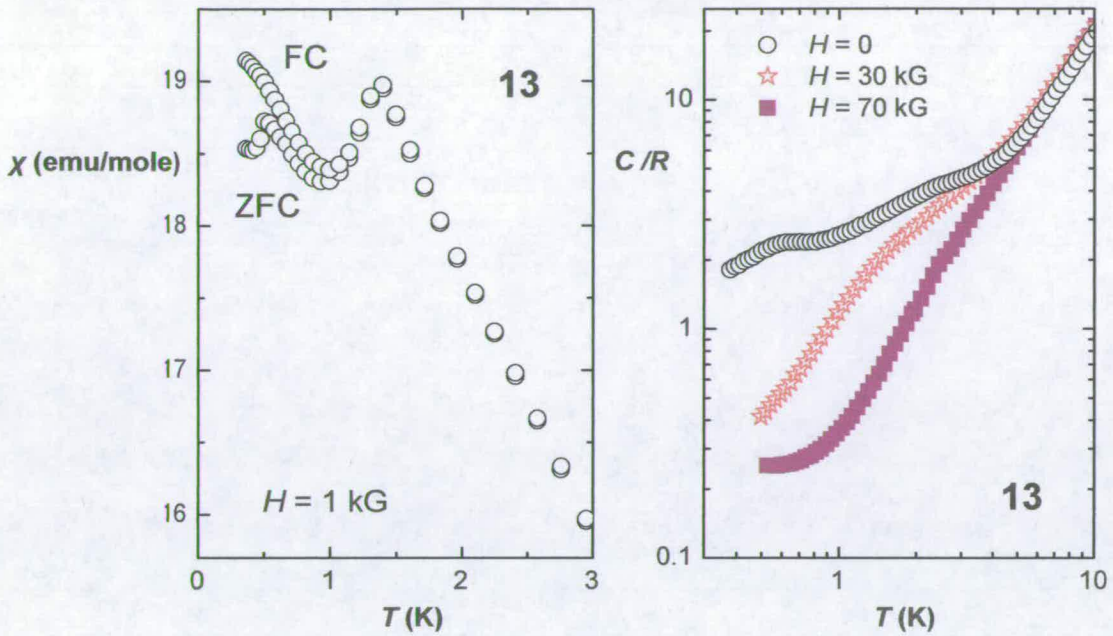

Figure 4.26. Left: dc susceptibility vs. T for **13** collected for $H = 1$ kG in the zero-field-cooled (ZFC) and field-cooled (FC) regimes. Right: specific heat normalized to the gas constant vs. T for **13** collected for $H = 0$, 30 and 70 kG, as labeled.

with different crystallographic forms of **13**. Four of the six Mn^{III} ions within the cluster core experience a Jahn-Teller (JT) elongation and two a JT compression. However only Mn9 and Mn10 reside "within" the core (Figure **4.10**), the others surrounding the periphery of the molecule and their JT elongations/compressions are likely sensitive to change/disorder. For **13**, this results in JT isomerism [8], i.e. two or more molecules differing in the relative orientation of one or more JT axes. Therefore, not all molecules are magnetically equivalent because of different spin states and/or anisotropies, yielding multiple superparamagnetic relaxation processes, thence multiple peaks in the susceptibility [9].

We performed similar FC and ZFC measurements at 1 kG for **15**, finding that magnetic irreversibility develops below ~ 1 K (Figure **4.27**). As for **13**, the specific heat rules out a phase transition as the possible reason for the susceptibility peak. Indeed, a broad bump is reported in the specific heat (Figure **4.27**) which is the Schottky-like anomaly normally encountered in superparamagnets. This shows up at zero-applied-field because the crystal-field splits the electronic levels, which are then

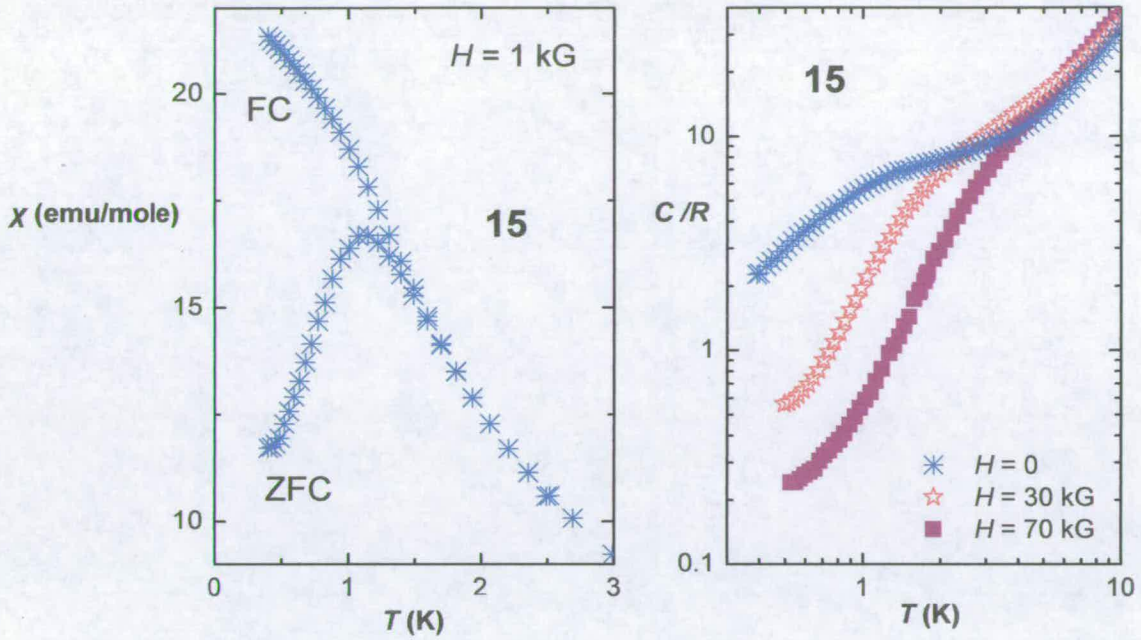

Figure 4.27. Left: dc susceptibility vs. T for **15** collected for $H = 1$ kG in the zero-field-cooled (ZFC) and field-cooled (FC) regimes. Right: specific heat normalized to the gas constant vs. T for **15** collected for $H = 0$, 30 and 70 kG.

further split by the applied-field causing the bump to move towards higher T for increasing field. We conclude that **15** behaves as a superparamagnet, and given that the blocking temperature T_B is typically 1/18 of the effective anisotropy barrier U [10], we finally obtain an estimate of $U \cong 18$ K for **15**. We refrain from estimating the molecular anisotropy because (anticipating the discussion below) the magnetic relaxation likely proceeds via excited spin states.

Contrary to the results for **11**, we note that for **13** and **15** (and hence **12** and **14**) no simple model of the magnetic contribution to the specific heat can be employed. It is straightforward to realize that the zero-field C of **13** and **15** is excessively large for temperatures below ~ 2 K, *i.e.* a temperature range in which the lattice contribution is negligible. Typical values should not exceed ~ $(1 - 2)$ R, as in **11**, provided that intermolecular interactions are absent [2]. The excess of magnetic specific heat in **13-15** must therefore arise from the presence of low-lying spin states other than the ground state. As we shall see in what follows, these accessible excited

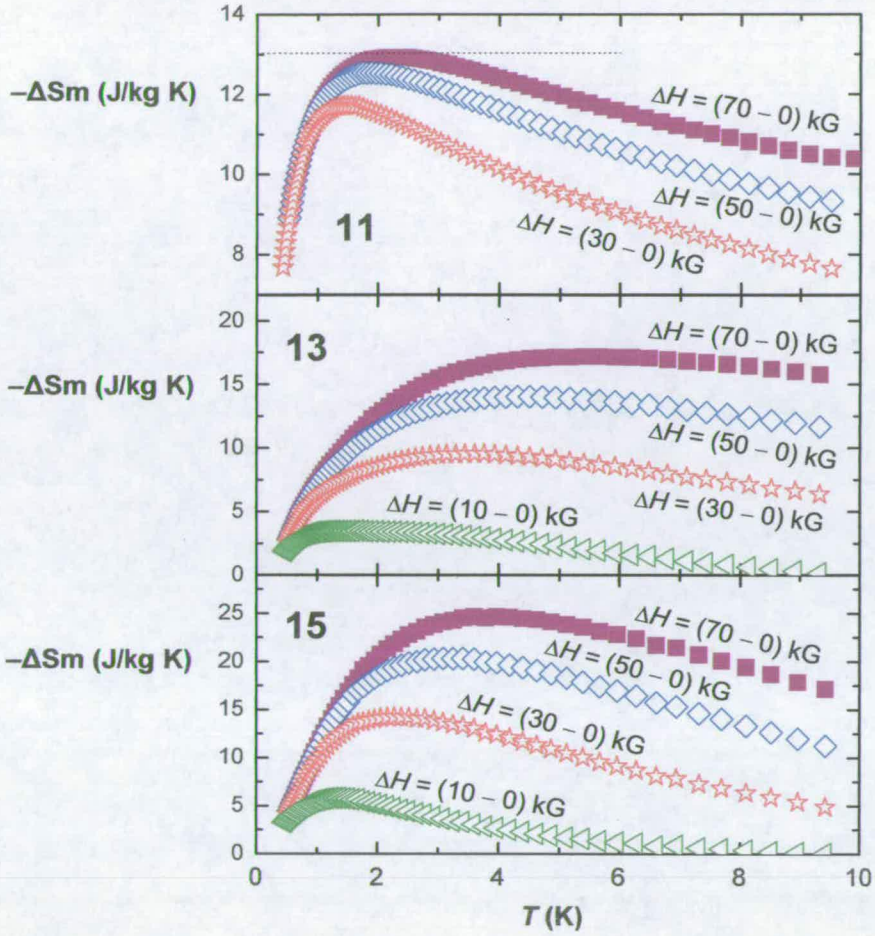

Figure 4.28. From top to bottom, magnetic entropy changes ($-\Delta S_m$) vs. T as obtained from the measurements of C in the indicated applied-field changes (ΔH) for **11**, **13** and **15**, respectively. Dotted line in the top panel is the limiting value of $R\ln(2S+1)$ for $S = 22$ (see text).

spin states have an *enormous* implications for the enhancement of the magnetocaloric effect (MCE).

The entropy of magnetic materials is intimately related with their capability of magnetic cooling through the MCE [2b], *i.e.* the change of the magnetic entropy ΔS_m upon a change in the applied magnetic field ΔH. The larger ΔS_m for a given ΔH, the better performance the investigated complex has in terms of refrigerant material. From the experimental specific heat C data of the investigated complexes (Figures **4.25-27**), we calculate $\Delta S_m(T,H) = \int[C(T,H_f)-C(T,H_i)]/T\ dT$ for selected field changes $\Delta H = H_f - H_i$. Note that the estimation of the lattice contribution to the specific heat

is irrelevant for our calculations, since we deal with differences between total entropies at different H. The so-obtained temperature-dependencies of ΔS_m for **11**, **13** and **15** are depicted in Figure **4.28** for several ΔH. As for **11**, it can be seen that $-\Delta S_m$ reaches a maximum value of 13.0 J kg^{-1} K^{-1} (or equivalently 3.8 R) at ~ 2.2 K for ΔH = (70 – 0) kG. This value corresponds to the full change of the total magnetic entropy R ln(2S+1) for a spin S = 22 (dotted line in the top panel of Figure **4.28**), and is one among the highest values ever reported for this temperature range [3]. Complexes **13-15** possess large field-stabilised spin states, as well as the presence of several excited spin states that are thermally accessible even at very low temperatures. This leads to an excess of magnetic entropy. Adding this extra contribution to the magnetic entropy effectively results in a MCE enhancement. For the maximum investigated ΔH = (70 – 0) kG we observe that $-\Delta S_m$ reaches the maximum value of 17.0 J kg^{-1} K^{-1} (equivalent to 5.4 R) at ~ 5.2 K for **13**, whereas **15** is even more impressive, achieving a remarkable value of 25 J kg^{-1} K^{-1} (equivalent to 10.2 R) at ~ 3.8 K. Both these values notably exceed the respective ones expected if ΔS_m were determined *just* by the spin ground-state, as in **11**. Let us assume, for instance, that **13** has a spin ground state S = 22. Without the degrees of freedom added from the other spin states, $-\Delta S_m$ cannot theoretically amount to more than R ln (2S+1) = 13.0 J kg^{-1} K^{-1} for this spin value - notably smaller than what is experimentally observed. We stress that the values reported in Figure **4.28** are exceptionally impressive: to our knowledge no other refrigerant material shows values as large as $-\Delta S_m$ = 25 J kg^{-1} K^{-1} for ΔH = (70 – 0) kG in the liquid-helium T-range [2,3].

Conclusions

In conclusion, our intial investigations into the coordination chemistry of ampH$_2$ and the closely related aepH$_2$ and H$_4$peol ligands have afforded beautiful and unusual mixed-valent decametallic Mn supertetrahedra and discs, and a

tetradecametallic disc. Complexes **11-13** are the first characterised Mn clusters (and an extremely rare examples of any transition metal cluster) containing the amp^{2-} ligand. Magnetic studies reveal complexes **11-14** to possess extremely large spin grounds state of $S = 22$ as a result of the dominant ferromagnetic exchange interactions between the metal centers; thus joining a select and illustrious band of molecules displaying this unusual combination. All five complexes show enormous magnetocaloric effect: **11-12** as a result of negligible zero-field splitting of the maximum possible ground state; **13-15** as a result of possessing a high spin-degeneracy at finite low temperatures. The investigation of novel molecular clusters with a high spin-degeneracy at finite low temperatures opens the way to important improvements in the MCE of molecular complexes, and this ultimately facilitates their use in magnetic cooling applications. To this end the complexes above are the very best cooling refrigerants for low-temperature applications. Furthermore they suggest a new synthetic strategy for obtaining novel molecules with even larger MCE: the introduction of ions (and ligands) that will promote weak ferro- or ferrimagnetic interactions leading to high spin ground states and easily accessible (low-lying), degenerate, excited states with large *S*-values.

References

[1] (a) D. Gatteschi and R. Sessoli, *Angew. Chem. Int. Ed.*, **2003**, *42*, 268. (b) D. Gatteschi, R. Sessoli, J. Villain, *Molecular Nanomagnets*, Oxford University Press, **2006**. (c) G. Aromí, E. K. Brechin, *Struct. Bonding* **2006**, *122*, 1.

[2] (a) M. Evangelisti, F. Luis, L.J. de Jongh, M. Affronte, *J. Mater. Chem.*, **2006**, *16*, 2534. (b) V.K Pecharsky, K.A. Gschneidner Jr., *J. Magn. Magn. Mater.*, **1999**, *200*, 44. (c) M. Affronte, A. Ghirri, S. Carretta, G. Amoretti, S. Piligkos, G. Timco, R.E.P. Winpenny, *Appl. Phys. Lett.*, **2004**, *84*, 3468.

[3] (a) M. Evangelisti, A. Candini, A. Ghirri, M. Affronte, E.K. Brechin, E.J.L. McInnes, *Appl. Phys. Lett.*, **2005**, *87*, 072504; (b) M. Evangelisti, A. Candini, A.

Ghirri, M. Affronte, S. Piligkos, E.K. Brechin, E.J.L. McInnes, *Polyhedron*, **2005**, *24*, 2573. (c) M. Manoli, R.D.L. Johnstone, S. Parsons, M. Murrie, M.Affronte, M. Evangelisti, E.K. Brechin, *Angew. Chem. Int. Ed.*, **2007**, 46, 4456.

[4] (a) M. Moragues-Canovás, C. E. Talbot-Eeckalaers, L. Catala, W. Wernsdorfer, E.K. Brechin, T. Mallah, *Inorg. Chem.*, **2006**, *45*, 7038. (b) M. I. Khan and J. Zubieta, *Prog. Inorg. Chem.*, **1995**, *43*, 1.

[5] Brechin, E.K. *Chem. Commun.*, **2005**, 5141.

[6] (a) S. Wang, H.-L. Tsai, E. Libby, K. Folting, W. E. Streib, D. N. Hendrickson, G. Christou, *Inorg. Chem.*, **1996**, *35*, 7578. (b) G. Aromí, M. J. Knapp, J.-P. Claude, J.C. Huffman, D.N. Hendrickson, G, Christou, *J. Am. Chem. Soc.*, **1999**, *121*, 5489. (c) D.P. Goldberg, A. Caneschi, C. D. Delfs, R. Sessoli, S.J. Lippard, *J. Am. Chem. Soc.*, **1995**, *117*, 5789.

[7] H. Thorp, *Inorg. Chem.*, **1992**, *31*, 1585.

[8] S. Sun, D. Ruiz, N.R. Dilley, M. Soler, J. Ribas, I.A. Guzei, A.L. Rheingold, K. Folting, M.B. Maple, G. Christou, D.N. Hendrickson, *Chem. Commun.*, **1999**, 1973.

[9] S.M.J. Aubin, Z. Sun, H. Eppley, E.M. Rumberger, I.A. Guzei, K. Folting, P.K. Gantzel, A.L. Rheingold, G. Christou, D.N. Hendrickson, *Inorg. Chem.*, **2001**, *40*, 2127.

[10] M. Evangelisti, A. Candini, A. Ghirri, M. Affronte, G.W. Powell, I. Gass, P.A. Wood, S. Parsons, E.K. Brechin, D. Collison, S.L. Heath, *Phys. Rev. Lett.*, **2006**, *97*, 167202.

Chapter 5
Magnetic Studies of Hexa-, Deca- and Dodeca-nuclear Manganese Complexes Based on Octahedra and Edge-Sharing Bioctahedra

Introduction

Chemists have developed a wide range of synthetic strategies and methods to both access new cluster families and to manipulate (and enhance the properties of) existing ones [1]. Among such methods have been the reaction of triangular $[Mn_3O(O_2CR)_6(py)_3]^+$ (R = Me, Et, Ph, $C(CH_3)_3$, etc; py = pyridine) complexes with chelating ligands such as 2,2′-bipyridine (bpy), 2-hydroxymethylpyridine (Hhmp), and various others, which causes a structural rearrangement to a higher nuclearity product [1]. Another strategy developed recently is 'reductive aggregation' in which a high oxidation state Mn source is dissolved in alcohol (e.g. MeOH) in the presence of potential bridging ligands, forcing a reduction of the manganese ions and a resulting structural aggregation to a polynuclear product, with the added possibility of the alcohol providing additional alkoxide (e.g. MeO^-) bridging ligands [2].

In this chapter these strategies have been combined by carrying out reactions in an alcohol-containing medium using tripodal alcohol chelating ligands, which have previously shown to be excellent building blocks for the synthesis of SMMs [3]. The eleven complexes we herein report can be divided into four categories that are based on Mn octahedra and edge-sharing bioctahedra and vary from single molecules (0D) to 1-D and 2-D polymers. These are: $Na_4[Mn_6O(OAc)_6(Br\text{-}mp)_4(MeOH)_4]$ (**16**), $Na_3[Mn_6O(OAc)_5(tmp)_4(N_3)(H_2O)_2]$ (**17**); $[Mn_{10}O_2Br_4(thme)_6(MeOH)_4]$ (**18**), $[Mn_{12}O_2(piv)_{10}(tmp)_4(MeO)_2(MeOH)_2]$ (**19**), $[Mn_{12}O_2(piv)_{10}(thme)_4(MeO)_2(MeOH)_2]$ (**20**), $[Mn_{12}O_2(OAc)_{10}(Hpeol)_4(MeO)_2(H_2O)_4]$ (**21**),

$[Mn_{12}O_2(OAc)_{10}(thme)_4(MeO)_2(H_2O)_4]$ (**22**), $[Mn_{12}O_2(OAc)_{10}(tmp)_4(MeO)_2(H_2O)_4]$ (**23**), $[Mn_{12}O_2(O_2CCPh_2)_{10}(Hpeol)_4(MeO)_2(H_2O)_2]$ (**24**), $[Mn_{12}O_2(O_2CCPh_2)_{10}(Hpeol)_4(OH)_2(H_2O)_2]$ (**25**); and $Na[Mn_{12}O_2(OAc)_{11}(Hpeol)_4(MeO)(OH)(H_2O)_3]$ (**26**).

Experimental Section

All manipulations were performed under aerobic conditions, using materials as received. $[Mn_3O(OAc)_6(py)_3]\cdot py$, $[Mn_3O(piv)_6(py)_3]\cdot py$, $[Mn_3O(O_2CPh_2)_6(py)_3]\cdot(ClO_4)$ and were prepared as previously described [4] .

➢ Synthetic Procedures

$Na_4[Mn_6O(OAc)_6(Br\text{-}mp)_4(MeOH)_4]\cdot MeOH$ (**16**·MeOH). $Mn(OAc)_2\cdot 4H_2O$ (0.500 g, 2.04 mmol), Br-mpH_3 (0.406 g, 2.04 mmol) and NaOH (0.110 g, 2.04 mmol) were stirred in MeOH (25 ml) for 3 hours. The black solution was then filtered and layered with Et_2O. Crystals of **16** formed in 10 days in a yield of approximately 20%. Anal. Calcd (found) for **16**, $C_{36}H_{66}Mn_6Na_4Br_4O_{29}$: C, 25.37 (25.18); H, 3.90 (3.67).

$Na_3[Mn_6O(OAc)_5(tmp)_4(N_3)(H_2O)_2]\cdot CH_3CN$ (**17**·CH_3CN). $Mn(OAc)_2\cdot 4H_2O$ (0.500 g, 2.04 mmol), H_3tmp (0.274 g, 2.04 mmol) and NaN_3 (0.133 g, 2.04 mmol) in CH_3CN (25 ml) were left stirring overnight. The pale yellow-brown solution was then filtered and layered with two volumes of n-hex/Et_2O (1/1). Crystals of **17** formed in two weeks in a yield of approximately 15 %. Anal. Calcd for **17**, $C_{34}H_{63}Mn_6Na_3N_3O_{25}$: C, 31.11 (31.00); H, 4.84 (4.71); N, 3.20 (3.33).

$[Mn_{10}O_2(thme)_6Br_4(MeOH)_4]\cdot 4MeOH$ (18·4MeOH). $MnBr_2\cdot 4H_2O$ (0.500 g, 1.74 mmol), H_3thme (0.209 g, 1.74 mmol) and NEt_3 (0.127 g, 1.74 mmol) were left stirring for two hours in MeOH (25 ml). The dark brown solution was then filtered and left to evaporate open in the atmosphere. Crystals of **18** formed in five days in a

yield of approximately 30 %. Anal. Calcd (found) for **18**, $C_{34}H_{70}Mn_{10}Br_4O_{24}$: C, 23.58 (23.42); H, 4.07 (4.04).

$[Mn_{12}O_2(piv)_{10}(tmp)_4(MeO)_2(MeOH)_2]$ (19). $[Mn_3O(piv)_6(py)_3]\cdot py$ (0.500 g, 0.45 mmol) and H_3tmp (0.061 g, 0.45 mmol) were left stirring in MeOH (25 ml) for 45 minutes. The pale brown solution was then filtered and layered with Et_2O. Crystals of **19** formed during one month in a yield of approximately 20%. Anal. Calcd (found) for **19**, $C_{78}H_{148}Mn_{12}O_{38}$: C, 39.81 (39.56); H, 6.34 (6.25).

$[Mn_{12}O_2(piv)_{10}(thme)_4(MeO)_2(MeOH)_2]$ (20). $[Mn_3O(piv)_6(py)_3]\cdot py$ (0.500 g, 0.45 mmol) and H_3thme (0.054 g, 0.45 mmol) were left stirring in MeOH (25 ml) for 45 minutes. The pale brown solution was then filtered and layered with Et_2O. Crystals of **20** formed during one month in a yield of approximately 20%. Anal. Calcd (found) for **20**, $C_{74}H_{138}Mn_{12}O_{38}$: C, 38.73 (38.69); H, 6.06 (5.78).

$[Mn_{12}O_2(OAc)_{10}(Hpeol)_4(MeO)_2(H_2O)_2]\cdot MeOH$ (21·MeOH). $Mn(OAc)_2\cdot 4H_2O$ (0.980 g, 4.00 mmol), H_4peol (0.130 g, 1.00 mmol) and NEt_3 (0.400 g, 4.00 mmol) were left stirring in MeOH (25 ml) for two hours. The dark brown solution was then filtered and layered with Et_2O. Crystals of **21** formed during one month in a yield of approximately 35%. Anal. Calcd (found) for **21**, $C_{43}H_{84}Mn_{12}O_{45}$: C, 26.08 (25.95); H, 4.28 (4.14).

$[Mn_{12}O_2(OAc)_{10}(thme)_4(MeO)_2(H_2O)_2]\cdot 2MeOH$ (22·2MeOH). $Mn(OAc)_2\cdot 4H_2O$ (0.500 g, 2.04 mmol), H_3thme (0.245 g, 2.04 mmol) and NEt_3 (0.264 g, 2.04 mmol) were left stirring in MeOH (25 ml) for two hours. The dark brown solution was then filtered and layered with Et_2O. Crystals of **22** formed during one month in a yield of approximately 45%. Anal. Calcd (found) for **22**, $C_{42}H_{80}Mn_{12}O_{40}$: C, 26.77 (26.76); H, 4.28 (4.74).

$[Mn_{12}O_2(OAc)_{10}(tmp)_4(MeO)_2(H_2O)_2]\cdot 2MeOH$ (23·2MeOH). $Mn(OAc)_2\cdot 4H_2O$ (0.735 g, 3.00 mmol), H_3tmp (0.135 g, 1.00 mmol) and NEt_3 (0.430 g, 3.00 mmol) were left stirring in MeOH (25 ml) for two hours. The dark brown solution was then filtered and layered with Et_2O. Crystals of **23** formed during one month in a yield of approximately 35%. Anal. Calcd (found) for **23**, $C_{46}H_{86}Mn_{12}O_{38}$: C, 28.98 (28.92); H, 4.55 (4.36).

$[Mn_{12}O_2(O_2CPh_2)_{10}(Hpeol)_4(MeO)_2(H_2O)_2]\cdot 6CH_3CN$ (**24**·$6CH_3CN$). $[Mn_3O(O_2CPh_2)_6(py)_3]\cdot(ClO_4)$ (0.270 g, 0.25 mmol), H_4peol (0.034 g, 0.25 mmol) were left stirring in $MeOH/CH_3CN$ (30 ml) for two hours. The pale brown solution was then filtered and layered with Et_2O. Crystals of **24** formed during two weeks in a yield of approximately 60%. Anal. Calcd (found) for **24**·CH_3CN, $C_{166}H_{163}Mn_{12}NO_{42}$: C, 56.91 (56.21); H, 4.68 (4.56); N, 0.40 (0.31).

$[Mn_{12}O_2(O_2CPh_2)_{10}(Hpeol)_4(OH)_2(H_2O)_2]\cdot 12CH_3CN$ (**25**·$12CH_3CN$). $[Mn_3O(O_2CPh_2)_6(py)_3]\cdot(ClO_4)$ (0.270 g, 0.25 mmol), H_4peol (0.034 g, 0.25 mmol) were left stirring in CH_3CN (25 ml) for three hours. The pale brown solution was then filtered and layered with Et_2O. Crystals of **25** formed during three weeks in a yield of approximately 45%. Anal. Calcd (found) for **25**·$2CH_3CN\cdot 2H_2O$, $C_{162}H_{169}Mn_{12}NO_{44}$: C, 55.69 (55.50); H, 4.87 (4.57); N, 0.40 (0.38).

$Na[Mn_{12}O_2(OAc)_{11}(Hpeol)_4(MeO)(OH)(H_2O)_3]\cdot 4CH_3CN\cdot H_2O$ (**26**·$4CH_3CN\cdot H_2O$). $Mn(OAc)_2\cdot 4H_2O$ (0.180 g, 0.75 mmol), H_4peol (0.068 g, 0.50 mmol) and NaOH (0.100 g, 0.25 mmol) were left stirring in $MeOH/CH_3CN$ (30 ml) for two hours. The dark brown solution was then filtered and layered with Et_2O. Crystals of **26** formed during one month in a yield of approximately 45%. **26**·$11/2CH_3CN\cdot 10H_2O$, $C_{46}H_{103.5}Mn_{12}NaNO_{55}$: C, 24.66 (24.31); H, 4.66 (4.38); N, 0.93 (0.90).

Results and Discussion

➢ Synthesis

Reaction of the $Mn(OAc)_2\cdot 4H_2O$ and one equivalent of Br-mpH_3 in the presence of NaOMe in MeOH affords the mixed-valent 1D polymer $Na_4[Mn^{III}_4Mn^{II}_2O(OAc)_6(Br\text{-}mp)_4(MeOH)_4]$ (**16**). The sodium ions are incorporated into the structure linking the metal octahedra together. The reaction of $Mn(OAc)_2\cdot 4H_2O$ and one equivalent of H_3tmp in the presence of NaN_3 in MeCN

affords the mixed-valent 2D polymer $Na_3[Mn^{III}_5Mn^{II}O(OAc)_5(tmp)_4(N_3)(H_2O)_2]$ (**17**). Complex **17** contains an end-on azide ligand coordinated to one of the six Mn ions. The metallic skeletons of **16** and **17** are based on octahedra held together by a combination of AcO^- ligands and tripodal alkoxides. Reaction of $MnBr_2{\cdot}4H_2O$ and one equivalent of H_3thme in the presence of Et_3N in MeOH affords the mixed-valent $[Mn^{III}_6Mn^{II}_4O_2(thme)_6Br_4(MeOH)_4]$ (**18**) whose metallic skeleton consists of an edge-sharing bioctahedron.

Reaction of the metal triangle $[Mn_3O(piv)_6(py)_3]{\cdot}py$ and one equivalent of H_3tmp in MeOH affords the mixed-valent $[Mn^{III}_4Mn^{II}_8O_2(piv)_{10}(tmp)_4(MeO)_2(MeOH)_2]$ (**19**). If the reaction is repeated with H_3thme, the analogous complex $[Mn^{III}_4Mn^{II}_8O_2(piv)_{10}(thme)_4(MeO)_2(MeOH)_2]$ (**20**) forms. Reaction of $Mn(OAc)_2{\cdot}4H_2O$ with H_4peol and Et_3N in a ratio 4:1:4 affords the complex $[Mn^{III}_4Mn^{II}_8O_2(OAc)_{10}(Hpeol)_4(MeO)_2(H_2O)_4]$ (**21**). If the latter reaction is repeated with H_3thme and H_3tmp in rations 1:3:1, then the complexes $[Mn^{III}_4Mn^{II}_8O_2(OAc)_{10}(thme)_4(MeO)_2(H_2O)_4]$ (**22**) and $[Mn^{III}_4Mn^{II}_8O_2(OAc)_{10}(tmp)_4(MeO)_2(H_2O)_2]$ (**23**) form, respectively. Reaction of the metal triangle $[Mn_3O(O_2CPh_2)_6(py)_3](ClO_4)$ with one equivalent of H_4peol in MeOH/MeCN and MeCN, affords the complexes $[Mn^{III}_4Mn^{II}_8O_2(O_2CCPh_2)_{10}(Hpeol)_4(MeO)_2(H_2O)_2]$ (**24**) and $[Mn^{III}_4Mn^{II}_8O_2(O_2CCPh_2)_{10}(Hpeol)_4(OH)_2(H_2O)_2]$ (**25**), respectively. The remaining complex $Na[Mn_{12}O_2(OAc)_{11}(Hpeol)_4(MeO)(OH)(H_2O)_3]$ (**26**) was made by the reaction of the $Mn(OAc)_2{\cdot}4H_2O$ and H_4peol in the presence of NaOMe in MeOH/MeCN. Complexes **19-26** are all based on a central edge-sharing bioctahedral core $[Mn^{III}_4Mn^{II}_8(\mu_4\text{-}O)_2]$ with two peripheral Mn ions capping the two sides of bioctahedron. In contrast to complex **18**, complexes **19-26** also incorporate carboxylates. Additionally, complex **26** consists of sodium ions that link the bioctahedra together.

The Mn-oxgen core of complexes **19–26** resembles the structural motif found in early transition metal polyoxometalates and the octanuclear Ba clusters $[Ba_8O_2]^{12+}$, $[Sr_6Ba_2O_2]^{12+}$ and $[Ba_8Eu_2O_2]^{12+}$, where the principle bridging ligand is also an

alkoxide group [5]. Similar cores are also found in the decanuclear complexes $[Fe_{10}O_2Cl_8(tmp)_6]$, $[(VO)_2Fe_8O_2Cl_6(tmp)_6]$ and $(NEt_4)_2[Mn_{10}O_2Cl_8(thme)_6]$ [6].

➢ Description of structures

In this section, we describe eleven complexes (Table **5.1**) based on octahedral and edge-sharing bioctahedral metal topologies varying in nuclearity from six to twelve, and ranging from single molecules (0D) to 3-D polymers.

Table 5.1. The formula, central core and crystal system of complexes **16-26**.

Complex	Core	Crystal System/ Space Group
$Na_4[Mn_6O(OAc)_6(Br\text{-}mp)_4(MeOH)_4]$ (**16**)	$\{Na_4[Mn^{III}_4Mn^{II}_2(\mu_6\text{-}O)]\}$	Orthorhombic/*Pbca*
$Na_3[Mn_6O(OAc)_5(tmp)_4(N_3)(H_2O)_2]$ (**17**)	$\{Na_3[Mn^{III}_5Mn^{II}(\mu_6\text{-}O)]\}$	Orthorhombic/*Pbca*
$[Mn_{10}O_2(thme)_6Br_4(MeOH)_4]$ (**18**)	$[Mn^{III}_6Mn^{II}_4(\mu_4\text{-}O)_2]$	Monoclinic/$P2_1/n$
$[Mn_{12}O_2(piv)_{10}(tmp)_4(MeO)_2(MeOH)_2]$ (**19**)	$[Mn^{III}_4Mn^{II}_8(\mu_4\text{-}O)_2]$	Monoclinic /$P2_1/c$
$[Mn_{12}O_2(piv)_{10}(thme)_4(MeO)_2(MeOH)_2]$ (**20**)	$[Mn^{III}_4Mn^{II}_8(\mu_4\text{-}O)_2]$	Monoclinic/$C2/c$
$[Mn_{12}O_2(OAc)_{10}(Hpeol)_4(MeO)_2(H_2O)_4]$ (**21**)	$[Mn^{III}_4Mn^{II}_8(\mu_4\text{-}O)_2]$	Monoclinic/$P2_1/n$
$[Mn_{12}O_2(OAc)_{10}(thme)_4(MeO)_2(H_2O)_4]$ (**22**)	$[Mn^{III}_4Mn^{II}_8(\mu_4\text{-}O)_2]$	Monoclinic/$P2_1/n$
$[Mn_{12}O_2(OAc)_{10}(tmp)_4(MeO)_2(H_2O)_2]$ (**23**)	$[Mn^{III}_4Mn^{II}_8(\mu_4\text{-}O)_2]$	Monoclinic/$P2_1/n$
$[Mn_{12}O_2(O_2CCPh_2)_{10}(Hpeol)_4(MeO)_2(H_2O)_2]$ (**24**)	$[Mn^{III}_4Mn^{II}_8(\mu_4\text{-}O)_2]$	Orthorhombic/*Pbca*
$[Mn_{12}O_2(O_2CCPh_2)_{10}(Hpeol)_4(OH)_2(H_2O)_2]$ (**25**)	$[Mn^{III}_4Mn^{II}_8(\mu_4\text{-}O)_2]$	Monoclinic/$P2_1/c$
$Na[Mn_{12}O_2(OAc)_{11}(Hpeol)_4(MeO)(OH)(H_2O)_3]$ (**26**)	$\{Na[Mn^{III}_4Mn^{II}_8(\mu_4\text{-}O)_2]\}$	Triclinic/$P\bar{1}$

They can be divided into 2 main categories: the first (category I) describes a class based on $[Mn_6]$ octahedra linked together by Na^+ anions to form 1-D chains and 2-D sheets (complexes **16-17**). The second category (II) describes eight edge-sharing bioctahedra and consist of a $[Mn_{10}]$ complex (**18**) and a family of $[Mn_{12}]$ capped edge-sharing bioctahedra (complexes **19-25**). Complex **26** consists of a similar

metallic skeleton with the difference being the $[Mn_{12}]$ units are linked together by Na^+ ions forming a 1-D chain.

$Na_4[Mn_6O(OAc)_6(Br\text{-}mp)_4(MeOH)_4]$ (16) crystallizes in the orthorhombic space group *Pbca* (Figure **5.1**; selected bond lengths and angles are given in Tables A.5.5-6). Table **5.2** lists the structural features common to category I complexes (**16-17**). A crystallographically imposed 3-fold axis (in **16**) runs through the central μ_6-O^{2-} ion that is surrounded by an octahedron of four Mn^{III} and two Mn^{II} ions. The cluster consists of a core that describes a mixed-valent $[Mn^{III}_4Mn^{II}_2(\mu_6\text{-}O)]$ octahedron, (Mn1, Mn2, Mn3, Mn4 = 3+, Mn5, Mn6 = 2+) (Figure **5.2**). All six Mn ions are six-coordinate and are bonded to the μ_6-O^{2-} central oxide (O26). The Mn^{3+} ions display Jahn-Teller elongations (Mn1-O17, 2.165 Å; Mn1-O40, 2.196 Å; Mn2-

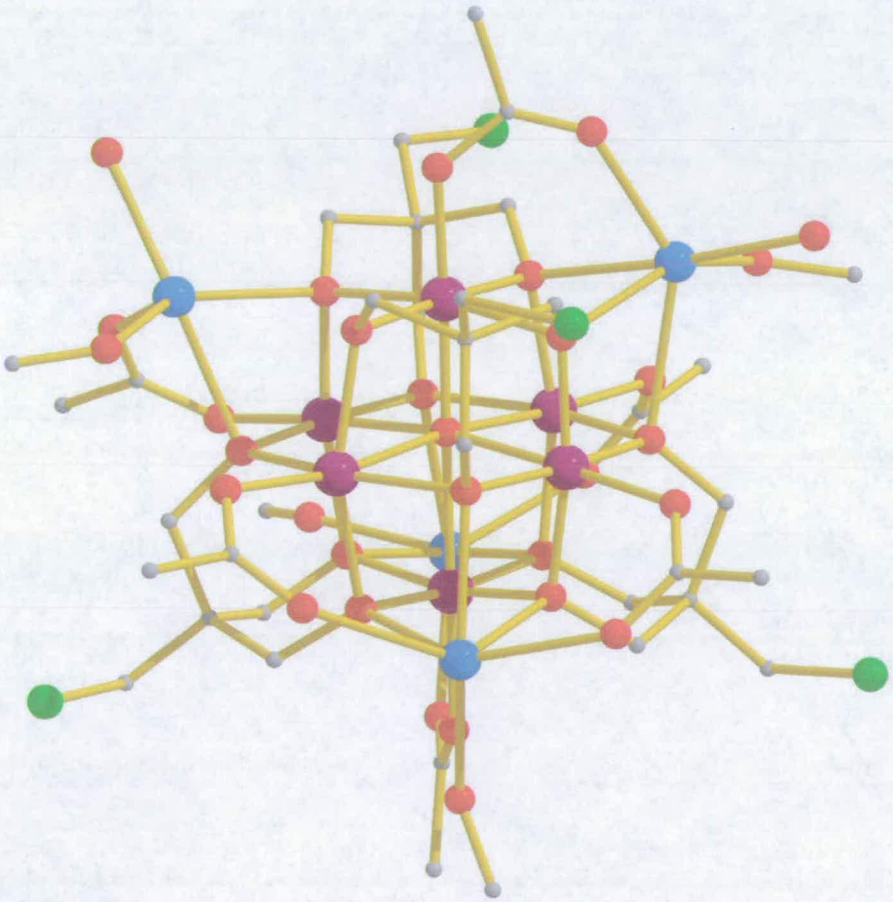

Figure 5.1. The structure of **16** in the crystal. Colour scheme: Mn: purple; Na: light blue; O: red; C: grey; Br: green.

O26, 2.377 Å; Mn2-O37, 2.090 Å; Mn3-O26, 2.265 Å; Mn3-O15, 2.126 Å; Mn4-O26, 2.304 Å; Mn4-O44, 2.129 Å) and are marked as black Mn-O bonds in Figure **5.2**: three are co-parallel (Mn1, Mn3, Mn4) with the remaining one perpendicular to these (Mn2). The four Na^+ ions are five- (Na9), six- (Na7, Na10) and seven-coordinate, (Na8), each capping one triangular face of the $[Mn_6]$ octahedron.

Table 5.2. Structural similarities of category I complexes (**16-17**).

		Coordination modes of AcO^-			Coordination modes of tripod^{3-}		
Complex	**# of AcO^-**	**# of $\eta^1:\eta^1:\mu$**	**# of $\eta^1:\eta^1:\mu_3$**	**# of tripods**	**# of $\eta^3:\eta^3:\eta^2:\mu_5$**	**# of $\eta^3:\eta^3:\eta^2:\mu_5$**	**Core**
16	6	4	2	4	1	3	$\{Na_4[Mn^{III}_4Mn^{II}_2(\mu_6\text{-}O)]\}$
17	5	3	2	4	3	1	$\{Na_3[Mn^{III}_5Mn^{II}(\mu_6\text{-}O)]\}$

The four tripodal ligands are fully deprotonated, Br-mp^{3-}. Three bridge in a $\eta^3:\eta^3:\eta^3:\mu_6$-fashion and one in a $\eta^3:\eta^3:\eta^2:\mu_5$-fashion (Figure **5.3**) spanning a trinuclear face of the octahedron and further bridging to the apical Na^+ ions. The six AcO^- ligands coordinate in two distinct ways: four in the usual $\eta^1:\eta^1:\mu$-fashion bridging one Mn and one Na ion; and two in a $\eta^2:\eta^1:\mu_3$-fashion bridging one Mn and two Na ions. The two latter Na^+ ions (Na8, Na9) form $\{Na_2(OAc)_2\}$ units (as shown in Figure **5.4**) that link the $[Mn^{III}_4Mn^{II}_2(\mu_6\text{-}O)]$ units together, propagating in a 1-D chain. The remaining coordination sites on the Na^+ ions are completed by terminal MeOH molecules.

There are a significant number of intra- and inter-molecular H-bonds. The AcO^- ligands are H-bonded to the terminal MeOH molecules on the neighbouring Na^+ ion (O…O, ~2.6-2.8 Å) or to the MeOH solvate molecules (O…O, ~2.75 Å). Additionally, H-bonds forms between the Br^- ions of the Br-mp^{3-} ligands and the MeOH solvate molecules (O…Br, ~3.2 Å). There are also intra-molecular H-bonds

formed by the acetate ligands and the terminal MeOH molecules of the neighbouring molecule (O…O, ~3.0 Å).

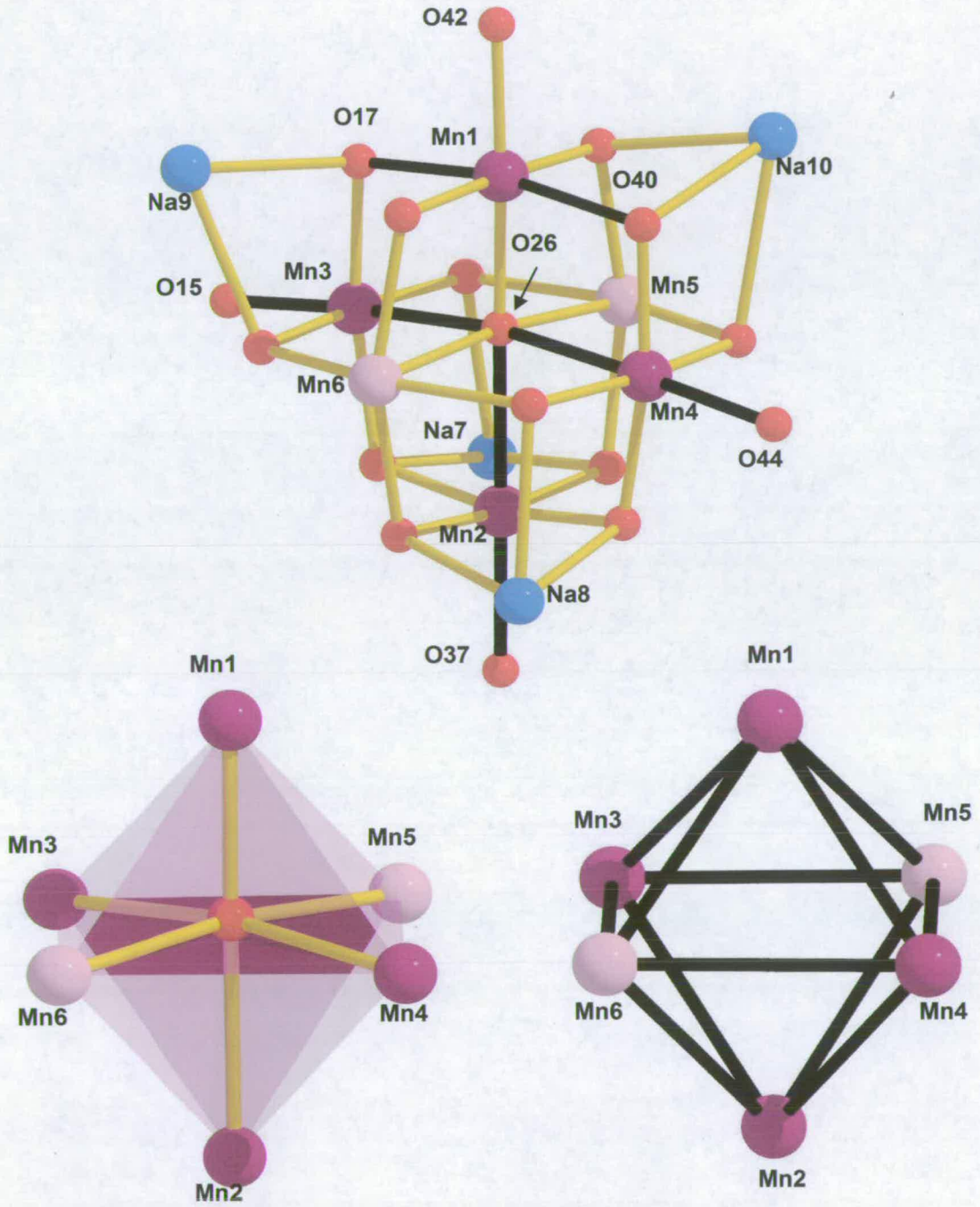

Figure 5.2. The Mn-Na-O core of **16** (top): the Jahn Teller axes are shown with black Mn-O bonds. The central metal-oxide core (bottom left) and the metallic skeleton (bottom right). Colour scheme: Mn(III): purple; Mn(II): pink; Na: light blue; O: red.

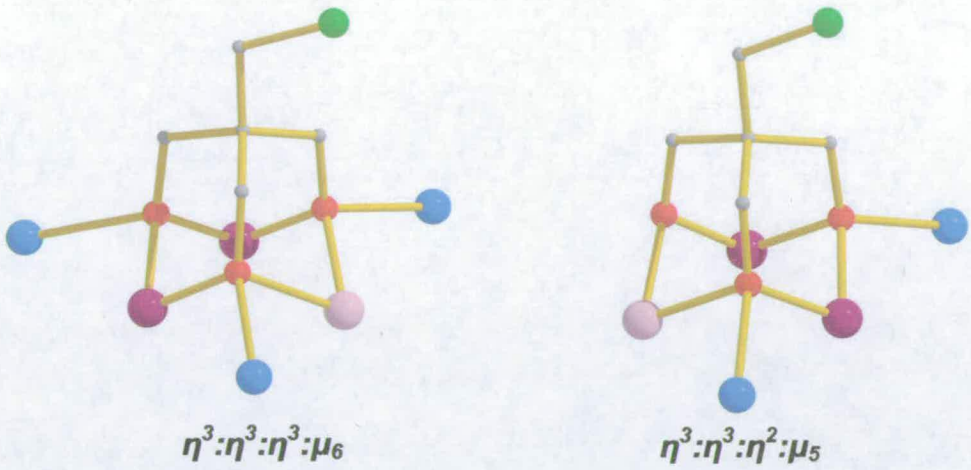

Figure 5.3. The coordination modes of Br-mp^{3-} and tmp^{3-}. Colour scheme same to Figure **5.1**.

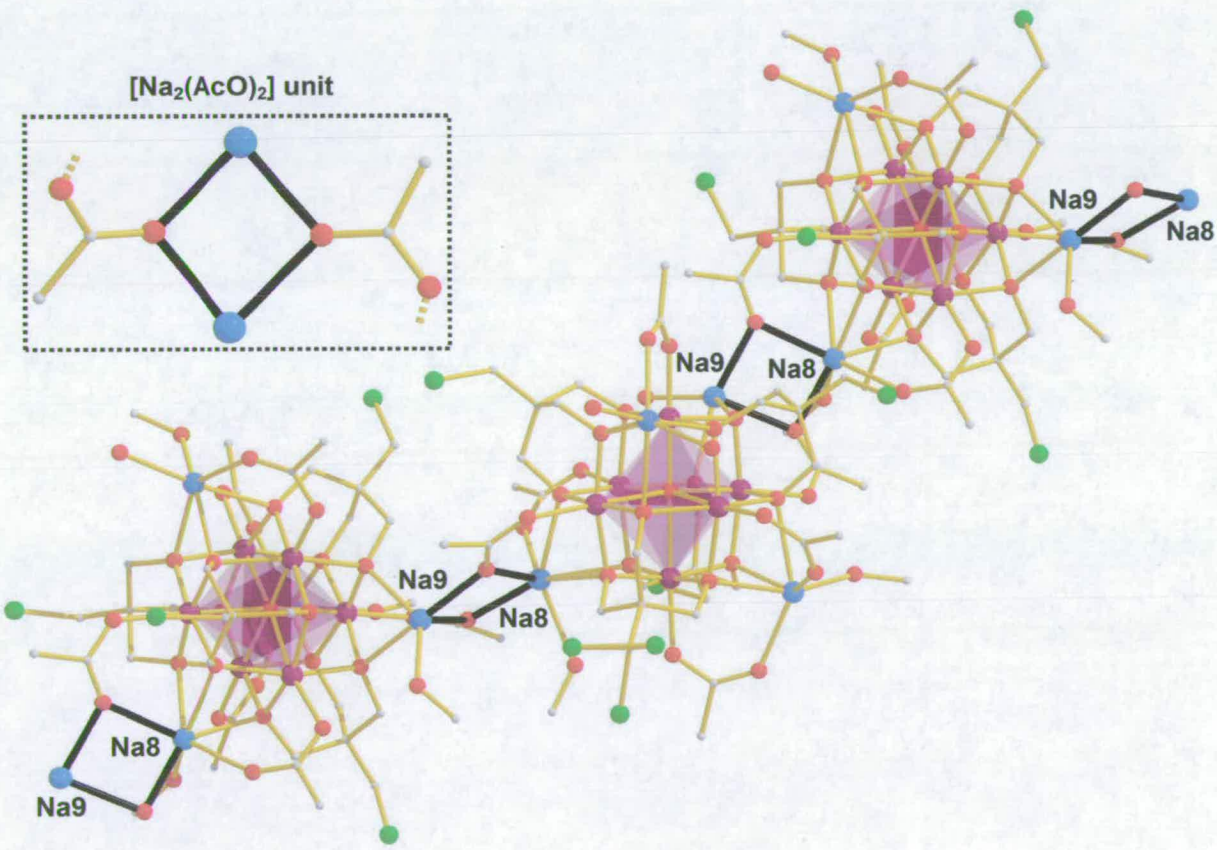

Figure 5.4. The polymeric 1-D chain of **16** in the crystal. Colour scheme: Mn: purple; Na: light blue; O: red; C: grey; Br: green.

$Na_3[Mn_6O(OAc)_5(tmp)_4(N_3)(H_2O)_2]\cdot CH_3CN$ (17) crystallizes in the orthorhombic space group *Pbca* (Figure **5.5**; selected bond lengths and angles are given in Tables A.5.7-8). A crystallographically imposed 3-fold axis runs through the central μ_6-O^{2-} ion which is surrounded by six Mn ions. The cluster consists of a core that describes a mixed-valent [$Mn^{III}_5Mn^{II}(\mu_6$-O)] octahedron, (Mn1, Mn3, Mn4, Mn5, Mn6 = 3+, Mn2 = 2+) (Figure **5.6**). The one Mn^{2+} ion (Mn2) is five-coordinate, while all five Mn^{3+} ions are six-coordinate. The μ_6-O^{2-} ion can be regarded as pseudo-octahedral given a long contact of 2.509 Å to O1. The Mn^{3+} ions display Jahn-Teller elongations (Mn1-O1, 2.304 Å; Mn1-O15, 2.064 Å; Mn3-O32, 2.112 Å; Mn3-O33, 2.132 Å; Mn4-O23, 2.098 Å; Mn4-O24, 2.109 Å; Mn5-O1, 2.324 Å; Mn5-O19, 2.072 Å; Mn6-N1, 2.116 Å; Mn6-O1, 2.300 Å; marked as black bonds in Figure

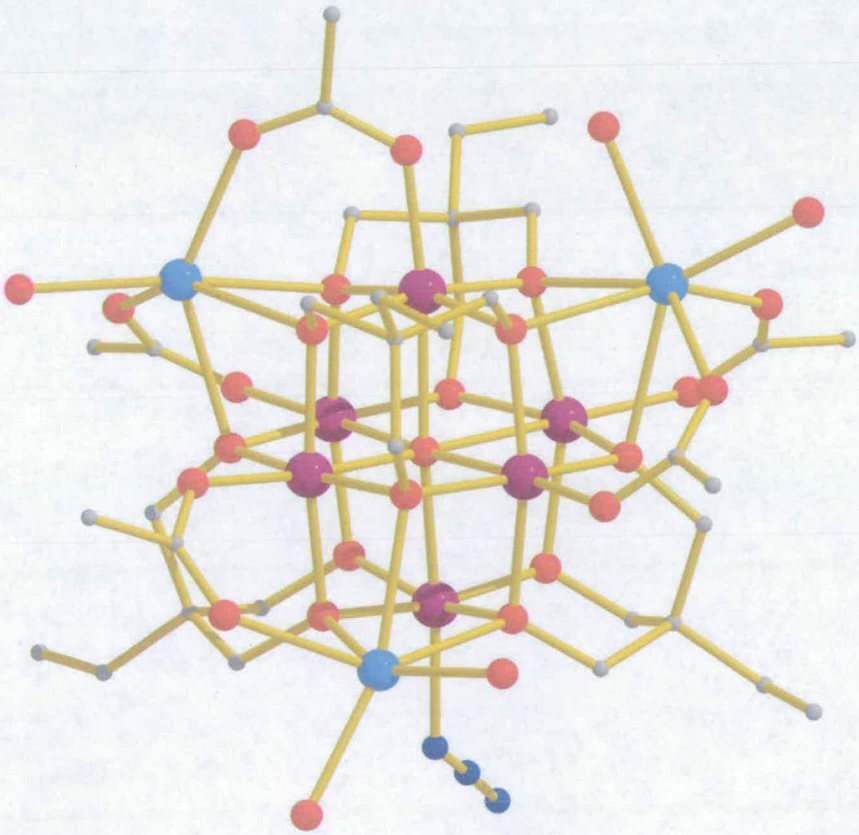

Figure 5.5. The structure of **17** in the crystal. Colour scheme: Mn: purple; Na: light blue; O: red; C: grey; N: blue.

5.6): four are co-parallel (Mn1, Mn3, Mn4, Mn6) with one perpendicular to these (Mn5). The three Na^+ ions are six- (Na2, Na3) and seven-coordinate (Na1).

The four tripodal ligands are fully deprotonated, tmp^{3-}, three of them bridge in a $\eta^3:\eta^3:\eta^2:\mu_5$-fashion and one in a $\eta^3:\eta^3:\eta^3:\mu_6$-fashion spanning a trinuclear face of the octahedron and further bridging to the apical Na^+ ions (Figure **5.3**). The five AcO^- ligands coordinate in two distinct ways: four in the usual $\eta^1:\eta^1:\mu$-fashion bridging one Mn and one Na ion; and two in a $\eta^2:\eta^1:\mu_3$-fashion bridging one Mn and two Na ions. The AcO^- ligands bridge two Na ions from neighbouring $\{Na_3[Mn^{III}_5Mn^{II}(\mu_6\text{-}O)]\}$ octahedral units forming $\{Na_2(OAc)_2\}$ that link $\{Na_3[Mn^{III}_5Mn^{II}(\mu_6\text{-}O)]\}$ moieties together into 2-D polymer propagated in three directions (Na1…Na3, Na3…Na1 and Na2…Na2) as shown in Figure **5.7**. The coordination spheres of Na1 and Na3 are completed by terminally bound H_2O molecules, and there is an end-on-azide ligand bonded terminally to Mn6.

There are a significant number of intra- and inter-molecular H-bonds. The AcO^- ligands are H-bonded to the terminal water molecules of the neighbouring Na^+ ion (O…O, ~2.8- 2.9 Å). The latter are H-bonded to the N-atom of the MeCN solvate molecules (O…N, ~2.8 Å). In addition, there are H-bonds formed by the water molecules and the terminal end-on-azides of the neighbouring molecule (O…N, ~3.0 Å)

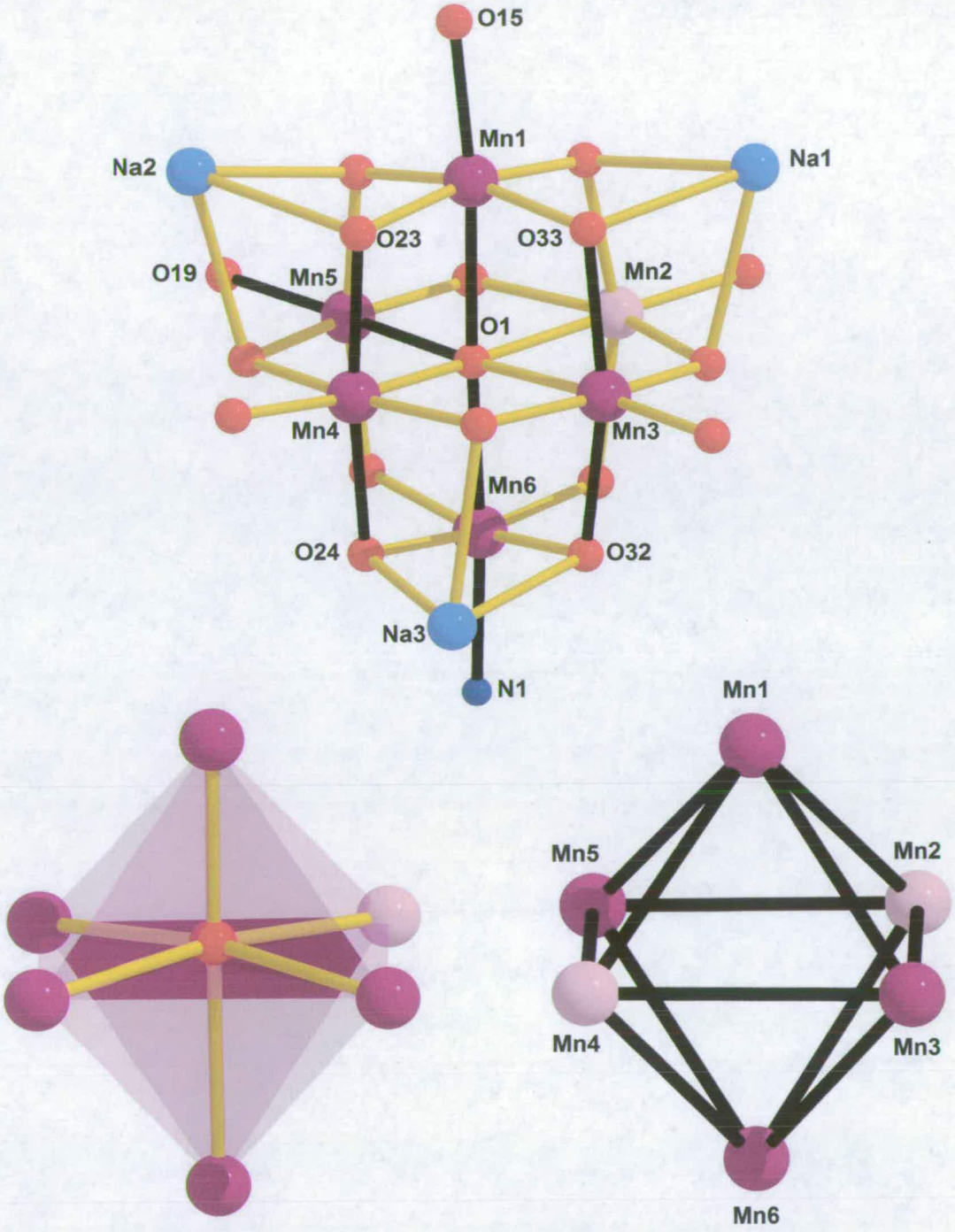

Figure 5.6. The Mn-Na-O core of **17** (top): the Jahn Teller axes are shown with black Mn-O bonds. The central metal-oxide core (bottom left) and the metallic skeleton (bottom right). Colour scheme: Mn(III): purple; Mn(II): pink; Na: light blue; O: red; N: blue.

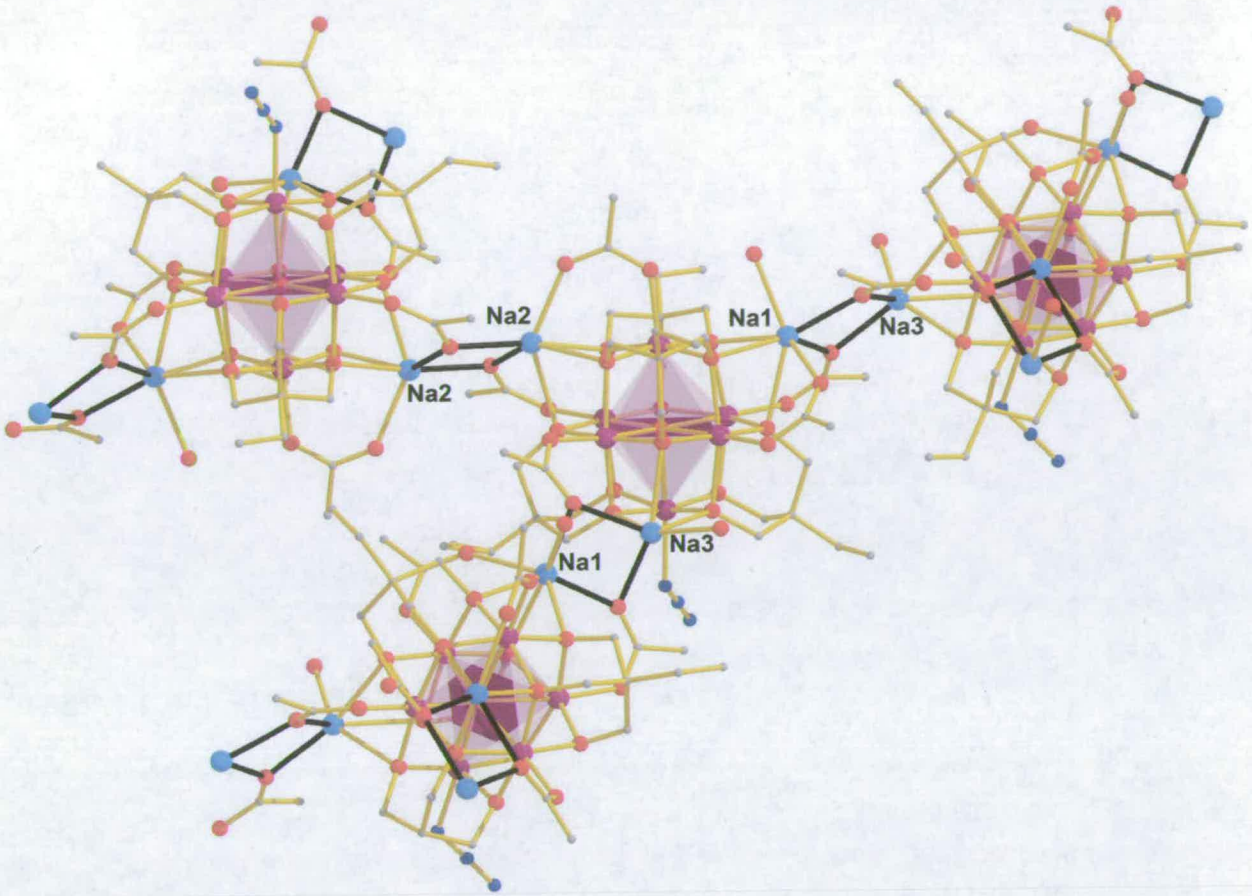

Figure 5.7. The 2-D polymer of **17** in the crystal. Colour scheme: Mn: purple; Na: light blue; O: red; N: blue; C: grey.

$[Mn_{10}O_2(thme)_6Br_4(MeOH)_4]$ (18) belongs to category II, and crystallizes in the monoclinic space group $P2_1/n$ (Figure **5.8**; selected bond lengths and angles are given in Tables A.5.9-10). The metallic skeleton describes a distorted edge-sharing bioctahedron held together *via* two central O^{2-} oxide ions resulting a $[Mn^{III}_6Mn^{II}_4(\mu_4\text{-}O)_2]$ core (Mn1, Mn2, Mn3 = 3+; Mn4, Mn5 = 2+ and symmetry equivalent) (Figure **5.9**). All six Mn^{3+} ions are six-coordinate and display Jahn-Teller elongations (Mn1-O4, 2.243 Å; Mn1-O40, 2.222 Å; Mn2-O123', 2.343 Å; Mn2-O401, 2.163 Å; Mn3-O123', 2.337 Å; Mn3-O402, 2.160 Å and s.e; marked as black bonds in Figure **5.9**): four are co-parallel (Mn1, Mn2 and s.e) with remaining two perpendicular to these (Mn3 and s.e). The Mn^{2+} ions are five-coordinate and bonded to the terminal Br^- ions (Mn4-Br4, 2.533 Å; Mn5-Br5, 2.565 Å and s.e).

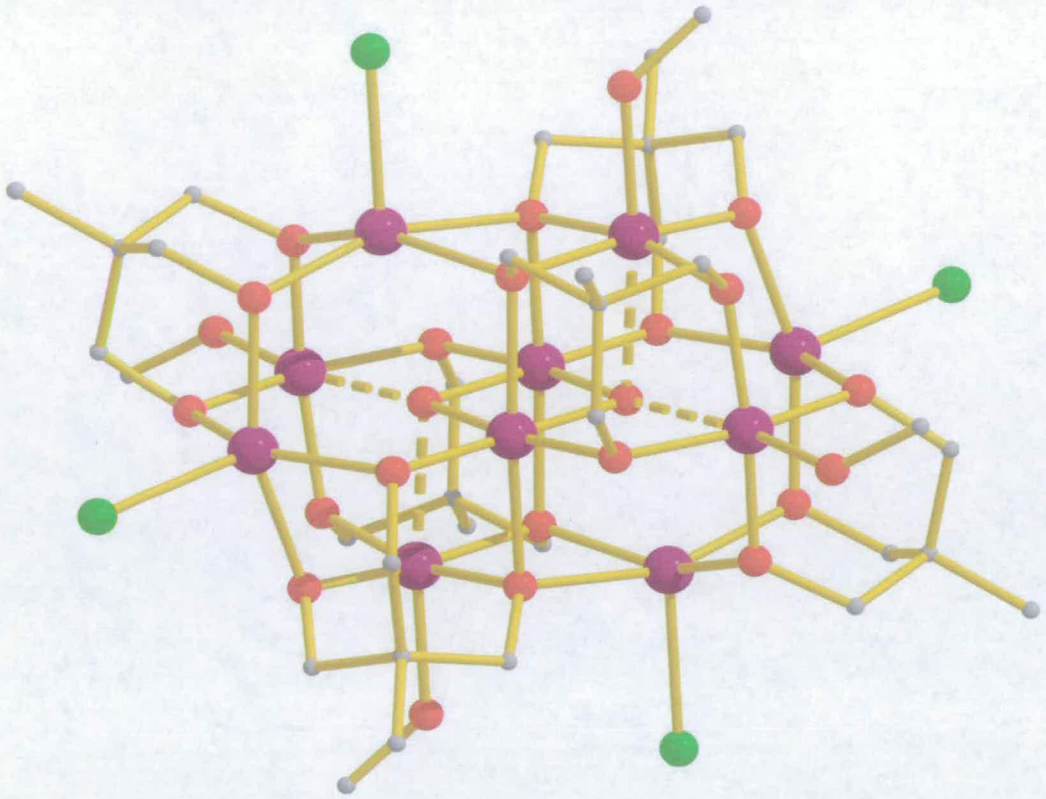

Figure 5.8. The structure of **18** in the crystal. Colour scheme: Mn: purple; O: red; C: grey; Br: green.

The two distorted octahedra share an edge along the Mn1-Mn1' vector. The two oxide ions can be described as four coordinate or pseudo-octahedral given the long contacts (Mn4-O123', 2.641 Å; Mn5-O123', 2.514 Å and s.e). The six tripodal ligands are full deprotonated, thme^{3-}. Four bridge in a $\eta^3:\eta^2:\eta^2:\mu_4$ coordination mode spanning a triangular face of one octahedron and further bridging to the apical Mn site on the neighbouring octahedron; and the remaining two bridge in a $\eta^2:\eta^2:\eta^2:\mu_3$ mode across a 'free' triangular face of an octahedron. Four terminal methanol molecules complete the coordination spheres of Mn2, Mn3 and s.e.

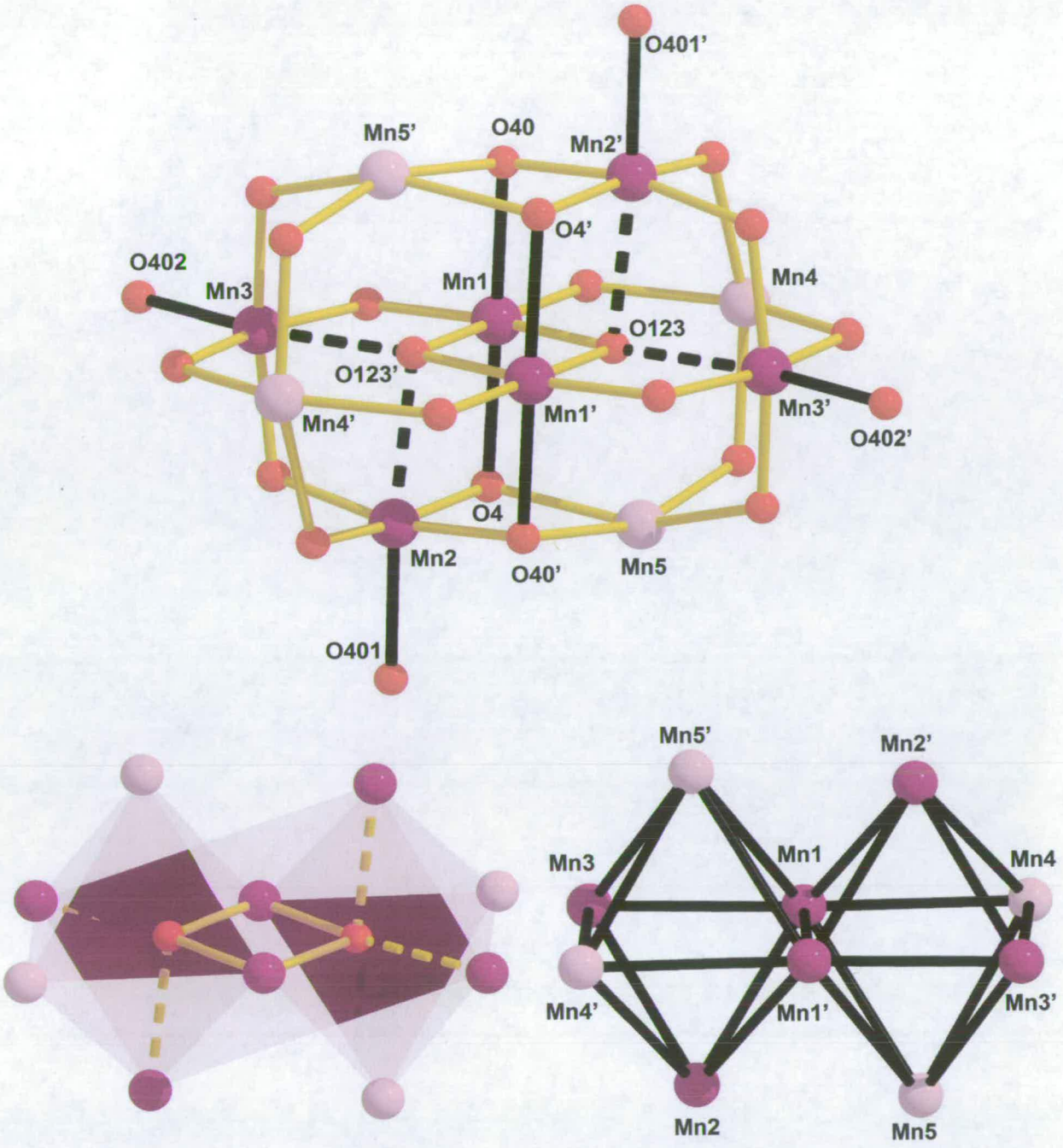

Figure 5.9. The Mn-O core of **18** (top): the Jahn Teller axes are shown with black Mn-O bonds. The central metal-oxide core (bottom left) and the metallic skeleton (bottom right). Colour scheme: Mn(III): purple; Mn(II): pink; O: red.

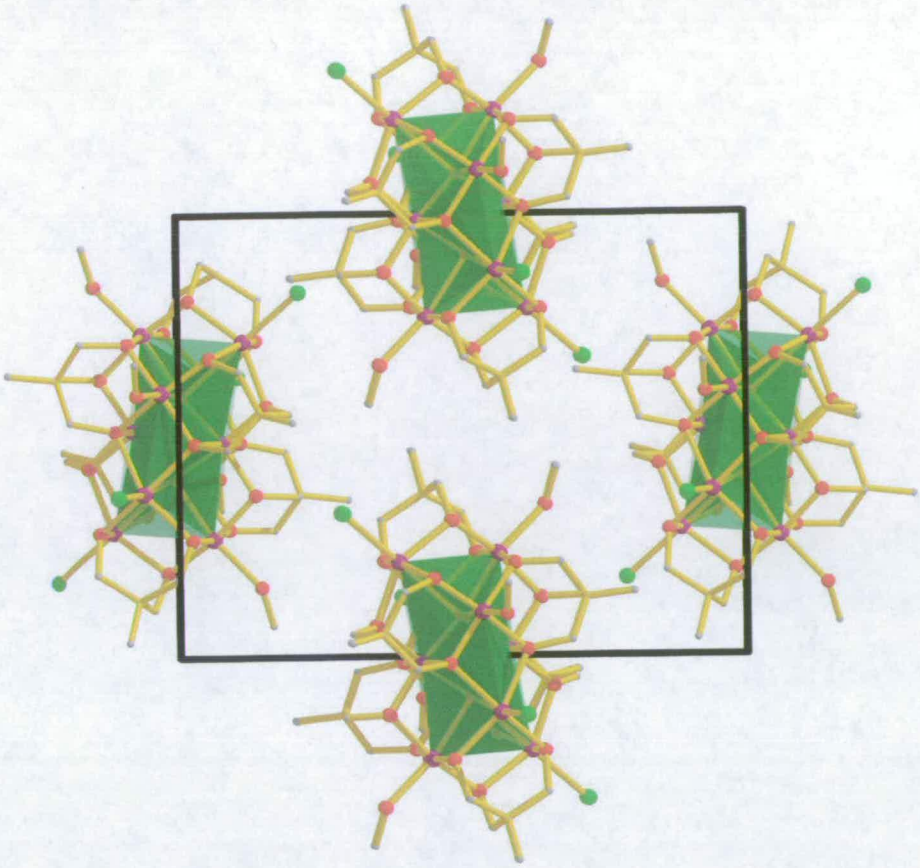

Figure 5.10. The packing of the molecules of **18** in the crystal viewed down the *c* axis.

There are a significant number of intra- H-bonds and short contacts. The terminal MeOH molecules that coordinate the Mn3 are H-bonded to the MeOH solvate molecules (O…O, ~2.62 Å), and the terminal MeOH molecules that coordinate to the Mn2 are H-bonded to the Br^- ion of the neighbouring Mn ion (Mn2) (O…Br, ~3.29 Å). Additionally, H-bonds form between the $thme^{3-}$ ligands and the MeOH solvate molecules (O…O, ~2.73 Å). The closest intermolecular Mn···Mn distance is ~7.3 Å and the molecules of **18** pack in the commonly observed brickwall pattern (Figure **5. 10**).

The category II also describes a family of eight $[Mn_{12}]$ complexes that consist of a metallic skeleton based on capped edge-sharing bioctahedra. Table **5.3** lists the structural features.

Table 5.3. Structural similarities of category II complexes (**19-26**).

	Coordination modes of RCO_2^-					Coordination modes of $tripod^{3-}$	
Complex	# of RCO_2^-	# of terminal	# of $\eta^1:\eta^1:\mu$	# of $\eta^2:\eta^1:\mu$	# of tripods	# of $\eta^3:\eta^3:\eta^2:\mu_5$	Core
19	10	-	8	2	4	4	$[Mn^{III}_4Mn^{II}_8(\mu_4\text{-}O)_2]$
20	10	-	8	2	4	4	$[Mn^{III}_4Mn^{II}_8(\mu_4\text{-}O)_2]$
21	10	2	4	4	4	4	$[Mn^{III}_4Mn^{II}_8(\mu_4\text{-}O)_2]$
22	10	2	4	4	4	4	$[Mn^{III}_4Mn^{II}_8(\mu_4\text{-}O)_2]$
23	10	4	4	4	4	4	$[Mn^{III}_4Mn^{II}_8(\mu_4\text{-}O)_2]$
24	10	4	6	-	4	4	$[Mn^{III}_4Mn^{II}_8(\mu_4\text{-}O)_2]$
25	10	4	6	-	4	4	$[Mn^{III}_4Mn^{II}_8(\mu_4\text{-}O)_2]$
26	11	2	2	-	4	4	$\{Na[Mn^{III}_4Mn^{II}_8(\mu_4\text{-}O)_2]\}$

Complex **$[Mn_{12}O_2(piv)_{10}(tmp)_4(MeO)_2(MeOH)_2]$ (19)** crystallizes in the monoclinic space group $P2_1/c$ (Figure **5.11**; selected bond lengths and angles are given in Tables A.5.11-12). The cluster consists of a central $[Mn^{III}_4Mn^{II}_6O_2]^{20+}$ core that can be described as two distorted octahedra (Mn1-Mn8, Mn11and Mn12) sharing an edge along the Mn3-Mn4 vector, and with two remaining Mn^{2+} ions (Mn9 and Mn10) each capping one face of the octahedra (Figure **5.12**). The Mn^{3+} ions (Mn3, Mn4, Mn8, Mn11) are at the centre of the cluster, two occupying the apical positions (Mn8, Mn11) and two sharing the common edge of the octahedra (Mn3, Mn4). The two oxide ions can be described as four coordinate or pseudo-octahedral given the long contacts (Mn2-O1, 2.797 Å; Mn7-O1, 3.296 Å; Mn6-O2, 2.879 Å; Mn12-O2, 3.293 Å) giving the overall metal-oxygen core is $[Mn^{III}_4Mn^{II}_8(\mu_4\text{-}O)_2]$. All four Mn^{3+} ions are six-coordinate and display Jahn-Teller elongations (Mn3-O31, 2.312 Å; Mn3-O43, 2.311 Å; Mn4-O24, 2.267 Å; Mn4-O42, 2.266 Å; Mn8-O113, 2.194 Å; Mn8-O2, 2.241 Å; Mn11-O17, 2.200 Å; Mn11-O1, 2.243 Å and s.e; marked as black bonds in Figure **5.12)**; and all are co-parallel. The Mn^{2+} ions are five- (Mn2, Mn6), six- (Mn7, Mn9, Mn10, Mn12) and pseudo six- coordinate (Mn1

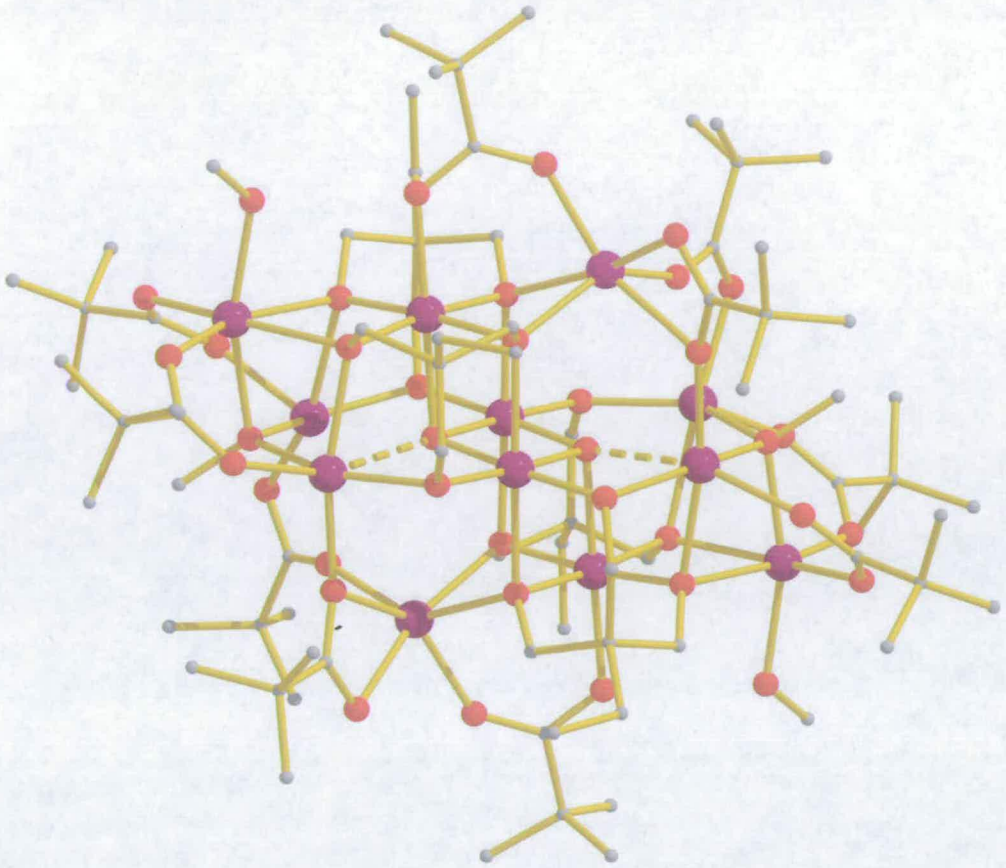

Figure 5.11. The structure of **19** in the crystal. Colour scheme: Mn: purple; O: red; C: grey.

and Mn4) having the long bonding distances 2.430 Å and 2.359 Å to the central oxides, O1 and O2, respectively.

All four tripodal ligands are full deprotonated, tmp^{3-}. Each bridges in a $\eta^3:\eta^3:\eta^2:\mu_5$ coordination mode spanning a triangular face of one octahedron and further bridging to the apical Mn site on the neighbouring octahedron and the peripheral face-capping Mn ions (Mn9, Mn10). The latter are also each connected to the central octahedra by a μ_3-OMe^- ligand (or by a μ_3-OH^- for **25** and by both for **26**) and two $\eta^1:\eta^1:\mu$ pivalate ligands (piv^-). The eight remaining carboxylates bridge in two different ways: two bridge the two Mn^{2+} ions in a $\eta^2:\eta^1:\mu$-fashion; and six in their usual $\eta^1:\eta^1:\mu$-mode. Two terminal MeOH molecules complete the coordination sphere of the peripheral face-capping Mn ions (Mn9 and Mn10).

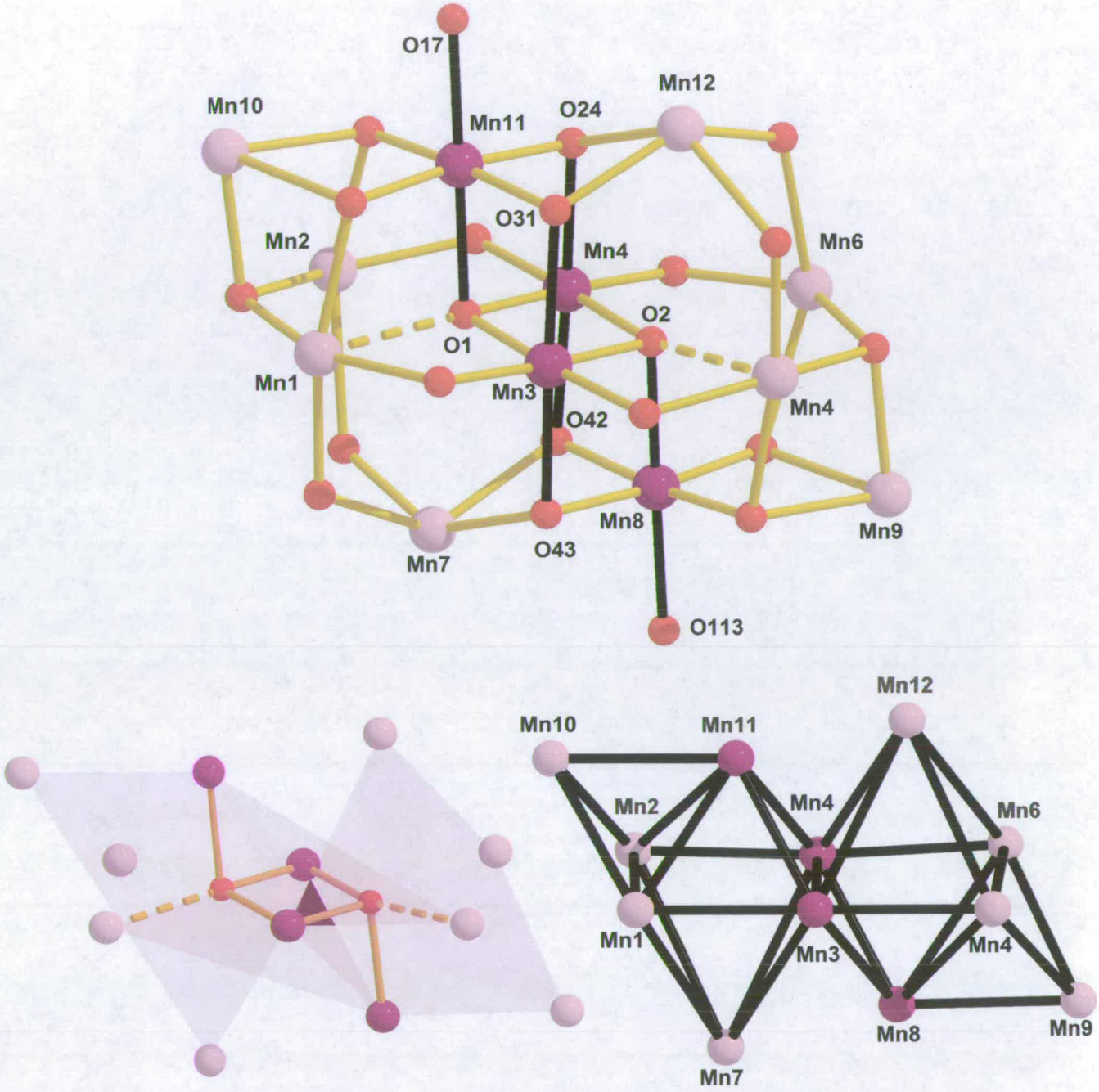

Figure 5.12. The Mn-O core of **19** (top): the Jahn Teller axes are shown with black Mn-O bonds. The central metal-oxide core (bottom left) and the metallic skeleton (bottom right). Colour scheme: Mn(III): purple; Mn(II): pink; O: red.

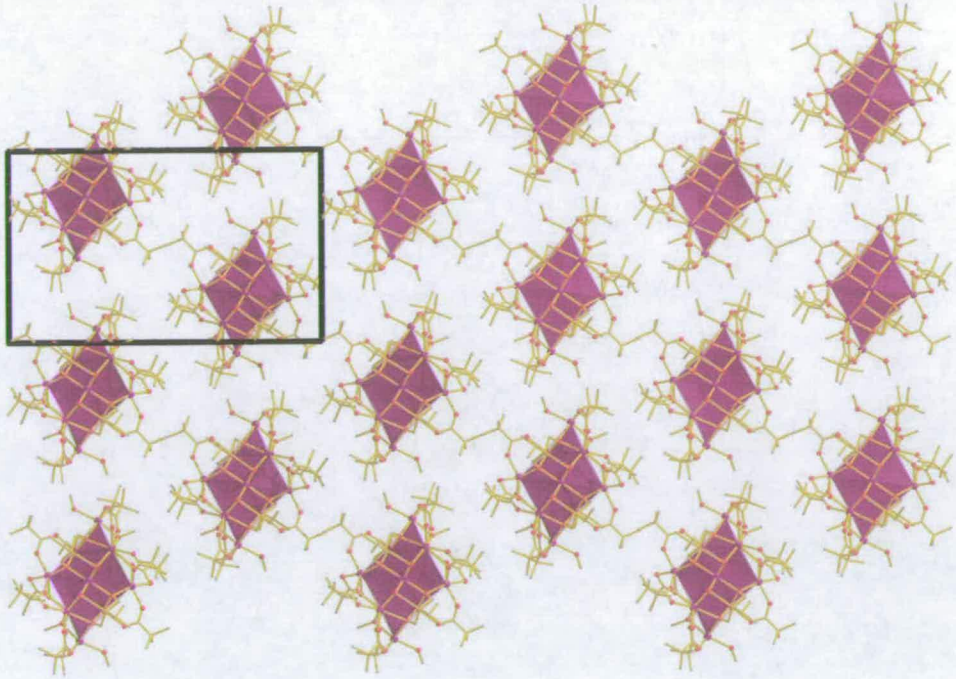

Figure 5.13. The packing of the molecules of **19** in the crystal viewed down the *c* axis.

The terminal MeOH molecules are H-bonded to neighbouring carboxylates (O…O, ~2.77 Å) on the same molecule and on neighbouring molecules (C…O, ~3.16 Å). The molecules of **19** pack in the commonly observed brickwall pattern in the crystal, with the closest intermolecular Mn···Mn distance being 10.07 Å between adjacent sheets and 6.21 Å within the same sheet (Figure **5.13**).

Complexes **20-26** have structures analogous to **19** with the only differences being limited to the presence of different carboxylates (-RCO_2^- where R= CH_3, $C(CH_3)_3$), tripodal ligands (tmp^{3-}, $thme^{3-}$, $Hpeol^{3-}$), symmetries/space groups (Table **5.1** and Tables A.5.2-4) and in the identity of the terminaly bound ligands (two MeOH molecules in **19**, **20** and **24**; two H_2O molecules in **23**, **25** and **26**; and four H_2O molecules in **21-22**). The differences in the coordination modes of the ten carboxylates are summarised in Table **5.3**.

$Na[Mn_{12}O_2(OAc)_{11}(Hpeol)_4(MeO)(OH)(H_2O)_3]$ (**26**) crystallizes in the triclinic space group $P\bar{1}$ (Figure **5.14**) with the asymmetric unit containing a half

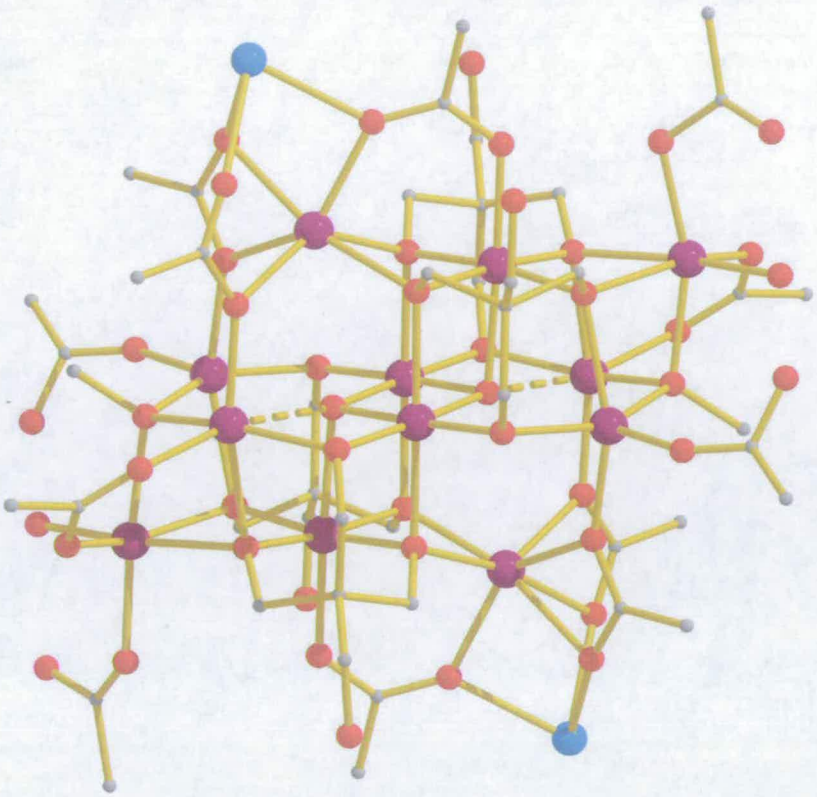

Figure 5.14. The structure of **26** in the crystal. Colour scheme: Mn: purple; O: red; C: grey; Na: pale blue.

cluster and two MeCN molecules of crystallization. Again the structure contains a face-capped [Mn_{12}] bioctahedra as in **19**, but they are now linked together *via* Na^+ ions into a 1-D chain (Figure **5.15**). The Na+ ions are bonded to a total of six carboxylates (O16, O20, O22 and s.e.) which each bridge to Mn6.

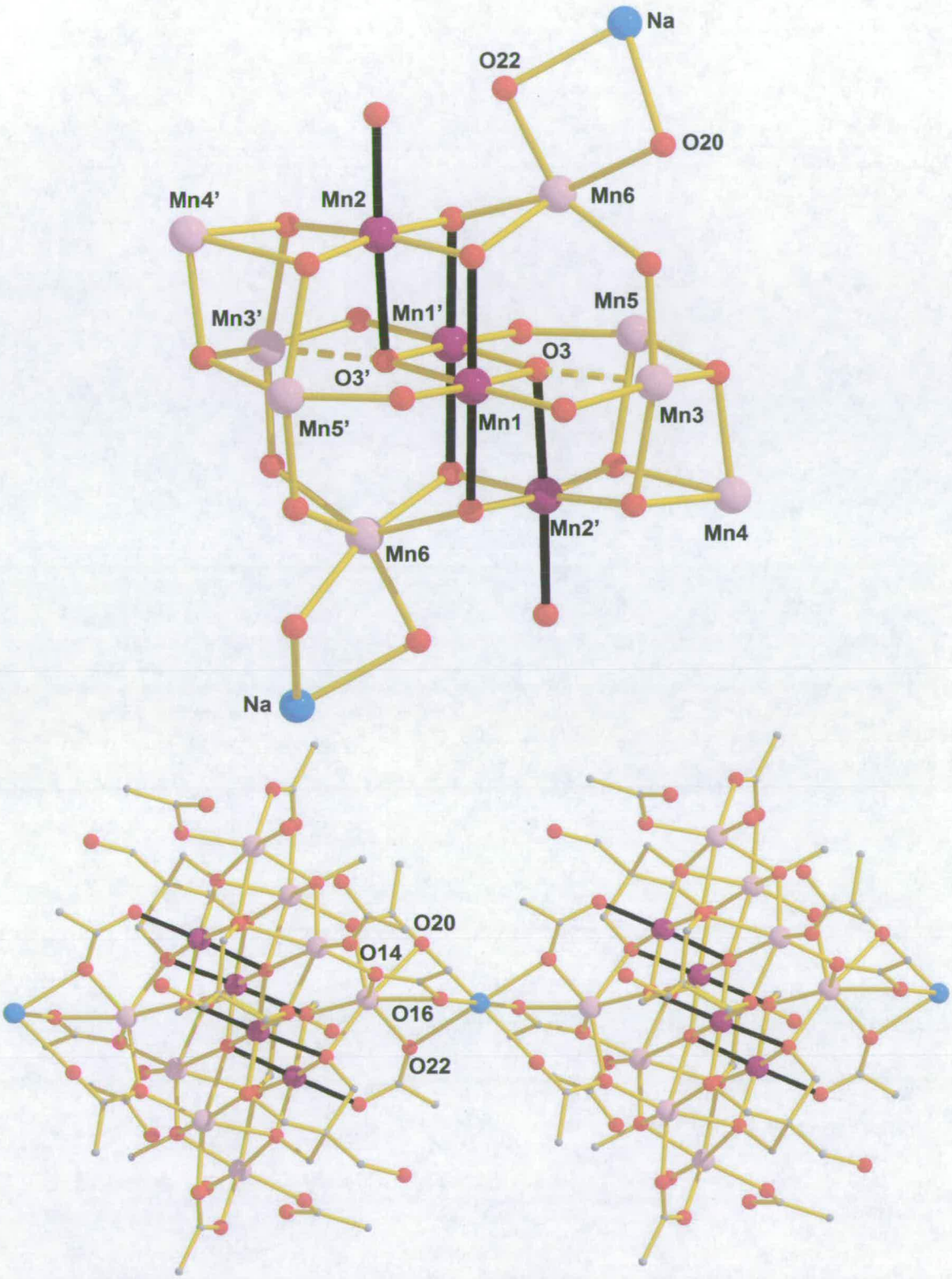

Figure 5.15. The Mn-O-Na core (top) and the polymeric 1-D chain (bottom) of **26** in the crystal. The black marked bonds (Mn-O) indicate the Jahn-Teller axes. Colour scheme: Mn(III): purple; Mn(II): pink; O: red; C: grey; Na: pale blue.

In all complexes, the oxidation states of the metal ions were assigned using a combination of bond length, charge balance considerations and BVS calculations (Table **5.4**) [7].

Table 5.4. BVS calculations of complexes **16-19**

Complex 16

Atom	Mn^{2+}	Mn^{3+}	Mn^{4+}	Ox.	Atom	Mn^{2+}	Mn^{3+}	Mn^{4+}	Ox.
Mn1	3.28	3.02	2.97	3+	Mn4	3.22	2.97	2.94	3+
Mn2	3.38	3.12	3.06	3+	Mn5	2.29	2.11	2.07	2+
Mn3	3.27	3.03	2.99	3+	Mn6	2.24	2.07	2.03	2+

Complex **17**

Atom	Mn^{2+}	Mn^{3+}	Mn^{4+}	Ox.	Atom	Mn^{2+}	Mn^{3+}	Mn^{4+}	Ox.
Mn1	2.57	3.09	3.02	3+	Mn4	3.34	3.08	3.02	3+
Mn2	2.09	1.94	1.90	2+	Mn5	3.29	3.04	2.98	3+
Mn3	3.25	3.00	2.94	3+	Mn6	3.33	3.07	3.00	3+

Complex **18**

Atom	Mn^{2+}	Mn^{3+}	Mn^{4+}	Ox.	Atom	Mn^{2+}	Mn^{3+}	Mn^{4+}	Ox.
Mn1	3.35	3.09	3.03	3+	Mn4	1.72	1.58	1.55	2+
Mn2	3.36	3.09	3.04	3+	Mn5	1.74	1.60	1.58	2+
Mn3	3.36	3.10	3.04	3+					

Complex **19**

Atom	Mn^{2+}	Mn^{3+}	Mn^{4+}	Ox.	Atom	Mn^{2+}	Mn^{3+}	Mn^{4+}	Ox.
Mn1	2.08	1.93	1.89	2+	Mn7	1.99	1.84	1.80	2+
Mn2	-	-	-	2+	Mn8	3.34	3.08	3.02	3+
Mn3	3.39	3.12	3.06	3+	Mn9	2.10	1.94	1.90	2+
Mn4	3.36	3.01	3.04	3+	Mn10	2.06	1.90	1.86	2+
Mn5	2.13	1.97	1.93	2+	Mn11	3.38	3.11	3.05	3+
Mn6	-	-	-	2+	Mn12	2.02	1.87	1.83	2+

Magnetic Studies

➢ Dc Magnetic Studies

Variable temperature dc magnetic susceptibility data were carried out on powdered microcrystalline samples of **16** and **18-26** in a field of 0.1 T and in the 5-300 K temperature range. The room temperature $\chi_M T$ value of **16** (Figure **5.16**) is approximately 18.76 cm^3 K mol^{-1} and decreases steadily upon cooling to a value of approximately 5.45 cm^3 K mol^{-1} at 5 K. The $\chi_M T$ value expected for an uncoupled $[Mn^{III}_4Mn^{II}_2]$ unit (g = 2.00) is approximately 23.5 cm^3 K mol^{-1}, higher than the measured value at 300 K. This behaviour is indicative of dominant antiferromagnetic exchange interactions between the metal centres with the low-temperature value indicating relatively small, $S \approx 3$, spin ground-state.

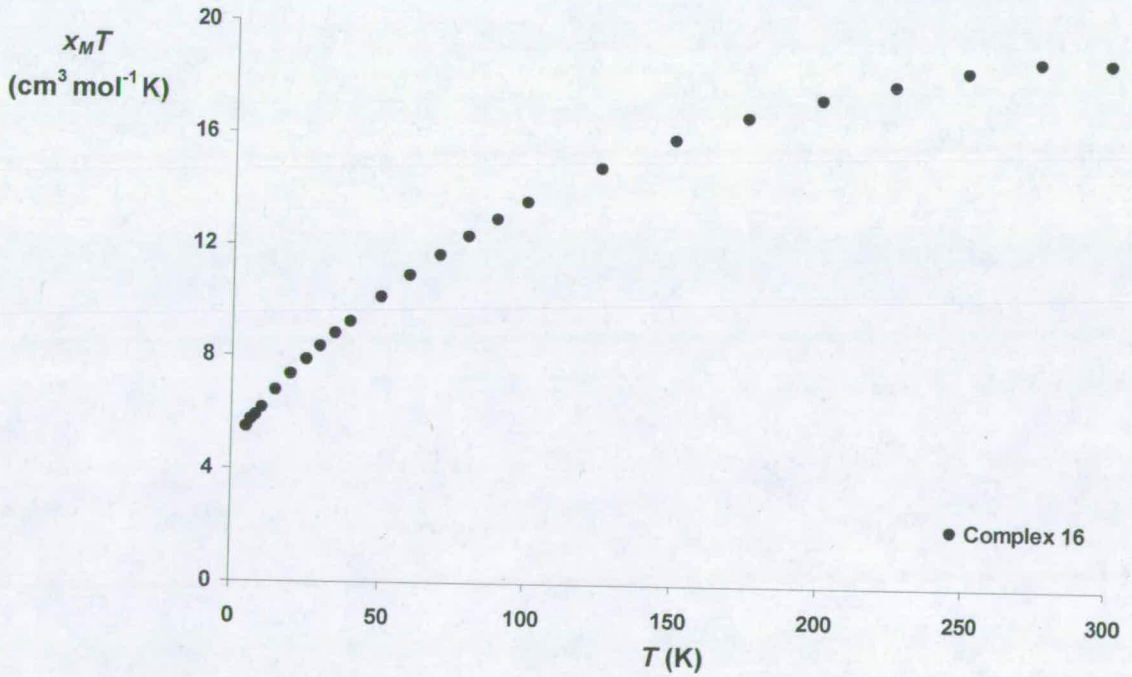

Figure 5.16. Plot of $\chi_M T$ vs T for complex **16** in the 5- 300 K temperature range in a field of 0.1 T.

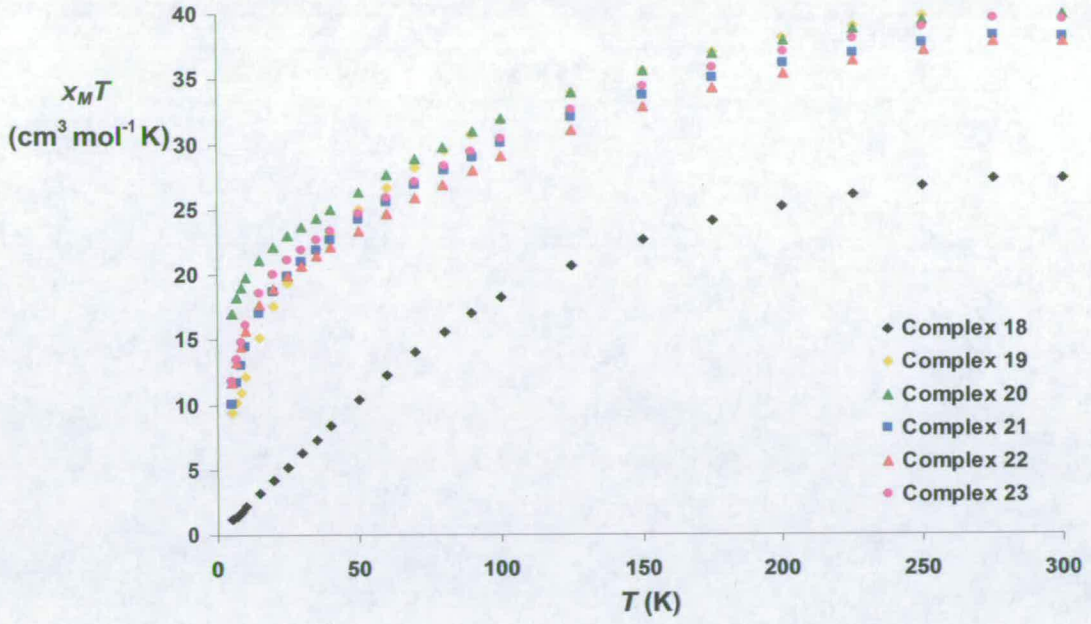

Figure 5.17. Plot of χ_MT vs T for complexes **18-23** in the 5- 300 K temperature range in a field of 0.1 T.

The room temperature $\chi_M T$ value of **18** (Figure **5.17**) is approximately 27.29 cm^3 K mol^{-1} and remains essentially constant as the temperature decreases until ca. 200 K (25.23 cm^3 K mol^{-1}) where it then decreases rapidly to a value of 1.17 cm^3 K mol^{-1} at 5 K . The $\chi_M T$ value expected for an uncoupled [$Mn^{III}_6Mn^{II}_4$] unit (g = 2.00) is approximately 35.50 cm^3 K mol^{-1}, higher than the measured value at 300 K. This behaviour is again indicative of dominant antiferromagnetic exchange interactions between the metal centres with the low-temperature value indicating S = 0 spin ground-state. Also shown in Figures **5.17-18** are the $\chi_M T$ versus T plots for the family of eight [Mn_{12}] complexes which consist of the same metallic skeleton [$Mn^{III}_4Mn^{II}_8$] (complexes **19-26**). The $\chi_M T$ value expected for an uncoupled [$Mn^{III}_4Mn^{II}_8$] unit (g = 2.00) is approximately 47.00 cm^3 K mol^{-1}, higher than the measured value at 300 K for all eight complexes. The room temperature $\chi_M T$ values of **19-23** are approximately 40.28, 39.88, 38.10, 37.76, 39.50 cm^3 K mol^{-1}, respectively, and decrease steadily to 25.00, 25.29, 24.16, 23.35 and 24.62 cm^3 K mol^{-1} until ca. 200 K where they then decrease rapidly to values of 9.37, 17.00, 10.09, 11.71 and 11.78 cm^3 K mol^{-1} at 5 K. This behaviour is again indicative of dominant antiferromagnetic

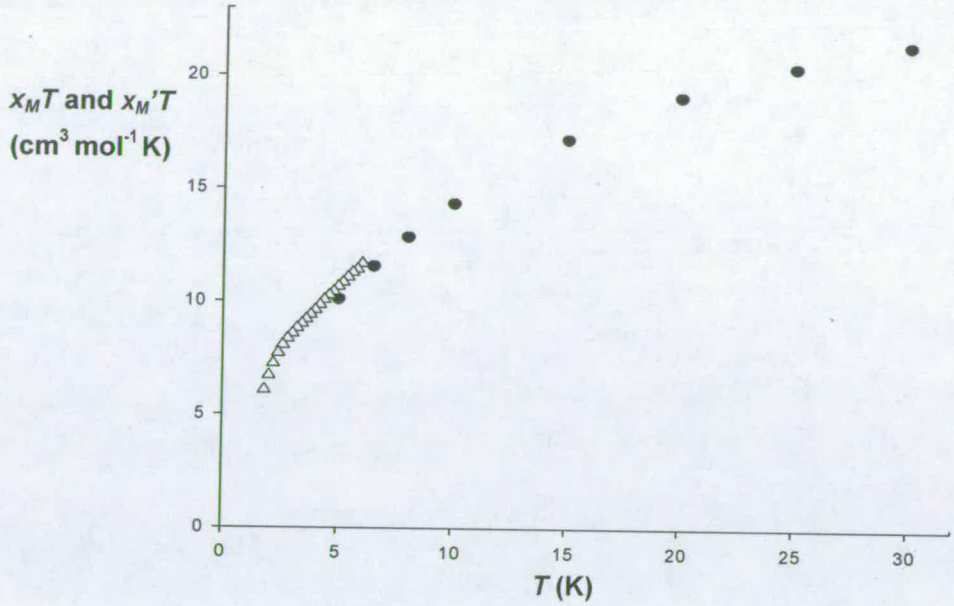

Figure 5.18. Plot of the dc $\chi_M T$ *vs.* T data (•) for complex **24** in the 5.0 - 30 K temperature range, and the $\chi_M' T$ *vs.* T data in the 1.8 – 6.0 K range from ac susceptibility measurements (Δ).

exchange interactions between the metal centres with the low-temperature values indicating relatively small ($S = 4 \pm 1$) spin ground-states.

The data for **24-26** are essentially identical, and in Figure **5.18** we show only the plot for **24**. The $\chi_M T$ value for **24** steadily decreases from 31.4 cm^3Kmol^{-1} at 300 K to 19.1 cm^3Kmol^{-1} at 20 K, and then decreases to 10.1 cm^3Kmol^{-1} at 5 K. The data strongly suggest predominantly antiferromagnetic exchange interactions.

Given the size and complexity of **16-26** (e.g. each of **19-26** contains eight Mn^{II} and four Mn^{III} ions with total spin values ranging from 0 to 28) it is not possible to apply the Kambe method to determine the individual pairwise exchange interaction parameters between the Mn ions. In order to determine the ground states of complexes **16**, **18-26,** variable temperature, and variable-field dc magnetization data were collected in the ranges 1.8–10 K and 0.1–7 T. The data were fitted by a matrix-diagonalization method to a model that assumes only the ground-state is populated, includes axial zero-field splitting ($D\hat{S}_z^2$), and carries out a full powder average [8]. The corresponding Hamiltonian is given by:

$$\hat{H} = D\hat{S}_z^2 + g\mu_B\mu_0 \hat{S}H \qquad (1)$$

where D is the axial anisotropy, μ_B is the Bohr magneton, μ_0 is the vacuum permeability, $\hat{S}_z$ is the easy-axis spin operator, and H is the applied field.

For complex **18** no satisfactory fit of the data was possible since the magnetization rises almost linearly with applied magnetic field indicating the existence of a $S \approx 0$ spin ground state, with the presence of many low-lying excited states of larger multiplicity that become populated with increasing field. For complexes **20-26** the fittings are essentially identical and again not very satisfactory (of poor quality) since there are many low-lying excited spin states lying close to the spin ground state. However, the best fit indicates $S = 4\pm1$. Low-lying excited states are a common problem in large clusters, particularly when there are multiple Mn^{2+} ions present, as is the case here, since these give weak exchange interactions.

Satisfactory fits were obtained for complexes **16** and **19**: the data are plotted as reduced magnetization ($M/N\mu_B$) versus H/T in (Figures **5.19-20**). The best fit for **16** obtained using only low field (0.1 T < H < 1 T) data is: $S = 3$, g = 1.97 and D = -

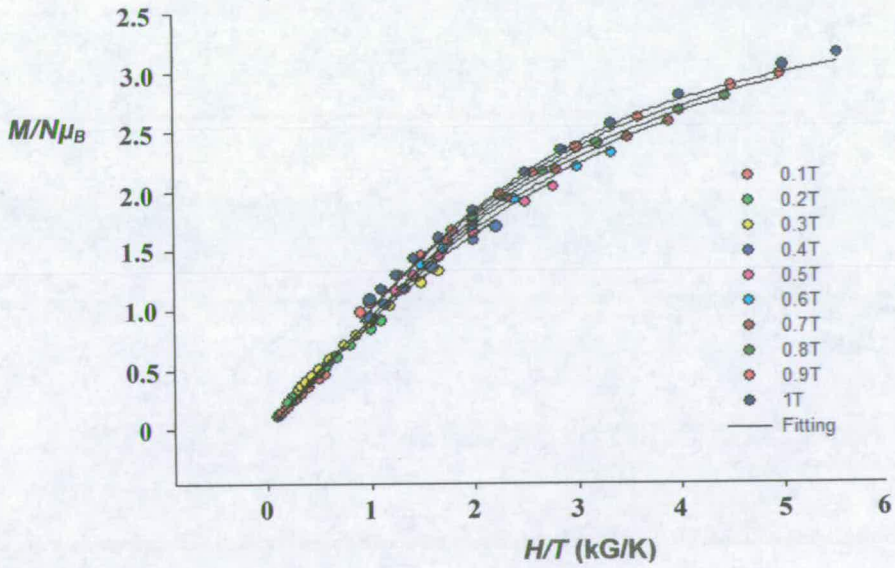

Figure 5.19. Plot of reduced magnetization ($M/N\mu_B$) vs H/T for **16**. The solid lines are the fit of the data to an $S = 3$ state with D = -1.12 cm^{-1} and g = 1.97.

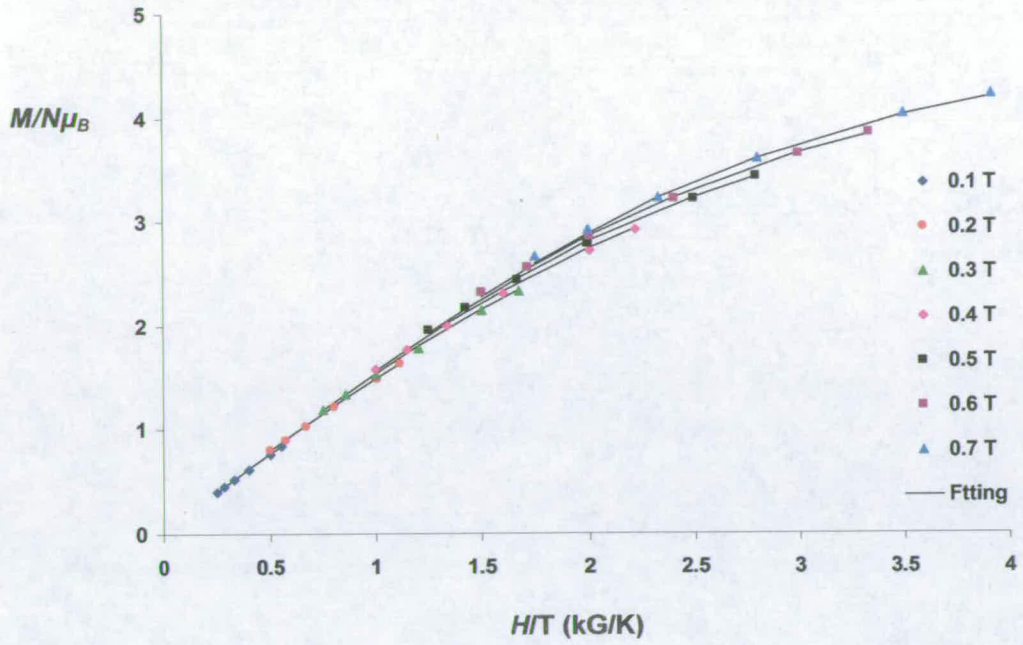

Figure 5.20. Plot of reduced magnetization ($M/N\mu_B$) vs H/T for **19**. The solid lines are the fit of the data to an $S = 4$ state with $D = -0.36$ cm^{-1} and g = 1.91.

1.12 cm^{-1}; for **19** the best fit obtained (again using only low field data 0.1 T < H < 0.7 T) affords: $S = 4$, g = 1.91 and $D = -0.36$ cm^{-1}. When fields up to 7 Tesla were employed a poorer quality fit was obtained. This is characteristic of low-lying excited states with S values greater than the ground state. Clearly the g-value for **19** is well below the expected value (i.e. 1.95–2.00) for such a complex and is a direct consequence of assuming only the ground state is populated. Table **5.5** summarises the magnetic data obtained for complexes **16-26**.

➢ Ac Magnetic Studies

In-phase (χ_M') and out-of-phase (χ_M'') ac susceptibility measurements were performed on complexes **16-26** in the 1.8-15 K range in a 3.5 G ac field oscillating at 5-1000 Hz. The ac data at 997 Hz for **16** is essentially superimposable with the dc data and

appear to be heading for $\chi_M'T \approx 5$ cm^3Kmol^{-1} at 0 K (Figure **5.21**), consistent with a small ground state spin value of $S \approx 3$, before a steeper drop at <3 K. This behaviour suggests the presence of excited states with larger S values. Frequency-dependent out-of-phase (χ_M'') ac susceptibility peaks or signals are not seen below approximately 3 K, thus complex **16** is not a single-molecule magnet. In-phase (χ_M') (Figure **5.22**) and out-of-phase (χ_M'') ac susceptibility measurements for **18** confirm that is an antiferromagnetic complex with ground state spin value of $S \approx 0$.

Table 5.5. *S*, *g* and *D* values were obtained from dc measurements for complexes **16-26**.

Complex	Core	$S_{G.S}$	*g*	$D(cm^{-1})$
$Na_4[Mn_6O(OAc)_6(Br\text{-}mp)_4(MeOH)_4]$ (**16**)	$[Mn^{III}_4Mn^{II}_2]$	3	1.97	-1.12
$Na_3[Mn_6O(OAc)_5(tmp)_4(N_3)(H_2O)_2]$ (**17**)	$[Mn^{III}_5Mn^{II}]$	-	-	-
$[Mn_{10}O_2(thme)_6Br_4(MeOH)_4]$ (**18**)	$[Mn^{III}_6Mn^{II}_4]$	0	-	-
$[Mn_{12}O_2(piv)_{10}(tmp)_4(MeO)_2(MeOH)_2]$ (**19**)	$[Mn^{III}_4Mn^{II}_8]$	4	1.91	-0.36
$[Mn_{12}O_2(piv)_{10}(thme)_4(MeO)_2(MeOH)_2]$ (**20**)	$[Mn^{III}_4Mn^{II}_8]$	4	2.16	-0.90
$[Mn_{12}O_2(OAc)_{10}(Hpeol)_4(MeO)_2(H_2O)_4]$ (**21**)	$[Mn^{III}_4Mn^{II}_8]$	4	poor fitting	
$[Mn_{12}O_2(OAc)_{10}(thme)_4(MeO)_2(H_2O)_4]$ (**22**)	$[Mn^{III}_4Mn^{II}_8]$	4	poor fitting	
$[Mn_{12}O_2(OAc)_{10}(tmp)_4(MeO)_2(H_2O)_2]$ (**23**)	$[Mn^{III}_4Mn^{II}_8]$	4	2.00	-0.42
$[Mn_{12}O_2(O_2CCPh_2)_{10}(Hpeol)_4(MeO)_2(H_2O)_2]$(**24**)	$[Mn^{III}_4Mn^{II}_8]$	4	poor fitting	
$[Mn_{12}O_2(O_2CCPh_2)_{10}(Hpeol)_4(OH)_2(H_2O)_2]$ (**25**)	$[Mn^{III}_4Mn^{II}_8]$	4	poor fitting	
$Na[Mn_{12}O_2(OAc)_{11}(Hpeol)_4(MeO)(OH)(H_2O)_3]$ (**26**)	$[Mn^{III}_4Mn^{II}_8]$	4	poor fitting	

The behaviour of complexes **19-26** is similar: below 10 K all show sloping lines with a slight decrease in $\chi_M'T$ with decreasing temperature, suggesting the presence of excited states with larger S values. Extrapolation of the slopes to 0 K gives values of ~9 cm^3 mol^{-1} K, suggesting spin ground states of $S = 4\pm1$, in agreement with the dc data. Frequency-dependent out-of-phase (χ_M'') ac susceptibility signals are seen for all complexes (**19-26**) below approximately 3 K (Figure **5.23**). The signals and peak maxima are observed along with a concomitant

decrease in the in-phase-signal. Both are suggestive of single-molecule magnetism behaviour - caused by the inability of **19-26** to relax quickly enough, at these temperatures, to keep up with the oscillating field.

➢ Single-Crystal Hysteresis Studies

In order to probe the possible SMM behaviour further, single-crystal magnetization vs applied dc field sweeps were performed for complexes **19-26** at various field sweep rates and temperatures using a micro-SQUID apparatus [9]. The obtained data for all complexes are somewhat similar and for the sake of brevity we present in Figure **5.24** only the data for **24–26**. Hysteresis loops were observed whose coercivity was strongly temperature and sweep rate dependent, increasing with decreasing temperature and increasing field sweep rate, as expected for the superparamagnetic-like behaviour of a SMM. Both **24** and **26** exhibit broad, poorly-resolved steps due to quantum tunnelling of magnetization (QTM), and **25** none at all, probably due primarily to step-broadening effects from the low-lying excited states, as well as distributions of local environments owing to ligand and solvent disorder, and (particularly for **25**) weak intermolecular interactions [3,4,10]. Magnetization vs time decay data were collected on **26**, which has the slowest relaxation at zero field, and used to construct an Arrhenius plot (Figure **5.25**); fitting of the thermally-activated region to the Arrhenius equation $\tau = \tau_0 \exp(U_{eff}/kT)$ gave U_{eff} = 13.9 K and $\tau_0 = 1.4 \times 10^{-8}$ s, where U_{eff} is the effective magnetization relaxation barrier.

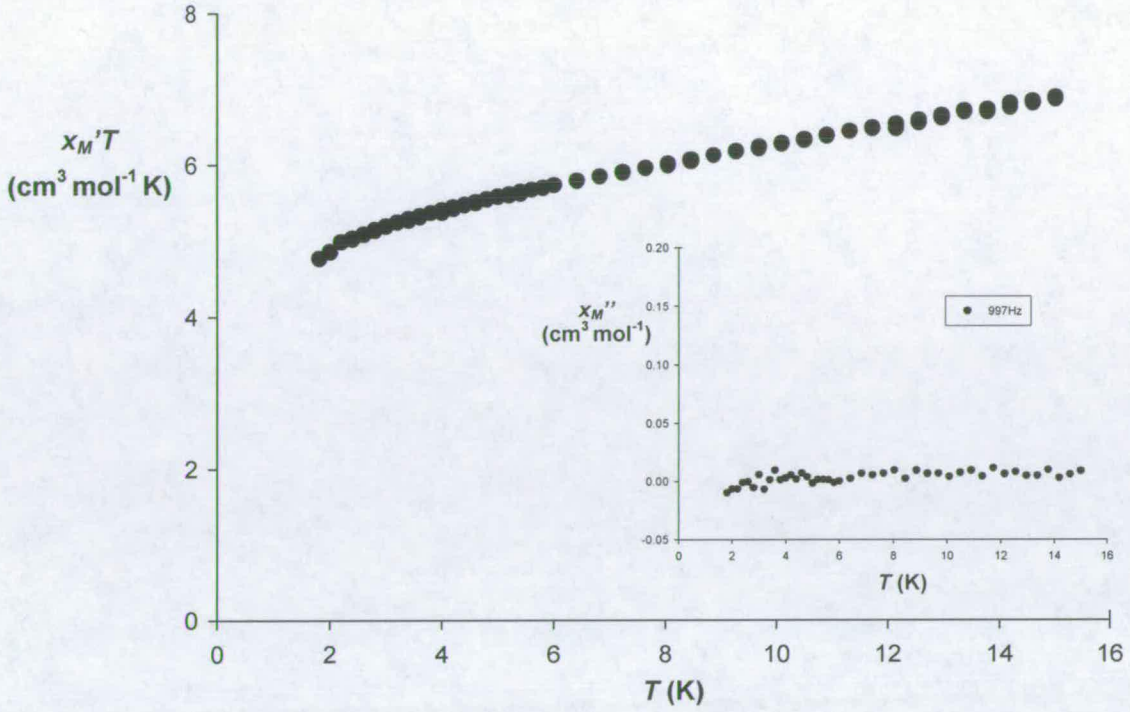

Figure 5.21. Plot of the in-phase (as $\chi_M'T$) and out-of-phase (χ_M'') ac susceptibility signal versus temperature for complex **16**.

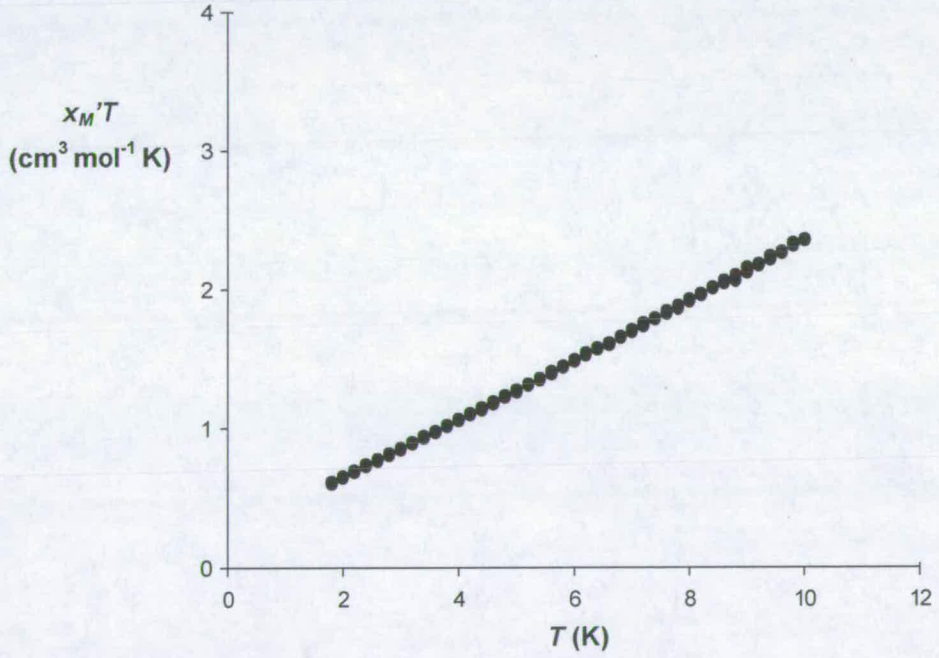

Figure 5.22. Plot of the in-phase (as χ_M'T) ac susceptibility signal versus temperature for complex **18**.

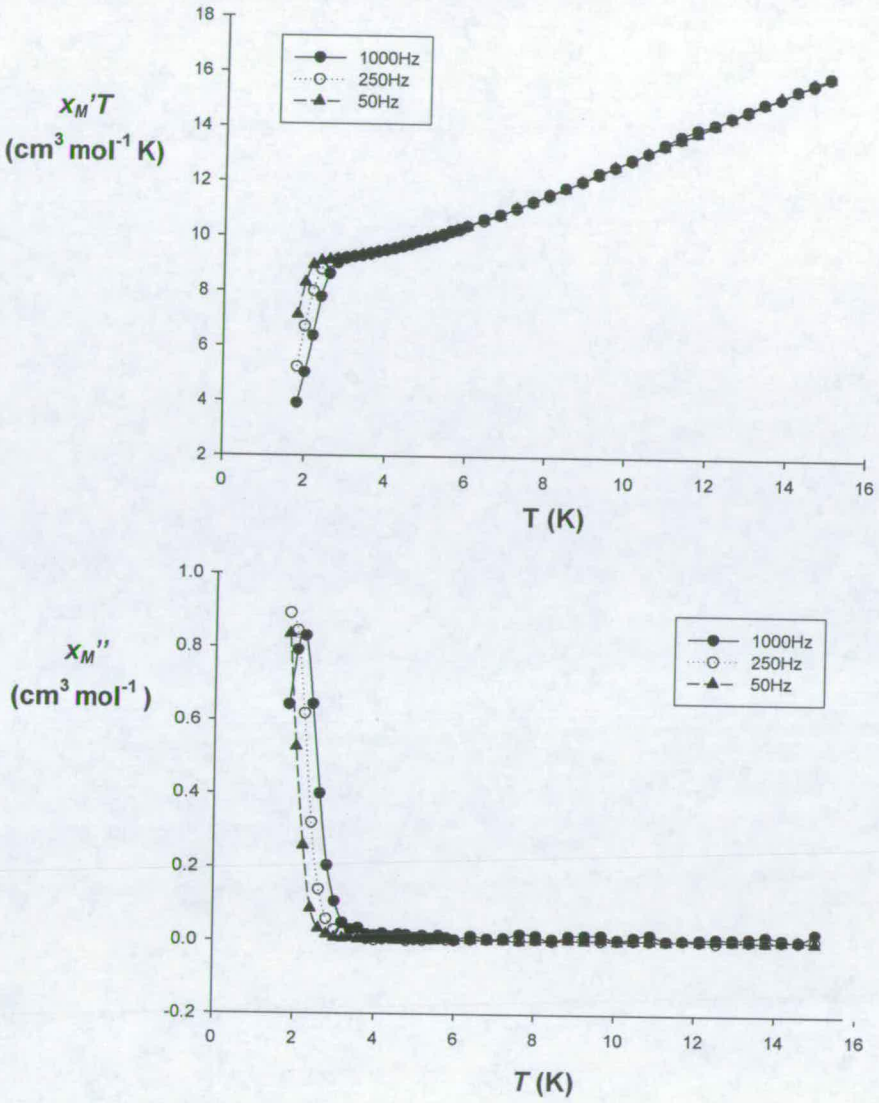

Figure 5.23. Plot of the in-phase (as $\chi_M'T$) (top) and out-of-phase (χ_M'') ac susceptibility signal (bottom) vs. temperature for complex **19**.

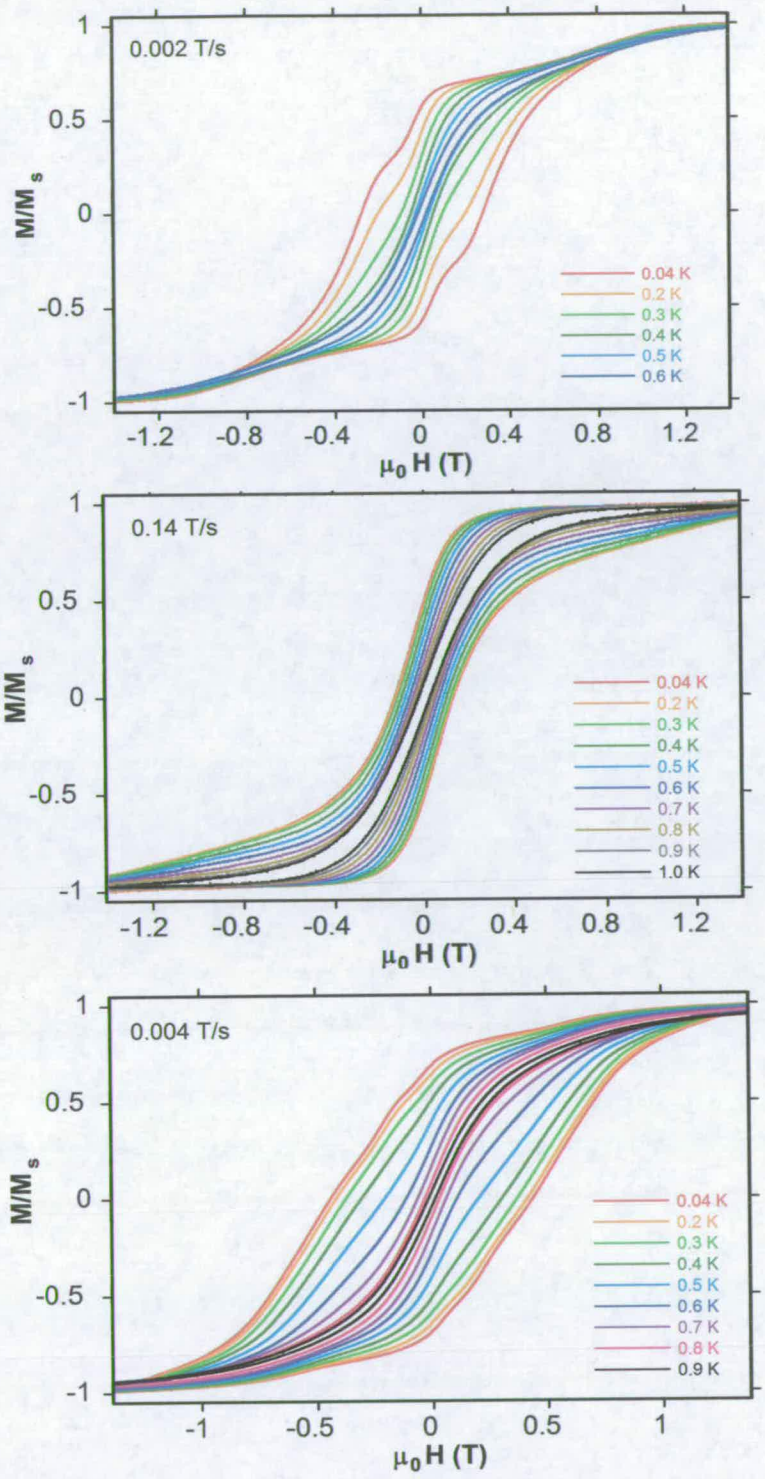

Figure 5.24. Single crystal magnetisation (M) versus field (H) hysteresis loops for complexes **24** (top), **25** (middle) and **26** (bottom) at the indicated field sweep rates and temperatures; the magnetisation is normalised to its saturation value (M_S).

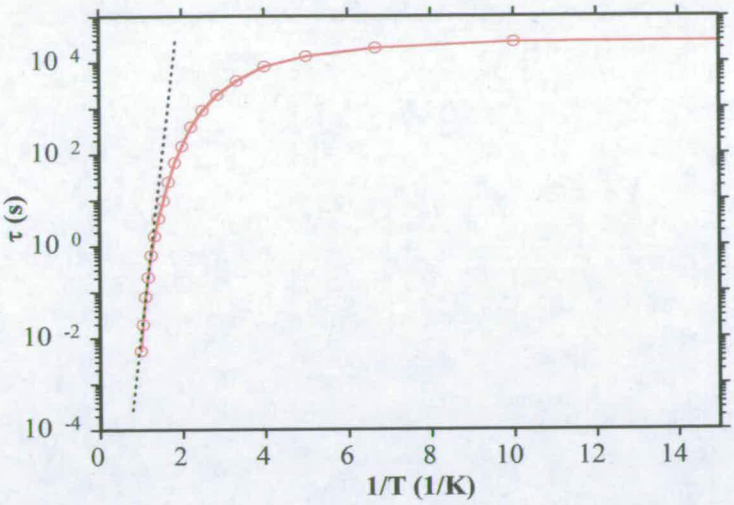

Figure 5.25. Arrhenius plot for **26**; the dashed line is the fit of the thermally-activated region to the Arrhenius equation.

Conclusions

In conclusion, the combination of a reductive aggregation route with tripodal alcohols has led to the formation of a family of eleven new clusters with unusual cores: two octahedral polymers, complexes **16** and **17** being 1-D and 2-D polymers, respectively; and nine edge-sharing bioctahedra: **18–26** of which complexes **19-26** are a new family of $Mn^{III}_4Mn^{II}_8$ SMMs. Complex **26** has a chain-like structure, although intermolecular interactions are not expected to be strong through the diamagnetic Na^+ ion, and the complex is magnetically not dissimilar to **19-25**.

References

[1] (a) M. Murugesu, M. Habrych, W. Wernsdorfer, K.A. Abboud, G. Christou, *J. Am. Chem. Soc.*, **2004**, *126*, 4766; (b) M. Soler, W. Wernsdorfer, K.A. Abboud, J.C. Huffman, E.R. Davidson, D.N. Hendrickson and G. Christou, *J. Am. Chem. Soc.*,

2003, *125,* 3576. (c) J.B. Vincent, C. Christmas, H.-R. Chang, Q. Li, P.D.W. Boyd, J.C. Huffman, D.N. Hendrickson and G. Christou, *J. Am. Chem. Soc.*, **1989**, *111*, 2086. (d) E. Bouwman, M.A. Bolcar, E. Libby, J.C. Huffman, K. Folting, and G. Christou, *Inorg. Chem.*, **1992**, *31*, 5185.

[2] (a) A.J. Tasiopoulos, A. Vinslava, W. Wernsdorfer, K.A. Abboud, G. Christou, *Angew. Chem. Int. Ed.*, **2004**, *43*, 2117; (b) A.J. Tasiopoulos, W. Wernsdorfer, K. Abboud and G. Christou, *Angew. Chem. Int. Ed.*, **2004**, *43*, 6338. (c) A.J. Tasiopoulos, W. Wernsdorfer, K.A. Abboud, and G. Christou. *Inorg. Chem.*, **2005**, *44*, 6324. (d) P. King, W. Wernsdorfer, K.A. Abboud, and G. Christou. *Inorg. Chem.*, **2005**, *44*, 8659.

[3] E. K. Brechin, *Chem. Commun.*, **2005**, 5141.

[4] (a) J.B. Vincent, H.R. Chang, K. Folting, J.C. Huffman, G. Christou, D.N. Hendrickson, *Am. Chem. Soc.*, **1987**, *109*, 5703. (b) J.B. Vincent, K. Folting, J.C. Huffman, G. Christou, *Inorg. Chem.*, **1986**, *25*, 996.

[5] (a) K.G. Caulton, M.H. Chisholm, S.R. Drake, K. Folding and J.C. Huffman, *Inorg. Chem.*, **1993**, *32*, 816; (b) W.J. Evans, D. G. Giarikos, M.A. Greci, J.W. Ziller, *Eur. J. Inorg. Chem.*, **2002**, 453.

[6] (a) M.I. Khan and J. Zubieta, *Prog. Inorg. Chem.*, **1995**, *43*, 1. (b) R.C. Finn and J. Zubieta, *J. Cluster. Sci.*, **2000**, *11*, 461; (c) M. Cavaluzzo, Q. Chen and J. Zubieta, *J. Chem. Soc., Chem. Commun.*, **1993**, 131.

[7] H.H. Thorp, *Inorg. Chem.*, **1992**, *31*, 1585.

[8] MAGNET, Davidson, E. R,. Indiana University.

[9] W. Wernsdorfer, *Adv. Chem. Phys.*, **2001**, *118*, 99.

[10] (a) E. Brechin, C. Boskovic, W. Wernsdorfer, J. Yoo, A. Yamaguchi, C. Sanudo, T. Concolino, A. Rheingold, H. Ishimoto, D. Hendrickson, G. Christou, *J. Am. Chem. Soc.*, **2002**, *124*, 9710; (b) M. Murugesu, J. Raftery, W. Wernsdorfer, G. Christou, E.K. Brechin, *Inorg. Chem.*, **2004**, *43*, 4203.

Conclusions

The goal of the project was successfully completed, resulting in the synthesis of twenty-five novel manganese clusters (using tripodal ligands) whose topologies are based on shared triangular [Mn_3] units. Some of these complexes behave as SMMs and five display an enhanced magnetocaloric effect (MCE) and have great potential as efficient magnetic refrigerants in low temperature applications.

A family of hexanuclear (and one dodecanuclear) mixed-valent, rod-like Mn complexes (**1-7**): $[Mn_6(OAc)_6(H_2tea)_2(tmp)_2]$ (**1**), $[Mn_6(OAc)_6(H_2tea)_2(thme)_2]$ (**2**), $[Mn_6(OAc)_6(H_2tea)_2(Hpeol)_2]$ (**3**), $[Mn_6(acac)_4(OAc)_2(Htmp)_2(aep)_2]$ (**4**), $[Mn_6(OAc)_8(tmp)_2(py)_4]$ (**5**), $[Mn_6(OAc)_8(thme)_2(py)_4]$ (**6**), $[Mn_{12}(Hthme)_8(thme)_2(py)_2Br_8]$ (**7**), whose structures are all based on edge-sharing triangles were synthesized. Magnetic studies reveal an important counter-complementarity effect which is responsible for a '*switch*' in ground state from $S = 0$ to $S = 4$ (for the hexanuclear complexes).

Rare examples of high-nuclearity "wheel-like" structures (**8-10**): $[Mn_{16}O_2(OMe)_{12}(tmp)_8(OAc)_{10}]$ (**8**), $[Mn_{22}O_6(OMe)_{14}(OAc)_{16}(tmp)_8(HIm)_2]$ (**9**), $[Mn_{22}O_6(OMe)_{14}(OAc)_{16}(Br\text{-}mp)_8(HIm)_2]$ (**10**) were made. The former (**8-10**) are amongst the largest nuclearity and highest spin Mn SMMs known - indeed the $S = 14$ ground state displayed by **8** is the largest seen for any Mn wheel.

Intial investigation of the coordination chemistry of $ampH_2$ and the closely related $aepH_2$ and H_4peol ligands have afforded beautiful and unusual mixed-valent decametallic Mn supertetrahedra: $[Mn_{10}O_4Br_4(amp)_6(ampH_2)_3(HampH_2)]Br_3$ (**11**), $[Mn_{10}O_4(OH)_{1.8}I_{2.2}(amp)_6(ampH_2)(HampH_2)_3]I_5$ (**12**) and a family of deca- and tetradecametallic "planar-discs": $[Mn_{10}(OH)_6(amp)_4(ampH)_4I_4(EtOH)_4]I_4$ (**13**), $[Mn_{10}(OH)_6(aep)_4(aepH)_4I_4(EtOH)_4]I_4$ (**14**), $[Mn_{14}(OH)_2(Hpeol)_4(H_2peol)_6I_4(EtOH)_6]I_4$ (**15**). Complexes **11-13** are the first characterised Mn clusters (and extremely rare examples of any transition metal clusters) containing the amp^{2-} ligand. Magnetic studies reveal complexes **11-14** to possess extremely large spin grounds state of $S = 22$ as a result of dominant

ferromagnetic exchange interactions between the metal centres; thus joining a select band of molecules displaying this unusual combination. All five complexes show an enhanced magnetocaloric effect: **11-12** as a result of negligible zero-field splitting of the maximum possible ground state; **13-15** as a result of possessing a high spin-degeneracy at finite low temperatures. The investigation of novel molecular clusters with a high spin-degeneracy at finite low temperatures opens the way to important improvements in the MCE of molecular complexes, and this ultimately facilitates their use in magnetic cooling applications. To this end the complexes above are the very best cooling refrigerants for low-temperature applications. Furthermore they suggest a new synthetic strategy for obtaining novel molecules with even larger MCE: the introduction of ions (and ligands) that will promote weak ferro- or ferrimagnetic interactions leading to high spin ground states and easily accessible (low-lying), degenerate, excited states with large *S*-values.

The combination of a reductive aggregation route with tripodal alcohols led to the formation of a family of eleven new clusters with unusual cores: two octahedral polymers: $Na_4[Mn_6O(OAc)_6(Br\text{-}mp)_4(MeOH)_4]$ (**16**) and $Na_3[Mn_6O(OAc)_5(tmp)_4(N_3)(H_2O)_2]$ (**17**) (1-D and 2-D polymers) respectively; and nine edge-sharing bioctahedra: $[Mn_{10}O_2Br_4(thme)_6(MeOH)_4]$ (**18**), $[Mn_{12}O_2(piv)_{10}(tmp)_4(MeO)_2(MeOH)_2]$ (**19**), $[Mn_{12}O_2(piv)_{10}(thme)_4(MeO)_2(MeOH)_2]$ (**20**), $[Mn_{12}O_2(OAc)_{10}(Hpeol)_4(MeO)_2(H_2O)_4]$ (**21**), $[Mn_{12}O_2(OAc)_{10}(thme)_4(MeO)_2(H_2O)_4]$ (**22**), $[Mn_{12}O_2(OAc)_{10}(tmp)_4(MeO)_2(H_2O)_4]$ (**23**), $[Mn_{12}O_2(O_2CCPh_2)_{10}(Hpeol)_4(MeO)_2(H_2O)_2]$ (**24**), $[Mn_{12}O_2(O_2CCPh_2)_{10}(Hpeol)_4(OH)_2(H_2O)_2]$ (**25**); and a bioctahedral polymer: $Na[Mn_{12}O_2(OAc)_{11}(Hpeol)_4(MeO)(OH)(H_2O)_3]$ (**26**) of which complexes **19-26** are a new family of $Mn^{III}_4Mn^{II}_8$ SMMs.

In conclusion, studies of the magnetic properties of **1-10** and **16-25** show that **5**, **6**, **8-10** and **19-26** are SMMs displaying beautiful and unusual structures, whilst complexes **11-15** display an enhanced magnetocaloric effect (MCE) being the best ever reported magnetic refrigerants at low temperatures, introducing a new area of research which looks very promising for real near-future application.

Publications

Mixed-Valent Supertetrahedra and Planar Discs as Enhanced Magnetic Coolers

M. Manoli, A. Collins, S. Parsons, A. Candini, M. Evangelisti, E.K. Brechin, *J. Am. Chem. Soc.*, **2008**, In Press.

Direct observation of mesoscopic quantum coherence in molecular nanomagnets

C. Schlegel, J. van Slageren, M. Manoli, E.K. Brechin, *Nature Mat.*, **2008**, submitted.

Ferromagnetic Ni^{II} Discs

R.T.W. Scott, L.F. Jones, I.S. Tidmarsh, M. Manoli, A. Collins, S. Parsons, W. Wernsdorfer, G. Aromí, E.J.L. McInnes, E.K. Brechin, *Chem.-Eur. J.*, **2008**, submitted.

High-Spin Mn Wheels

M. Manoli, M. Murugesu A. Prescimone, A. Mishra, R. Bagai, S. Parsons, W. Wernsdorfer, G. Christou, E.K. Brechin, *Inorg. Chem.*, **2007**, *46*, 6968.

A Ferromagnetic Mixed-Valent Mn Supertetrahedron: Towards Low-Temperature Magnetic Refrigeration with Molecular Clusters

M. Manoli, R.D.L. Johnstone, S. Parsons, M. Murrie, M. Affronte, M. Evangelisti, E.K. Brechin, *Angew. Chem. Int. Ed.*, **2007**, *46*, 4456.

A high-spin molecular wheel from self-assembled '*Mn rods*'

M. Manoli, A. Prescimone, A. Mishra, S. Parsons, G. Christou and E.K. Brechin, *Dalton Trans.*, **2007**, 532.

New octa- and dodecametallic mixed-valent Mn rods

M. Manoli, C.J. Milios, A. Mishra, G. Christou and E.K. Brechin, *Polyhedron*, **2007**, *26*, 1923.

A Family of [Mn_6] Complexes Featuring Tripodal Ligands

C.J. Milios, M. Manoli, G. Rajaraman, A. Mishra, L.E. Budd, F. White, S. Parsons, W. Wernsdorfer, G. Christou, E.K. Brechin, *Inorg. Chem.*, **2005**, *45*, 6782.

Conferences attended

"**MAG-NET Magnetism Workshop**", Cambridge, U.K, September 2005 (poster presentation).

"**EastChem Symposium**", St Andrews and University of Edinburgh, June 2006 (five minutes presentation).

"**10th ICMM Conference: International Coference on Molecule-based Magnets**", Victoria, Vancouver Island, British Colombia, August 2006 (poster presentation).

"**MAG-NET Magnetism Workshop**", Edinburgh, U.K, August 2006 (poster presentation).

"**ScotCHEM Computational Chemistry Symposium**", St. Andrews, U.K, April 2007 (poster presentation).

"**2nd North America-Greece-Cyprus Workshop on Paramagnetic Materials**", Syros, Greece, June 2007 (fifteen minutes presentation).